UNIVERSITÉ DU LUXEMBOURG

PhD-FSTC-2011-19
The Faculty of Sciences, Technology and Communication

DISSERTATION

Defense held on 28/10/2011 in Luxembourg
to obtain the degree of

DOCTEUR DE L'UNIVERSITÉ DU LUXEMBOURG
EN PHYSIQUE

by

Jes K. LARSEN

Born on the 27th of April 1983 in Nakuru (Kenya)

INHOMOGENEITIES IN EPITAXIAL CHALCOPYRITES STUDIED BY PHOTOLUMINESCENCE

Dissertation defense committee

Dr. Susanne SIEBENTRITT, Dissertation supervisor
Professor, Université du Luxembourg

Dr. Levent GÜTAY
Université du Luxembourg

Dr. Jürgen CHRISTEN
Professor, Otto–Von–Guericke Universität, Magdeburg

Dr. Roland SCHEER
Professor, Martin–Luther–Universität, Halle–Wittenberg

Dr. Roland SANCTUARY, Chairman
Professor, Université du Luxembourg

Contents

1 Introduction

For more than 30 years the chalcopyrite $Cu(In,Ga)Se_2$ materials have been described as a "promising candidate" for thin film solar cell applications. The work on chalcopyrite–based solar cells started in the early 1970s, even though the first reports on synthesis and characterization of $CuInSe_2$ and $CuGaSe_2$ were published already in 1953 [1]. The pioneering work was mainly performed at the Bell Laboratories, where a $CuInSe_2$ solar cell with a 12 % efficiency was demonstrated under outdoor illumination "on a clear day in New Jersey" in 1975 [2, 3].
Today, $Cu(In,Ga)Se_2$ can be regarded as a mature technology. $Cu(In,Ga)Se_2$–based small area solar cells with an efficiency of above 20% has been realized lately [4], and chalcopyrite based solar cells are not any more restricted to the research laboratory. In these years $Cu(In,Ga)Se_2$ solar cells are installed on rooftops of the electricity consumers. With an annual production of $Cu(In,Ga)Se_2$ commercial solar modules of 439 MW in 2010 (an increase of 144 % compared to 2009) the market is developing rapidly. An even higher growth rate in the production of 193 % is expected in 2011 [5]. The efficiency of thin film chalcopyrite modules is approaching the one obtained by small scale laboratory cells, though a large efficiency gap still remains. The highest efficiency of a commercial size module is 15.7 % [6], while the current world record for modules out of mass production is 13.4 % [7].
Even though high efficiencies have been demonstrated and the $Cu(In,Ga)Se_2$ technology is entering the market for commercial solar cells, there are still many questions regarding basic material properties that remain unanswered. The fact that so good results have been obtained may even be regarded as a minor miracle in the light of the many unsolved mysteries [8].
The aim of this work is to investigate some of the aspects of the $CuGaSe_2$ and $CuInSe_2$ materials that are not yet understood. The investigations are all related to different kinds of inhomogeneities observed in the absorber material. Chapter 2 will form the foundation for this by giving a general introduction to the chalcopyrite material system and explaining some of the aspects that are already well understood.
In order to understand the inherent properties of chalcopyrites, and unambiguously ascribe the observations to different effects, it is necessary to be able to investigate material with as few artefacts as possible. It is for example highly desirable to be able to exclude the effects of grain boundaries and interfaces, which are often seen to affect the device properties of chalcopyrite solar cells [9, 10]. In this work this is achieved by investigation of single crystalline material epitaxially grown on GaAs. With this approach one can exclude the influence of grain boundaries on the measurement results. The studies furthermore focus on only the properties of the absorber material. The formation of a p–n junction with appropriate choice of buffer material is avoided, thereby simplifying the studied system.
High efficiently solar cells are based on $Cu(In,Ga)Se_2$ – an alloy containing both In and Ga [4]. Balancing the [Ga]/[In] ratio allows tuning of the band gap to match the solar spectrum ideally [3, 8]. One disadvantage of the $Cu(In,Ga)Se_2$ alloy is, however, that

inhomogeneities of the band gap can potentially occur due to local fluctuations of the [Ga]/[In] ratio [11]. In this work the effect of alloying is avoided by restricting the study to only the ternary $CuInSe_2$ and $CuGaSe_2$.
Following this argumentation $CuInSe_2$ and $CuGaSe_2$ samples investigated in this study are grown epitaxially on GaAs. All epitaxial samples investigated in this work are grown by metalorganic vapour phase epitaxy (MOVPE). The MOVPE system is a new installation installed four months after my arrival at the University of Luxembourg. A part of this work is therefore devoted to development and establishment of a growth process yielding high quality epitaxial samples. This is the topic of chapter 3.
The main tool for analysis in this work is photoluminescence (PL). The advantage of PL is that it is a contact free, and non–destructive measurement technique. Room temperature PL gives insight into the optoelectronic properties of the material and can be analysed to extract information about parameters that directly influence the performance of solar cells such as the band gap and splitting of quasi–Fermi levels [11, 12]. PL performed at low temperature is, furthermore, a very sensitive tool to study defects in the material [10]. In this work the advantages of PL are utilized in a system with sub–micron spatial resolution. This opens the possibility to study interesting effects such as spatial variation of defect related recombination and the influence of localized secondary phases.
Various inhomogeneities are investigated in this work with PL. One of the studied effects is potential fluctuations. Several studies have shown that Cu-poor ([Cu]/[III]<1, where [III] is the concentration of In and Ga) $Cu(In,Ga)Se_2$ shows potential fluctuations at low temperatures which dramatically reduce the mobility and thus the diffusion length in solar cells [10, 13, 14, 15]. It is however often assumed that the fluctuations persist at room temperature [16, 17]. In order to characterize the properties of these fluctuations and their temperature dependence epitaxial $CuGaSe_2$ and $CuInSe_2$ absorbers are examined by temperature and intensity dependent photoluminescence. Record $Cu(In,Ga)Se_2$ solar cells with an efficiency around 20% are obtained for [Cu]/[III] ratios ranging from 0.80 to 0.92 [4]. Chalcopyrites with a significant Cu deficiency are therefore industrially relevant as well as scientifically interesting. This is the topic of chapter 4.
Chalcopyrites grown under Cu–rich conditions (meaning [Cu]/[III] > 1) are not less interesting than their Cu–poor counterparts. It has even been shown that many properties such as defect densities, transport properties and bulk recombination are improved when growing under Cu–excess [15, 14, 18, 19]. The record devices with efficiencies exceeding 20 % are obtained by a three stage process [4]. This commonly applied growth process, interestingly also involves a growth stage with Cu–excess where Cu_xSe crystallites form at the surface [20]. A simplified process, which still includes a Cu–excess phase, is also used in industrial production [21]. The Cu–excess step is usually thought to be necessary to achieve large grains [22]. Nevertheless, the fundamental effect of the very common Cu–excess stage on crystal quality is not fully understood yet, calling for further well designed experiments in which the effect of grain size, morphology, and alloying of In and Ga can be excluded, allowing for an investigation of solely the effect of the Cu–excess on the absorber properties. This will be one of the experiments discussed in chapter 5 along with other results of spatially resolved photoluminescence.

Background and Review 2

This chapter gives an introduction to the chalcopyrite material, heteroepitaxial growth, and the main experimental method used in this work, namely photoluminescence.
Basic material properties of the chalcopyrite materials $CuGaSe_2$ and $CuInSe_2$ will be presented. This includes a description of the crystal structure, the phase diagram and the band structure of the two materials, followed by a discussion of defect formation in chalcopyrites. Further material properties of $CuInSe_2$ and $CuGaSe_2$ are collected in appendix C.
The second section of this chapter aims to describe some of the phenomena encountered when performing heteroepitaxial growth experiments. This includes a discussion of the lattice mismatch, the critical thickness and the consequence of different thermal expansion coefficients of layer and substrate. This section is finalized by a discussion of the strain measured in epitaxial $CuGaSe_2$ and $CuInSe_2$ and the influence of strain on the band gap.
The third section finally focuses on the theoretical background of low temperature photoluminescence. This is included since photoluminescene is the main experimental technique used in this work. A brief explanation of other experimental techniques is found in appendix D. The in–depth description of photoluminsece is included since it is important to understand the various transitions that can be observed in the measurements. The theory of different transition types observed at low temperature and the experimental discrimination between them is presented. Experimental PL results from literature are finally discussed and a model that describes the experimentally observed defect transitions in $CuInSe_2$ and $CuGaSe_2$ is presented. The theory of room temperature photoluminescence will be discussed in chapter 5.

2.1 Introduction to Chalcopyrite Materials

2.1.1 Crystal Stucture

$CuGaSe_2$ and $CuInSe_2$, both ternary I–III–VI_2 compounds, crystallize in the chalcopyrite lattice structure. The chalcopyrite lattice is tetragonal with a unit cell that is described by the lattice constants a and c, as shown in figure 2.1.
The chalcopyrite structure can be derived from the crystal structure of the II–VI semiconductor ZnSe (a structure also known as zincblende). By isoelectronic substitution of the group II element (Zn) with with an equal amount of elements from group I (Cu) and elements from group III (Ga or In) the chalcopyrite lattice can be derived. It is, however, a bit more complicated than the simple substitution due to the different chemical nature of the elements. Where the ZnSe unit cell is cubic the chalcopyrite unit cell contains two ZnSe unit cells stacked on top of each other thereby becoming tetragonal. A tetragonal distortion η observed in $CuGaSe_2$ and $CuInSe_2$ can be defined as $\eta = \frac{c}{2a} \neq 1$. The tetragonal distortion is a result of the different chemical nature of the bonds. The bond strength of the Cu–Se and the III–Se bonds differ leading to slightly different bond lengths [3].

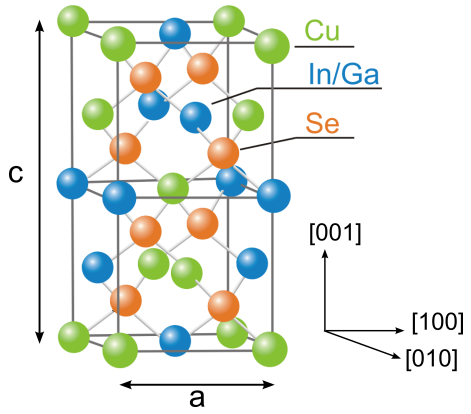

Figure 2.1: Unit cell of the chalcopyrite structure of Cu(In,Ga)Se_2 [23].

From X–ray diffraction measurements values of the lattice constants and the tetragonal distortion can be determined. For $CuInSe_2$ the unit cell is slightly dilated along the c–axis giving $\eta = 1.006$ [24]. The unit cell of $CuGaSe_2$ is on the other hand compressed along the c–axis leading to $\eta = 0.982$ [25]. The lattice constants used here are given in table 2.1. Another difference between the ZnSe structure and the chalcopyrite is the anion displacement to position u also arising due to different bond lengths of Cu–Se (R_{I-VI}) and III–Se (R_{III-VI}). The position of the Se atom is given by:

$$u = \frac{1}{4} + \frac{R_{I-VI}^2 - R_{III-VI}^2}{a^2}, \tag{2.1}$$

where a is the lattice constant of the short edge of the unit cell [26]. With values for the bond length in $CuInSe_2$ [27] of $R_{I-VI} = 2.484$ Å and $R_{III-VI} = 2.586$ Å a Se displacement of $u = 0.23$ is found, slightly different from $u = 0.25$ for ZnSe. For $CuGaSe_2$ an $u = 0.264$ has been theoretically calculated [28].
The different bond lengths and the displacement of the Se atom from its zincblende position has an influence on the electronic structure of the chalcopyrite since a crystal field arises. This issue will be discussed in section 2.1.3.

2.1.2 Phase Diagram

In order to grow high quality epitaxial absorber layers it is advantageous to know the phase diagram of the material system. This knowledge is needed to predict the phases present under different growth conditions. Phase diagrams are in principle only valid under equilibrium conditions but still give an idea which phases one can expect under different growth conditions. The phase diagram for the Cu–Ga–Se system [29] and the Cu–In–Se system [30] will be discussed in the following.
Thin films prepared under Se excess, have compositions that fall on or very close to the pseudo-binary line between Cu_2Se and In_2Se_3 for indium containing material and Ga_2Se_3 for gallium containing material [3]. It is therefore relevant to investigate this pseudobinary section of the phase diagrams. Figure 2.2 shows the phase diagrams of this section near the compositions where the chalcopyrite phase is stable.
The material system Cu–In–Se is well characterized compared to the less studied Cu–Ga–Se system [31]. According to Stanbery, who reviewed the phase diagram of $CuInSe_2$ there are, however, many inconsistencies and incompleteness to be found in the extensive

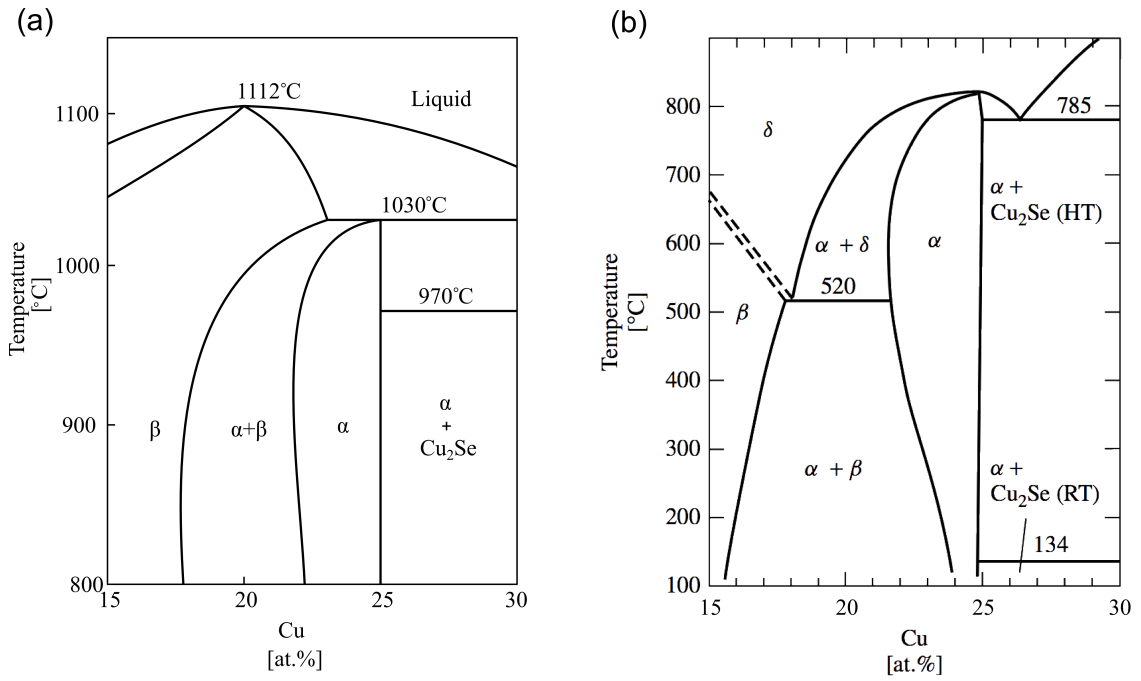

Figure 2.2: (a) Phase diagram for the Cu–Ga–Se system along the Cu_2Se–Ga_2Se_3 pseudobinary section. The phase labelled α is the chalcopyrite and the β region contains the ordered defect compound (ODC) phase $CuGa_5Se_8$. Redrawn after [29]. (b) Phase diagram of the Cu-In-Se system along the pseudo–binary section between Cu_2Se and In_2Se_3. The α phase is the chalcopyrite, δ is the high temperature zincblende phase and β an ordered defect compound (ODC) phase. Cu_2Se exist in a high–temperature (HT) phase and a room–temperature phase (RT) [30]. Notice that the temperature scales of the phase diagrams are different.

literature on the subject [31]. It will therefore only be attempted to give an overview of the general properties of the material system.

Figure 2.2(b) shows the phase diagram along the Cu_2Se–In_2Se_3 pseudobinary section. The region labelled α represent the compositions, which crystallize in the chalcopyrite structure. It is noticed that the chalcopyrite phase at 100 °C is found for a Cu content in the range between $\approx$ 24 % and $\approx$ 24.9 %. This means that the chalcopyrite phase can exist with a significant deviation from stoichiometry. The chalcopyrite in which [Cu]/[III]<1 is said to be Cu–poor. In order to form these materials a large number of Cu vacancies must be formed.

When the Cu content is increased above $\approx$ 24.9 %, one enters the Cu–rich growth regime ([Cu]/[III]>1), and a secondary phase consisting of Cu_xSe with x$\approx$2 appears in addition to the chalcopyrite. In other words, the chalcopyrite is not able to accommodate a Cu-excess and the additional Cu ends up in the Cu_xSe phase. On the Cu–rich side of the phase diagram it is interesting that the chalcopyrite phase is not stable for a Cu–In–Se composition with a Cu content of 25 %. In equilibrium it is found that samples with the stoichiometric $CuInSe_2$ composition in fact consist of a mixture of slightly Cu–poor chalcopyrite and a secondary Cu_xSe phase. In other words, perfectly stoichiometric $CuInSe_2$ does not exist under equilibrium conditions [31].

The other phases seen in figure 2.2(b) should also be briefly discussed. The high temperature zincblende δ phase, where the occupation of the III and Cu positions is disordered, is found with a wide range of compositions. This phase is unstable at room temperature and therefore normally not observed. This phase is under equilibrium conditions transformed into the chalcopyrite α phase around 800 °C for samples with a composition close

to the stoichiometric point. The phase labelled β is the rather controversial ordered defect compound (ODC). There is no agreement whether the β phase is a single phase with a wide existence range or if this part of the phase diagram is in fact composed of a series of closely spaced phases with narrow ranges of stability. At least eight different compounds have been found in this region of the phase diagram, the most commonly mentioned is the $CuIn_3Se_5$. For even more Cu–poor compositions the ODC also referred to as the γ phase with the composition $CuIn_5Se_8$ is found [31].
Figure 2.2(a) shows the phase diagram of the Cu–Ga–Se system along pseudobinary section $(Cu_2Se)_{x-1} - (Ga_2Se_3)_x$ [29]. The lowest temperature in this diagram is 800 °C, but the general characteristics of the phase diagram are similar to the more studied Cu–In–Se system. It can therefore be expected that the overall behaviour will be the same. Like the In containing chalcopyrite, the Ga containing chalcopyrite structure is stable with a significant Cu–deficiency. Also for both material systems, a secondary Cu_xSe appears when crossing the border to the Cu–rich regime.
In the Ga containing material it is similarly found that phases such as $CuGa_3Se_5$ [32] or $CuGa_5Se_8$ [33] are found under very Cu–poor growth conditions. These phases are included in the region labelled β in the phase diagram. This region of the phase diagram with a high mole fraction of Ga_2Se_3 is not well characterized [29].

2.1.3 Fundamental Band Gap

Chalcopyrites have a direct band gap located at the center of the Brillounin zone known as the Γ point. The electronic structure of the chalcopyrites is, like the crystal structure, closely related to the structure of ZnSe. Figure 2.3 illustrates how the electronic structure at the Γ point can be derived from ZnSe.

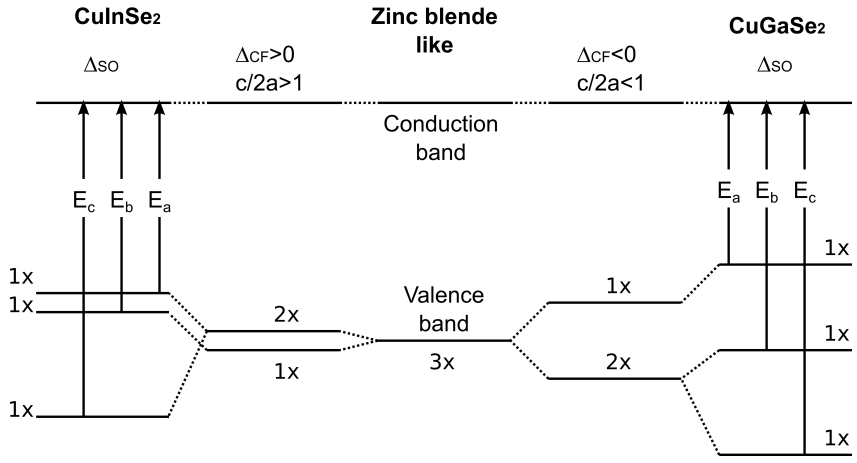

Figure 2.3: The band structure of $CuInSe_2$ and $CuGaSe_2$ as it is derived from the cubic zincblende by taking the spin orbit and crystal field splitting into account. The degeneracy of the valence band is denoted $3x, 2x, 1x$. The three fundamental band gaps E_a,E_b, and E_c are indicated [23, 34].

The ZnSe structure has one conduction band and a three–fold degenerate valence band at the zone center if spin orbit coupling is ignored. The fact that atoms are displaced from their ideal zincblende positions in the chalcopyrite structure leads to the appearance of a crystal field splitting Δ_{CF} of the valence bands. Due to the crystal field splitting which is negative in $CuGaSe_2$ ($\eta = 0.982$) and slightly positive in $CuInSe_2$ ($\eta = 1.006$) the valence band splits into a non-degenerate level and a twofold degenerate level. This

is, however, not a complete description of the band structure. The spin–orbit coupling due to the interaction of the electron spin with its angular momentum leads to further splitting of the valence bands. If the effect of spin–orbit splitting Δ_{SO} is taken into account it is realized that the valence band in chalcopyrites is in fact composed of three non–degenerate bands as illustrated in figure 2.3 [34]. Please note that the zincblende band structure is hypothetically shown without spin–orbit coupling in the figure.
The presence of three valence bands leads to three fundamental band gaps with energies E_a, E_b, and E_c. The energies of these band gaps are collected in appendix C. It is worth noticing that for $CuInSe_2$, which has a very small tetragonal distortion the crystal field splitting is so small that the difference between the a band gap E_a and the b band gap E_b is experimentally very difficult to distinguish at room temperature [34].

2.1.4 Defects in Chalcopyrites

Formation of crystal defects in chalcopyrites plays a key role in the performance of the material in a solar cell device. In general crystal defects can be grouped in four classes:

1. Dislocations or line defects where several atoms are misaligned in the crystal. The two basic types of dislocations are screw and edge dislocations. During epitaxial growth line dislocations often develop into threading dislocations [35].

2. Planar defects which can be understood as an array of dislocations. An example of a planar defect is a grain boundary where the crystal orientation changes abruptly at the interface. Another example is a stacking fault, which is an interruption of the atomic layer stacking order [36].

3. Three dimensional defects where a part of the crystal is either missing (voids) or replaced by another material (inclusions).

4. Point defects occurring at single lattice points. This includes both extrinsic and intrinsic defects. In $Cu(In,Ga)Se_2$ intrinsic defects are extremely important since they are responsible for doping of the material [37]. Since these defects are also involved in the photoluminescence transitions observed in $CuGaSe_2$ and $CuInSe_2$ the intrinsic defects will be briefly discussed. The three different types of native point defects that can appear are [38]:

    - A vacancy is an unoccupied lattice site. Vacancies are e.g. denoted V_{Cu} meaning a vacancy at the Cu lattice position.
    - An interstitial is an atom occupying a position in the crystal that is usually not occupied. Interstitials are e.g. denoted Cu_i meaning a Cu atom in an interstitial lattice site.
    - An antisite is an atom of one species placed on the lattice position of another species. Antisite defects are e.g. denoted In_{Cu} meaning that an In atom is occupying a Cu lattice site.

Some point defects form very easily in chalcopyrites. According to the reviews [31, 37] and the most cited work on the topic [39] the isolated point defects in $CuInSe_2$ and $CuGaSe_2$ with the lowest formation enthalpy are the cation antisites Cu_{III}, III_{Cu} and the copper vacancy V_{Cu}. The defect formation enthalpy is, however, not a simple constant. It

depends on the Fermi level and the composition of the material. The Cu vacancy has for example lower formation enthalpy and is more likely to form in material grown under Cu–poor conditions [39]. Due to the dependency of the formation enthalpy on the Fermi level the formation of different defects is not independent. If for example a positively charged In_{Cu}^{2+} donor is formed this leads to an increase of the Fermi level since two free electrons are released. The increased Fermi level will at the same time lower the formation energy of negatively charged V_{Cu}^{-}, making it more probable to form Cu vacancies [37]. In this way a Cu–vacancy can form as a counter reaction to the increase of the Fermi level. This self–compensating effect explains the doping limits observed in chalcopyrites [10].
In $CuGaSe_2$ the V_{Cu}^{-} has a very low formation enthalpy that even becomes positive when the Fermi level is raised. This means that the formation of Cu vacancies becomes exothermic. The fact that the formation enthalpy becomes positive already before the Fermi level reaches mid–gap explains that $CuGaSe_2$ cannot become n–type. In $CuInSe_2$, the Fermi energy for which the formation of Cu vacancies becomes positive lies above mid-gap. This explains that $CuInSe_2$ can become n–type under Cu–poor and Se–poor conditions [40]. The Fermi level dependent defect formation enthalpy also explains the doping limits for extrinsic dopants [39].
The ability to form large concentrations of defects has important consequences for the material. For $CuInSe_2$ first principles calculations have revealed that In_{Cu} and V_{Cu} can form in very large concentrations of several percent. These two defects are known to form a neutral strongly bound defect complex consisting of $(In_{Cu}^{2+} + 2V_{Cu}^{-})$. This explains that $CuInSe_2$ can exist with a significant Cu–deficiency [37].
The chemical nature of defects in chalcopyrites is not only investigated in theoretical calculations. Experimental studies of vacancies in $CuInSe_2$ with positron annihilation lifetime measurements are also available. Based on investigations of epitaxial layers on GaAs it has been proposed that the $(V_{Se} - V_{Cu})$ divacancy is the most probable defect [41]. A similar conclusion is drawn in a recent positron Doppler spectroscopy study performed in collaboration between our group and the positron annihilation spectroscopy group at Aalto University, Finland. In the not yet published work it is proposed that the divacancy $(V_{Se} - V_{Cu})$ and a defect related to the single vacancy V_{Cu} are the dominating defects in $CuGaSe_2$ and $CuInSe_2$ [42].
Experimental information about defects can also be obtained with photoluminescence measurements, various capacitance methods and Hall measurements. Low temperature PL measurements are utilized to obtain information about the energetic distance of shallow defects to the bands. Capacitance measurements yield information about the energetic position of deeper defects, and Hall measurements can give defect densities and the energetic position of the shallow defects [37]. All these methods have in common that they do not give direct information about the chemical nature of the defects involved in the transitions. Energies of shallow defects identified with PL measurements are discussed in section 2.3.8.

2.2 Hetero–epitaxial Growth of Chalcopyrites on GaAs

One of the main aims of this work is to develop an epitaxial growth process. This section therefore discusses the issues and problems of heteroepitaxial growth from a theoretical and experimental point of view. The aim is to introduce and discuss the general problems

that are faced when performing heteroepitaxial growth. Issues treated here are important to understand and have in mind when performing epitaxial growth experiments. Since the effects discussed in this section also affect the properties of the final layers, it is important to be aware of these effects when investigating the properties of the epitaxial absorber layers.
The term epitaxy is used to describe the process in which single crystalline material is grown onto a single crystalline substrate so that the grown layer has the same structural orientation as the substrate. If the growing layer and the substrate are the same material one talks of homo–epitaxy (e.g. GaAs on GaAs). If the substrate and growing layer are different materials (e.g. $CuGaSe_2$ on GaAs) it is referred to as hetero–epitaxy.
When attempting to grow hetero–epitaxially one faces a series of problems. The two materials generally have different lattice constants giving rise to a lattice mismatch m:

$$m = \frac{a_{substrate} - a_{layer}}{a_{layer}}, \tag{2.2}$$

where $a_{substrate}$ and a_{layer} are the lattice constants of the substrate and layer respectively. This lattice mismatch gives rise to strain in the growing layer and eventually introduction of misfit dislocations. In epitaxial films misfit dislocations (typically edge dislocations) often lead to threading dislocations that extend throughout the film and terminate at the surface [43, 44] as illustrated in figure 2.4.

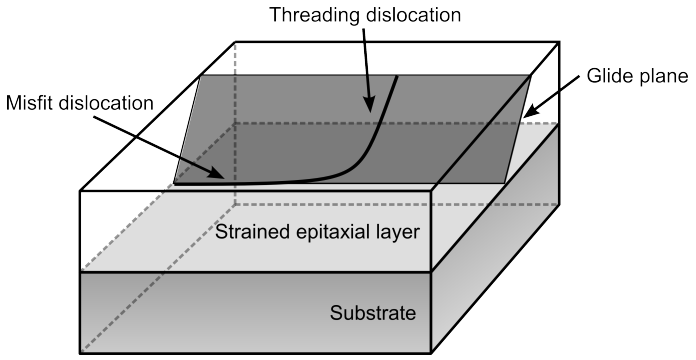

Figure 2.4: Illustration of a treading dislocation that extends from the substrate–layer interface to the surface of the layer. The dislocation is able to move in a glide plane in the crystal. Redrawn after [44].

A high density of threading dislocations is very deleterious to the material quality by leading to short minority carrier lifetimes [45, 46, 43]. Transmission electron microscopy (TEM) investigations of $Cu(In,Ga)Se_2$ epitaxially grown on GaAs(001) have demonstrated a high concentration of threading dislocations of $\approx 10^9$ cm^{-2} [47].
Another property of the material system that is very important for the success of the growth experiment is the difference in thermal expansion coefficients between the substrate and the epitaxial layer. Growth is typically performed at several hundred degrees Celsius, after which the sample is cooled down. If the layer and the sample contract at very different rates during the cool down this also leads to strain in the layer. In the worst case this can even lead to crack formation.
Other problems commonly encountered when performing hetero–epitaxy growth experiment includes: Low thermal conductivity of the growing layer, contamination of the film by elements from the substrate, reactivity of the substrate and layer, and poor wetting of the substrate. All these effects can influence the resulting properties of the epitaxial layer [45]. The following will focus only on the issues related to the lattice and thermal

expansion mismatches.

2.2.1 Lattice Mismatch and Critical Thickness

The lattice mismatch between the chalcopyrite layer and the GaAs substrate affects the growing layer severely. In the beginning of the growth while the layer is very thin the chalcopyrite will adapt the lattice constant of GaAs. The growing layer will be highly strained in this phase of the growth known as pseudomorphic growth. As the layer thickness increases the amount of elastic strain energy also increases. At some layer thickness, known as the critical thickness, d_c it becomes energetically favourable to reduce the strain by introduction of misfit dislocations. Growth beyond this layer thickness leads to relaxation of the layer by introduction of dislocations [46].

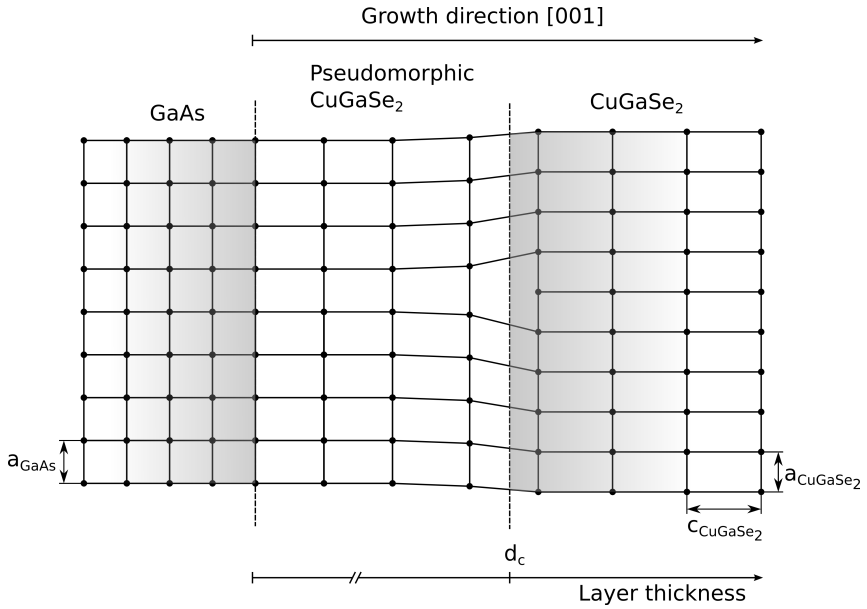

Figure 2.5: Illustration of hetero–epitaxy of $CuGaSe_2$ on GaAs substrate. The lattice mismatch is overcome by introduction of a dislocation when the layer reaches the critical thickness d_c [48].

Figure 2.5 illustrates the interface region of $CuGaSe_2$ with a misfit dislocation grown on GaAs. The standard model applied to predict the critical thickness is the so-called Matthews and Blakeslee approach. In this model the dislocation forms when its energy of formation is lower than the strain energy it relaxes [46]. This model is, however, rather complex in its entirety and requires precise knowledge of many material parameters and geometry of the dislocations involved. Since some material parameters such as the elasticity and Possion ratio may differ from their bulk values in very thin films further difficulties arise in the application of the exact Matthews and Blakeslee model [46].
As discussed by Dunstan et al. one can as a general rule of thumb use a simple approximation to estimate the critical thickness of the epitaxial layers [49]. In general it is found that the critical thickness is inversely proportional to strain due to the lattice mismatch $d_c \propto m_{GT}^{-1}$, where m_{GT} is the lattice mismatch at growth temperature.The proportionality factor was empirically determined for III-V semiconductor heterostructures to yield [50]:

$$d_c \approx \frac{0.8\text{nm}}{m_{GT}} \tag{2.3}$$

In order to determine the critical thickness, it is necessary to know the lattice mismatch. If

it is assumed that the layer grows with the c–axis perpendicular to the GaAs(001) surface (see section 3.6.3), the lattice mismatch that must be taken into account is the difference between the a–axis of the chalcopyrite and the a–axis of GaAs at growth temperature. The length of the a–axes at growth temperature is given by $a_{GT} = a + a\alpha_a\Delta T$, where ΔT is the temperature difference between room and growth temperature and α_a is the thermal expansion coefficient.
The lattice parameters are collected along with other material properties in table 2.1. Lattice parameters given in the table are found in powder diffraction files of the International Centre for Diffraction Data (ICDD) database. The citations in the table refer to the papers, which form the basis for the lattice parameters given in the ICDD database.
Applying equation (2.3) and equation (2.2) the critical thickness can be determined to $d_c = 43$ nm for $CuInSe_2$ and 153 nm for $CuGaSe_2$. These values are, as mentioned earlier, just estimates. When the layer reaches the critical thickness dislocations will form, which relaxes the layer. This does, however, not necessary also mean that the layer is totally relaxed [49]. Residual strain can remain and additional strain can appear during cool down as discussed in the following section.

Property	$CuInSe_2$	$CuGaSe_2$	GaAs
a (Å)	5.760 [24]	5.614 [25]	5.6538 [51]
c (Å)	11.591 [24]	11.022 [25]	c = a
$\alpha_a(\cdot 10^{-6}\ K^{-1})$	10.3 [52], 11 [53]	13.1 [54]	5.7 [55], 6 [56], 6.9 [51, 57]
$\alpha_c(\cdot 10^{-6}\ K^{-1})$	7.9 [52], 8.4 [53]	5.2 [54]	$\alpha_c = \alpha_a$
C_{13} (GPa)	45 [58]	53 [58]	–
C_{33}(GPa)	63 [58]	72 [58]	–
$\epsilon_{\parallel,a}$(%)	-1.84	0.71	–
$\epsilon_{\parallel,c}$(%)	-2.45	2.59	–
d_c (nm)	43	153	–

Table 2.1: Collection of material properties for $CuInSe_2$, $CuGaSe_2$, and GaAs: Lattice parameters a and c, thermal expansion coefficients along the a–axis α_a and c–axis α_c, and elastic stiffness components C_{13} and C_{33}. Since the elastic stiffness of $CuGaSe_2$ is not available the values for $AgGaSe_2$ are used. Calculated properties of the hetero–epitaxial system: strain in a pseudomorph layer for growth with the a–axis parallel to the substrate $\epsilon_{\parallel,a}$ and the c–axis parallel to the substrate $\epsilon_{\parallel,c}$. d_c is the critical thickness.

Before moving on to the issue of strain due to different thermal expansion coefficients, the assumption that the c–axis is perpendicular to the surface when growing on GaAs(001) should be discussed briefly. If the chalcopyrite a–axis is oriented $\parallel$ to the GaAs surface the strain of the a–axis is denoted $\epsilon_{\parallel,a}$. One can in a similar fashion describe the strain along the c–axis, in the case where it is parallel to the GaAs surface $\epsilon_{\parallel,c}$. For the two different orientations the strain of the chalcopyrite parallel to the substrate surface is given by:

$$\epsilon_{\parallel,a} = \frac{a_{str} - a}{a}, \qquad \epsilon_{\parallel,c} = \frac{c_{str} - c}{c},$$

where a is the a–axis of the unstrained chacopyrite and a_{str} is the length of the stained a–axis. Similarly c is the length of the unstrained c–axis and c_{str} is the length of the strained c–axis.
In the pseudomorph chalcopyrite growing with $c \perp$ the GaAs surface we have $a_{str} = a_{GaAs}$. In this case the strain parallel to the GaAs surface is simply given by the lattice mismatch $\epsilon_{\parallel,a} = m$. If the layer would grow with the c–axis parallel to the GaAs surface the length of the c–axis would assume the value $c_{str} = 2a_{GaAs}$. The strain in the

pseudomorph layers calculated with this approach are given in table 2.1.
Based on the amount of the lattice mismatch in the two cases it is possible to predict the preferred layer orientation. For both $CuInSe_2$ and $CuGaSe_2$ it is seen that the lattice mismatch is considerably lower when the *c*–axis grows perpendicular to the substrate surface. The layer will, therefore, preferentially grow with this orientation. Experimentally this expectation has been confirmed in previous growth experiments [48, 59]. In section 3.6.2 it is demonstrated that this is also the case in layers grown in this work.

2.2.2 Difference of Thermal Expansion Coefficients

The lattice mismatch is not the only problem of hetero–epitaxy. The difference in thermal expansion coefficients of the substrate and film also strongly affect the strain in the final film. The total strain in the layer due to the combination of the lattice mismatch and the effect of different expansion coefficients is given by [60]:

$$\epsilon_{\parallel,a} = R(\alpha_a^{layer} - \alpha_a^{substrate})\Delta T + (R-1)\frac{a_{substrate} - a_{layer}}{a_{layer}}, \tag{2.4}$$

where a degree of relaxation $0 \leq R \leq 1$ has been introduced. ΔT is the difference between growth temperature and room temperature, and α_a^{layer}, $\alpha_a^{substrate}$ are the thermal expansion coefficients along the *a*–axis of the layer and the substrate, respectively. The meaning of R in the two extreme cases should be briefly discussed.
R = 0 is the extreme case of pseudomorhic growth where the layer totally adapts the lattice constant of the substrate. In this case the thermally induced strain does not play a role, as the strain in the layer is determined solely by the lattice mismatch. This will be the case in films thinner than the critical thickness d_c.
The other extreme case where R=1 is the case where the strain due to lattice mismatch has been totally relaxed at the growth temperature. When the layer is cooled down the layer will again be strained due to the difference of thermal expansion coefficients. The final strain in the layer is in this case solely determined by the thermal expansion mismatch.
If the strain due to the lattice mismatch would be totally relaxed when the layer thickness reaches the critical thickness d_c, the case with $R = 1$ should describe all films thicker than d_c. It is, however, found that residual strain remains due to the lattice mismatch even for films thicker than d_c [49]. In reality $0 \leq R \leq 1$ therefore applies for films thicker than d_c.
The actual strain measured in $CuInSe_2$ and $CuGaSe_2$ layers grown on GaAs is discussed in the following section.

2.2.3 Strain Measured in Epitaxial Layers

Strain in epitaxial chalcopyrite layers has been observed previously. In the previous section it was discussed how the *a*–axis is strained due to the lattice and thermal expansion mismatch. The strain in the *a*–axis also manifests itself by a change of the length of the *c*-axis. The strain along the *c*–axis $\epsilon_{\perp,c}$ due to a strain of the *a*–axis parallel to the substrate $\epsilon_{\parallel,a}$ is given by:

$$\epsilon_{\perp,c} = -2\frac{C_{13}}{C_{33}}\epsilon_{\parallel,a}, \tag{2.5}$$

where C_{13} and C_{33} are elements xy in the elastic stiffness tensor C_{xy} [61]. This expression is a linear approximation only valid for small strains. The components of the elastic

stiffness tensor for $CuGaSe_2$ and $CuInSe_2$ found by theoretical calculations are given in table 2.1.
Since the $CuGaSe_2$ layer grows with the *c*–axis perpendicular to the GaAs surface, the length of the *c*–axis is measurable in XRD measurements. The strain of the *c*–axis measured by XRD in the work of Bauknecht [48] will be summarized here.

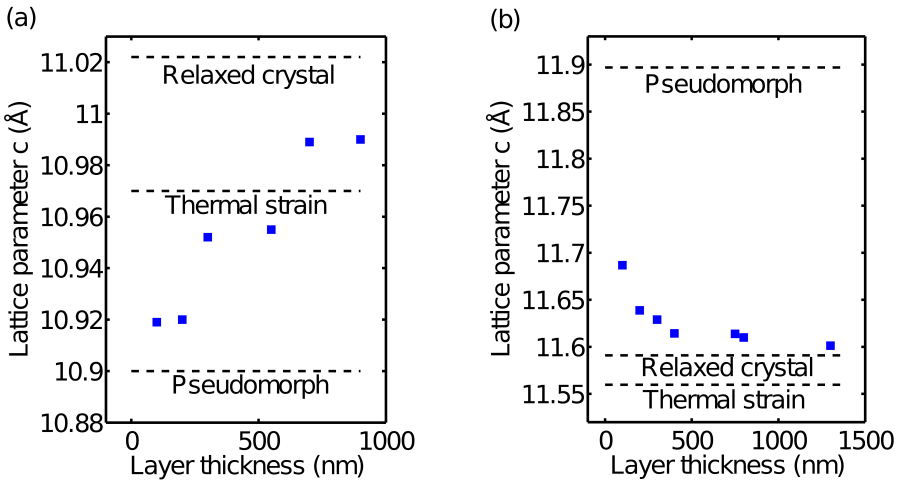

Figure 2.6: Evaluation of strain in epitaxial layers from XRD measurements. (a) Length of the *c*–axis as a function of layer thickness for $CuGaSe_2$ redrawn from [48] (b) Length of the *c*–axis as a function of layer thickness for $CuInSe_2$ based on measurement of samples from this work.

Figure 2.6(a) shows the *c*–axis of $CuGaSe_2$ measured by XRD as a function of layer thickness. It is observed that the length of the *c*–axis approaches the value of the totally relaxed crystal with increasing layer thickness. The expected length of the *c*–axis calculated using equation (2.4) and equation (2.5) assuming $R = 0$ for pseudomorph growth is shown. The line indicates the *c*–axis that is expected in a pseudomorph layer with a thickness below d_c. It is seen that the lattice parameter is larger than expected for pseudomorph growth, showing that all samples are thicker than the critical thickness. It is noticed that *c* increases with increasing layer thickness approaching the value expected in unstrained $CuGaSe_2$. The reason why the unstrained case in not observed might be partly due to residual strain and partly due to the fact that the thermally induced strain is expected to shorten the *c*–axis as well.
The line labelled thermal strain was calculated from equation (2.4) and equation (2.5) with $R = 1$ assuming that the layer is totally relaxed at the growth temperature and strained only during cool down. This illustrates the upper limit expected for the length of the *c*–axis. It is noticed that the thickest samples investigated are relaxed to a higher degree than expected from the thermal expansion mismatch. This can be related to development of cracks in the film relaxing the layer even further [48]. The probability of crack evolution increases with increasing layer thickness due to increasing strain energy with layer thickness. The development of cracks will be further investigated in section 5.5.1. Similar results as discussed here for $CuGaSe_2$ have been obtained for the $CuGaS_2$/GaAs(001) and $CuAlSe_2$/GaAs(001) systems [61].
Strain in $CuInSe_2$ grown on GaAs has the same origin as discussed for $CuGaSe_2$. The system is, however, different since pseudomorph $CuInSe_2$ grows with a lattice constant *c* that is longer than in relaxed $CuInSe_2$. The thermally induced strain during cool down

of $CuInSe_2$ that is relaxed at the growth temperature will, on the other hand, result in a lattice constant c smaller than in the relaxed crystal. This is illustrated in figure 2.6(b) with the lines indicating the length of the c–axis under the different assumptions.
In order to investigate the strain in $CuInSe_2$ layers, XRD measurements were performed on epitaxial samples grown in this work. The lattice parameter c extracted from the measurements is shown in figure 2.6(b). The length of the c–axis due to thermal strain ($R = 1$) and pseudomorph growth ($R = 0$) were calculated using equation (2.4) and equation (2.5) with the parameters given in table 2.1. For $CuInSe_2$ it is observed in analogy with $CuGaSe_2$ that the lattice parameter approaches that of the relaxed crystal as the layer thickness is increased. The fact that the points fall far from the value expected for pseudomorph growth shows that all layers have a thickness higher than the critical thickness. Since the thickness of the thinnest sample is 100 nm, this result is in agreement with the expectation ($d_c = 43$ nm). All strain due to the lattice mismatch is, however, not released, but some degree of residual strain is still observed. The amount of residual strain reduces as the layer thickness is increased. In the case of $CuInSe_2$ the thermal mismatch actually aids to reduce the residual strain during cool down. The fact that the cool down releases the strain is also observed by SEM investigations of the final layers, where cracks in the $CuInSe_2$ are rarely observed in contrast to $CuGaSe_2$ layers. The case where the layer is totally relaxed at growth temperature is, however, not observed. The thickest layers end up with a lattice constant very close of the one observed in unstrained crystals.

2.2.4 The Influence of Strain on the Band Gap

As described in the previous section hetero–epitaxial growth often results in layers that are strained. The stain affects the semiconductor by changing energetic positions of the valence and conduction bands. Since the energetic transitions measured by photoluminescence depend on the magnitude of the band gap, it is important to be aware of the influence of strain when analysing the results. Figure 2.7 shows the variation of the conduction and valance bands of $CuGaSe_2$ at the Γ point due to strain.

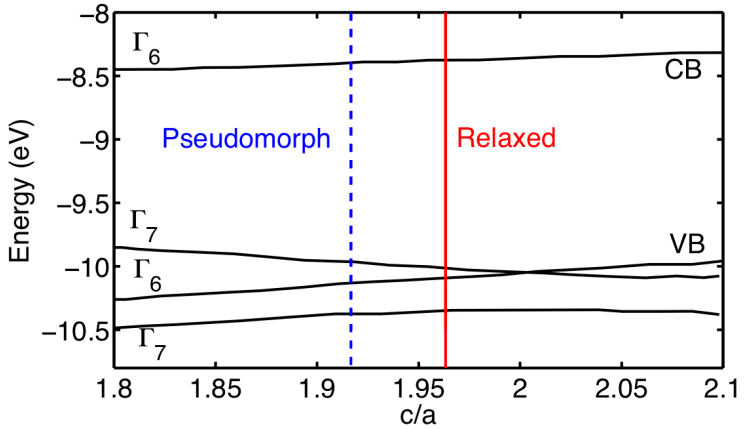

Figure 2.7: Influence of strain on the band ordering and band gap in $CuGaSe_2$ from tight–binding calculations [48, 62].

The variation of the band gap is calculated from a theoretical tight–binding model, where the wavefunctions are described by a linear combination of atomic orbitals [62]. The energies of the bands are shown as a function of the c/a ratio. An increase in this value cor-

responds to a compressive strain of the unit cell a–axis whereas a lower c/a corresponds to tensile strain of the a–axis. In the figure the c/a ratio of relaxed $CuGaSe_2$ is shown along with the c/a ratio expected for pseudomorph $CuGaSe_2$/GaAs(001). As shown in the previous section it is experimentally found that the strain in the layer lies between these limits. In the figure it is seen that the band gap is reduced due to the lattice mismatch, which induces a tensile strain along the a–axis of the $CuGaSe_2$ crystal. According to the calculation the band gap of pseudomorph $CuGaSe_2$/GaAs(001) is reduced by almost 70 meV compared to the relaxed crystal. The samples investigated in this study are thicker than the critical thickness, and a lower band gap narrowing due to strain can therefore be expected. One should, however, be aware that residual strain in the layer leads to peak shifts in photoluminescence measurements.
Strain in $CuInSe_2$ affects the band gap as well. The material properties that are used in the tight–binding calculation shown in figure 2.7 are the bond lengths and a parameter taking the chemical nature of the elements into account. Since Ga and In are both group III elements the parameter accounting for the chemical nature is similar. One can therefore expect that the behaviour seen in figure 2.7 will be similar for $CuInSe_2$. As mentioned previously a small positive crystal field splitting is present $CuInSe_2$. The order of the top most valence bands in $CuInSe_2$ is therefore switched. The band order in figure 2.7 switches close to $c/a = 2$, which is in fact very close to $c/a = 2.01$ found in relaxed $CuInSe_2$. When pseudomorphic $CuInSe_2$ is grown on GaAs(001) the a–axis is compressed and the c–axis is stretched relative to the relaxed crystal leading to an increase in the c/a ratio. With the approach presented in the previous section one can estimate $(c/a)_{pseudomorph} = 2.1$. In figure 2.7 it is seen that the bands are almost parallel as the c/a is increased from 2.01 to 2.1. Almost no change of band gap due to the residual strain can therefore be expected in epitaxial $CuInSe_2$ layers.

2.3 Low Temperature Photoluminescence: A tool for Defect Spectroscopy

Photoluminescence is used as the primary tool to investigate epitaxial $CuInSe_2$ and $CuGaSe_2$ layers in this work. A detailed description of the theory of the method is therefore included here.

2.3.1 The Basic Principle of Photoluminescence

Photoluminescene describes the process in which charge carriers generated by light absorption recombine radiatively. The photoluminescence process can be described in three general steps explained in the following [63, 64]:

1. The main requirement for emission of photoluminescence is that the electronic system is not in equilibrium. In order to obtain luminescence from a system it is therefore necessary to perturb the system in a way that results in a non–equilibrium situation. In PL experiments a non-equilibrium distribution of charge carriers is obtained by illumination with light [63]. Illumination of a semiconductor with light of energy higher than the band gap $\hbar\omega > E_g$ excites electrons across the band gab resulting in free electrons in the conduction band (CB) and free holes in the valence band (VB).

2. The generated charge carriers will thermalize with the lattice in a time scale of picoseconds. This results in a rapid establishment of a quasi-equilibrium where charge carriers are distributed at band edges and in defect levels at low temperatures [63].

3. The electrons and holes recombine radiatively giving rise to luminescence with photon energy equal to the energy difference between the two states involved in the transition. The typical time scale of radiative recombination is in the order of nanoseconds to microseconds [63].

Depending on the sample quality, electronic defect structure, temperature etc. one will observe PL originating from different energetic states [64]. Figure 2.8 illustrates schematically possible radiative transitions in a semiconductor. The difference between these transition types will be discussed in the following sections.

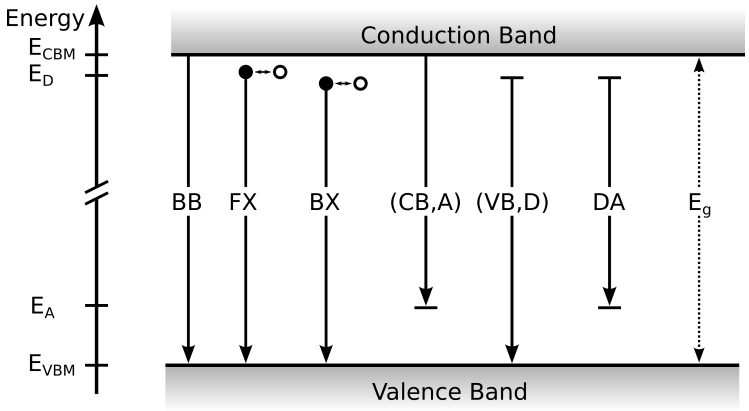

Figure 2.8: Schematic illustration of radiative transitions in a semiconductor. The illustrated transitions include Band–to–Band Recombination (BB), Free Exciton (FX), and Bound Exciton (BX). Recombination of free electrons with acceptors (CB,A) and free holes with donors (VB,D) are both classified as Free–to–Bound recombination (FB). Recombination of electrons in donor states with holes in acceptor states are called Donor–Acceptor Pair recombination (DA).

2.3.2 Band–to–Band Recombination

In general a fraction of the excited charge carriers remain in the band states. The density of carriers that remain in the bands is, however, strongly dependent on the temperature. At low temperatures the charge carriers tend to form excitons or get trapped in defect states from which they recombine as explained in the following sections. When the temperature is increased the excitons dissociate and defect related luminescence is quenched due to re–emission of the charge carriers to the bands. The radiative recombination from the conduction band to the valence band therefore becomes more dominant at higher temperatures [63]. For further details on band–to–band recombination see section 5.1.1.

2.3.3 Excitonic Recombination

Excitonic luminescence is the recombination of electron–hole pairs bound together by Coulomb interactions. Excitons can only form in material of sufficient purity and quality [64]. In material with high concentrations of defects, excitons will dissociate due to the presence of local fields. Excitonic emission can, likewise, only be observed at very

low temperatures where the thermal energy is smaller than the exciton binding energy ($k_BT < E_{EX}$) since thermal dissociation occurs at elevated temperatures [63, 64].
One distinguishes between two types of excitons based on their spatial extension: (1) highly localized Frenkel excitons with an electron–hole distance in the order of the lattice constant and (2) Wannier–Mott excitons that extend significantly further with an electron–hole distance of several times the lattice constant. Wannier–Mott are typically found in materials in which the reduced mass of the exciton is low. This is the case in Cu(In,Ga)Se_2 because of the low effective electron mass $m_e^* << m_0$ (see table in appendix C) [65].

Free Excitons

Wannier–Mott type free excitons are well described by the hydrogen model. The binding energy of the exciton in this model is given by [63]:

$$E_{FX,n} = \frac{m_r e^4}{2\hbar^2 \left[4\pi\epsilon_0\epsilon_r(0)\right]^2} \frac{1}{n_q^2} \tag{2.6}$$

where m_r is the reduced mass $1/m_r = 1/m_e^* + 1/m_h^*$, n_q quantum number, $\hbar$ is the reduced Planck constant, e is the elementary charge, $\epsilon_r(0)$ is the relative dielectric constant, and ϵ_0 is the permittivity of free space.
In order to estimate the exciton binding energy, it is necessary to know the effective masses. This is not trivial, since it has recently been shown by a theoretical evaluation that the effective hole mass in Cu(In,Ga)Se_2 is anisotropic [66]. An experimental study of the reduced mass is available for both $CuInSe_2$ [67] and $CuGaSe_2$[68]. Based on the shift of excitonic luminescence in a magnetic field a reduced effective mass can be determined [67, 68]. The experimentally determined value can be expected to represent an average over the anisotropic hole mass. To simplify the evaluation here, the experimentally determined reduced masses will therefore be used.
For $CuInSe_2$ with a reduced mass of $m_r = 0.095m_0$ [67] and a dielectric constant of $\epsilon_r(0) = 13.6$ (see table C.1) equation (2.6) gives a binding energy of the exciton of $E_{FX} = 7$ meV. This is in very good agreement with the experimentally determined binding energy of excitons in $CuInSe_2$ of 7 meV [67, 69] and 7.5 meV [70].
A similar estimation for $CuGaSe_2$ using the experimentally determined reduced effective mass $m_r = 0.115m_0$ [68] and a dielectric constant of $\epsilon_r(0) = 11$ (see table C.1) yields E_{FX}= 12.9 meV, which is almost identical to 13 ± 2 meV found experimentally [48]. Thus, the hydrogen model gives a very good description of the exciton in this case.
When measuring photoluminescence, the energy of the emitted photons is simply the band gap minus the binding energy of the exciton [63, 64]:

$$\hbar\omega_{FX} = E_g - E_{FX,n} \tag{2.7}$$

One will rarely observe excitons of $n_q > 1$ except in very good crystals, since the intensity of the exciton decreases as $I_{FX} \propto n_q^{-3}$ [71].

Bound Excitons

When a sample contains a small number of donors or acceptors excitons can bind to these via van der Waals interactions. Excitons can bind to neutral or charged defects in the material. Since the interaction of excitons with defects lowers the energy it is likely

to form bound excitons. These bound excitons can be described as molecular bonds in the hydrogen analogy. An exciton bound to a neutral defect can be considered as a H_2 molecule, whereas an exciton bound to a positively charged donor can be regarded as the hydrogen molecular ion H_2^+ [64]. The energy of photons emitted due to recombination of bound excitons is given by [63, 64]:

$$\hbar\omega_{BX} = E_g - E_{BX}, \tag{2.8}$$

where the E_{BX} is the binding energy of the bound exciton. The binding E_{BX} depends on the ionization energy and charge state of the defect to which the exciton binds. The binding energy of the exciton is, according to Haynes rule [72], proportional to the ionization energy of the defect E_D or E_A. The proportionality constant C depends on the effective masses of the electrons m_e^* and holes m_h^* in the material. For neutral defects the binding energy in general increases as the ratio m_h^*/m_e^* increases as discussed in details in [64]. For excitons bound to neutral defects the binding energy can be expressed as

$$E_{BX} = C_{A^0/D^0} E_{A/D} + E_{FX} \tag{2.9}$$

By convention the energy of the exciton bound to neutral defects is expressed as a sum of the free exciton energy and the additional term due to binding to the defect. For excitons bound to charged defects this is by convention expressed as the complete binding energy:

$$E_{BX} = C_{A^-/D^+} E_{A/D} \tag{2.10}$$

The proportionality constants C have been calculated for neutral defects [73] and charged defects [74].
The photon emitted from recombination of a BX has lower energy than a corresponding FX. An approach to distinguish BX from FX in a PL spectrum is to investigate the linewidth. Since the bound excitons are not able to move in the crystal, they do not posses kinetic energy. The linewidth of bound excitons is therefore expected to be narrower for bound than for free excitons [64].

Characteristics of Excitons in Photoluminescence

When performing PL measurements it is often of great importance to be able to distinguish the different types of transitions. This can be achieved by analysis of temperature and excitation dependent behaviour of the intensity and energetic position of the peak. In general, one can describe the photoluminescence intensity I_{PL} measured with increasing excitation density P_{exc} according to the power law [10]:

$$I_{PL} \propto P_{exc}^k \tag{2.11}$$

For excitons it is in principle expected that the exponent k in equation (2.11) equals 2 under high injection conditions, since the excitonic emission depends on the concentration of both electrons n and holes p: $I_{PL,EX} \propto n \cdot p$ [63], where n and p are both proportional to P_{exc}. In reality one finds $1 < k < 2$ since excitonic recombination competes with other radiative and non–radiative recombination pathways [75]. The peak position of the excitons remains constant when the excitation density is increased unlike e.g. donor–acceptor–pair (DAP) recombination discussed in the next section [10].
When the temperature is increased the energy of the excitonic recombination is expected to follow the temperature dependence of the band gap. The intensity is, however, rapidly

decreased as the temperature is increased, so in the case of Cu(In,Ga)Se_2 where the band gap stays almost constant from 1–100 K [70, 76, 77, 78], it is not expected that any shift of the excitonic emission can be observed. As the temperature is increased one will on the other hand observe a continuous transition from excitonic recombination to band–to–band recombination.
The intensity of the excitonic luminescence decreases rapidly with increasing temperature due to thermal dissociation of the exciton. By measurement of the quenching behaviour it is possible to determine the exciton binding energy.
The temperature dependence of a luminescence intensity I_{PL} in competition with a thermally activated process can in general be described by [10]:

$$I_{PL} \propto \frac{1}{1 + b \exp\left(\frac{E_{act}}{k_B T}\right)}, \tag{2.12}$$

where b is a proportionality constant, k_B is the Boltzmann constant, T is the temperature, and E_{act} is the activation energy of the quenching process. For a study of the exitonic recombination as a function of temperature, the activation energy E_{act} corresponds to the exciton binding energy [10].

2.3.4 Donor–Acceptor–Pair Recombination

States with energies in the otherwise forbidden band gap occur in semiconductors due to either the presence of impurities or crystal defects. Shallow defects that are responsible for doping of the material can be described with the hydrogen model mentioned in section 2.3.3. The only difference is that the reduced mass of the exciton m_r in equation (2.6) should be replaced with the effective mass of the charge carriers in the nearest band (m_e^* for donors and m_h^* for acceptors). This simple model can be applied for acceptors in chalcopyrites since the valence band degeneracy is lifted due to the crystal field mentioned in section 2.1.3.
To give an idea of the accuracy of the hydrogen model for the description of shallow defects, the ionization energies can be estimated using the same material properties used to calculate of the exciton binding energy in section 2.3.3. For $CuGaSe_2$ with $m_e^* = 0.14 m_0$ [79], the experimentally determined reduced mass leads to an effective hole mass of $m_h^* = 0.64 m_0$ [68]. With these values and $\epsilon_r(0) = 11$ [80] (see appendix C) an estimate of the defect ionization energies gives $E_D = 16$ meV and $E_A = 72$ meV.
For $CuInSe_2$ the effective mass electron is in the order $m_e^* = 0.09 m_0$ [66, 79]. If assuming this effective electron mass, the hole mass determined from the reduced mass reported in [67] strongly overestimates the acceptor energy. Instead if the commonly used value of $m_h^* = 0.71 m_0$ [65] is assumed, with the dielectric constant $\epsilon_r(0) = 13.9$ [81], one finds $E_D = 7$ meV and $E_A = 52$ meV. These energies very similar to the experimentally determined defect energies discussed in section 2.3.8. Even though the absolute values are not exactly in agreement with the experimentally found defect levels the result clearly shows some notable facts. The acceptor level is deeper than the donor level in both $CuInSe_2$ and $CuGaSe_2$ as a result of $m_h^* > m_e^*$. The calculation also predicts correctly that the defect levels in $CuInSe_2$ are more shallow than in $CuGaSe_2$.
With both acceptors and donors simultaneously present recombination of charge carriers via two defect states can occur. If the concentrations of both defects are lower than the Mott concentration the defects can be described by the following model. The Mott condition is given by $N_M a_B \approx 0.27$, where a_B is the effective Bohr radius of the defect state. The

Mott concentration is an estimation of the critical concentration N_M above which defect states begin to interact [82]. An estimation of the Mott concentration is given in section 4.2.
In a donor–acceptor–pair transition the initial state consists of a neutral donor and a neutral acceptor. When the transition occurs the electron is transferred from the donor to the acceptor leading to a final state with charged donor and acceptor. Schematically this can be written:

$$D^0 + A^0 \rightarrow \hbar\omega + D^+ + A^- \tag{2.13}$$

Since the donor is positively charged and the acceptor negatively charged in the final state, an amount of energy due to Coulomb interaction between the two will be liberated. This energy E_C is transferred to the emitted photon, thereby increasing the photon energy. The emitted energy due to the DAP recombination can therefore be described by [10, 63, 64]:

$$\hbar\omega = E_g - (E_A + E_D) + E_C, \tag{2.14}$$

where E_A and E_D are the energetic distances between the defect state and the band edge for the acceptor level and donor level respectively. E_C is the Coulomb energy due to interaction of a donor and an acceptor separated by a distance r:

$$E_C = \frac{e^2}{4\pi\epsilon_0\epsilon_r(0)r} \tag{2.15}$$

It is here noticed that the emitted energy depends on the distance between the defects involved in the transition. This fact turns out to be important in order to identify a transition as being of the DAP type [64]. If for example the defect density in the material is in the order 10^{16} cm^{-3} the average distance between donors and acceptors will be $r = 40$ nm [13]. With $\epsilon_r(0) = 11$ (see appendix C) equation (2.15) gives a Coulomb energy $E_C = 3$ meV.

Characteristics of Donor–Acceptor–Pair Recombination in Photoluminescence

As the excitation density is increased the density of occupied donors and acceptors increases. This leads to a decrease of the average distance between occupied donors and acceptors from which recombination can occur. The decreased average inter pair distance r is responsible for an increase of the Coulomb term in equation (2.14) and hence a blue shift of the emitted luminescence. The upper limit of this blue shift can be estimated by replacement of r in equation (2.15) by two times the effective Bohr radius $2a_B$ of the defect with the largest spatial extension [77, 83, 84]. For $CuInSe_2$ where $m_e^* << m_h^*$ [65] the donors have a much larger Bohr radius than the acceptors. In this case the maximum shift due to the Coulomb term is determined by the ionization energy of the donor. For $CuInSe_2$, with the material parameters used in section 2.3.3 the effective Bohr radius of the donors is found to be $a_B = 8$ nm. This leads to a maximum shift of the DAP recombination due to the Coulomb energy of 6.6 meV.
When the blue shift is measured experimentally it is found that the shift of the peak maximum $\hbar\omega$ is linear with the logarithm of the excitation density P_{exc} [10]:

$$\hbar\omega = \hbar\omega(P_0) + \beta \log\left(\frac{P_{exc}}{P_0}\right) \tag{2.16}$$

A blue shift of $\beta = 1 - 3$ meV/decade of the DAP recombination as function of excitation density is typically measured for $CuGaSe_2$ [13], $CuInSe_2$ [14], and $Cu(In,Ga)Se_2$ [15]. These observations are all below the limit for the total shift. In studies where larger shifts are observed the DAP theory is no longer adequate. This is e.g. the case in semiconductors dominated by potential fluctuations discussed in chapter 4. The exponent k in equation (2.11) for DAP transitions have experimentally been found to be $k < 1$. This result is supported in literature by a model describing the recombination via various pathways with a set of coupled differential equations also finding that $k < 1$ for DAP transitions [75].
When the temperature is increased one observes a blue shift of the peak due to recombination from donors and acceptors with lower inter defect distance r. The reason for this is related to thermal emptying of the defect states with increasing temperature. The probability of recombination between short distance pairs is higher than for pairs with higher spatial separation because the tunnelling probability decreases with distance. When the defects are thermally emptied the short distance pairs will dominate because these are the ones with the highest probability and shortest life time [85].
From the quenching behaviour of the DAP luminescence intensity as a function of temperature it is possible to extract two activation energies. The most shallow defect is emptied first giving rise to one activation energy. As the temperature is increased further the observed transition is in fact of free–to–bound character. The dominating activation energy extracted from the quenching process corresponds to the ionization energy of the deepest of the involved defects [86].

2.3.5 Free–to–bound Recombination

Free charge carries in the bands can recombine radiatively with charged defects. There are two possible processes which can both be called free–to–bound recombination. Electrons in the conduction band can recombine with holes in acceptor states (CB,A). The other possibility is recombination of free holes with electrons in a donor state (D,VB). The peak energy of free–to–bound recombination is given by [10]:

$$\hbar\omega_{FB} = E_g - E_{D/A} + \frac{k_B T}{2}, \tag{2.17}$$

where E_g is the band gap, $E_{D/A}$ is the energetic distance of the donor or acceptor defect to the band edge, and $k_B T$ is the thermal energy [10].

Characteristics of Free–to–bound Recombination in Photoluminescence

FB and DAP recombination have similar peak positions in PL. FB recombination can, however, be distinguished from DAP recombination in excitation dependent PL measurements, since the peak position of FB recombination is independent of the excitation density in contrast to DAP recombination where a small blue shift is expected. For FB transitions the exponent k in equation (2.11) is expected to be $k = 1$, since the luminescence intensity is proportional to either the excess electron or hole concentration, both of which proportional to the excitation density. It is observed that $k < 1$ due to competition with other recombination channels [10].
In temperature dependent measurements of an FB transition one expects to see a shift of the peak with the band gap and $k_B T/2$. The activation energy determined from the

quenching with increasing temperature can, as mentioned for the DAP transition, give information about the defect energy.

2.3.6 Phonon Replicas of Radiative Recombination

Interaction with phonons in the radiative recombination process can lead to phonon replicas of peaks. When this occurs one can observe the zero–phonon line ($\hbar\omega_{peak}$) of e.g. excitonic or DAP recombination in the spectrum and additionally a number of phonon replicas with lower energy. In the process the energy of the involved phonon $\hbar\omega_{phonon}$ is transferred to each of the N phonons participating in the process. Several phonon replicas with energies $\hbar\omega_N$ can therefore appear in the spectrum:

$$\hbar\omega_N = \hbar\omega_{peak} - N \cdot \hbar\omega_{phonon} \tag{2.18}$$

Phonon replicas are often observed in polar semiconductors. In some cases as many as many as 6 phonon replicas are observed [87]. The intensity of the phonon replica decreases with the number of involved phonons. The intensity of I_N the N-th replica can be described with

$$I_N \propto \exp(-S)\frac{S^N}{N!}, \tag{2.19}$$

where S is the so-called Huang-Rhys parameter [36]. This parameter depends on the strength of the coupling to the lattice. For weak coupling $S << 1$, the zero phonon line is the strongest [36]. This is the case for phonon replicas of free exictons in most semiconductors [88]. In order to observe phonon replicas the crystal quality must be good [36].

2.3.7 How to Distinguish Different Types of Recombination

In the preceding sections it has been described why different types of transitions behave differently. In order to give an overview of the temperature and excitation dependencies of the transition types the characteristics are summarized in table 2.2. The entry PF describes the characteristics observed in the presence of strong potential fluctuations. This phenomena that occurs in semiconductors with a high degree of compensation will be discussed in details in chapter 4.

	Temperature dependence		**Excitation density dependence**	
Transition type	Peak energy	PL intensity	Peak energy	PL intensity
EX	Follows E_g	$E_{act} = E_{exc}$	Constant	1<k<2
FB	Follows $\frac{k_B T}{2}$ and E_g	$E_{act} = E_{defect}$	Constant	k<1
DAP	Small blue shift	$E_{act} = E_{defect}$	β of few meV/decade	k<1
PF	Non–monotonous		β of 5–25 meV/decade	$k \approx 1$

Table 2.2: Characteristic properties of different transition types in excitation and temperature dependent PL measurements. EX: excitonic recombination, FB: free–to–bound recombination, DAP: donor–acceptor–pair recombination, and PF: recombinations in presence of potential fluctuations [10].

2.3.8 Shallow Defects in Chalcopyrites

Defect spectroscopy by photoluminescence measurements of chalcopyrites have been performed for more than 25 years. A summary and discussion of the results can by

found in the book chapter by Siebentritt [10]. The model for recombination presented here explains some of the most reliable PL reports in literature. The models have been developed through an extensive low temperature PL study of epitaxial $CuGaSe_2$ [48] and $CuInSe_2$ [59]. This model only deals with the shallow defect levels observed in PL. These are also the defects that are responsible for doping of the material.
It has been demonstrated that the electronic structure of $Cu(In,Ga)Se_2$ changes smoothly from pure $CuInSe_2$ to pure $CuGaSe_2$ [86]. The recombination model for the two materials are therefore very similar with the main difference being the ionization energies of the defects. This can be explained by the hydrogen model as described in section 2.3.4.

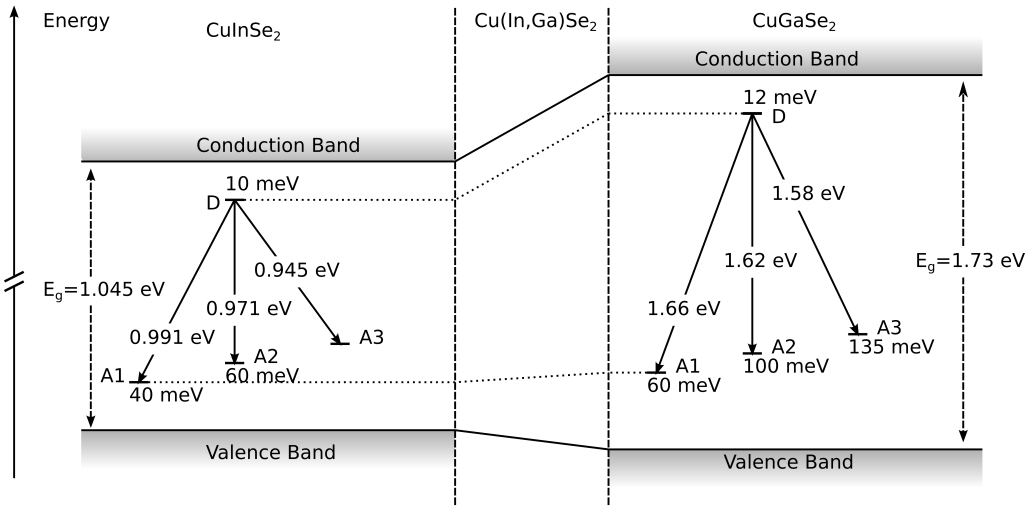

Figure 2.9: Recombination model for $CuInSe_2$ and $CuGaSe_2$ based on PL measurements. The defect ionization energies and transition energies are indicated [10, 13, 48, 59, 86].

In PL spectra of epitaxial absorbers one typically observes DAP recombination via the defect levels shown in figure 2.9. The three DAP transitions shown in figure 2.9 are referred to as DA1, DA2 and DA3. It has been found that the growth conditions strongly influence the presence of certain transitions in the PL spectrum. When the material is grown under Cu–rich conditions the DA2 transition dominates the PL spectrum. The DA1 transition is absent in very Cu–rich material with [Cu]/[III] $\geq$ 1.2. When the Cu–excess during growth is decreased the DA1 peak gradually appears in the PL spectrum. The intensity of the DA2 peak decreases simultaneously. For material grown with a composition very close to stoichiometry [Cu]/[III] $\approx$ 1 the DA2 peak totally vanishes and the PL spectrum is dominated by the DA1 peak. The relative PL intensity of the DA1 and the DA2 peak is therefore a reliable measure of the [Cu]/[III] ratio during growth under Cu–rich conditions [13, 89]. When the [Cu]/[III] ratio is decreased even further the material is grown under Cu–poor conditions ([Cu]/[III]$<$ 1). Material grown under Cu–poor conditions is highly compensated, resulting in a high density of charged defects and a low net carrier concentration [10]. Since the random distribution of charged defects cannot be screened by the remaining free charges a randomly fluctuating Coulomb potential remains. These fluctuations will locally perturb the band structure [90]. The photoluminescence from a highly compensated semiconductor is influenced by the magnitude of the fluctuations since the carriers recombine from spatially separated potential wells. In material dominated by potential fluctuations a red shifted asymmetrically broadened PL spectrum is observed as seen in figure 2.10 [13]. Potential fluctuations are discussed in further details in chapter 4.

It is important to be aware that these signatures refer to the growth conditions as the defect structure is defined during the growth. Subsequent etching in KCN that removes the excess Cu in the Cu_xSe phase does not change the signatures observed in PL [48].
The typical photoluminescence characteristics discussed here have all been observed in samples investigated in this work. Figure 2.10 shows the photoluminescence spectra containing the characteristic peaks described in literature [10, 13, 48, 59, 86].

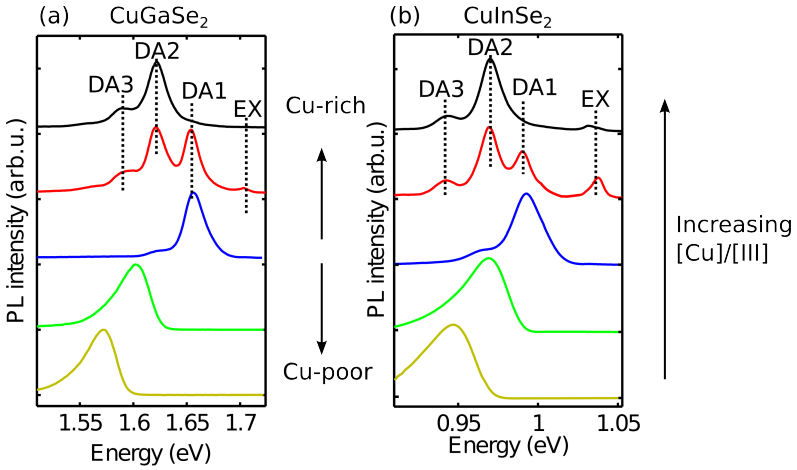

Figure 2.10: Photoluminescence spectra measured at 10 K showing the typically observed transitions and their dependency on the layer composition.

In the previous discussion the DA3 transition has been neglected. There is no reported composition dependency for this transition. This peak observed in the PL spectrum is ascribed to a phonon replica in an earlier study [13]. It could, however, based on spatially resolved cathodoluminescence be demonstrated that the peak is a third DAP transition [91]. This issue will be further investigated in section 5.4.1.
Several experiments performed throughout this work apply the recombination model presented here in the interpretation of the results.

Growth and Structural Characterization

3

In order to understand the inherent properties of chalcopyrites it is necessary to be able to investigate material with as few artefacts as possible. It is for example highly desirable to exclude the effects of grain boundaries and interfaces which affect the device properties of chalcopyrite solar cells [8, 37, 92]. In this work only bare absorber materials are investigated in order to exclude any effects of the measured properties introduced by junction formation. By investigation of single crystalline material one can furthermore exclude the influence of grain boundaries on the measurement results.
High efficiency solar cells are made form alloys containing both In and Ga. This potentially leads to band gap fluctuations due to inhomogeneous variations of the local of the [Ga]/[In] ratio [11]. The effect of alloying can be avoided by restricting the study to the ternary $CuInSe_2$ and $CuGaSe_2$. The study presented here therefore focuses on the development of a growth process for production of epitaxial samples of the ternaries.
This chapter contains a description and discussion of the growth experiments performed in this work. The first three sections describe the equipment and the parameters used when growing $CuInSe_2$ and $CuGaSe_2$. This includes a discussion of the functioning of the MOVPE system as well as a discussion of the metal organic precursors. The second part of the chapter focuses on the results of the growth experiments. This includes a discussion of the tools used for monitoring the process, some examples of growth optimization experiments, verification that epitaxial growth is obtained and finally development of a growth model that explains effects observed during the growth at high temperature.

3.1 Principle of Metalorganic Vapour Phase Epitaxy

Metaloragnic vapour phase epitaxy (MOVPE) is a technique to grow epitaxial thin films from metal organic precursor materials. The method is based on the exact control of the flow of gases carrying well defined amounts of the precursors. This is achieved by passing a carrier gas through so-called bubblers where it picks up vapours of the metal organic material and transports it to a reactor. The metalorganic molecules decompose when they reach the heated reactor and release the metal that is deposited on a substrate. In order to obtain epitaxial growth a single crystalline substrate is used.
The advantage of MOVPE is that the technique offers high control of layer thickness, composition, doping etc. by exact control of gas flows. This opens the possibility to e.g. grow very well defined layers of different materials with atomic layer abrupt interfaces [93].
MOVPE, like all other crystal growth techniques, is highly complex. Early attempts to grow epitaxially from metalorganics were largely empirical, where the MOVPE process had the character of a 'black box'. While the technology was still young the developments were driven by a 'turning the knobs' approach until the materials with the desired properties were obtained. This approach was used due to the complexity of the multicomponent systems typically of interest. Much has been achieved since these initial experiments [93]. The worlds most efficient triple junction solar cells with efficiencies

above 40 % are for example produced with MOVPE [94]. It is, however, inaccurate to claim that all aspects of the MOVPE process are thoroughly understood [93].
The aim of the following section is not to give a deep insight into all the details and complexity of MOVPE growth. This section is meant only to introduce the basics needed to understand the growth experiments.

3.2 The Metalorganic Vapour Phase Epitaxy System

The MOVPE–setup used in this work is a commercial AIX 200 system produced by the company Aixtron. Figure 3.1 shows schematically the main components and gas lines of the AIX 200.

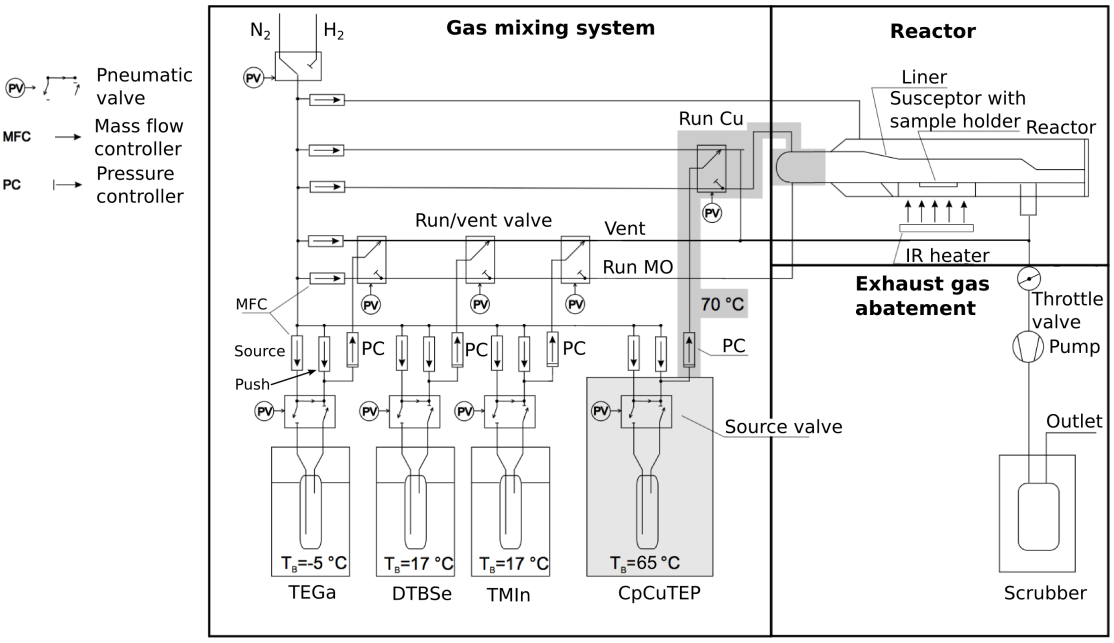

Figure 3.1: Schematic illustration of the MOVPE system showing the gas lines and the main mass flow controllers and valves. The Cu–precursor is transported to the reactor in a separate heated line illustrated with gray colouring. The reactor consists of two concentric quartz tubes and a graphite susceptor.

The system can be divided into three main parts: gas mixing system, reactor, and exhaust gas abatement. The general principle of the system will be described in the following.

3.2.1 Gas Mixing System

Either H_2 or N_2 is supplied to the gas mixing system through the pneumatic valve in the upper left corner of figure 3.1. The figure shows the system in the base state where it is purged with N_2. When a process is started the pneumatic valve switches to H_2 that is used as carrier gas during the process. The gas mixing system contains the metal organic precursors, which are kept in stainless steel containers called bubblers. These are kept at a well defined temperature in water baths. The Cu–source is, unlike the other precursors, kept in an oven in order to be able to achieve a higher temperature. The Cu–precursor is furthermore build in so that it enters the reactor in a separate line. Since the Cu–source is kept at 65°C the downstream lines are heated to 70°C to avoid condensation in the lines. It is important that the bubblers are kept at constant temperature since the vapour

pressure of the metal organics, as any other substance, depends on the temperature. If the vapour pressure varies, this leads to variation of the molar fluxes. The pressure in the bubblers is controlled by pressure controllers (PC) as depicted in figure 3.1.
To open the bubblers the pneumatic valves are switched and the gas is led through the bubblers. Two mass flow controllers are associated with each bubbler. One of these controls the amount of gas flowing in the bubbler (source MFC in figure 3.1) and the other regulates the amount of diluting gas (push MFC in figure 3.1). In all experiments the sum of the flow through the source and push MFCs is kept constant. The mass flow controllers determine the amount of gas lead into each bubbler and therefore also the molar flux of each metalorganic source material. The exact adjustment of the gas flow gives high control of the amount of metalorganic that is brought into the reactor.
In figure 3.1 it is seen that the metalorganics can be directed either to a run–line or a vent–line. The gases carrying the MOs are diluted in these lines with an amount of gas controlled by the run or vent MFCs. It is possible to switch between the two lines with pneumatic valves. The run–line leads the gas into the reactor whereas the vent–line leads directly to the exhaust. The advantage of the run/vent valves is that the gas can be switched off very abruptly. The system is used in the beginning and end of each process. The gas is first let through the vent giving a few minutes for the flow to stabilize before it is switched to the run–line to start growth.

3.2.2 Reactor

The reactor consists of two concentric horizontal quartz tubes, a graphite susceptor with a rotating sample holder and an infrared heating source as shown in figure 3.1. The inner quartz tube known as the liner has a rectangular cross–section designed to obtain a laminar gas flow over the susceptor. The liner can be removed and cleaned in concentrated HNO_3 when needed. The outer quartz tube is flushed with gas in order to cool down the walls of the liner. On top of the outer quartz tube a window is installed facilitating in-situ reflectance measurements as described in section 3.2.4.
The susceptor made of siliconcarbide covered graphite is inserted in the liner. It contains a sample holder that can be rotated with a gas foil rotation system. This system takes advantage of the momentum of a dedicated gas flow to rotate the sample holder. The aim of sample rotation is to obtain more homogeneous layers. This is especially critical since Cu tends to decompose earlier in the reactor than the other components. The susceptor that contains a thermocouple in its core is heated by absorption of infrared light from the heat source.
The reactor can be opened into a glovebox where substrates are loaded and samples can be taken out. The glovebox contains dry nitrogen with concentrations of oxygen and water below 0.1 ppm. By using the glovebox it is possible to avoid contamination of the reactor with water and oxygen. It is furthermore used to help preventing contamination of wafer surface with dirt before deposition and the film surface after deposition. The glovebox also prevents potentially toxic materials from the reactor or GaAs dust to enter the laboratory environment.

3.2.3 Exhaust Gas

Below the reactor in figure 3.1 a pump and valve are shown. The combination of the two is used to control the pressure in the reactor. Usually a reactor pressure of 50 mbar

is used during the run. The exhaust gas that is pumped from the reactor is sent to a scrubber that cleans the gas by adsorption of poisonous compounds before the gas is let out. The scrubber is of the type Cleansorb CS050CS from the company CS Clean Systems.

3.2.4 In–situ Reflectance

In epitaxial growth, like for any other growth, it is valuable to have real time in–situ information about the properties of the growing film. Valuable parameters like growth rate and surface roughness can be obtained by in–situ reflectance measurements. A commercial system designed for surface reflectance measurements (EpiRAS 200) from the company Laytec has been installed in the MOVPE system for this purpose. The system facilitates spectroscopic reflectance measurement of light from a Xe light source. By measurement of the reflectance of light with 4–6 selected wavelengths as a function of time during the growth process information about the development of the growth is obtained.

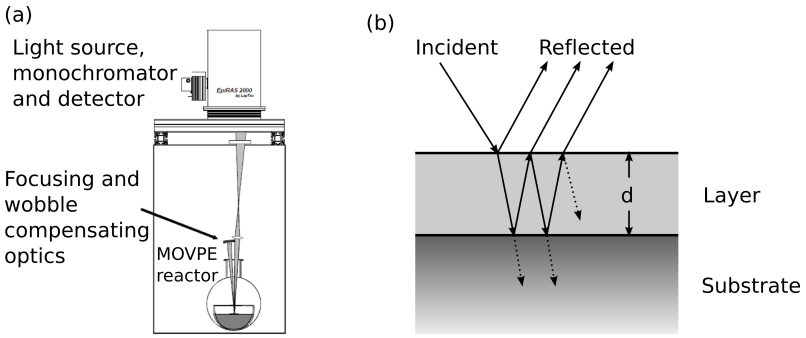

Figure 3.2: (a) Schematic illustration of the Laytec EpiRAS 200 system for in–situ reflectance measurements installed in the MOVPE system. (b) Fabry–Perot oscillations due to interference in the growing layer.

Figure 3.2(a) illustrates the reflectance measurement setup installed in the MOVPE system. The system contains a Xe light source emitting light in a wide wavelength range. The light is focused onto the sample surface by a lens placed on top of the reactor. The light is reflected from the sample surface and detected by a detector on a monochromator placed on top of the MOVPE system. A wobble mirror is installed to send light reflected in another angle, due to wobbling of the substrate, back onto the substrate. This is done in order to avoid losing the light beam because of wobbling of the substrate.
In this work the intensity of reflected light is measured at a few predefined wavelengths as a function of growth time. The so–called reflectance-transients obtained in this way give information about the growth rate and roughening of the sample surface. When light with photon energies lower than the band gap of the layer is used the photons are not absorbed by the growing film. The light is therefore able to travel through the layer and be reflected at the layer/substrate interface. The interference between the light reflected at the surface of the film and from the layer/substrate interface will interfere as shown in figure 3.2(b). Since there is a phase difference between the light beams that travel though the layer and the beam that is reflected from the surface constructive or destructive interference occurs, giving rise to Fabry–Perot oscillations. The phase difference depends on the optical properties of the layer as well as the layer thickness. Constructive interference will occur if the path difference equals an even number m of the wavelength λ. For normal incidence maximum reflectance is therefore observed if $m_i\lambda = 2n_r d$, where n_r is the refractive index, m_i is an integer and d is the layer thickness.

While reflectance–transients are measured the thickness of the layer d increases continuously with $d = r_g t$, where t is the time and r_g is the growth rate. This gives rise to modulations in the intensity of the reflected light over time. Maxima will be observed when $r_g t = \frac{m_i \lambda}{2 n_r}$ and minima in the reflectance transient are observed for $r_g t = \frac{(m_i + \frac{1}{2})\lambda}{2 n_r}$. Based on only the maxima and minima observed in the reflectance transient it is therefore possible to estimate the growth rate. Software supplied with the EpiRAS 20 system contains a more advanced algorithm to fit the exact shape of the transient. This model is able to take the wavelength dependence of the refractive index and the absorption coefficient into account and fit the shape of the modulations in the transient to obtain information about the growth rate and the thickness of the layer [95].
In addition to the growth rate, it is possible to extract information about the quality of the surface. Roughening of the surface leads to increased diffuse scattering. The amount of light reflected onto the detector therefore decreases if the surface roughens. The mean value of the reflectance signal will therefore decrease in case of increased surface roughening [95].

3.2.5 Precursor materials

Metal–organic precursors are materials that contain metal ions in a complex with organic ligands. While MOVPE was still a novel technique the only precursor materials available were compounds manufactured for other purposes. As MOVPE became an established production method many new metalorganic compounds have been developed.
Precursor materials for use in MOVPE should ideally have the flowing properties [93]:

1. High vapour pressure is desired in order to achieve sufficient material flux and obtain high growth rates. A vapour pressure of at least 1 mbar at room temperature is preferred for the metalorganic that limits the growth rate, and at around 10–60 mbar for the precursor that is supplied in excess. Typically higher vapour pressures are found for materials with low molecular mass and in compounds with the weakest intra–molecular interactions.

2. Liquid precursors are preferred since the vaporisation rate from solids depend on the surface area, which can change over time. Use of solid precursors can therefore lead to problems with reproducibility.

3. The metalorganic should totally decompose at growth temperature. The decomposition temperature should, however, be sufficiently high so that it does not decompose during storage. Too low decomposition temperature can also lead to premature decomposition in the reactor.

4. The metalorganic must be pure to avoid contamination of the samples. It is especially important to avoid presence of oxygen in the precursor.

5. Combination of precursors leading to parasitic reactions are not desirable, since this can lead to reduction of the reaction efficiency, inhomogeneity of the layers and irreproducibility.

All precursor materials should preferably fulfil these conditions. The precursor materials that were found best suited and applied in this study are:

- Cyclopentadienyl-Copper-Triethylphosphine (CpCuTEP), $C_5H_5CuP(C_2H_5)_3$

- Triethylgallium (TEGa), $(C_2H_5)_3Ga$
- Trimethylindium (TMI), $(CH_3)_3In$
- Ditertiarybutylselenium (DTBSe), $((CH_3)_3C)_2Se$

The chemical structure of the precursor materials are shown in figure 3.3.

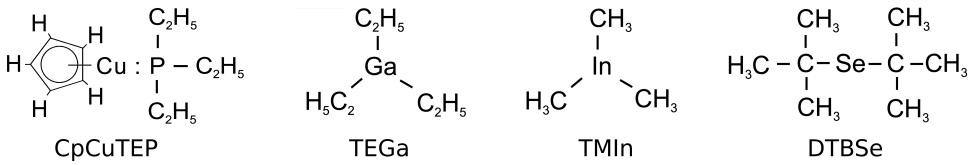

Figure 3.3: Chemical structures of the metalorganic source materials.

For growth of Cu(In,Ga)Se_2 compounds good candidates for In, Ga, and Se precursors are available in the form of TMIn, TEGa, and DTBSe. These standard materials are often used for fabrication of (III–V) or (II–VI) semiconductors and possess most of the desired properties. It is, however, not possible to find a Cu–precursor that posses all the desired properties. This becomes obvious when examining the vapour pressures and decomposition temperatures of the precursors shown in table 3.1.

Property	CpCuTEP	TEGa	TMIn	DTBSe
$\log(p_v)$ (mmHg)	7.26 - 3059/T(K)	8.08-2162/T(K)	10.52-3014/T(K)	7.87 - 2040/T(K)
$T_{D,i}/T_{D,t}$ (°C)	80/120 [96]	225/340 [97]	250/340[98]	300[99]/n.a.
T_{bub} (°C)	65	-5	17	17
$p_v(T_{bub})$ (mbar)	0.021	1.37	1.78	2.82 (9.11)
p_{bub} (mbar)	95	1000	1000	300

Table 3.1: Physical properties of the metalorganics. Vapour pressure of precursors p_v as a function of temperature were supplied by the producer SAFC Hitech for all precursors except for CpCuTEP that was estimated from [100, 48]. $T_{D,i}$ is the temperature where decomposition begins and $T_{D,t}$ is the temperature of total decomposition. T_{bub} is the bubbler temerature, $p_v(T_{bub})$ is the vapour pressure of the precursor at the bubbler temperature, and p_{bub} is the pressure in the bubbler. The vapour pressure of the precursors at the bubbler temperature is calculated with the parameters given in the first row. For DTBSe the observed consumption does not agree with the calculated vapour pressure of 9.11 mbar. From the consumption it was estimated that the DTBSe vapour pressure is rather 2.82 mbar at 17°C.

The CpCuTEP material, used as the Cu–precursor, is problematic for several reasons. It has a very low vapour pressure compared to the other metalorganics. It therefore has to be heated, which is problematic, since the downstream line must also be heated. Even when increasing the bubbler temperature to 65°C, the vapour pressure of CpCuTEP is still more than 50 times lower than the other precursors. The Cu–source is, furthermore, problematic because of its low decomposition temperature starting already at 80°C. This limits the maximum source temperature, since the precursor molecules would start decomposing in the bubbler and the lines already at 80°C. The low decomposition temperature furthermore leads to premature decomposition of the Cu earlier in the liner than the other components. CpCuTEP is finally problematic since it is a solid at 65°C. Variation of the evaporation rate from the solid can therefore lead to reproducibility issues [93].
Following from the previous discussion it is obvious that CpCuTEP is not ideal. It is therefore desirable to find an alternative Cu–precursor with higher vapour pressure

and decomposition temperature. Alternative Cu–sources have been tested in a previous investigation [101]. It was found that the oxygen containing precursors that were tested could be applied to grow polycrystalline films. In order to grow epitaxial films oxygen free precursors should be used. The metalorganic cyclopentadienyl–copper–tertiarybutylisocyanide (CpCuCNtBu) that has a higher vapour pressure and decomposition temperature than CpCuTEP was among the investigated precursors. No improvement of the growth rate over CpCuTEP could however be obtained using this or other of the tested precursors in the study. It was furthermore concluded that good layer/substrate interfaces could only be obtained with CpCuTEP [101]. CpCuTEP is therefore used in the present study in absence of a better alternative.

3.2.6 Substrate

The choice of substrate plays an important role for the outcome of epitaxy experiments. It has e.g. been observed that the orientation of epitaxially grown chalcopyrite depends on the type of substrate [102]. In section 2.2 it is discussed how the physical properties of the substrate such as lattice parameter and thermal expansion coefficient influence the properties of the epitaxial layers.
The substrate used in all experiments of this study is GaAs with (001) orientation from the company Wafer Technology. Two types of substrates were used: Zn–doped (p–type) and undoped (semi–insulating). Except for doping the substrates are identical. The wafers are sold as epi–ready, meaning that they have been polished, etched, and packed in an inert gas atmosphere. The wafers are unpacked in the glove–box and put directly into the reactor before deposition.

3.3 Process Parameters

When performing a growth experiment the process parameters are adjusted to obtain the desired growth conditions. The process follows a recipe, which is modified for each experiment.

3.3.1 The Process Recipe

The recipe defines step by step the course of the entire run. The principal steps of the growth process will be outlined in the following:

- Before the process is started a leak test is performed by pumping the system down after which the throttle valve is closed and the pressure is monitored. If the pressure does not increase the process can continue.
- N_2 is switched off and H_2 is turned on.
- The reactor pressure is adjusted to 50 mbar.
- Bake–out: The temperature in the reactor is increased to 650°C and kept at this temperature for 5 minutes.
- The reactor temperature is lowered to the growth temperature of 470°C for $CuInSe_2$ and 520°C for $CuGaSe_2$.

- Pre–growth: The bubbler flows are adjusted and the bubblers are opened. The gas flow directed into the vent line is allowed to stabilize for 3 minutes.

- Growth: The gases containing the metalorganics are switched from the vent to the run–line and the growth begins. The growth time is varied between 1 hour and 16 hours depending on the desired layer thickness.

- Cool down: The gas flow is switched to the vent–line and the heater is switched off. Shortly after the bubblers are closed and the pressure is increased to 950 mbar. In some experiments the Se–bubbler is kept open during cool–down to prevent potential re-evaporation of Se.

- When the temperature reaches 170°C H_2 is switched off and the system is purged with N_2.

3.3.2 Adjustment of Partial Pressures

It has been demonstrated for $CuGaSe_2$ [48] and $CuInSe_2$ [59] that the final layer composition measured in terms of [Cu]/[Ga] or [Cu]/[In] is linearly proportional to the ratio of the partial pressures of the precursor materials in the gas phase (p_{Cu}/p_{Ga} or p_{Cu}/p_{In}). In order to control the composition of the layers the partial pressures of the metalorganics in the reactor are therefore varied by variation of the flow through each bubbler. The partial pressure of the metalorganic in the reactor p_{MO} is given by

$$p_{MO} = p_R \frac{Q_s}{Q_{tot}} \frac{p_v(T)}{p_{bub} - p_v(T)}, \tag{3.1}$$

where Q_s is the gas flow through the source, Q_{tot} is the total gas flow through the reactor, p_R is the reactor pressure, p_{bub} is the bubbler pressure and $p_v(T)$ is vapour pressure of the source material at temperature T [103]. From equation (3.1) it is seen that a decrease of the bubbler pressure leads to an increased partial pressure of the metalorganic in the reactor. This is the reason why a low pressure is used in the CpCuTEP bubbler compared to the other bubbles. With a total flow of 5 l/minute and the vapour pressures and bubbler pressures given in table 3.1 the flow though each bubbler is adjusted to obtain the partial pressures shown in table 3.2. The partial pressures given in the table is the range that was found suitable to obtain epitaxial growth.

Property	CpCuTEP	TMGa	TMIn	DTBSe
$CuGaSe_2$ growth: Partial pressure p_{MO} (mbar)	0.45	0.14–0.66	–	7.4–9.2
$CuInSe_2$ growth: Partial pressure p_{MO} (mbar)	0.45	–	0.32 – 0.81	21–28

Table 3.2: Range of partial pressures used to grow epitaxial $CuGaSe_2$ and $CuInSe_2$.

It is noticed that the a significant Se–overpressure is used with $p_{Se}/(p_{Cu}+p_{Ga}) \approx 9$ for $CuGaSe_2$. For $CuInSe_2$ the Se overpressure needed to obtain good results is even higher with $p_{Se}/(p_{Cu}+p_{In})>20$. The Se overpressure is needed in order to avoid Se re-evaporation that has often been reported in literature as for example discussed in [104, 105].

3.4 Characterization of the Growth Process

The development of a MOVPE process to grow high quality epitaxial chalcopyrites will be discussed in the following. The process developed here is based on a recipe used in a similar MOVPE system at Helmholtz–Zentrum Berlin. The MOVPE system used in this work is a new installation. One of the first tasks of this work is therefore to establish growth process parameters. The establishment of an epitaxial growth process and knowledge of the structural properties of the resulting layers is the prerequisite for further studies of the properties of chalcopyrites.
The following sections contains the results of growth experiments performed in this work. This includes a demonstration and discussion of the tools applied to monitor and develop the epitaxial growth process. A few examples of optimization of process parameters and discussion of their influence on the epitaxial growth are subsequently presented. It is demonstrated that epitaxial growth of high quality material is obtained after optimization of the growth conditions. The chapter is finally ended with the development of a model to explain effects that are observed during the epitaxial growth process.

3.4.1 Reflectance as a Tool for Process Monitoring

The in–situ reflectance equipment installed in the MOVPE is used to extract information about the real time evolution of the growth. This is a valuable tool that aids understanding of the growth process. The reflectance transient is utilized several times throughout this section to understand the growth. Here it will be demonstrated with an example how the reflectance transient can be interpreted. This will be utilized in later growth experiments.
Figure 3.4 shows an example of the effect of Cu_xSe development on the reflectance transient. The Cu_xSe crystallites form when growing under Cu–rich conditions as explained in section 2.1.2. The reflectance transients of three $CuGaSe_2$ samples are shown. This is combined with SEM micrographs of these samples showing the surface morphology. In the SEM micrographs it is observed that the density of Cu_xSe crystals on the sample surface is decreased when going from (a) to (c).
It is noticed that the average reflectance measured during growth of these samples is decreasing for sample (a) and (b), whereas the average value remains almost constant for sample (c). The decrease in the reflectance can be interpreted as a sign of increased surface roughness due to increased diffuse scattering. This interpretation is clearly verified with the SEM micrographs showing the highest Cu_xSe density for sample (a) and the lowest for sample (c). The decrease of the reflectance signal can therefore often be related to the development of the secondary Cu_xSe phase as crystals on top of the growing layer.
When comparing the reflectance transients, it is furthermore seen that the oscillation period is getting shorter when going from (a) to (c). The oscillation period is related to the growth rate of the layer as mentioned in section 3.2.4. The initial growth rate can be determined to be 130 ± 5 nm/h for sample (c) compared to 115 ± 5 nm/h for sample (a). It is also noticed that the oscillation period increases with time for all processes presented here. This indicates that the growth is slowing down as the growth proceeds. A growth rate of about 80 ± 5 nm/h can be estimated for all three samples by fitting the reflectance transient at the end of the growth. This is significantly lower than the initial growth rate of 130 ± 5 nm/h for sample (c).

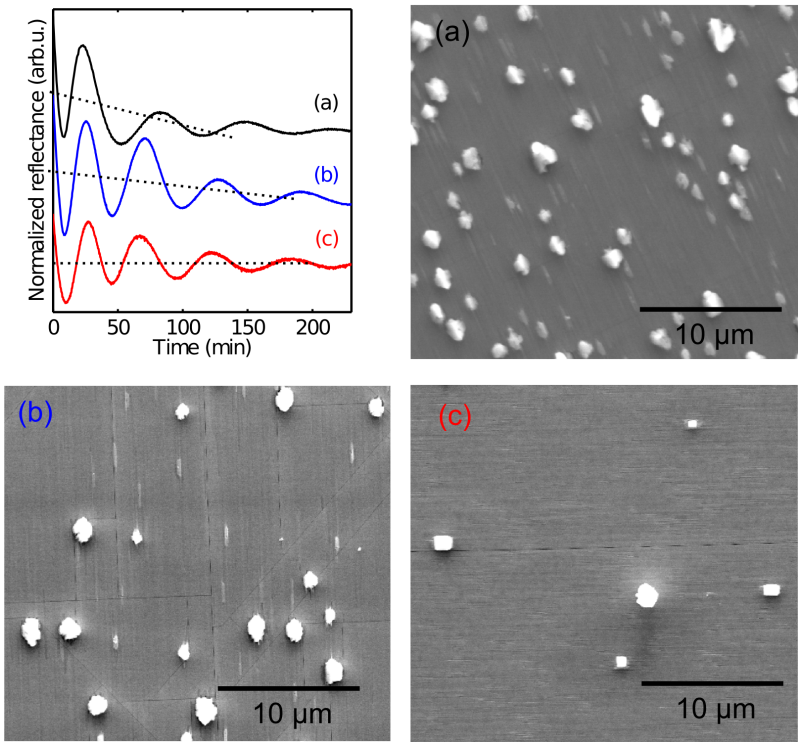

Figure 3.4: Example of the reflectance transients for three samples grown at 570 °C with decreasing density of Cu_xSe crystals going from (a) to (c) as seen in the corresponding SEM micrographs.

It seems that the lower initial growth rate of sample (a) and (b) is related to a higher Cu–excess. For these samples with a higher density of Cu_xSe the oscillation length increases faster than for the sample with a lower Cu_xSe density (c). This means that the growth slows down faster with increasing Cu–excess even though the same growth rate is obtained when fitting the last oscillations. This might be related to the presence of two phases competing for the supplied Cu. With higher excess of Cu the incorporation in Cu_xSe rather than in the $CuGaSe_2$ layer becomes more dominant. The decrease of the growth rate with increasing Cu–excess has been also observed for $CuInSe_2$ in earlier studies [59].

3.4.2 Photoluminescence as Tool for Process Control

Low temperature PL is used as a tool to verify the properties of each sample in the development of a process for growth of epitaxial samples. As discussed in section 2.3.8 the shallow defects in $CuGaSe_2$ and $CuInSe_2$ are well described with a model with one donor and three acceptors. The correlation between the observed DAP transitions and the composition of the layer is exploited to monitor and understand the growth process in the present study.
PL is measured for the vast majority of samples grown during the development of the growth process and for all samples grown for different purposes. The measurements are performed for mainly two reasons. Firstly, it is used to verify the sample composition. This is done by comparison with earlier PL studies where the appearance of the peaks have been related to the [Cu]/[III] ratio as discussed in section 2.3.8. This relationship has furthermore been verified in this work (see e.g. the results discussed in section 3.7).

Secondly, PL is performed to investigate the quality of the grown samples. Features like peak width and the appearance or absence of excitonic luminescence can both give information on whether the sample is of good quality. It is furthermore possible to obtain an idea about strain and homogeneity of samples based on the PL measurements. The strain is observed as a peak shift due to widening or narrowing of the band gap. One can obtain information about sample homogeneity by scanning the laser spot across the sample surface and comparing the obtained spectra. This can be done in an approximate and qualitative fashion by movement of the sample by micrometer screws or in a more detailed way by scanning an area of the surface with the μ–PL setup discussed in section 5.3.
The extensive collection of measurements, can be compared to the model described in section 2.3.8 to further support the energies of the transitions found in previous studies. Figure 3.5 shows the PL peak positions measured for $CuGaSe_2$ samples grown as a function of the sample number. Figure 3.5(a) contains only the peaks that could be attributed to either excitonic recombination or to one of the DAP transitions. Peaks that did not fit into this model are collected in figure 3.5(b) indicated with triangles. The squares in this figure are peaks that show the characteristic behaviour observed in the presence of potential fluctuations discussed in further details in chapter 4. Figure 3.6 shows the same measurements performed on $CuInSe_2$ samples grown and studied in this work. The labelling is the same for both figures.

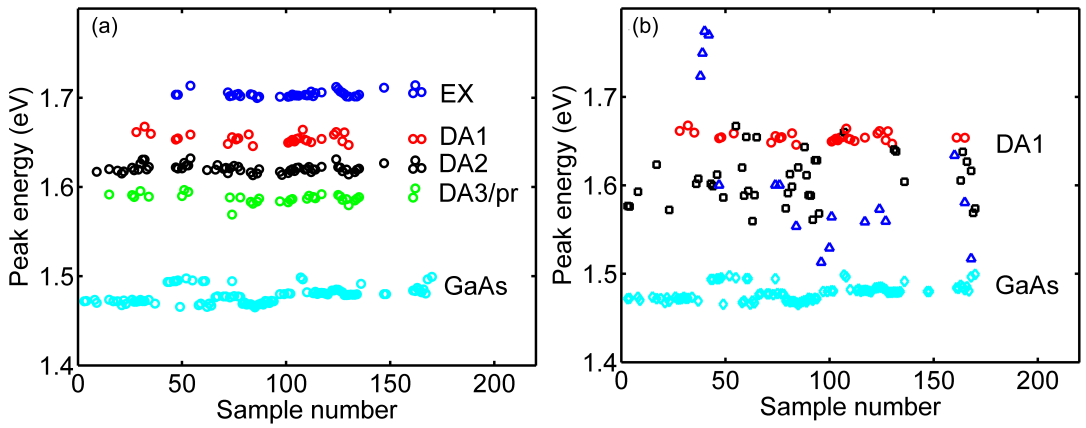

Figure 3.5: (a) PL peak positions for all measured Cu–rich $CuGaSe_2$ samples that fit the model of Bauknecht [48]. The label EX is given to peaks with the energetic position and intensity dependent behaviour typical for excitons. DA1 and DA2 indicates the peaks of donor–acceptor pair type with energies agreeing with defect model. The peak labelled DA3/pr could be a mixture of the DA3 transition and a phonon replica. (b) PL of samples with the signature of potential fluctuations (squares) and peaks that could not be explained with the standard model (triangles). As a reference the DA1 and GaAs peaks from (a) are also shown.

One notices that the peaks measured in this study are nicely separated into four separate groups. The separation between the groups is a first indication that the model containing three DAP transitions is generally valid for all Cu–rich samples grown in this study. The scatter of the points around the average values have several reasons. Samples presented in the figure are grown under different conditions with e.g. varying growth temperature and layer thickness. This can give rise to different strain in the layers and therefore different peak positions. Another possible source or error that cannot be totally excluded is an uncertainty introduced due to small inaccuracies in the wavelength calibration even though care is always taken to minimize this error. It is estimated that the error in the

wavelength calibration does not exceed 0.5 nm. The GaAs peak position is not always constant neither. This is partly due to the mentioned source of inaccuracy and the fact that different substrates are used. A difference is always observed between undoped and Zn–doped substrates. It is furthermore possible that small variations between different batches can exist.
Figure 3.5(a) shows clearly that the first growth experiments performed involved a few adjustments before a good standard recipe is obtained. A few examples of such optimizations are discussed in the following section. It is seen that the first samples are very Cu–rich showing only the DA2 transition or Cu–poor with signs of potential fluctuations. After some runs it is seen that a DA1 finally appears in the PL spectrum of the measured samples. This is an indication that the recipe has been adjusted to obtain samples with a composition very close to perfect stoichiometry. It is an important prerequisite to know the process parameters to obtain stoichiometric growth. From this point on, it is possible to choose the desired composition of the grown samples by fine tuning the relative partial pressures of the metalorganics. After growth of around 50 samples it is finally possible to observe excitonic recombination in the PL of the deposited $CuGaSe_2$ layers. This is a first indication that good quality layers have been obtained. When comparing the development of the process for growth of $CuInSe_2$ in figure 3.6 with that of $CuGaSe_2$ in figure 3.5 it is noticed that excitons appear after much fewer attempts for $CuInSe_2$. This is the case since experience gained from growth of $CuGaSe_2$ could be transferred to $CuInSe_2$.

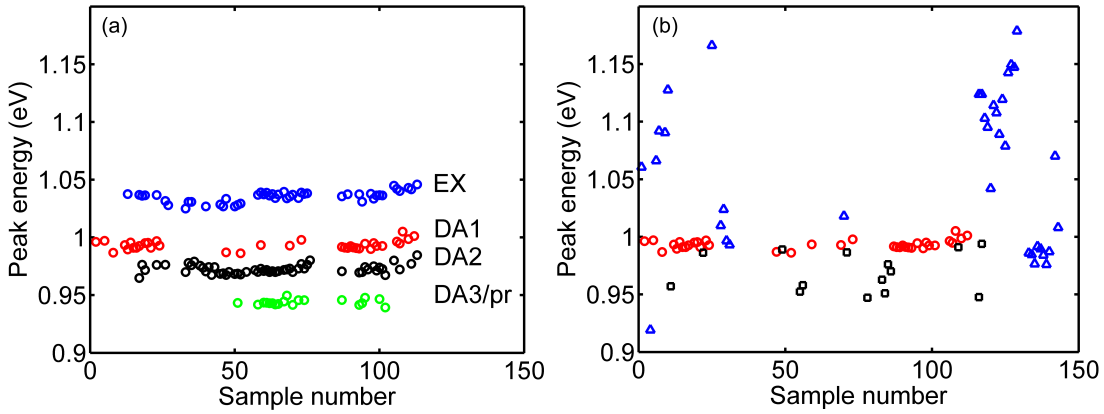

Figure 3.6: (a) PL peak positions for all measured $CuInSe_2$ samples that fit in the model of Rega [59]. The label EX is given to peaks with the energetic position and intensity dependent behaviour typical for excitons. DA1 and DA2 indicates the peaks of donor–acceptor pair type with energies agreeing with defect model. The peak labelled DA3/pr could be a mixture of the DA3 transition and a phonon replica. (b) PL of samples with the signature of potential fluctuations (squares) and peaks that could not be explained with the standard model (triangles). As a reference the position of the DA1 peak is also shown.

The average energies of the DAP and EX transisions shown in figure 3.5 and figure 3.6 are collected in table 3.3. These values should be compared to the transition energies found in literature. Both free and bound excitons have been observed in PL measurements on epitaxial $CuGaSe_2$ layers. For $CuGaSe_2$ a FX energy of 1.707 eV and a BX energy of 1.7027 eV have been reported [48]. This measurement is performed on epitaxial samples very similar to the ones studied in this work. These values are very similar to 1.704 eV found here. It should be noticed that this value has a contribution from both free and bound excitons. An energy between the one found for bound exictons and free excitons is therefore expected. Studies of polycrystalline $CuGaSe_2$ have identified free exciton

transitions at 1.723 eV and bound excitions at 1.719 and 1.706 eV respectively [106, 107]. An average of these values is slightly larger than the energy found here. This is due to the presence of strain in the epitaxial $CuGaSe_2$ layer that gives rise to a decrease of the band gap.

Transition type	$CuGaSe_2$	$CuInSe_2$
EX	1.704 eV	1.035 eV
DA1	1.655 eV	0.993 eV
DA2	1.621 eV	0.972 eV
DA3	1.588 eV	0.944 eV

Table 3.3: Average of photoluminescence transitions determined from samples grown in this study.

For $CuInSe_2$ an exciton energy of 1.032 eV measured on an epitaxial layer has been reported earlier [59]. This agrees very well with the average exciton energy of 1.035 eV determined in this study. For single crystal $CuInSe_2$ samples a FX recombination energy of 1.041 eV and several BX transitions in the range 1.038-1.028 eV have been reported [108]. In polycrystalline material similar values have been found with a FX energy of 1.041 eV and BX transitions in the range 1.038-1.025 eV [109]. A broad exciton peak with a contribution of both FX and BXs with these energies can be expected to have an energy very similar to the exciton transitions observed in epitaxial layers. This agrees with the expectation that the band gap of $CuInSe_2$ is not strongly influenced by strain in the layer as discussed in section 2.2.4.
The values obtained in this study for the DA1 and DA2 transitions are almost identical to the results of earlier studies discussed in section 2.3.8. This confirms that the transitions observed in the epitaxial samples grown in this study and earlier studies such as [13, 14, 48, 59] have the same origin. It should be mentioned that the large number of samples investigated in the present study adds further evidence to the defect model presented in the introduction. The strong support for this model presented here allows to apply the defect model in further investigations in the following chapters of this work.
So far the DA3 transition was not mentioned since it is often questionable if this is in fact an independent DAP transition or rather a phonon replica. It is shown by CL that this luminescence peak can be related to a third DAP transition [91]. This is concluded from the observation that the intensity of the peak varied spatially independently of the other DAP transitions. In these samples the peak could therefore not be a phonon replica of one of the other DAP transitions. Similar results will be shown with μ–PL studies in chapter 5. It is, however, not always found that this peak is spatially independent from the DA1 and DA2. In some cases there are indications that the peak is in fact a phonon replica. It most cases the peak is probably due to a contribution from both a phonon replica and a DA3 transition. The presence of the DA3 and phonon replica is discussed further in section 5.4.1.
Figure 3.5(b) and figure 3.6(b) show the peaks that do not fit the standard DAP model. This includes the Cu–poor samples that are dominated by potential fluctuations at low temperatures.
The square symbols show the energetic peak positions of samples with characteristics of potential fluctuations, i.e. an asymmetrically broadened peak showing a significant blue shift of the peak with increasing excitation. These characteristics are typically seen for samples grown under Cu–poor conditions. It is noticed that these samples all have

PL peaks that are either around the energetic position of the DA1 peak or red shifted compared to this DAP transition. This is related to the fact that potential fluctuations give rise to a disturbance of the band edges leading to a red shift of the peak relative to the unperturbed case observed in Cu–rich material where the DA1 is observed (see chapter 4).
The triangular symbols in figure 3.5(b) and figure 3.6(b) show the energetic position of peaks that could not be ascribed to either DAP transitions or classified as samples with dominating potential fluctuations. These peaks can have several origins. A large number of the peaks with energies higher than the band gap of the chalcopyrite are most likely related to the ODC structure (see phase diagram in section 2.1.2). This is supported by the finding that these peaks appear in material that have been grown under very high Cu–deficiency. A band gap of 1.86 eV has been reported for the ODC material $CuGa_3Se_5$ [32]. Similar band gap at 10 K of 1.917 eV has been measured for the even more Cu–poor ODC $CuGa_5Se_8$ [33]. Radiative luminescence from defects in the band gap of one of these materials could therefore be a source of the peaks observed in the very Cu–poor samples. The observations for In–containing samples is similar to the result obtained for the Ga containing counterparts. A 10 K band gap between 1.25 and 1.28 eV has been reported for a compounds with approximatively the $CuIn_3Se_5$ composition [110, 111]. The peaks observed in very Cu–poor samples with energies higher than the band gap of $CuInSe_2$ can therefore also be related to ODC structures.
Other peaks below the band gap are sometimes observed that do not energetically fit in the defect model. These are included in order to investigate if the defect model should include additional levels. There are, however, not many peaks that appear with the same or at least very similar energy. Only for $CuGaSe_2$ several peaks are located around 1.56 eV. This peak could, however, be a second phonon replica to the DA2 peak involving two phonons of energy 33 meV [112]. The remaining peaks seen in figure 3.5(b) and figure 3.6(b) have not been identified.

3.5 Optimizing Growth Conditions

In order to obtain epitaxial growth it is necessary to tune the parameters of the process. Parameters that have been adjusted in order to optimize the growth process include: gas flow through each bubbler (Cu,Ga,In,Se), Cu bubbler temperature and pressure, ratios of upper (Cu) and lower (other MOs) gas flows, total gas flow, bake–out temperature, substrate rotation speed, and reactor temperature during growth. A few examples of the influence of some of these growth parameters are presented in the following sections.

3.5.1 Cu–Bubbler Temperature

A sample series where only the temperature of the Cu–bubbler is varied has been performed. The aim of increasing the bubbler temperature is to increase the growth rate since the vapour pressure is increased with increasing temperature. The Cu metalorganic limits the growth rate because of its low vapour pressure relative to the other precursors as mentioned in section 3.2.5. It is therefore desirable to increase the amount of Cu–precursor transported to the reactor and thereby increasing the partial pressure of Cu during the deposition. One must, however, be aware that the lines bringing the precursor to the reactor must be heated to avoid condensation. Also one has to be aware that the

metalorganics will decompose if the temperature is increased too much leading to deposition of Cu in the bubbler and the lines. For CpCuTEP the decomposition temperature is 80 °C. The temperature in the bubbler and the line should therefore be kept significantly lower than this limit.

Cu bubbler temperature	60 °C	62 °C	65 °C
[Cu]/[Ga]	0.75	0.87	1.05
Growth rate (nm/h)	90–85	85–79	≈80

Table 3.4: Composition measured by EDS of $CuGaSe_2$ layers grown with variation of the temperature of the Cu bubbler. Growth rates are estimated from fits of the reflectance transients.

In order to examine the effect of the Cu–bubbler temperature a small series of three samples are grown, where the only difference between the samples is the bubbler temperature. The resulting composition measured with EDS is presented in table 3.4. The result clearly shows an increase of the Cu–content in the samples with increasing bubbler temperature as expected. The fact that more Cu is incorporated shows that this approach facilitates faster growth. It is, unfortunately not possible to see an increase of the growth rate but rather a decrease. One should, however, keep in mind that it can be difficult to compare the growth rate of samples with different [Cu]/[Ga] ratios due to the development of Cu_xSe as discussed in section 3.4.1. The appearance of Cu_xSe tend to slow down the growth of the $CuGaSe_2$ layer, which counteracts the potentially increased growth rate.

3.5.2 Influence of Selenium Excess

This section presents the influence of another parameter that influences the properties of the samples, namely the effect of the Se–overpressure. An example is presented for $CuInSe_2$ that needs higher Se–excess to grow epitaxially than $CuGaSe_2$ [59].
A series of four samples is grown to investigate the effect of the Se–overpressure in the gas phase during growth on the properties of the final $CuInSe_2$ layers. The excess partial pressure of the Se–precursor for the samples investigated here is collected in table 3.5. All other parameters are kept the same for the sample series.

Sample number	#1	#2	#3	#4
$\frac{p_{Se}}{p_{Cu}+p_{In}}$	16	20	24	26
Initial growth rate (nm/h)	–	89±5	115±5	112 ±5
Peak shift in PL excitation dependence β (meV/decade)	3	1	15	16

Table 3.5: Influence of the Se precursor excess in the gas phase during growth of four $CuInSe_2$ layers. Initial growth rates are estimated by fits of the first few oscillations of the reflectance transients. The shift of the main PL peak β with increasing excitation density is also included.

The reflectance transients measured during the growth of these samples is shown in figure 3.7(a). It is noticed that the reflectance transients of sample #1 only oscillates once before the sample surface gets very rough and the reflectance drops. Sample #2 also roughens as seen by the decreasing reflectance. The effect of roughening is, however, much lower for this sample and three entire oscillations are observed. The final two samples with the highest Se–excess in the gas phase are very similar, showing four and a half

oscillations and much lower degree of roughening. The fact that more complete oscillations are seen in sample #3 and #4 than in sample #1 and #2 shows that the growth rate increases with increasing Se–excess. This is also expressed in the fitted growth rates displayed in table 3.5. Judging from these results only it seems that increasing the Se–excess is beneficial for the epitaxial growth giving both smoother surfaces and larger growth rates.

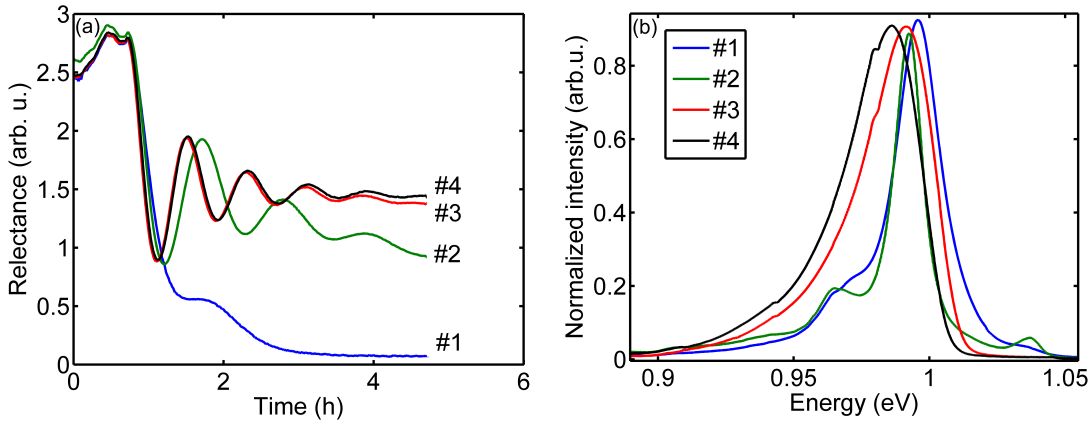

Figure 3.7: (a) Reflectance transient measured during growth of samples with increasing Se–overpressure from #1 to #4 (b) 10 K photoluminescence spectra of these samples.

This conclusion must, however, be revised when the photoluminescence spectra measured on the final films are taken into account. These are shown in figure 3.7(b). The PL measurement of sample #1 shows a relatively broad DA1 peak and a low energy shoulder. This peak can be ascribed to a DAP transition based on the β value of 3 meV/decade (see table 3.5). Sample #2 has a peak with a very similar energy, probably the DA1 transition, as well as a peak ascribed to the DA2 and an exciton. It is noticed that the DA1 peak observed in sample #2 is significantly narrower than the peak measured in sample #1. The fact that the transition is narrower and the appearance of an exciton are both indications that the crystal quality is initially improved as the Se–excess is increased. When the Se–excess is further increased for sample #3 and #4 it is realized that this is not a general trend. Sample #3 shows the typical PL of weak potential fluctuations with an asymmetrically broadened peak that blue shifts with increasing excitation. Sample #4 shows the sign of even deeper potential fluctuations with a larger blue shift with increasing excitation (see β values in table 3.5). This indicates these samples are highly compensated. The defect concentrations are high in these materials, which seems to contradict that higher Se–excess is beneficial as argued initially. The behaviour that the material becomes compensated is normally observed when the [Cu]/[In] ratio is lower than one. This could indicate that the [Cu]/[In] ratio decreases with increasing Se–excess during the growth. This idea is in fact supported by investigation of the surface morphology that shows Cu_xSe on sample #1 typical for Cu–rich material and faceting on sample #3 typical for Cu–poor material. This result demonstrates the complexity of the MOVPE process that is sometimes difficult to predict. Many parameters influence the final result and a small change in one parameter might influence other parameters.
The result indicates that the overpressure of Se in the gas phase influences the amount of Cu and In incorporated in the layer. It is important to be aware of this effect since many samples in this work are grown with different [Cu]/[III] ratios by variation of the partial

pressure ratio of p_{Cu} and p_{Ga} keeping the partial pressure of p_{Se} constant. In such sample series it can not be excluded that the incorporation of Se also changes when the partial pressures of Cu and Ga or In are varied.

3.5.3 Optimization of Growth Temperature

The growth temperature is an important process parameter. Several properties of the growth process and the final layers depend on the growth temperature. The growth dynamics for example are significantly affected by the growth temperature. A detailed study of the growth dynamics at high growth temperature is presented in section 3.7. This section is devoted to the investigation of a $CuGaSe_2$ sample series where the only process parameter differing between the samples is the reactor temperature. The growth time is four hours for all samples investigated here. An overview of the growth temperatures and growth rates of the samples studied in this section is given in table 3.6.

Sample number	#1	#2	#3	#4	#5	#6	#7
Reactor temperature	490 °C	500 °C	510 °C	520 °C	530 °C	550 °C	570 °C
Growth rate (nm/h)	55±5	58±5	105±5	102±5	102±5	96±5	89±5
β (meV/decade)	2	2	4	8	11	14	14

Table 3.6: Growth rates estimated from reflectance transients of $CuGaSe_2$ layers grown with variation of the reactor temperature. The shift of the main PL peak β with increasing excitation density is also included.

When the reactor temperature is increased from 490 °C to 510 °C an increase in the growth rate, determined from the reflectance transient, is observed. The growth rate then remains constant for temperatures between 510 °C and 530 °C. When the temperature is increased further the growth rate decreases again.
In order to understand the observed temperature dependence, consideration of some theories of MOVPE growth is useful. The observed behaviour might be related to changes in the growth limiting mechanism. Generally speaking the growth rate can be limited by mass transport, reaction kinetics or thermodynamic effects [93]. In the low temperature regime the increase of growth rate with temperature can be related to reaction kinetics [93]. This explanation relies on the fact that several activation barriers must be overcome in the chemical reactions taking place in the reactor. The thermal energy needed to overcome these barriers is supplied by increasing the temperature.
A temperature region with more or less constant growth rate is frequently observed in MOVPE growth. The limiting factor when this case is observed, is often mass transport. Since gas diffusion is almost temperature independent mass transport limited growth is almost temperature independent [93]. This could also be a part of the explanation for the behaviour observed here.
The final decrease of growth rate with increasing temperature might be related to thermodynamically limited growth. This could e.g. be re-evaporation of elements as a consequence of the increased temperature. Another explanation for the decreasing growth rate is the premature upstream loss of Cu.
These explanations for the observed behaviour are, admittedly, rather of speculative character. If these speculations should be verified a comprehensive series of experiments varying e.g. substrate orientation, flow rates, rotation speed should be performed.
In order to investigate the effect of growth temperature on the optoelectronic properties

of the absorbers 10 K PL measurements are performed. The PL measurement can, furthermore, be used to judge the composition of the samples and give further insight into the reason for growth rate variation. The result is shown in figure 3.8.

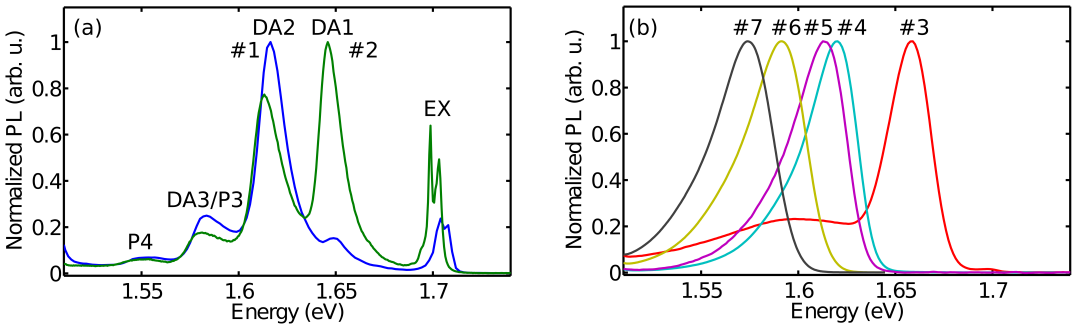

Figure 3.8: 10 K PL of $CuGaSe_2$ layers grown at temperatures increasing from #1 to #7. (a) Sample #1 and #2, and (b) sample #3 to #7.

The PL spectra are separated into two figures for clarity. Figure 3.8(a) shows the PL spectra of the samples grown at the lowest temperatures. These both show peaks due to DAP and exciton recombination. Both show two peaks with energies slightly above 1.7 eV, probably due to FX and BX recombination demonstrating good crystal quality. Also both samples display two phonon replicas supporting this statement. Sample #1 is dominated by DA2 recombination indicating high Cu–excess during growth. Sample #2 displays both DA2 and DA1 peaks, a signature of a slightly less Cu–rich growth. The samples grown at higher temperatures are shown in figure 3.8(b). Except sample #3 these all show clear Cu–poor signatures. The increasing red shift relative to the DA1 peak position and increasing β value (see table 3.6) with increasing growth temperature indicates higher Cu–deficiency. The interpretation of the PL spectrum of sample #3 is not straight forward in terms of the defect model. The energy of the dominating peak is around the DA1, but the peak is broadened and shifts with excitation (see table 3.6), indicating some degree of potential fluctuations. This points towards a composition with a [Cu]/[Ga] ratio around 1 or slightly lower, which fits with the tendency observed in the sample series. The broad peak around 1.6 eV is less easily interpreted. It might be related with a surface layer with a different composition. One can imagine that the surface responsible for the largest contribution to the signal is less compensated giving rise to the main peak. The low energy peak could be due to a underlying layer with a higher degree of compensation. Similar results have been obtained for samples with a very Cu-poor surface layer [113]. Why this should arise for these particular growth conditions is, however not clear. When summing up the results the tendency is clear that the [Cu]/[Ga] ratio decreases with increasing growth temperature. This observation is not unique for $CuGaSe_2$, but also observed in a similar experiment done on $CuInSe_2$. This change of composition might also be a part of the reason for the observation that the growth rate decreased at low temperature, due to the development of the secondary Cu_xSe phase under Cu–rich conditions. This has previously lead to lower growth rates as discussed in section 3.4.1. The reduction of the growth rate due to Cu_xSe formation is, however, much smaller than the growth rate decrease observed here. This indicates that other effects such as reaction limited growth [93] play the main role at low growth temperature.
The reason for decreasing [Cu]/[Ga] ratio with increasing temperature is probably related to the low decomposition temperature of Cu relative to the other precursors. This

leads to deposition in the entrance of the reactor before the precursors reach the substrate. This tendency is increased with increasing temperature, hence the lower Cu content in the layers. The fact that Cu deposits early in the reactor is also observed by inspection of the liner after a growth process. The entrance to the liner is always covered by a layer of Cu, supporting explanation of Cu–loss proposed here. Another effect that can explain the decreasing [Cu]/[Ga] ratio is the decomposition of the GaAs substrate. Ga released from the substrate is incorporated into the layer leading to an increase of the [Cu]/[Ga] ratio. This effect is stronger with increased growth temperature as discussed in section 3.7.
The fact that the composition depends on the temperature once again demonstrates the complexity of the growth process, where change of one parameter influence several properties. It can therefore be difficult to investigate the effect of solely one parameter at a time. Despite the complexity and sometimes unexpected effects a process yielding high quality epitaxial layers was developed. The structural properties of these layers will be the topic of the next section.

3.6 Verification of Epitaxial Growth of Chalcopyrites on GaAs

In order to verify that epitaxial growth is obtained TEM and EBSD measurements are performed. The orientation of the layers is, furthermore, investigated by XRD measurements. A description of the XRD technique is available in section D.3, and the EBSD method is discussed in general terms in section D.2.

3.6.1 The $CuGaSe_2$/GaAs Interface

Lamella of the $CuGaSe_2$ layers on GaAs are prepared with a focused ion beam followed by ion milling. The thin lamella containing a cross–section of the $CuGaSe_2$/GaAs interface are subsequently investigated by TEM. Figure 3.9 shows the $CuGaSe_2$/GaAs interface region.
It is noticed that the crystal planes in the GaAs continue nicely into the GaAs layer as shown in figure 3.9 with a blue dotted line. This demonstrates that the $CuGaSe_2$ layer grows epitaxially on the GaAs(001) surface in the studied area. The only difference seen between the $CuGaSe_2$ and the GaAs in the TEM image is that the contrast varies in the $CuGaSe_2$ layer on a length scale of a few nanometers. This variation not observed in the GaAs could be due to variations of the [Cu]/[Ga] ratio [114]. The angle between the interface and the crystal planes is estimated to $\approx 55^\circ$, which indicates that these planes are the (111) planes in GaAs corresponding to the (112) planes in $CuGaSe_2$.

3.6.2 Crystal Quality measured by Electron Backscatter Diffraction

Electron backscatter diffraction (EBSD) measurements are performed to verify that the layers grow epitaxially on large areas and to show that the grown layers are of good crystal quality. The measurements are performed with an angle of 70 degrees between the sample surface and the direction to the detector.
Figure 3.10 shows the resulting EBSD patterns. The result shows that the [221] crystal direction is pointing more or less straight at the detector. This is due to the angle between the sample and the detector. When correcting for this angle, one finds that the [001] crystal direction is perpendicular to the sample surface (the angle between the [221] and

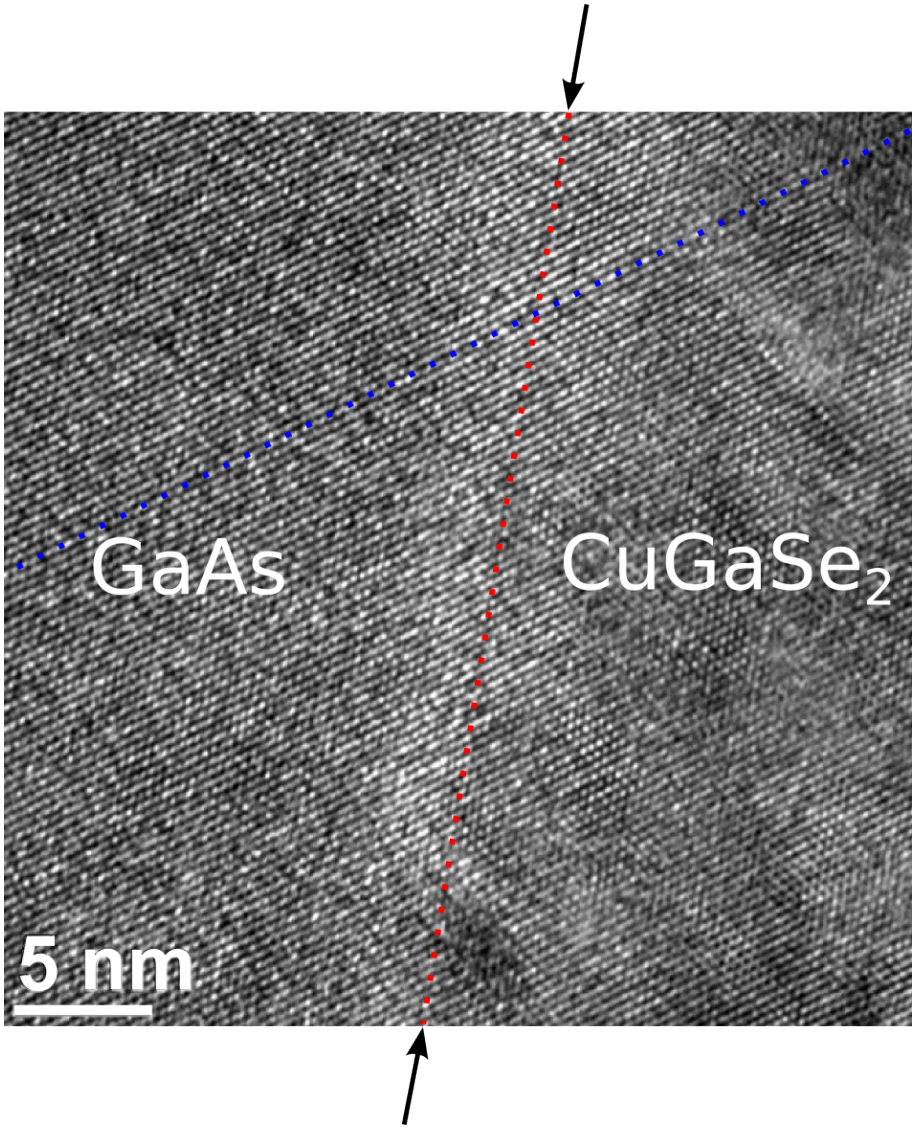

Figure 3.9: TEM cross section of the $CuGaSe_2$/GaAs interface demonstrating epitaxial growth. The arrows and the red dotted line indicates the interface. The blue dotted line correspond to the (111) plane in GaAs.

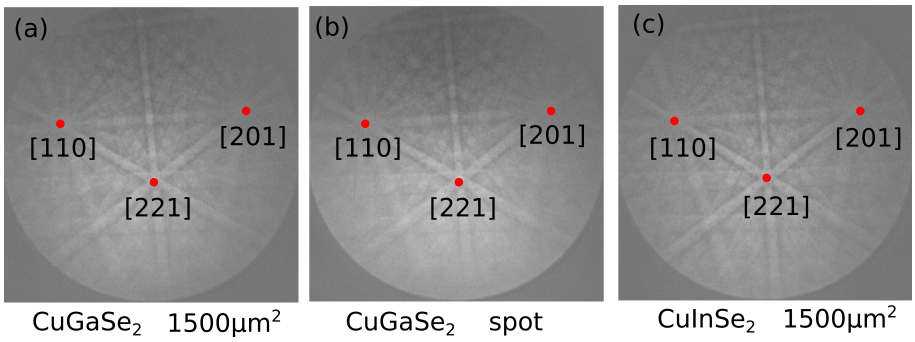

Figure 3.10: EBSD patterns obtained from KCN etched Cu–rich $CuGaSe_2$ and $CuInSe_2$ under an angle of 70 degrees. (a) and (c) are obtained for an area of 1500 μm^2, while (b) is the EBSD pattern measured on a spot the size of the electron beam.

[001] directions is ≈19.5°). This confirms that the layer grows in the [001] direction as found by XRD measurements discussed in the next section.
EBSD measurements are performed with two different approaches. Figure 3.10(a) and (c) are measured by collection of back scattered electrons from an area of $\approx$ 1500 μm^2, while scanning the electron beam across the sample surface. Figure 3.10(b) is obtained by collection of back scattered electrons from only one point of the sample. The information obtained from this measurement is very local and originates from an area with the size of the spot of the electron beam with a radius in the range $\approx 10 - 100$ nm [115]. It is hardly possible to distinguish the pattern measured on a spot and on a larger area of the same sample surface in figure 3.10(a) and (b). In both cases a large number of sharp lines are visible in the patterns. The fact that many sharp lines are observed is proof that the quality of the crystal is good. If the crystal would have been highly defected these lines would blur out and eventually not be visible [116, 117]. The fact that the EBSD pattern obtained from an extended area and a spot measurement are of similar high quality demonstrates that the layer is epitaxial. Similar high quality EBSD patterns are obtained for $CuInSe_2$ layers grown on GaAs(001) as seen in figure 3.10(c).

3.6.3 Crystal Orientation

Since chalcopyrite can grow with different orientations on GaAs it is necessary to investigate the crystal orientation of the layers. In figure 3.11 it is shown that the *c*–axis of the chalcopyrite can be oriented either parallel or perpendicular to the (001) GaAs surface. As shown in section 2.2.3 for $CuInSe_2$ the lattice mismatch between the *a*–axis of $CuInSe_2$ and GaAs amounts to -1.8%. If the crystal would grow with the *c*–axis parallel to the GaAs substrate the lattice mismatch will be -2.4%. Similarly for $CuGaSe_2$ it is shown that the lattice mismatch for the *a*–axis is 0.7 % and 2.6% for the *c*–axis.

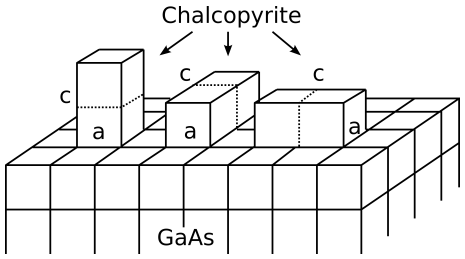

Figure 3.11: Illustration of heteroepitaxy of tetragonal chalcopyrite on the cubic (001) GaAs subtrate. The *c*–axis of the chalcopyrite can either be oriented parallel to the surface of the substrate or perpendicular to the substrate surface [61, 118].

Based on the lattice mismatch alone, it is therefore expected that both $CuInSe_2$ and $CuGaSe_2$ will grow with the *c*–axis perpendicular to the substrate surface (along the [001] direction). XRD measurements on several samples are performed in order to verify that this is actually the case. The measurements are performed in the standard $\theta - 2\theta$ configuration, where both the source and detector are moved simultaneously while the angle between the source and detector is 2θ. Figure 3.12 shows the two regions of the diffractogram in which peaks are observed. As expected and found in previous studies of $CuGaSe_2$/GaAs(001) no peaks are observed outside these regions [48]. The measurement shown here is a typical example of a diffractogram measured for $CuInSe_2$. In order to aid the interpretation of the result a measurement of a GaAs wafer is included as a reference.

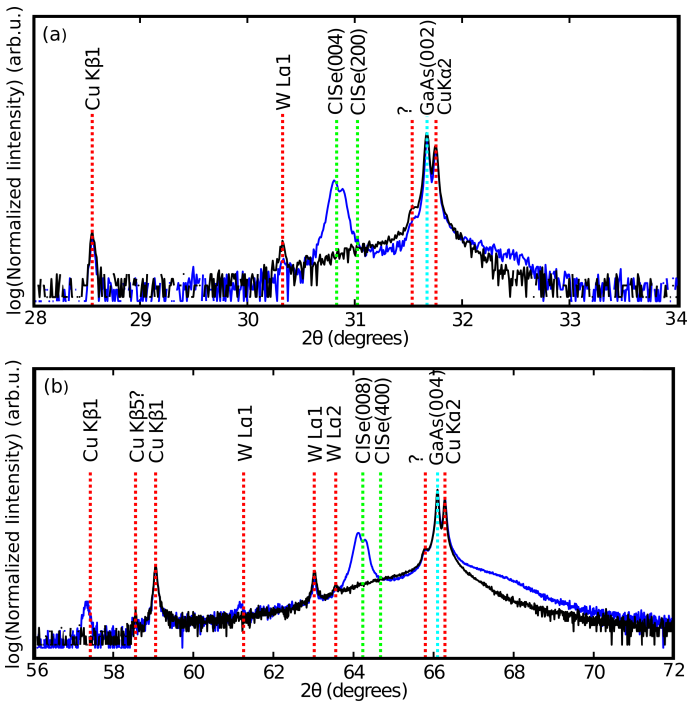

Figure 3.12: $\theta - 2\theta$ XRD of epitaxial $CuInSe_2$ (blue) and GaAs (black). The green lines indicate data base values for the reflections of $CuInSe_2$. The cyan line is the database value of the GaAs reflexes. All red lines indicate instrumental artefacts. The peak labelled '?' is an unidentified artefact that is specific to the used instrument. (a) contains the reflections observed at low angles and (b) the reflections at higher angles.

One notices that several peaks are visible in the diffractogram of the GaAs substrate, these peaks are therefore not of relevance in understanding the layer orientation. These peaks should, however, be commented. All peaks seen in the measurement of GaAs are also found in measurements of $CuInSe_2$. The dominating reflections are as expected the GaAs reflections of the (002) and (004) planes that are perpendicular to the [001] substrate normal. The angle of the main peaks agrees very well with the database values for GaAs obtained from the International Centre for Diffraction Data (ICDD). This is indicated with the cyan lines, that shows the ICDD value for the GaAs (002) and (004) diffraction lines. All the peaks indicated by red lines are artefacts that originates from several wavelength components in the X–ray beam. The main component of the X–ray beam is the Cu $K\alpha_1$ component. Normally one expects to measure mainly a contribution from X–rays of this wavelength. This is also the case here, but a contribution from X–rays with several other wavelengths is additionally observed. Based on wavelengths of X–ray transitions from National Institute of Standards and Technology and Braggs law (see appendix D), the angles of the various X–ray components could be identified. The most prominent are the different Cu lines, Cu $K\alpha_2$ and Cu $K\beta_1$, but tungsten lines W $K\alpha_1$ and W $K\alpha_1$ are also observed. These are observed due to ageing of the X–ray tube [120].
The diffraction peak around 30.8° and 64.2° are only observed in the $CuInSe_2$ sample and not in GaAs. These two peaks both show splitting into a Cu $K\alpha_1$ and Cu $K\alpha_2$ in analogy with GaAs. In the high angle part of the diffractogram replicas of the 64.2° $CuInSe_2$ peak are seen due to Cu $K\beta_1$ at 57.4° and W $K\alpha_1$ at 61.2°. This means that only two peaks that are observed in the measured sample can be ascribed to Cu $K\alpha_1$ diffraction on $CuInSe_2$.
The green lines in figure 3.12 indicates the position of the relevant $CuInSe_2$ given in ICDD.

It is seen that the peaks observed agree well with the (004) and (008) planes. This shows that the [001] direction or the *c*–axis of the $CuInSe_2$ unit cell is perpendicular to the substrate surface. If the $CuInSe_2$ *c*–axis had been parallel to the GaAs surface one would have expected to see the (200) and (400) reflexes illustrated in the figure.
A very slight shift of the $CuInSe_2$(004) and $CuInSe_2$(008) peaks to lower angles compared to the reference data can be observed in figure 3.12. This shift can be explained by a small tensile strain of the *c*–axis due to the lattice mismatch as discussed for measurements on samples with different thicknesses in section 2.2.3.
The orientation with the *c*–axis $\perp$ to the surface is preferred since domains with different orientation cannot occur. If the *c*–axis is $\parallel$ to the surface it is possible that the *c*–axis could point in either the [100] or [010] directions. This opens for the possibility to form domains with different orientations as illustrated in figure 3.11 [96]. It can therefore be expected that the layer is structurally more perfect when the chalcopyrite grows with the *c*–axis $\perp$ to the surface. Formation of domains of different orientations would lead to additional strain between the domains. The avoidance of stress energy that would otherwise build up between different domains is therefore an additional driving force for the orientation with *c*–axis $\perp$ to the surface.

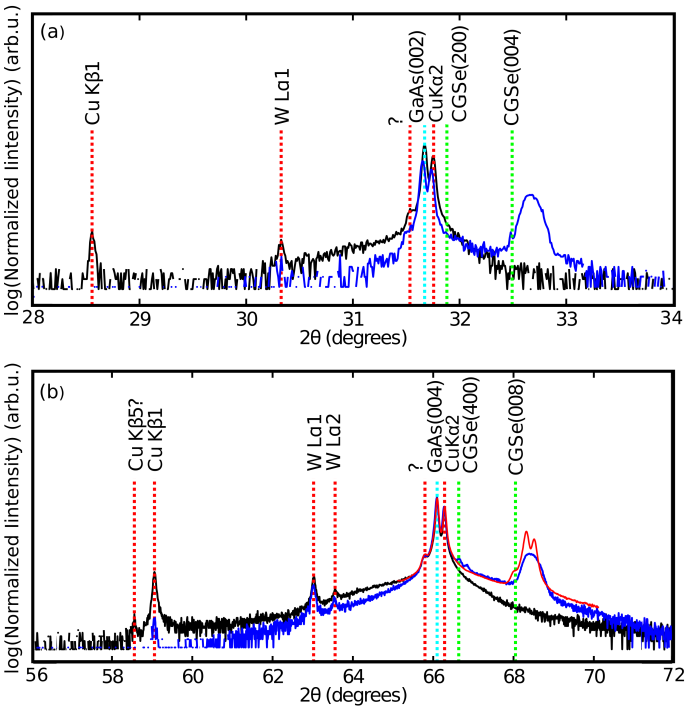

Figure 3.13: $\theta - 2\theta$ XRD of epitaxial $CuGaSe_2$ (blue) and GaAs (black). The green lines indicate data base values for the reflections of $CuGaSe_2$. The cyan line is the database value of the GaAs reflexes. All red lines indicate instrumental artefacts. The peak labelled '?' is an unidentified artefact that is specific to the used instrument. The blue curve is the sample produced in run number 5, whereas the red curve is measured on the sample from run number 54. (a) contains the reflections observed at low angles and (b) the reflections at higher angles.

One last feature in the diffractograms of $CuInSe_2$ shown in figure 3.12 is worth noticing. On the high angle side of the GaAs peak a shoulder is observed in both parts of the figure. This shoulder is located around the diffraction angle observed in $CuGaSe_2$ that will be discussed in the following. The appearance of the bump could therefore be an indication that Ga in–diffusion from the substrate leads to a layer in the interface region consisting

of $CuGaSe_2$. This issue will be discussed further in section 3.8.
Figure 3.13 shows a similar result obtained for $CuGaSe_2$ grown on GaAs(001). The diffraction peaks observed in the $CuGaSe_2$/GaAs system are basically of the same origin as discussed in the case of $CuInSe_2$. It is noticed that the $CuGaSe_2$ peak is observed at the high angle side of GaAs. The separation between the (200)/(400) and (004)/(008) angles are much higher in $CuGaSe_2$ than $CuInSe_2$. This happens since $\eta = c/2a$ has a larger deviation from 1 in $CuGaSe_2$ than in $CuInSe_2$.
It is observed that the position of the diffraction peaks of $CuGaSe_2$ falls close to the literature values of the (004) and (008) planes showing that $CuGaSe_2$, just as $CuInSe_2$, grows in the c[001] direction. The distance between the peak position and the literature value is, however, larger in the case displayed for $CuGaSe_2$. This can be related to strain in the sample. The $CuGaSe_2$ peak is additionally broadened in the example shown here (the blue curve in figure 3.13). This might be related to a larger strain distribution in the layer or a less ideal crystal quality with a high density of structural defects such as stacking faults and dislocations. The low quality XRD pattern obtained from the sample might be related to the fact that it is one of the first grown in the MOVPE machine (run number 5). In order to show that the quality of the XRD pattern improved with further optimization of the growth conditions a sample from run 54 in shown as a comparison (red curve in figure 3.13). For this sample the peak is clearly spit into a Cu Kα_1 and Cu Kα_2 indicating better crystal quality.

3.7 Model for Cu–rich $CuGaSe_2$ Growth at High Temperatures

This section is devoted to an investigation of the dynamics of the epitaxial growth of $CuGaSe_2$ under Cu–rich conditions. The observations observed here are valid for a growth temperature of 570 °C. Several effects discussed here are not observed at lower temperatures as discussed at the end of the section.
In the following the development of layer composition and sample morphology during the growth process will be studied. Special attention is given to the development of the secondary phase Cu_xSe that forms on the surface under Cu–rich growth conditions. In order to understand the growth dynamics a combination of in–situ reflectance measurements and ex–situ studies by SEM, XPS, and depth profiling AES are applied.
The samples studied in this section are all grown under the same conditions. A basic recipe with all growth parameters, i.e. temperatures, pressures, and gas flows kept constant is used. The only parameter that is changed from process to process is the duration of the growth. The standard recipe leads to an effective growth rate of about 100 ± 5 nm/h, which is typical for most samples grown in this work. The growth rate is calculated from in–situ reflectance measurements by fitting the Fabry–Perot oscillations. In the present study the growth rate remained almost constant throughout the entire process. The thickness of the final films are confirmed by SEM investigation of the layer cross sections.
In order to study the temporal development of the layer during growth the four samples representing different process stages are obtained by interruption of the growth after 1, 2, 3, and 4 h. An additional sample grown with a similar 8 h process, is produced for cross sectional cathodoluminescence measurements. This layer with a thickness close to 800 nm is used for cross–section studies since a thicker sample is preferred to study in-depth variations by CL.

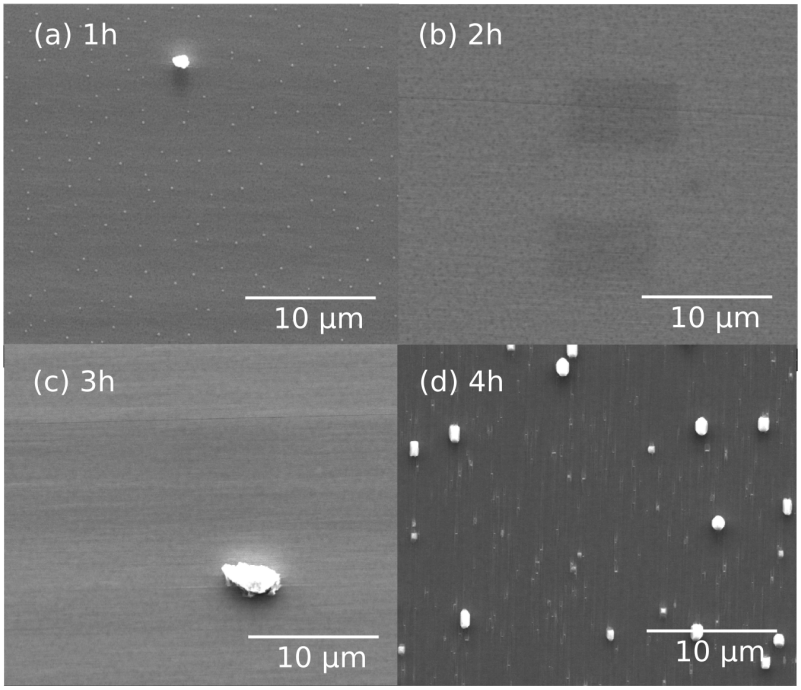

Figure 3.14: SEM micrograph of the epitaxial $CuGaSe_2$ surface after (a) 1 hour, (b) 2 hours, (c) 3 hours, (d) 4 hours of growth.

Figure 3.14 shows SEM micrographs of the surfaces of the samples after different growth times. After 1 hour of growth (figure 3.14(a)) droplets with diameters of about 100 nm are visible on the sample surface. It has unfortunately not been possible to determine the composition of these droplets with any techniques used here. It is, however, observed that the droplets seem to either evaporate or melt and float away if the electron beam is focused onto these droplets in an attempt to perform EDS measurements. This could indicate that these droplets consist of a material with a low melting point such as elemental gallium [121]. This idea is supported by the fact that similar droplets are observed on GaAs wafers that are annealed at 570 °C. These droplets appear due to decomposition of GaAs into Ga(l) and $1/4As_4$(g) [122]. GaAs is thermally unstable at temperatures higher than 500 °C due to the high volatility of As. With increasing temperature a change in stoichiometry of the GaAs surface towards [As]/[Ga] < 1 has been observed [123]. The formation of Ga droplets on the $CuGaSe_2$ sample surface is an indication that the layer is saturated with Ga during the first hour of growth.
After 2 hours of growth these droplets have vanished as seen in figure 3.14(b). The sample surface appears very smooth. The dark dots visible in the image are most probably related to voids at the $CuGaSe_2$/GaAs interface. These so–called Kirkendall voids have been observed previously in Cu(In,Ga)Se_2 grown on GaAs. The origin of the voids is diffusion and accumulation of vacancies [47, 124]. When examining the samples under study here in cross–sectional SEM such voids are also observed at the interface as seen in figure 3.20.
After 3 hours of growth (figure 3.14(c)) the interface voids are less visible. This is probably due to the increased thickness of the layer. Except a dust particle on the SEM micorgraph the sample is totally smooth at this stage of the growth.
The SEM micrograph in figure 3.14(d) shows the sample surface after 4 hours of growth.

It is obvious that the sample morphology has changed significantly during the final hour of growth. A high density of crystals with sizes around 1 μm with lighter contrast have appeared on the sample surface. These are Cu_xSe crystallites that form during Cu–rich growth as discussed in section 2.1.2.
Figure 3.15 shows an AES and EDS study of the chemical composition of the crystallites that based on the phase diagram are expected to have a composition close to Cu_2Se.

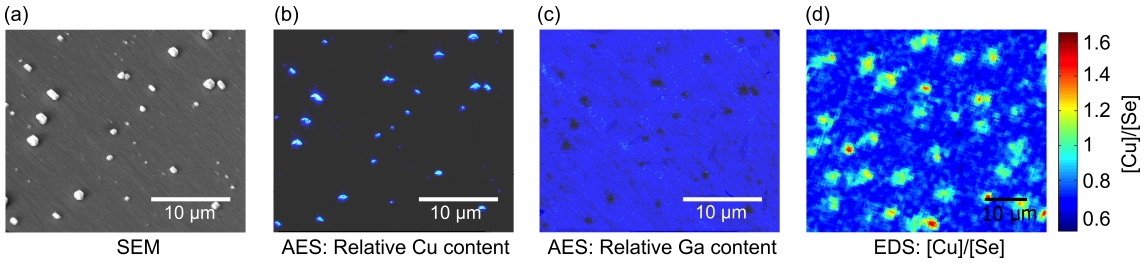

Figure 3.15: Chemical surface composition studied by AES and EDS of Cu–rich $CuGaSe_2$. (a) SEM micrograph showing crystallites in light contrast. (b) Spatial distribution of the Cu content of the area shown in (a). (c) Spatial distribution of the Ga content of the area shown in (a). Since the AES data are not quantified these images merely show concentration variations. (d) [Cu]/[Se] ratio extracted from an EDS measurement of a similar sample.

Figure 3.15(a) shows the SEM micrograph obtained from the area investigated with AES. The very surface sensitive spatially resolved AES composition analysis has not been quantified. The element composition of Cu (figure 3.15(b)) and Ga (figure 3.15(b)) therefore only show relative spatial variations in the elements. By comparison of the Cu–content in figure 3.15(b) to the locations of the crystallites in the SEM image (figure 3.15(a)) it is noticed that the crystallites are clearly richer in Cu than the underlying film. The map of the Ga content in figure 3.15(c) furthermore shows that these crystallites have a low Ga content compared to the film. These observations support the assumption that the crystallites consist of Cu_2Se, where no Ga should be measured and the relative Cu content is high (66 atomic % in Cu_2Se compared to 25 atomic % in $CuGaSe_2$).
A similar Cu–rich sample is studied in EDS to give further indication for the composition of the crystallites. The analysis of the EDS measurement showed that the [Cu]/[Se] has the highest contrast compared to e.g. [Cu]/[Ga] in this particular measurement even though the [Cu]/[Ga] ratio is expected to show the strongest variation. The absence of a strong variation in the [Cu]/[Ga] ratio may be related to a contribution to the signal from the layer underneath the crystallites. Here it should be kept in mind that EDS has a much larger probing depth than AES. The [Cu]/[Se] ratio measured in the sample is shown in figure 3.15(d). In Cu_2Se, one expect to find [Cu]/[Se] = 2, whereas [Cu]/[Se]=0.5 is expected in $CuGaSe_2$. In figure 3.15 it is observed that the [Cu]/[Se] ratio varies from 0.6 in between the crystals up to 1.6 on the crystallites. This could indicate a Se–poor $CuGaSe_2$ layer and Cu–poor Cu_2Se. One however, should remember that the EDS technique has certain limitations. The accuracy of the EDS technique in the order of 5% (relative) and matrix effects can play a role. It would therefore be inaccurate to claim that the exact composition of the secondary phase is determined in this measurement. The crystallites will thus be referred to as Cu_xSe.
The composition of Cu_xSe has been investigated in a more exact study [125, 126]. In epitaxial $CuGaSe_2$ grown under Cu–rich conditions on GaAs, it is found by XRD that the Cu_xSe crystallines formed on the surface predominantly consist of a cubic or tetragonal phase of $Cu_{2-y}Se$ with $0.1 < y < 0.4$ [125, 126]. Since the samples studied in [125, 126] are

very similar to ones studied here, it can be expected that this is also the case here.
The reason for the sudden appearance of Cu_xSe will be discussed later in this section.

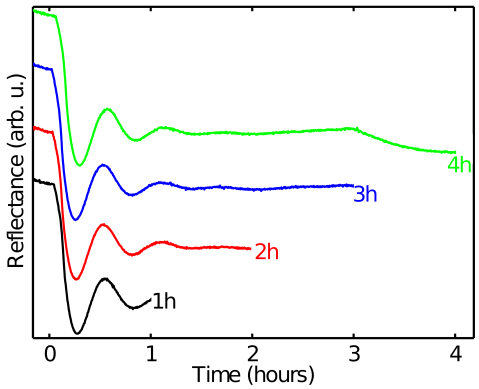

Figure 3.16: Reflectance transients measured at 3 eV during growth of sample series with the same recipe but different process durations.

Figure 3.16 shows the results of time dependent in–situ reflectance measurements for the four processes described above. All measurements are performed with a photon energy of 3 eV. The transients show the same behaviour for all processes during the part of the growth they have in common. This indicates good reproducibility of the recipe. Because of the similarity of the transients the following discussion will focus on the 4 hour transient.
In the beginning of the process, before the growth starts the reflectance signal from the GaAs surface is high. The signal decreases steeply as $CuGaSe_2$ starts growing on the surface. This drop in reflectance is due to the lower refractive index of $CuGaSe_2$ (n_r(3 eV)=3.34)[34] compared to GaAs (n_r(3 eV)=4.5) [127]. After the initial drop of reflectance Fabry–Perot oscillations appear as the film grows. Since the photon energy is above the band gap of $CuGaSe_2$ the amplitude of the observed oscillations decreases, due to light absorption, as the layer gets thicker. It should be noticed that the mean value of the reflectance stays constant for process durations $\leq$ 3 hours. This indicates that the surface of the layer is smooth during this growth stage, and that the layer has a constant refractive index. For longer process durations a sudden decrease in the reflectance signal is observed. This is seen after 3 hours and 5 minutes of growth in the top curve in figure 3.16. This drop of the reflectance signal is correlated to roughening of the surface, which starts when passing this point in time. The roughness is dramatically increased as the growth continues. By comparison of the SEM results shown in figure 3.14 with the roughness information of in-situ reflectance it is possible to infer that the decrease of the reflectance signal is directly connected to the formation and growth of Cu_xSe crystals on the $CuGaSe_2$ surface.
At first glance it is surprising that this sudden change in surface morphology appears in a process where the supply of all source materials is kept constant. In order to understand this, the evolution of the composition has been analysed with XPS and low temperature PL. The PL spectra for all samples are shown in figure 3.17. Low temperature PL measurements are sensitive to the defect structure as described in section 2.3.8. Since the defect structure depends strongly on the composition of the layer during growth the PL fingerprints can be used to extract information about the [Cu]/[Ga] ratio of the layer. Initially after 1 and 2 hours of growth the PL shows a red–shifted asymmetrically broadened

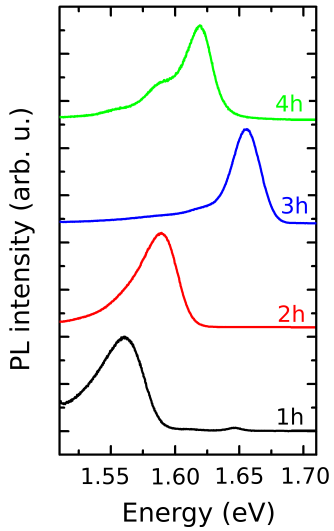

Figure 3.17: 10 K photoluminescence spectra of the samples grown with different process durations.

peak, the typical signature of potential fluctuations. This is a sign that the absorber is Cu-poor. The peak is positioned at a lower energy after 1 hour of growth compared to the peak after 2 hours of growth. This indicates that the sample has a larger Cu–deficiency during the first hour of growth. The sample is still Cu–poor after two hours of growth, but the [Cu]/[Ga] ratio has increased compared to the first stage of growth. After 3 hours of growth the PL signature has changed from that of a Cu–poor chalcopyrite to that of a stoichiometric ([Cu]/[Ga]$\approx$ 1). This is seen by the appearance of the DA1 peak discussed in section 2.3.8. Finally, after 4 hours of growth the PL spectrum is dominated by the DA2 transition, indicating Cu–rich growth conditions. The DA2 peak is typically found to dominate in material with a significant Cu–excess ([Cu]/[Ga]$>$ 1.2). All these observations point in the direction that the [Cu]/[Ga] ratio is not constant during the entire process as initially expected.

Growth time	1 h	2 h	3 h	4 h
[Cu]/[Ga]	0.7	0.7	0.9	$>$1

Table 3.7: Surface composition of the samples grown with different process durations measured by XPS.

The composition of the topmost surface layer is examined by XPS in order to verify these results. The XPS spectra are shown in figure 3.23. Quantification of the XPS measurement are performed considering the Cu 3p and Ga 3p contributions to the signal. When the evaluation is based on these peaks an information depth of around 6 nm is obtained (see section 3.7.1). The resulting composition expressed in terms of the [Cu]/[Ga] ratio is shown in table 3.7. Note that it is not possible to extract reliable data for the composition of the 4 hour layer from XPS, since the strong Cu and Se signals originating from the Cu_xSe crystals on the surface superimpose and mask the signal from the bulk.
The results extracted from low temperature PL can be regarded as more bulk sensitive than the XPS results. Based on the extinction length of the excitation light it can be estimated that the main contribution for the PL signal originates from the top 100 nm of the layer [34]. Both XPS and PL point to the same result; the layer is Cu-poor in the beginning of the process and turns Cu–rich for longer process durations. This is in agreement

with the observation that Ga droplets form on the surface in the beginning of the process, indicating that the layer is saturated with Ga. As the growth proceeds these droplets disappear since the layer changes composition. The observation of temporal changing layer stoichiometry is also in agreement with development of Cu_xSe crystals only in the end of the growth, once the layer turns Cu–rich.

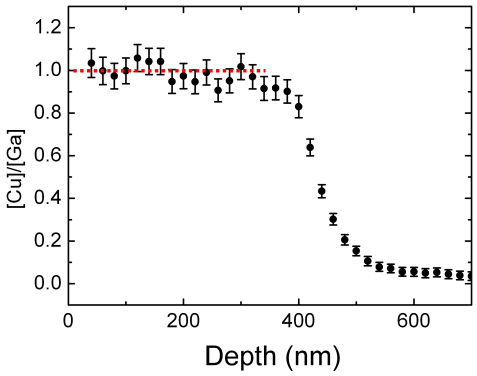

Figure 3.18: AES depth profile of the [Cu]/[Ga] ratio in the 400 nm layer (the 4 hour process).

The discovery of the variation of the composition with growth time gives rise to the question whether this causes an in–depth compositional gradient in thick layers. Figure 3.18 shows the [Cu]/[Ga] ratio of the 4 h sample obtained by AES depth analysis. The AES analysis is done with the same equipment as the previously mentioned XPS studies. AES is used for depth resolved experiments instead of XPS due to technical limitations of the equipment. It is seen that the [Cu]/[Ga] ratio of the $\approx$ 400 nm film is constantly about 1 throughout the entire film. This indicates that there is no gradient in composition of the final film after the growth process.

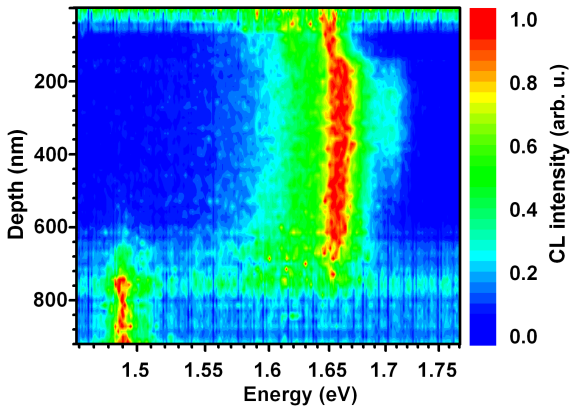

Figure 3.19: Cross sectional CL of a $CuGaSe_2$ layer grown under Cu–rich conditions measured at 6 K. The CL in the bottom of the image originates from GaAs.

In order to verify this result 6 K CL measurements are performed on the cross–section of a 800 nm $CuGaSe_2$ film grown with a very similar recipe with a slightly lower Cu–excess in the gas phase. The result is shown in figure 3.19, where each line corresponds to a full CL spectrum measured at a given depth. A SEM micrograph of the cross section is obtained simultaneously making it possible to determine the position from which the CL spectra originate. The $CuGaSe_2$ layer emits luminescence around 1.65 eV and is therefore easily distinguishable from the GaAs substrate, which appears at the bottom of the image

exhibiting a peak at around 1.49 eV. Low temperature CL and PL both give information about the defect structure in the material. It has been shown for $CuGaSe_2$ that the same DAP transitions are observed with both methods [91]. It is therefore possible to interpret the CL results with respect to the defect model presented in section 2.3.8. The peak at 1.65 eV corresponds to the DA1 transition, which is only observed in stoichiometric absorbers. This peak is visible throughout the entire layer, showing that the layer has the same defect structure. This, in turn, agrees with the AES result also showing that the entire layer has the same composition.
Based on these results it can be concluded that the variation of the [Cu]/[Ga] ratio with time does not result in a gradient in the final sample. The reason for this is related to the high diffusion constant of Cu in $CuGaSe_2$ [128]. Because Cu rapidly diffuses throughout the film at growth temperature the entire layer obtains a homogeneous composition.
In the following a growth model, that explains the observations presented here, will be proposed. The basic idea of the model is illustrated in figure 3.20.

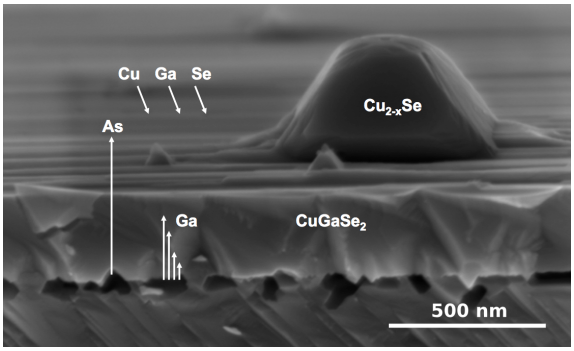

Figure 3.20: SEM cross section of a $CuGaSe_2$ layer grown under Cu–rich conditions. Kirkendale voids are visible at the interface and a Cu_xSe crystal is seen on top of the layer. It is illustrated how decomposition of the GaAs substrate leads to an extra supply of Ga.

The first important element in the model is the decomposition of GaAs at elevated temperatures. It is well known that arsenic desorbs from GaAs when it is heated [122, 129, 130, 123]. This decomposition releases excess Ga into the growing layer. It has been observed that evaporation of As and incorporation of Ga in a metal film occurs already at a temperature of 420° C [130]. When growing a $CuGaSe_2$ thin film the [Cu]/[Ga] ratio in the layer is therefore not proportional to the material supply from the gas phase. The effective material supply of Ga includes both the Ga coming from the substrate and the gas phase. It is proposed that the excess Ga from the substrate leads to the observed Cu–poor growth in the beginning of the process. As the deposited layer grows thicker, less Ga from the substrate reaches the surface. Consequently, the material supply at the layer surface approaches the amount supplied in the gas phase, as the layer thickness increases. Since the recipe discussed in this study is developed to grow Cu–rich $CuGaSe_2$, the characteristics of the layer therefore switches from Cu–poor to Cu–rich when a certain thickness has been obtained. When the layer grows beyond this thickness Cu_xSe begin to form at the surface as expected under Cu–rich growth conditions. The model is supported by a study of Ga diffusion in $CuInSe_2$, where it is shown that the Ga diffusion decreases when the layer approaches stoichiometry [124]. The combination of the effect of decreasing Ga diffusion and increasing thickness jointly contribute to the reduction of the Ga supply from the substrate. This explains the increase in [Cu]/[Ga] ratio with increasing growth time.

In order to explain that the [Cu]/[Ga] ratio is homogeneous throughout the final layer, it is necessary to investigate the diffusion coefficients of the elements in $CuGaSe_2$ in further detail. Most studies of diffusion coefficients in literature focus on $CuInSe_2$. It has, however, been demonstrated that the inter–diffusion in a $CuInSe_2/CuGaSe_2$ couple annealed at 650 °C resulted in very similar diffusion coefficients of Ga in $CuInSe_2$ and In in $CuGaSe_2$. Both diffusion coefficients are under these conditions determined to be in the order of 10^{-11} cm^2s^{-1} [131, 132]. At lower temperatures in the range 400 °C – 600 °C the diffusion coefficient of In in $CuGaSe_2$ is found to vary from $3.5{\cdot}10^{-13}$ cm^2s^{-1} to $4.5{\cdot}10^{-12}$ cm^2s^{-1} [131, 132]. A detailed study of the out–diffusion of Ga from GaAs into $CuInSe_2$ at 725 °C investigate the effect of the layer composition on the diffusion coefficient [124]. It is found that the diffusion coefficient of Ga is strongly dependent on the [Cu]/[In] ratio of the layer, being lowest around the stoichiometric composition with $2.7{\cdot}10^{-13}$ cm^2s^{-1} at [Cu]/[In]$\approx$ 1 and higher in Cu–rich films with $5{\cdot}10^{-11}$ cm^2s^{-1} at [Cu]/[In]= 1.4 and in Cu–poor films with $7{\cdot}10^{-12}$ cm^2s^{-1} at [Cu]/[In]= 0.43. The diffusion of Se in $CuInSe_2$ has been studied with a radioactive tracer experiment [133]. In this investigation a diffusion coefficient of Se at 700 °C of the order $2{\cdot}10^{-13}$ – 10^{-12} cm^2s^{-1} has been found [133]. The diffusion of Cu in $CuInSe_2$ has similarly been studied with a radioactive tracer [128]. Here it is found that the diffusion coefficient in the temperature range 380 – 430 °C vary in the range 10^{-8} – 10^{-9} cm^2s^{-1} [128]. Since this experiment is performed at a lower temperature than the other studies mentioned here it can be expected that the diffusion coefficient of Cu under similar conditions will be even higher. Based on these numbers it can therefore be assumed that the diffusivity of Cu will exceed the diffusivity of both Ga and Se at the growth temperature by orders of magnitude. This explains that [Cu]/[Ga] ratio becomes homogeneous throughout the final layer.
When it is observed that Ga from the substrate is incorporated in the thin film, it is also relevant to ask what happens to the As from the substrate. This issue is investigated with SIMS depth profiling measurements discussed in section 3.8.
The proposed model explains the development of the [Cu]/[Ga] ratio from Cu-poor to Cu-rich with increasing growth time. One remaining open question at this point is the influence of Cu_xSe on epitaxial growth of the $CuGaSe_2$ for the long duration processes. This will be the topic of the following section.

3.7.1 Epitaxial Growth in the Presence of Copper Selenide

When a secondary phase develops during growth further epitaxial growth can be problematic. If the secondary phase forms on the surface with random crystal orientations it is possible that these prevent further epitaxial growth leading to a polycrystalline film.
In order to examine the development of the epitaxial growth of $CuGaSe_2$ in the presence of Cu_xSe, $CuGaSe_2$ samples grown under Cu–rich conditions are investigated with SEM, EBSD, XRD, and AES.
From cross sectional SEM measurements as shown in figure 3.20 it is seen that the Cu_xSe crystals appear only on the surface of the $CuGaSe_2$ layer. It is also known that the layer grows epitaxially even after the formation of Cu_xSe. These observations indicate that Cu_xSe can be transformed continuously to epitaxial $CuGaSe_2$ during growth.
In order to support this hypothesis a growth experiment is designed. A sample is grown with a slightly modified recipe with Cu–excess for the first 4 hours of the growth and conditions identical to the samples discussed in the previous section. In the end of the process the Cu–source is switched off while the Ga and Se source are kept on. The in–situ

reflectance measurement of this growth is shown as the bottom curve in figure 3.21.

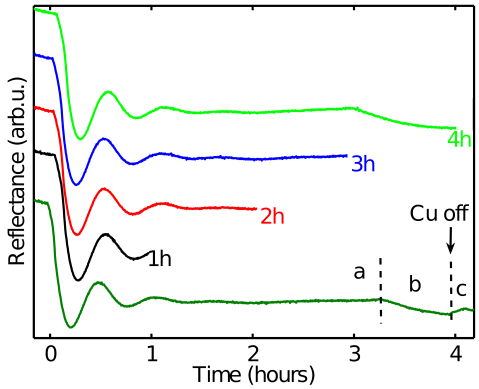

Figure 3.21: Reflectance transients measured during growth of sample series with the same recipe but different process durations. The lowest curve shows a process in which the Cu–precursor is switched off in the end of the run.

Three stages are visible in the growth reflectance transient. For the first 3 hours and about 15 minutes of growth (a) the layer grows under Cu–poor conditions leading to a smooth surface. At a point of growth the stoichiometric point is reached after which the sample grows under Cu–rich conditions (b). This leads to formation of Cu_xSe and roughening of the sample, hence the decreasing reflectance. After 4 hours of growth the Cu supply is switched off and an increase in reflectance is observed (c). This increase can be explained by a decrease of surface roughness. The smoothing of the surface is an indication that the density of Cu_xSe decreases or that the shape of the surface structures changes. The process is terminated when the real–time in–situ reflectance stopped increasing. The resulting duration of the final conversion step (c) amounts to 12 minutes.

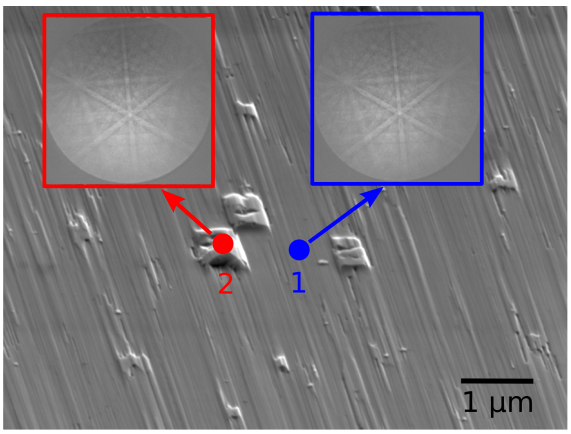

Figure 3.22: SEM micrograph of epitaxial bumps on a $CuGaSe_2$ surface arising after a growth step that converts Cu_xSe into $CuGaSe_2$ by switching off the Cu supply. The EBSD patterns demonstrate that the bumps are epitaxial.

Figure 3.22 shows local EBSD measurements on a SEM micrograph of this $CuGaSe_2$ sample under an angle of 70°. The bumps seen on the sample surface are not Cu_xSe as one could imagine. These bumps are in fact composed of $CuGaSe_2$ as confirmed by the EBSD pattern that is exactly the same on the bump and the surface of the film in between the bumps. This also proves that these bumps have the same crystal orientation as the rest of

the layer. They are epitaxial in other words. It is therefore demonstrated that Cu_xSe can be continuously converted into epitaxial $CuGaSe_2$ during the growth process.

Formation of a Continuous Layer of Cu_xSe

The results presented here demonstrate that Cu_xSe can be turned into $CuGaSe_2$ during the growth. When looking into literature several studies for the growth in presence of Cu_xSe are, available e.g. [134, 135, 136, 137]. It has been proposed in literature that Cu_xSe exist in a liquid phase floating on top of the layer during the growth [135]. The reflectance transients discussed in the previous section, however, show that the surface roughens already during the growth when Cu_xSe forms on the surface. This contradicts that Cu_xSe is liquid during growth in agreement with the conclusion of Niki et al. [134]. In the work by Niki it is proposed that Cu_xSe forms a thin continuous layer on the top of the absorber layer when grown under Cu–rich conditions in addition to Cu_xSe crystallites. This is proposed to explain the high conductivity of Cu–rich samples, that could be reduced by KCN etching, whereby the Cu_xSe layer is removed [134].
In order to examine the presence of a thin continuous layer of Cu_xSe on the layers an evaluation of the low kinetic energy photo electrons based on the XPS measurement discussed in section 3.7 is performed. The result of the XPS measurement is shown in figure 3.23.

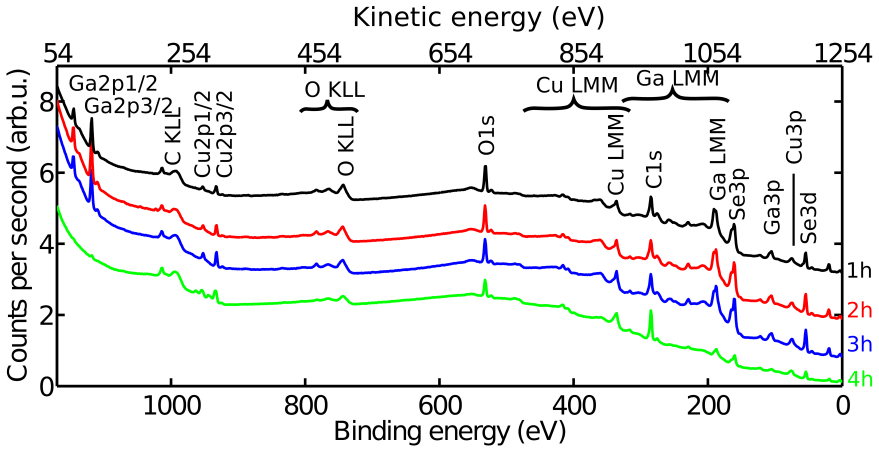

Figure 3.23: XPS spectra measured on four samples with growth durations between 1 and 4 hours. The peaks labelled KLL and LMM are due to Auger electrons.

Figure 3.23 shows the main electron peaks ascribed to copper, gallium and selenium but it is noticed that a contribution from contamination of oxygen and carbon also contribute to the signal. The lower x–scale in figure 3.23 shows the binding energy E_B. In the following the kinetic energy E_K of the detected electrons will be discussed. These are related via $E_K = \hbar\omega - E_B$, where $\hbar\omega = 1253.6$ eV is the energy of the X–rays from the Mg Kα source as shown as the upper x–axis in figure 3.23. The signal from the XPS measurement can be quantified to yield relative element concentrations discussed in the following.
The low kinetic energy electrons with energies in the range 100-300 eV are not able to escape from deep inside the material. In this kinetic energy range the mean free path of electrons is limited to only a few monolayers [138]. Based on reference [139] and assuming that the detected electrons originate from three times the mean free path, the analysis depth can be estimated. In case of $CuGaSe_2$ an evaluation of the low kinetic elections

means quantification based on the Ga 2p, Cu 2p electrons. This evaluation of the XPS data gives an information depth of around 2 nm, compared to around 6 nm obtained when the quantification is based on the photo electrons with kinetic energies in the range 1100 – 1200 eV (Cu 3p, Ga 3p and Se 3d) discussed earlier in this section. For Se no low kinetic energy electrons are detected. To quantify the amount of Se it is therefore necessary to use the Se 3d photo electrons with a kinetic energy of 1200 eV. The contribution from Se to the signal therefore contains information from a depth of around 6 nm. If the element is distributed heterogenously in depth this will of course give rise to inaccurate quantification. Also one should notice that oxygen and carbon on the surface gives rise to a significant signal. This is especially prominent for the sample with a growth time of 4 hours where more carbon is seen. The surface contamination leads to a decrease of especially the low kinetic energy electrons (Ga 3p and Cu 2p) while the high kinetic energy electrons are less affected. This certainly leads to inaccuracies when attempting to quantify the element concentrations.
The evaluation based on high kinetic energy electrons that can escape from deeper within the material is shown in table 3.7 on page 57 expressed as the [Cu]/[Ga] ratio. The result of most surface sensitive evaluation is shown in figure 3.24. The figure depicts the elemental concentrations for the four samples with different growth time discussed in the previous section.

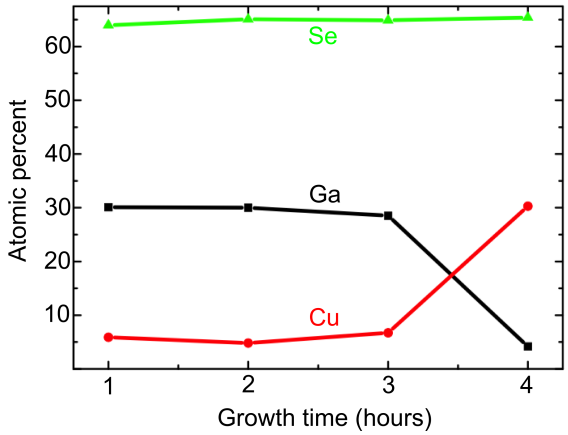

Figure 3.24: Composition of the top surface measured by evaluation of low kinetic energy electrons (Ga 2p and Cu 2p) and Se 3d in XPS study of samples grown with different process durations.

First, it is noticed that the absolute values obtained with this analysis do not agree with the composition of stoichiometric $CuGaSe_2$. For the first 3 hours of growth while the layer grows under Cu–deficiency the [Cu]/[Ga] ratio is very low, much lower than the one obtained by the more bulk sensitive evaluation. This could be related to the very thin layer of ODC that has been found on the surface of Cu–poor chalcopyrites [140]. The composition measured for the first 3 hours is not far from the ODC material $CuGa_5Se_8$,where Cu: 7%, Ga: 36%, Se: 57% is expected. It must, however, be kept in mind that the Se signal used in this quantification has a contribution from a larger depth than that of Cu and Ga. This questions the absolute concentrations obtained with the very surface sensitive evaluation. One furthermore has to keep in mind that contamination with oxygen and carbon decreases the signal from low kinetic energy electrons more than high kinetic energy electrons. In this case this can lead to an overestimation of the Se content. The ratio [Cu]/[Ga]$\approx$ 0.2 during the first three hours can, however, still be trusted. This leads to the conclusion that the top 2 nm of the layer is extremely Cu–poor in the beginning of

the growth.
After 4 hours of growth the surface composition changes significantly. The [Cu]/[Ga] ratio is suddenly higher than 7 and hardly any Ga is observable. This dramatic change of surface composition can not be explained by the partial coverage of the surface by Cu_xSe crystals. The SEM micrograph showing the surface of this sample is seen in figure 3.14(d). Based on this SEM micrograph it can be estimated that the Cu_xSe crystals cover about 2 % of the total surface. 98 % of the $CuGaSe_2$ surface is therefore still exposed. The dramatic decrease of the Ga signal can therefore not be explained by the partial coverage of Cu_xSe crystals. The reason for the large change could be explained by a continuous Cu_xSe film forming on the surface. Another possible explanation for the low Ga 3p signal is that this sample had a significantly higher carbon contamination (see figure 3.23). This leads to a reduced signal of especially the low kinetic energy electrons.
If the carbon contamination is not the reason for the observed behaviour the result confirms observations in previous studies that the $CuGaSe_2$ surface is covered by a thin Cu_xSe layer in addition to the Cu_xSe crystals. The thickness of this layer is, however, so thin that it is only measurable when the XPS data originating from the first 2 nm is taken into account.

3.7.2 Temperature Dependence of Void Formation

The decomposition of the substrate is dependent on the growth temperature. Since the substrate decomposition leads to formation of voids and diffusion of Ga into the substrate it is desirable to decrease the growth temperature. Figure 3.25 shows the SEM cross sections of two samples grown at different temperatures.

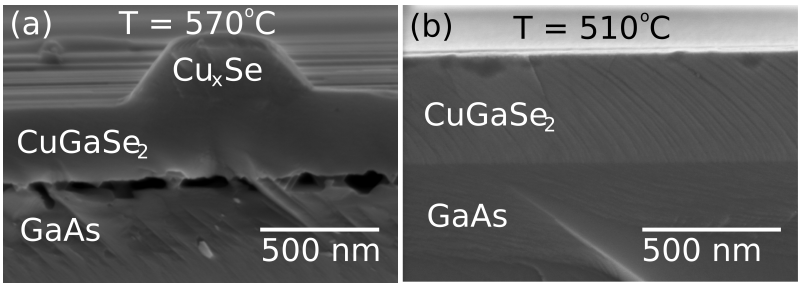

Figure 3.25: Examples of cross sections of samples grown at different temperatures. (a) $CuGaSe_2$ layer is grown at 570 °C and contains voids at the interface. (b) $CuGaSe_2$ layer is grown at 510 °C without interface voids.

The sample shown in figure 3.25(a) is grown at 570 °C clearly showing the voids in the interface region. This sample also interestingly shows a cross section of a Cu_xSe, where it can be observed that the Cu_xSe crystal is only present at the sample surface. It does not extend into the layer, in agreement with the discussion in the previous sections.
The sample in figure 3.25(b) is grown at a lower temperature of 510 °C. The cross section shows that the interface between the $CuGaSe_2$ layer and the GaAs substrate is very smooth under these growth conditions. The void formation can therefore be efficiently avoided by reduction of the growth temperature. It is furthermore expected that the in–diffusion of Ga from the substrate will be decreased at lower temperature.
This observation in combination with the results discussed in section 3.5.3 lead to modification of the standard recipe of $CuGaSe_2$ growth to temperature to a temperature of 520 °C rather than 570 °C used in the original recipe. The reduced growth temperature

furthermore has the advantage that the Ga supply from the substrate is reduced. The sudden drop in reflectance shown in figure 3.21 due to the transition from Cu–poor to Cu–rich growth conditions is therefore not observed at a growth temperature of 520 °C.

3.8 Composition Gradients and Inter–diffusion in Epitaxial Thin Films

As shown in the previous section, GaAs decomposes at elevated temperatures leading to diffusion of Ga from the substrate. It is therefore necessary to investigate if As released from the substrate remains in the film. Another interesting question that should be investigated is whether Ga is present in the $CuInSe_2$ layers leading to formation of a $Cu(In,Ga)Se_2$ interface region. In order to answer these questions depth resolved SIMS investigations are performed on a $CuInSe_2$ sample grown at 470 °C and a $CuGaSe_2$ layer grown at 570 °C, both with a thickness of around 400 nm. A basic description of the SIMS technique is included in appendix D.6.

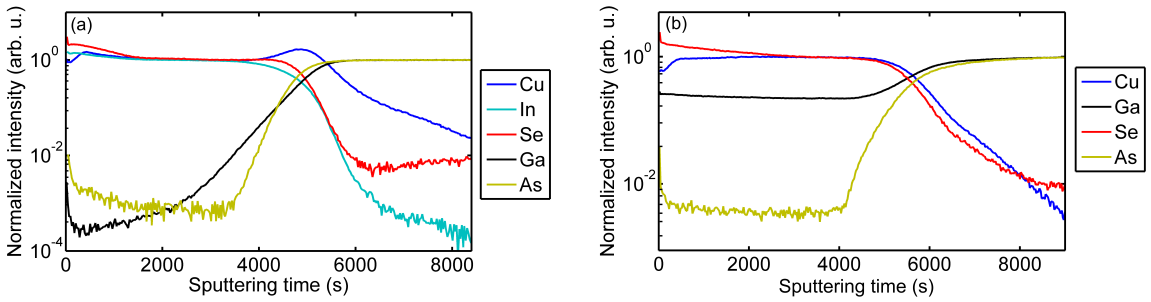

Figure 3.26: (a) SIMS depth profile of a $CuInSe_2$ layer on GaAs. (b) SIMS depth profile of a $CuGaSe_2$ layer on GaAs.

Figure 3.26(a) shows the normalized element concentration profiles of a $CuInSe_2$ layer measured with SIMS. It is first noticed the interface seems poorly defined in the SIMS measurement with a profile of As stretching into the layer and In and Se stretching into the substrate. The width of the interface region can, based on the sputtering rate, be estimated to around 60 nm. This does not seem to agree with the result from cross–section TEM investigation in section 3.6.1 that showed that the interface appears to be abrupt. There are several possible reasons for the appearance of a broadened interface. First it is possible that the elements inter–diffuse. There is also the possibility that roughness of the samples gives rise to a broadened interface in the SIMS measurement. Finally it is possible that the interface broadens because elements are pushed further into the sample during the sputtering process.
It is noticed that the signal from Ga and As do not show the same behaviour as expected if no intermixing would take place. Since the Ga signal extends further into the $CuInSe_2$ layer the result indicates that $CuInSe_2$ contains Ga near the interface. Based on the different profile of Ga and As the distance from the interface where Ga seems to be present can be estimated. It may be assumed that the point where the As signal reaches its minimum and starts to fluctuate after a sputter time of around 3500 seconds represent the sputtering time where a contribution from the substrate begins to appear. The Ga signal already starts to increase after around 2200 seconds, significantly earlier than the signal

of the substrate seems to appear. With a sputter rate of approximately $8.4 \cdot 10^{-2}$ nm/s in the $CuInSe_2$ layer, this leads to a thickness of close to 100 nm. If this estimation is to believed one can expect that the fist 100 nm of all $CuInSe_2$ layers grown in this project in fact contain an amount of Ga. The interface region therefore seems to consist of rather $Cu(In,Ga)Se_2$ than $CuInSe_2$.
In the XRD measurement of a $CuInSe_2$ sample shown in figure 3.12 on page 51 a bump is observed on the high angle side of the GaAs peak. It is possible that this bump is related to an interface layer rich in Ga. The position of the broad bump could indicate that a layer of pure $CuGaSe_2$ in fact forms at the interface or at least a $Cu(In,Ga)Se_2$ layer with a high [Ga]/[In] ratio. The SIMS observation presented here, support that Ga is present in the layer close to the interface. The results do, however, not prove that a Ga rich $Cu(In,Ga)Se_2$ layer exist at the interface region. Formation of an interface $CuGaSe_2$ layer when growing $Cu(In,Ga)Se_2$ epitaxially on GaAs has, however, been observed in literature [47]. In [47] it is observed that a $CuGaSe_2$ layer is formed when $Cu(In,Ga)Se_2$ with [In]/[Ga]=2 is grown at 570°C. It is also concluded that no pure $CuGaSe_2$ layer could be observed if the layer is grown at 500°C. In this case a gradient of Ga is observed, similarly to the results presented here.
In figure 3.26(a) it is noticed that the Cu seems to extend further into the substrate than In and Se that are broadened by the effects discussed earlier. This could indicate that Cu diffuses into the GaAs layer. The validity of the Cu profile measured for this sample is, however, questionable. It shows a high content of Cu at the interface. A feature which has not been observed for any other sample with any measurement technique applied in this work. To my knowledge there have also been no reports in literature that could explain this behaviour. Also increasing signals of all elements are seen at the sample surface, which points towards an artefact observed at the surface and interface. This could by a matrix effect e.g. related to the accumulation of primary Cs^+ ions in the layer and different sputter rates of the same element in different matrices.
Figure 3.26(b) shows the Cu, Ga, Se, and As profiles in the $CuGaSe_2$ layer grown with the four hour process discussed in the previous section. It is demonstrated that this layer has a homogeneous [Cu]/[Ga] ratio with AES depth profiling and a CL cross section measurement. The same appears to be the case in the SIMS measurement presented here. The SIMS measurement of this sample does not display the Cu accumulation at the interface. It does however also show a Cu–poor and Se rich surface. A result that is clearly not in agreement with the XPS measurement that showed a Cu_xSe layer formation on this surface. The behaviour observed at the surface in the SIMS measurements is probably therefore related to artefacts.
Regarding the out–diffusion of As into the layer it would be interesting to be able to determine the concentration of As in the layer. The signal from As in the bulk of the layer is so low that it can be regarded as being below the instrument limit of the operation mode where the sample is bombarded by Cs^+ ions and clusters of As–Cs^+ are detected. All elements M are detected as MCs^+ molecules in order to reduce the matrix effects. Under the experimental conditions it is, unfortunately not possible to determine the detection limit (see further explanation in appendix D). In a similar SIMS study of diffusion of As into $Cu(In,Ga)Se_2$ from GaAs, it is found that the As concentration is too small to cause significant doping [47].

3.9 Summary

Epitaxial $CuInSe_2$ and $CuGaSe_2$ layers with wide range of compositions from Cu-rich to Cu–poor are grown in this work. In–situ reflectance measurements proves to be a good tool to monitor the process by yielding useful information about surface roughness and growth rate. PL measured at low temperature is used as a tool to understand and develop the epitaxial growth process and to control the layer composition. The process recipe is improved through a series of optimization growth experiments where the influence of various parameters is tested. It is often found that parameters influenced the growth in more than one way. It is for example demonstrated that changes of the growth temperature lead to changes of the layer composition. As a result of the growth experiments an epitaxial process for production of high quality epitaxial $CuInSe_2$ and $CuGaSe_2$ is obtained as demonstrated with TEM and EBSD studies.
A study of the growth dynamics at 570 °C demonstrate the importance of the growth temperature. Via study of four samples grown with the same recipe but for different growth times a model for the dynamics of the growth is developed. A recipe designed to achieve Cu–rich growth conditions is used in this study. The sample composition develops from Cu–poor to Cu–rich with increasing process duration. This behaviour can be explained by Ga supply from the GaAs substrate, which especially affects the composition of the thinnest layers. Interestingly, this evolution of layer composition does not lead to depth inhomogeneities in the final samples. The depth profile shows a very uniform [Cu]/[Ga] ratio.
As the composition of the layers switches from Cu–poor to Cu–rich a secondary Cu_xSe phase appears on the surface. The epitaxy of $CuGaSe_2$ is not hampered by the presence of the secondary Cu_xSe phase. The results indicate that Cu_xSe is converted continuously to $CuGaSe_2$ during the epitaxial growth. There is no reason to assume a different behaviour for $CuInSe_2$ regarding the effect of Cu_xSe. In addition to the Cu_xSe crystallites it is found that a thin continuous film cover the $CuGaSe_2$ layer when grown under Cu–rich conditions. Under Cu–poor growth conditions the surface is found to be extremely Cu–poor, probably due to formation of an ODC on the layer surface. By reduction of the growth temperature to 500 °C it is shown that the tendency to form voids at the interface and in–diffusion of Ga is reduced. For $CuInSe_2$ growth it is demonstrated that the decomposition of the substrate leads to an interface region of around 100 nm where the Ga in–diffusion leads to formation of $Cu(In,Ga)Se_2$.

Photoluminescence of Compensated Chalcopyrites

4

It has been demonstrated that chalcopyrites grown under Cu-poor ([Cu]/[III]<1) conditions are highly compensated, resulting in a high density of charged defects and a low net carrier concentration [10, 13, 15]. Since the random distribution of charged defects cannot be screened by the remaining free charges a spatially fluctuating Coulomb potential remains. These fluctuations will locally perturb the band structure [90]. The photoluminescence from a highly compensated semiconductor is influenced by the magnitude of the fluctuations since the carriers recombine from spatially separated potential wells. The characteristics of potential fluctuations have been observed in PL spectra at low temperature in numerous studies e.g. [13, 15, 83]. It is, however, often assumed that the fluctuations persist at room temperature [16, 17]. In order to characterize the properties of these fluctuations and their temperature dependence epitaxial $CuGaSe_2$ and $CuInSe_2$ absorbers are examined by temperature and intensity dependent photoluminescence.

4.1 Potential Fluctuations in Highly Compensated Semiconductors

A semiconductor with both donors and acceptors present at comparable concentrations is compensated. The degree of compensation, which depends on the relative acceptor and donor concentrations, is defined as $K = N_D/N_A$ in a p–type semiconductor. Material that is highly compensated ($K \approx 1$) has properties that are significantly different from weakly compensated material. One example of a property that is strongly influenced is radiative recombination. A weakly compensated semiconductor can be described by the standard theory for DAP recombination explained in section 2.3.4. In material that is highly compensated the PL characteristics are significantly different.
The aim of this section is to present a model that can explain the properties of Cu–poor Cu(In,Ga)Se_2 in PL measurements. In the following we will therefore consider a highly compensated p–type semiconductor. At low temperatures all donors in this material will be ionized and the donated electrons will be trapped by acceptors $N_D = N_D^+ = N_A^-$, where N_D and N_A are the concentrations of donors and acceptors respectively and the superscripts indicate the charge state. This results in a high concentration of charged defects N_C in the semiconductor $N_C = N_A^- + N_D^+$. These defects are randomly distributed in the crystal. In the p–type material a number of acceptors remain uncompensated. These will be neutral at low temperatures $N_A^0 = N_A - N_D$, but will be ionized as the temperature is increased. It can therefore be assumed that the hole density at an elevated temperature (e.g. room temperature) will be $p = N_A - N_D$. The electrostatic potential in this material varies throughout the crystal and will differ from the pure crystal by the Coulomb potential produced by the ionized defects in the crystal. Since the charged defects are distributed randomly, this leads to a random electrostatic potential that modulates the band energies. At low temperature the fluctuations are not screened, since the free charge carrier density is low compared to the density of ionized defects.
The average amplitude of the fluctuations has been determined by Shklovskii and Efros

[90]. The general idea will be outlined here. Consider a typical fluctuation of size R_f. The mean number of charged defects in this volume is $N_C R_f^3$. Since it is assumed that the defects are distributed according to Poisson statistics the standard deviation is the square root of the mean $\left(N_C R_f^3\right)^{1/2}$. The potential due to this defect fluctuation is given by

$$\gamma(R_f) = \frac{e^2}{4\pi\epsilon_0\epsilon_r R_f}\left(N_C R_f^3\right)^{1/2}, \tag{4.1}$$

where e is the elementary charge, ϵ_0 is the permittivity of free space and ϵ_r is the static dielectric constant of the material. γ can be understood as the lowering (or increase) of the energy of a test charge in a typical fluctuation of size R_f. The spatial extension of the typical fluctuation R_f has yet to be determined. In order to find R_f it is necessary to take screening into account. A fluctuation will be totally screened when the number of free charge carriers p in the volume R_f^3 equals the mean number of charged defects in the same volume. This can be expressed as $pR_s^3 = \left(N_C R_s^3\right)^{1/2}$, where R_s is the so–called screening length. Rearrangement of the equation gives an expression for the screening length:

$$R_s = \frac{N_C^{1/3}}{p^{2/3}} \tag{4.2}$$

Large (and deep) fluctuations that are larger than the screening length ($R > R_s$) will be screened. Fluctuations that are smaller than the screening length ($R < R_s$) will, however, persist. It is therefore argued that the typical size of the fluctuation is given by the screening length [90]. Inserting equation (4.2) in equation (4.1) therefore yields the amplitude of the average potential fluctuation:

$$\gamma(R_s) = \frac{e^2}{4\pi\epsilon_0\epsilon_r}\frac{N_C^{2/3}}{p^{1/3}}. \tag{4.3}$$

To get a feeling of the typical magnitude of the potential fluctuation an example will be presented here. If it is assumed that $N_A \approx N_D$ the density of free charge carriers at room temperature is approximately $p = (1-K)N_C/2$. Assuming a total density of charged defects of $N_C = 10^{18}$ cm^{-3} and a degree of compensation K= 0.99 therefore gives a free charge carrier density of $p = 5 \cdot 10^{15}$ cm^{-3}. Inserting these values and $\epsilon_r = 11$ for $CuGaSe_2$ [80] in equation (4.3) yields a value for the amplitude of the fluctuations of 76 meV. Equation (4.3) is widely used in papers to explain the behaviour of compensated semiconductors [141, 142, 17, 143]. It is, however, a relatively simple approach and the general validity of equation (4.3) can be questioned.

One can also attempt to calculate the typical fluctuation length at low temperature where the charge carrier concentration is very low. If a charge carrier density of $p < 10^6$ cm^{-3} is assumed one finds a screening length of more than one meter and a fluctuation amplitude of more than 100 eV using the same parameters as in the previous example. These values are clearly unrealistic. This simple approach is therefore only useful to give an idea of the physics involved. A more sophisticated approach to take the screening phenomena into account should be developed in order to improve this model.

For very low charge carrier densities the model presented here clearly fails. When the sample is measured in PL it is, however, under illumination. Under these conditions a high density of charge carriers is generated. In 10 K PL measurements a fluctuation amplitude of 15–70 meV is measured (see section 4.5.1). In the following it will be estimated

if this is a realistic value for a cold sample under illumination. It is assumed that all excess acceptors are neutral at 10 K, that is $p \approx 0$ in absence of photo–excited charge carriers. In order to obtain a fluctuation amplitude of 15–70 meV it is necessary to generate a photo carrier density in the order of $10^{15} - 10^{16}$ cm^{-3} to screen potential fluctuations generated by 10^{18} cm^{-3} defects according to equation (4.3). To estimate if this is a realistic value for the excess charge carrier density Δp it is necessary to determine the volume in which the charge carriers are generated. The penetration depth of the laser can be estimated as the inverse of the absorption coefficient α^{-1}. With an absorption coefficient of α(514 nm)$\approx 1 \cdot 10^5$ cm^{-1} [144] this gives a penetration depth of $\approx$ 100 nm. The charge carrier generation rate can therefore be estimated to $G = 6 \cdot 10^{24}$ s^{-1}cm^{-3} based on the excitation density used in the experiment. Under steady state conditions, the excess charge carrier density is given by $p = G\tau$, where τ is the carrier lifetime [145, 146]. The charge carrier life time measured in Cu(In,Ga)Se$_2$ depends strongly on the measurement conditions. The lifetime found immediately after sample preparation was e.g. 100 ns, but this life time decreased to only 1 ns after exposure to air for only 24 hours. Also, the injection level is important for the measured life time. One typically finds around 8 ns for bare absorbers under high injection conditions [147]. This is very similar to a life time of the order 10 ns reported for CuGaSe$_2$ in [148]. Using a carrier life time of $\tau = 10$ ns a value of $p = 6 \cdot 10^{16}$cm^{-3} is found. Based on this evaluation it is therefore likely that the fluctuations of the measured depth appear at low temperature under the given excitation density.

4.2 Photoluminescene of Compensated Semiconductors

It is evident that the presence of potential fluctuations will significantly affect the properties of a semiconductor. Fluctuations are clearly visible in photoluminescence measurements as discussed from a theoretical standpoint [149, 150] as well as experimentally in numerous studies e.g. [13, 151, 152]. Description of radiative recombination in the presence of potential fluctuations is, however, not straight forward. In the following it will be explained that several recombination bands are theoretically and experimentally found in highly compensated semiconductors. The comprehensive but not easily comprehensible review by Levanyuk and Osipov deals with the theory of luminescence in semiconductors dominated by potential fluctuations [149]. The main results will be briefly summarized here. The model describes a p–type material where the heavy doping condition (Mott condition) is fulfilled for donors but not for acceptors. The Mott condition given by $N_M a_B^3 \approx 0.27$, where a_B is the effective Bohr radius of the defect gives in approximation of the critical concentration N_M above which defect states begin to interact [82]. For CuGaSe$_2$, using the same material parameters as in section 2.3.4 to calculate defect ionization energies, Bohr radii for the donor and acceptor are $a_{B,D} = 4.2$ nm and $a_{B,A} = 0.9$ nm respectively. This gives Mott concentrations of $N_{M,D} = 2.7 \cdot 10^{17}$ cm^{-3} for the donors and $N_{M,A} = 2.7 \cdot 10^{19}$ cm^{-3} for the acceptors. In the range between $N_{M,D}$ and $N_{M,A}$ the heavy doping condition is only fulfilled for the donors. This is generally found in most direct–gap semiconductors with defect concentrations in the range $10^{17} - 10^{19}$ cm^{-3} when the effective mass of the electrons is much smaller than for the holes $m_e^* << m_h^*$ [149]. Heavy doping is achieved when the distance between the defects is lower than the Bohr radius of the state leading to overlapping defect states. Due to the overlap of the very shallow donor states it is assumed that the donor state are no longer localized but merges with

the fluctuating conduction band. The deeper acceptor states, however, remain localized but smear out into a band due to the potential fluctuations. This is illustrated in figure 4.1.

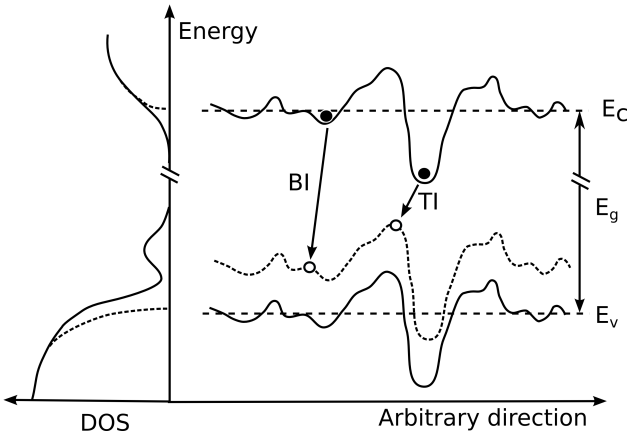

Figure 4.1: Schematic illustration of potential fluctuations in a highly compensated semiconductor. The vertical dashed lines show the valence and conduction band in absence of potential fluctuations. The solid line are the band edges in presence of the spatial fluctuations. The fluctuating dashed line illustrates an acceptor level [150]. Recombination of BI (band–impurity) type and TI (tail–impurity) type are illustrated.

It is often assumed in literature that this model is adequate to describe Cu(In,Ga)Se_2 [15, 83, 153]. According to this model one distinguishes between two main radiative recombination channels; tail–impurity (TI) recombination and band–impurity (BI) recombination. These channels that are dominant at low temperature and excitation are illustrated in figure 4.1. TI recombination occurs between electrons that are trapped in localized states in the conduction band with holes in a nearby acceptor state. The localized states in the conduction band occur at regions where an unusual high number of donors are clustered together in a small volume. It should be mentioned that these localized well states are only present at very low numbers compared to the number of typical fluctuations of size R_s and depth γ. Electrons are considered to be free in the typical fluctuations. The TI recombination channel can be compared to DAP recombination since it involves two localized states [149]. The so called band–impurity (BI) recombination involves free electrons in the typical fluctuations with holes bound to localized acceptor states. It is therefore comparable to a free–to–bound recombination process [149]. The temperature dependence of the TI and BI channels will be further discussed in section 4.5.3.

The advantage of the model by Levanyuk and Osipov is that it can explain the appearance and disappearance of several bands as the temperature is changed. A slightly simplified version of this model sometimes referred to as quasi–donor–acceptor–pair (QDAP) recombination is, however, often presented in literature [13, 143, 141, 151]. In this version of the model the recombination in the presence of potential fluctuations is described as a tunnel process between a donor level and an acceptor level. This model is able to explain the main characteristics of PL spectra of compensated semiconductors such as peak energy and excitation density dependence. These characteristics are discussed in the following section along with different approaches to estimate the amplitude of potential fluctuations from PL spectra.

4.3 Estimation of the Fluctuation Amplitude by Photoluminescence

Potential fluctuations have been discussed for decades in literature as described in the previous section. Several ideas for estimation of the amplitude of fluctuations have therefore been proposed. This section will aim to describe approaches that can be applied to estimate the amplitude of the fluctuations from PL measurements.

4.3.1 Peak Position Relative to Flat Band Conditions

In the presence of potential fluctuations it can be argued that the PL peak is lowered in energy by an amount equal to 2γ. If it is assumed that the observed luminescence is due to donor–acceptor pair recombination, the maximum of the PL peak can therefore be expressed as:

$$\hbar\omega_{max} = Eg - (E_D + E_A) + E_C - 2\gamma \tag{4.4}$$

This simple measure of the average fluctuation depth is in fact applied in numerous studies in literature [13, 83, 142, 143, 151, 154]. In most of these studies, the Coulomb term E_C is, however, ignored. This leads to an overestimation of the amplitude of the potential fluctuations. It should also be kept in mind that this approach is simplistic. Equation (4.4) is for example not valid in the case that the observed luminescence is due to tail–impurity recombination rather than quasi–donor–acceptor recombination.

4.3.2 Excitation Density Dependence

A sign of potential fluctuations in a semiconductor is a strong blue shift of the PL peak energy with increasing excitation density that can not be explained within the standard theory of DAP recombination described in section 2.3.4. This behaviour has been observed in numerous compensated materials such as ZnSe [143], GaAs [142, 151], $CuGaSe_2$ [13] and $CuInSe_2$ [155], and $Cu(In,Ga)(S,Se)_2$ [83]. It has been observed that the magnitude of the shift per decade, often referred to as β in literature (see definition in equation (2.16)), is related to the degree of compensation [13, 142]. A value of β up to 25 meV/decade has been observed in strongly compensated semiconductors [142]. It has even been proposed that the magnitude of the shift β is proportional to the average fluctuation amplitude γ [83, 151, 154]. The reason for the peak shift is explained as reduction of the fluctuation potential by several authors [13, 83, 143, 154]. It is argued that the peak energy shifts to higher energies due to flattening of the fluctuations for two reasons. First, the photogenerated carriers neutralize the charged defects, which decreases N_C in equation (4.3) and therefore reduces the fluctuation amplitude. The excited charge carriers, secondly, increases the free charge carrier density p in equation (4.3) leading to decrease of the fluctuations due to increased screening. Another explanation for the peak shift as a function of excitation that does not rely on flattening of the bands has been proposed [142]. These authors explain the shift as a result of filling the states in the deeper potential wells. As the excitation is increased probability to occupy wells of lower depth is increased. The PL is therefore dominated by recombination from wells of lower amplitude at high rates of excitation. The problem with this explanation is, however, that it does not take screening into account. When potential wells are filled it is expected that the potential flattens out

due to screening. Since this is ignored in this model, it is questionable if it describes the situation correctly.

4.3.3 Analysis of the Peak Shape

The density of states (DOS) from which carriers recombine affects the low energy tail of the PL peak, whereas shape of the high energy tail is characterized by thermal broadening [149, 156]. Since the density of states depends on the amplitude of the potential fluctuations, it has been proposed that analysis of the low energy peak shape can be utilized to extract information about the potential fluctuations [17]. Two models for the low energy peak shape have been proposed. For fluctuations that are sufficiently deep the tail states can be described by a Gaussian distribution. This is comparable to recombination via the TI path discussed in section 4.2. This defect–like description of the density of states leads to an expression for the low energy emission tail [149, 157]:

$$I_{PL}(\hbar\omega) \propto \exp\left(-\frac{(\hbar\omega - E_o)^2}{2\gamma^2}\right) \tag{4.5}$$

where E_0 according to Levanyuk and Osipov [149] is the energy of the transition in the unperturbed semiconductor in absence of potential fluctuations. Experimental results however finds that E_0 is affected by the potential fluctuations [17].
Shallower fluctuations are better described by Urbach tails with a density of states that decays exponentially. This model corresponds to recombination of BI type discussed in section 4.2. The low energy spectral peak shape in this tail–like case is therefore better described by [149]:

$$I_{PL}(\hbar\omega) \propto \exp\left(-\frac{\hbar\omega - E_0}{\gamma}\right) \tag{4.6}$$

These expressions can be utilized to extract information about the fluctuation amplitude γ by fitting the shape of the low energy peak slope of the PL spectrum.

4.3.4 Temperature Dependence

The influence of the temperature on the peak position of compensated semiconductors has been investigated in several studies, see for example [15, 48, 83, 151, 152, 158]. When the temperature is varied over the entire range from 5 K to room temperature these studies report that the peak shifts in a non–monotonous fashion as a function of temperature. In studies where a shorter temperature interval is investigated only a part of this behaviour is measured. This is for example the case in the thesis of Bauknecht where the temperature is varied from 10 – 80 K. In this temperature range a red shift is observed in agreement with the other studies mentioned above. As the temperature is increased it is commonly observed the peak energy reaches a minimum at a certain temperature T_{min} after which the peak shifts to higher energies for higher temperatures [15, 83, 152, 158]. The explanation often given for these observations is that a transition from TI to BI recombination occurs [15, 83, 152]. Jagomägi et al. however claims that BI recombination alone is responsible for the observations [158] based on the theory of Osipov et al. [150]. A similar temperature dependence is observed for the samples measured in this study. The results are presented and discussed in section 4.5.2 where a model explaining the temperature dependence of the peak position is presented.

4.4 Experimental Setup for Global Photoluminescence Measurements

The measurements presented in this chapter were performed on a PL setup with a spot size of around 100 μm. It is therefore referred to as global PL to distinguish it from μ–PL discussed in chapter 5. The setup is schematically illustrated in figure 4.2.

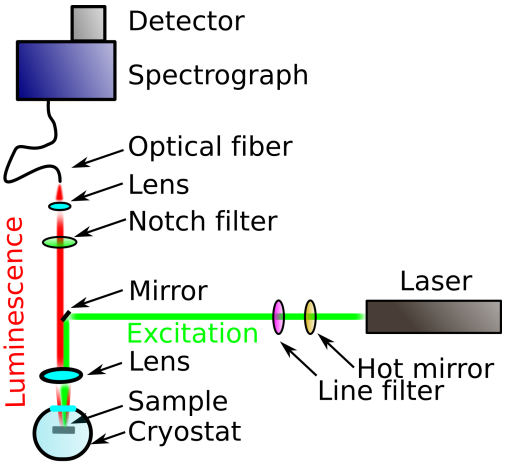

Figure 4.2: Illustration of the setup used for macro PL measurements.

The 514.5 nm line of an argon ion laser is used in all experiments. Since the laser emits numerous plasma lines over a wide wavelength range it is necessary to filter these out. These will otherwise overlap with the measured PL spectra. In order to remove these plasma lines over a wide wavelength range a hot mirror is used. This removes the plasma lines in the range 720 nm to 1500 nm. The plasma lines emitted very close to the laser line are, however, transmitted by the hot mirror. Therefore a line filter is needed. The line filter transmits in a narrow wavelength window of 5 nm centred at the laser wavelength. This filter reflects plasma lines with wavelengths close to the laser wavelength but transmits light of more than 700 nm. The combination of the hot mirror and line filter therefore removes plasma lines over a wide wavelength region. In case plasma lines are still detected if e.g. long integration times are necessary an additional short–pass edge filter can often remove these.
The PL setup utilizes a confocal approach, where the excitation laser light is focused onto the sample with the same lens that collects the emitted PL. In this way the focus of the collection and excitation is the same. In order to achieve this in practice a small mirror just large enough to reflect the laser beam is placed in front of the focusing and collecting lens. This mirror is as small as possible in order to reduce the amount of shadowing of the emitted PL. When the sample is perfectly in focus the PL is collected in a parallel beam. This beam passes through a notch filter that removes only the laser by reflection of light from 512 to 519 nm, so that the laser light does not enter the spectrograph and potentially damage the cameras. One has to be careful that the notch filter can give rise to interferences in the PL signal. This is especially problematic at long wavelengths. If interferences are observed the notch filter can be replaced by edgefilters. The PL that is transmitted by the notch filter is focused onto an optical fiber. The fiber brings the light into the spectrograph where it is spectrally dispersed by a grating. The PL is either detected by a Si CCD camera or an InGaAs detector array, both of which able to record

an entire spectrum at once. The InGaAs detector has a sensitivity range from 800 nm to 1700 nm and is therefore used to measure $CuInSe_2$ that emits around 1240 nm. The Si detector is sensitive to light in the wavelength range from 300 nm to 1000 nm, and can therefore be applied to measure PL emitted from $CuGaSe_2$ that emits around 750 nm.
Typically laser powers in the range 1-100 mW are used. This gives a photon flux of $10^{19} - 10^{21}$ photons/(cm^2·s), which is equivalent to about 70–7000 suns in the case of $CuGaSe_2$. This is estimated based of the sun irradiation above the band gap of $CuGaSe_2$ of $1.5{\cdot}10^{17}$ photons/(cm^2·s) [159, 160]. The results presented in the following section are measured at 10 K. In section 4.5.2 results from a temperature dependent study where the temperature is varied from 10 K – 300 K are presented.

4.5 Investigation of Potential Fluctuations by Photoluminescence

This section is devoted to discussion of the results obtained from a series of $CuGaSe_2$ films grown under Cu–poor conditions. The results will be discussed in relationship to the models for a highly compenstated semiconductor presented in the previous section. First, various approaches for determination of the potential fluctuations are applied to the results. This is followed by a section in which the temperature dependence of the potential fluctuations is discussed.

4.5.1 Estimation of the Potential Fluctuation Amplitude at 10 K

There are several approaches to estimate the amplitude of potential fluctuations from PL measurements. In the following the amplitude will be estimated applying the various methods. The results obtained from measurement of a series of six samples are presented in the following section. Samples are measured with EDS to determine their composition. A summary of the results is given in table 4.1 at the end of the section. In the following the samples are sorted with increasing [Cu]/[Ga] ratio.

Peak Shift Relative to Donor–Acceptor Recombination

It is here assumed that the luminescence seen in the Cu–poor compensated $CuGaSe_2$ is due to the same DAP transition observed in stoichiometric weakly compensated $CuGaSe_2$ in which the potentials are not fluctuating. The peak observed in the stoichiometric material is the so–called DA1 transition discussed in section 2.3.8. In this case it is reasonable to calculate the average fluctuation amplitude as two times the peak shift relative to the DA1 peak as shown in equation (4.4).
The PL spectra of the samples measured at 10 K with the same excitation density are shown in figure 4.3. A stoichiometric sample showing the DA1 peak is included as reference. In order to calculate the fluctuation amplitude it is necessary to know the Coulomb term E_C in equation (4.4). This problem is, however, not straight forward, since the concentration of the donors involved in the DA1 transition is not known. It has previously been observed that the degree of compensation increases with increasing acceptor concentration [161]. For a high degree of compensation close to 1, an acceptor concentration of the order $N = 10^{18}$ cm^{-3} was found, significantly higher than a density close to $N = 10^{16}$ cm^{-3} observed in samples with low degree of compensation (K = 0.2) [161]. Assuming a defect density of $N = 10^{18}$ cm^{-3} the mean distance between defects

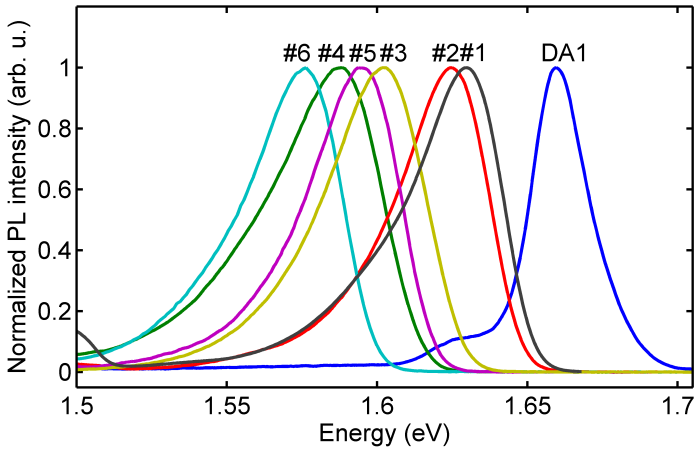

Figure 4.3: 10 K PL spectra of Cu–poor samples measured at an excitation density of $\approx 10^{22}$ cm^{-2}s^{-1}. A stoichiometric film showing the DA1 transition is included as reference.

is $r_{DA} = (\pi N/2)^{-1/3} = 8$ nm. Inserting this value for the intra pair distance in equation (2.15) gives a Coulomb energy of 15 meV. A defect density of $N = 10^{16}$ cm^{-3} on the other hand gives a much lower Coulomb energy of $E_C = 3$ eV. This gives an idea of the influence of the Coulomb term for samples with different degree of compensation. Since the concentration of the donors involved in the transition is not known, the Coulomb energy cannot be determined for the measurements performed here. Instead it must be kept in mind that the fluctuation amplitude determined here is overestimated due to the negligence of the Coulomb term. The fluctuation amplitude calculated from equation (4.4) neglecting the Coulomb term gives 16 meV for the least shifted sample and up to 42 meV for the sample with the largest shift compared to the DA1 transition. The average fluctuation amplitude obtained from the peak position $\gamma_{\Delta E}$ for all samples is collected in table 4.1.
The general trend shows a red–shift of the peak as the [Cu]/[Ga] is lowered, which agrees with the expectation. With increasing Cu–deficiency the charged defect concentration increases and therefore the fluctuation amplitude. Only sample #4 does not follow this trend. This sample has a peak energy lower than expected when comparing to the other samples. Estimates of γ by other methods in the following, however confirms that sample #5 has deeper fluctuation depth than #4 even though the opposite seem the case when estimating γ from the peak position. The reason for this deviation from the trend could indicate that the experimental conditions were not the same for this sample. If for example the focus was not perfect when sample #4 was measured, the excitation density on the sample is lower than expected. This would lead to lower photo carrier density and hence less screening. This could explain that the peak position is lower than expected in energy relative to the other samples.

Shift as Function of Excitation

The blue shift of the PL peak for increasing excitation density is related to the potential amplitude as discussed in section 4.3.2. The blue shift can be explained by flattening of the fluctuations due to neutralization of the defects and screening by the photogenerated carriers. The effect of excitation is more pronounced for deeper potential fluctuations. It is therefore expected that the peak shift increases with larger potential fluctuation ampli-

tude γ. Figure 4.4 shows fits of the peak shift β as a function of the excitation density.

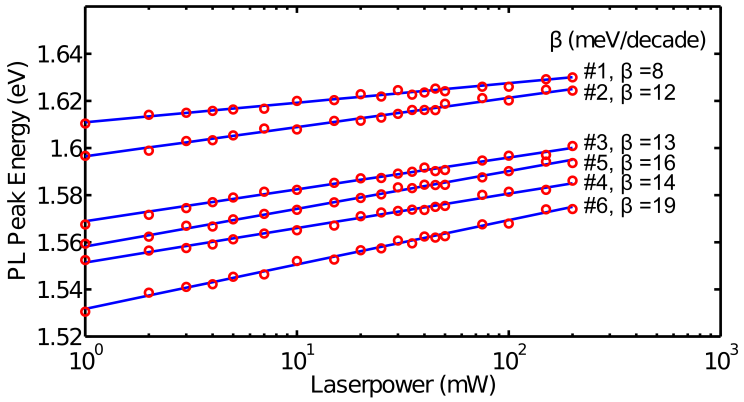

Figure 4.4: PL peak shift as function of excitation density measured at 10 K for the Cu–poor samples #1 - #7.

The values for the peak shift is in the order $8 - 19$ meV/decade, which is very similar to the observations by other authors [13, 83]. It is noticed that β is increasing with decreasing [Cu]/[Ga]. This confirms that the amplitude of the potential fluctuations increases with increasing Cu deficiency as expected. An interesting observation is that the peak shifts linearly with the logarithm of the excitation density. This is commonly found experimentally in literature [142, 143, 151], but not in agreement with the theoretical prediction of equation (4.3). According to this theory it is expected that γ and therefore the peak shift should decrease as (excitation density)$^{-1/3}$. This observation questions the general validity of equation (4.3).

Fitting of the Low Energy Slope

In order to obtain another estimate of γ from the measured PL spectra the low energy slope of the PL spectrum is fitted according to equation (4.5) and (4.6). The best fits are shown in figure 4.5. The values for γ_{fit} obtained by fitting are collected in table 4.1.

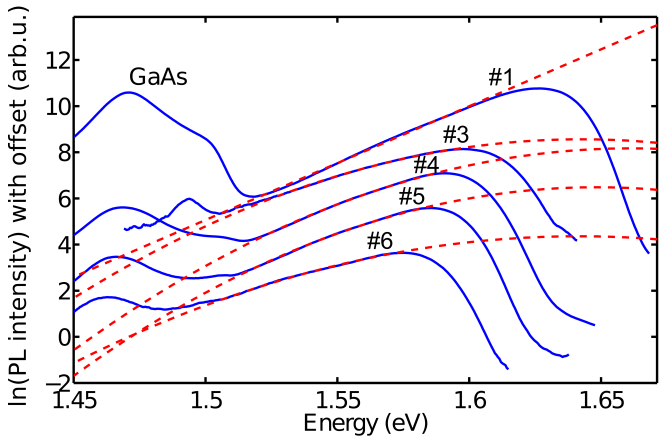

Figure 4.5: 10 K PL spectra and fits of the low energy slope for estimation of γ_{fit}.

For the two samples with the lowest Cu–deficiency it is found that equation (4.6) gave the best fit. This is in agreement with the expectation that this model that assumes exponentially decaying tail states describes small fluctuations well. The rest of the samples with

a lower [Cu]/[Ga] are best fitted with equation (4.5) that assumes a defect–like Gaussian distribution of the density of states. The result is essentially in agreement with the expectation that the density of states due to the low energy tail has a Gaussian shape for large fluctuations. The limit between fluctuations best fitted by the exponential tails and the Gaussian tail shape is $\gamma \approx 40$ meV. This is exactly the same result obtained in an earlier study [17]. The value for E_o in equation (4.5) found by fitting lies between 1.64 eV and 1.66 eV. E_o is theoretically supposed to be the energy of the transition for unperturbed bands, in this case around 1.66 eV. Some of the fits obtained are therefore in agreement with this expectation, whereas a lower energy is found for other fits. It has previously been seen that E_o is not necessary the flat band transition energy [17]. In this study it is also found that E_o can be influenced by the potential fluctuations. The result of this approach to estimate γ shows the same trend as the other methods applied in this study: The fluctuation amplitude increases as the Cu–deficiency increases.

Comparison of Methods for Fluctuation Amplitude Estimation

The preceding subsections contain several estimations of the fluctuation amplitude. In order to compare the results obtained with the different methods, all results are collected in table 4.1.

Sample	[Cu]/[Ga]	β	$\gamma_{\Delta E}$	γ_{fit}
#1	1.04	8	16	24
#2	0.94	12	17	20
#3	0.95	13	30	42
#4	0.90	14	36	49
#5	0.89	16	33	51
#6	0.84	19	42	58

Table 4.1: Meaurement of the fluctuation amplitude by different approaches. Samples are sorted with respect to [Cu]/[Ga] determined by EDS. β has the unit (meV/decade) and γ is given in meV.

The tendency that the fluctuation amplitude increases with decreasing [Cu]/[Ga] ratio is clear for all evaluation methods. The absolute values of [Cu]/[Ga], however, indicate that sample # 1 should be Cu–rich with [Cu]/[Ga] = 1.04 even though the sample clearly shows the signatures of a Cu–poor absorber. Since the [Cu]/[Ga] ratio is measured by EDS the accuracy of the technique must be taken into account to explain this. With EDS it is possible to determine the concentration of an element with an accuracy of about 5% in relative numbers [115]. If a sample is perfectly stoichiometric one expects to measure 25 atomic % of both Cu and Ga, one could in the worst case measure 26% Cu and 24 % Ga. This would not give the expected [Cu]/[Ga] = 1 but one would find [Cu]/[Ga] = 1.08, significantly higher than expected. This could be the explanation for a wrong absolute value of the [Cu]/[Ga] ratio. Another possibility is at a matrix effect leads to overestimation of the [Cu]/[Ga] ratio. For the measurement the EDS is calibrated with pure elements. This, however, has the disadvantage that matrix effects can influence the result. It could e.g. be that X–rays are differently absorbed in the $CuGaSe_2$ matrix than in the pure elements. This leads to an error of the measured element concentrations. In general we have observed a tendency that the [Cu]/[Ga] ratio is overestimated by EDS measurement, which could also explain the measured [Cu]/[Ga] higher than one. Since

all samples are measured in a row it is, however, still possible to trust the trend.
Comparison of the result obtained from the peak shift $\gamma_{\Delta E}$ with the result of fitting γ_{fit} shows the same trend but the absolute value of γ_{fit} is $\gamma_{\Delta E}$ larger than in most cases. All values are, however, within the values that can be estimated for a semiconductor with $N_C = 10^{18}$ cm^{-3} under the experimental conditions. It is therefore difficult to highlight one approach as being more exact than the other. It should be mentioned that neither of the methods is very accurate. Both approaches merely give an indication of the magnitude of the potential fluctuations and show the expected trend.

4.5.2 Temperature Dependence of the Peak Position

The approaches demonstrated in the previous section will be applied in the following to obtain information about the temperature dependence of the potential fluctuations in chalcopyrites.
Figure 4.6 shows the PL of sample #3 as the temperature is varied from 10 K to room temperature.

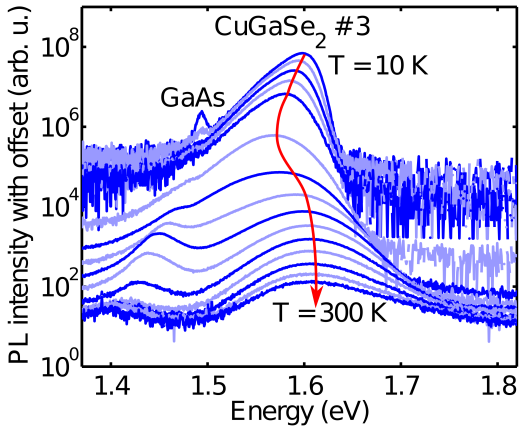

Figure 4.6: PL of a compensated $CuGaSe_2$ sample measured from 10 K to room temperature.

In addition to a non–monotonic peak shift, the peak shape changes significantly. It is noticed that the high energy slope flattens significantly with increasing temperature. The reason for this is that the thermal distribution of charge carriers, responsible for the high energy slope, broadens (the thermal broadening is described in further details in section 5.1.1). Changes in the low energy peak slope is discussed in the end of the section. First, focus will be turned to the peak position, since it gives direct information about the potential amplitude as discussed in the previous section.
Figure 4.7 shows the peak position of the samples in table 4.1 as a function of temperature. The energy of the excitonic emission of a $CuGaSe_2$ absorber grown under Cu–rich conditions is included (EXC) as reference. This sample does not show the effect of potential fluctuations and the energy plotted in figure 4.7 is the energy of the excitonic recombination that evolves to band–to–band recombination as the temperature is increased. It is noticed that this curve remains almost constant in the range 10–100 K, which shows that the band gap remains almost constant in this region. This is essentially in agreement with the results presented in earlier studies [70, 76, 77, 78]. Above this region the band gap decreases with 7–20 meV per 100 K [70, 76, 77, 78]. From the shift of the exciton that

develops into a band–to–band transition (EXC in figure 4.7) it is estimated that the band gap decreases with ≈ 15 meV per 100 K in the sample studied here.

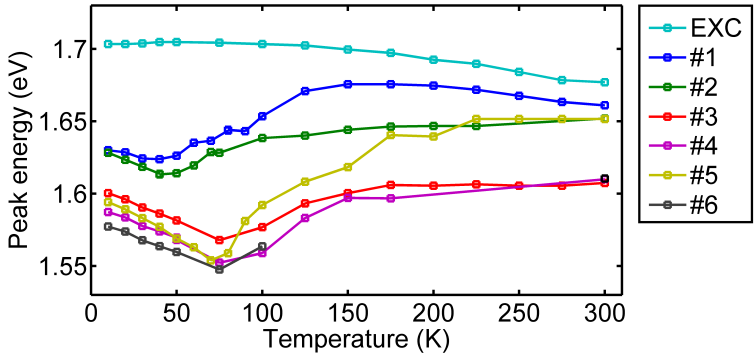

Figure 4.7: Temperature dependence of PL peak energies for samples with different [Cu]/[Ga] ratio.

The Cu–poor $CuGaSe_2$ absorbers all show a similar behaviour as a function of temperature. When the temperature is increased from 10 K the peak position initially shifts to lower energies. After the initial red shift the peak position reaches a minimum at a temperature T_{min} and blue shifts for higher temperatures. This change of behaviour is seen in all Cu–poor samples. The shift of the peak finally reaches a plateau for temperatures higher than about 150 K for all samples except the least Cu–poor sample. This sample shows a red shift again for high temperatures.
Figure 4.8 illustrates the model for potential fluctuations applied here to explain the observed behaviour. To explain the temperature dependence only the band edges are illustrated in figure 4.8. In reality the acceptor state illustrated in figure 4.1 is present and follows the bands.

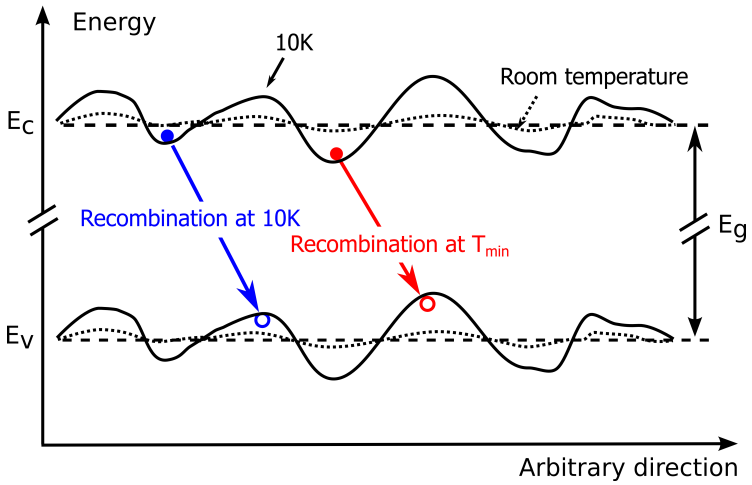

Figure 4.8: Schematic illustration of the change of the fluctuating band edges as the temperature is changed.

At very low temperature (10 K) the generated charge carriers end up in local potential valleys that are not the absolute minima and recombine from there. It is in other words not possible to define a single quasi–Fermi level that is valid throughout the excited volume. This is in agreement with observations in literature where it is argued that quasi–equilibrium is not achieved at low temperatures due to the barriers between potential valleys [151, 162]. At low temperatures the occupation may instead be described by lo-

cal quasi–Fermi levels [83]. As the temperature is increased the additional thermal energy enables the charge carriers to overcome potential barriers between the local minima and recombine from valleys of lower energy, hence the initial red shift until T_{min}. As the temperature is increased further the free charge carrier concentration is increasing, since the remaining acceptors, which are not compensated, become ionized. The free charges screen the charged defects, flattening the fluctuations, which explains the blue shift between T_{min} and 150 K. As the temperature is increased it is in addition expected to observe more band–to–band recombination and less defect related recombination. This change towards band–to–band dominated recombination leads to a blue shift of the peak as well. For higher temperatures it is expected that the peak red shifts, since the band gap shrinks in this temperature regime. This is however only observable if the fluctuations totally flatten in this temperature region. If small fluctuations are still present the blue shift due to flattening of the bands and the shrinking of the band gap with increasing temperature will cancel each other. This explains the plateau for most of the samples in figure 4.7. The fact that the curves flatten out, however, indicates that the amplitude of the fluctuations is significantly reduced at room temperature. The only Cu-poor sample that shows a red shift for high temperatures is the sample with the highest [Cu]/[Ga] ratio (#1). Since the peak energy decreases with a rate very similar to the band gap shrinkage for this sample it can be concluded that the potential fluctuations seen at low temperatures have totally disappeared at room temperature in this sample. This observation is in agreement with the observation of the previous section that the sample with the highest [Cu]/[Ga] shows the lowest amplitude of the fluctuations whereas samples with a lower [Cu]/[Ga] show stronger fluctuations.

T_{min}, the temperature where the peak energy position is minimum in figure 4.7, is another indication of the fluctuation amplitude. The trend visible in figure 4.7 is that T_{min} increases as the Cu–deficiency increases. This is due to a higher amplitude of the potential fluctuations for these samples, and therefore higher barriers between the local potential valleys. The deeper the fluctuations, the more free charge carriers are needed in order to flatten the bands. The sufficient charge carrier concentration is therefore obtained at higher temperatures for deeper fluctuations. Another effect is that a higher temperature is needed to overcome the barriers between potential valleys in order to reach the deepest valleys. The combination of these effects leads to an increase of T_{min} in samples with a larger fluctuation amplitude.

It is striking that the peak position for all samples does not end up at the same energy at room temperature, although it is expected that the PL measured at room temperature is due to band–to–band recombination. The samples with a high Cu deficiency have lower peak positions at room temperature than the less Cu–poor samples. This can however be explained by the increased influence of Urbach tails in combination with a lower band gap in slightly Cu–poor material [70, 163].

Figure 4.9 shows the results of a temperature and excitation dependent PL study. In order to prove that the observations discussed in this chapter are not unique for $CuGaSe_2$ similar measurements are performed for $CuInSe_2$. One example of a temperature dependent PL measurement on $CuInSe_2$ is included in figure 4.9(c),(d). Since the results are very similar for both materials the following discussion is relevant to both materials.

Figure 4.9(a) and (c) shows the peak energy of a highly compensated $CuGaSe_2$ absorber (#1) and a highly compensated $CuInSe_2$ sample, respectively, as a function of temperature. Each line is measured at a different excitation intensity. At low temperatures the peak position is dependent on the excitation intensity (higher for higher excitation inten-

sity). This is quantified in terms of β as shown in figure 4.9(b) and (d). The magnitude of β initially increases with increasing temperature until the temperature region of T_{min} in figure 4.9(a) is reached, where it reaches its maximum. At higher temperatures β decreases and the curves in figure 4.9 approach each other. At temperatures above 150 K the peak position is essentially independent of the excitation intensity and β reaches zero.

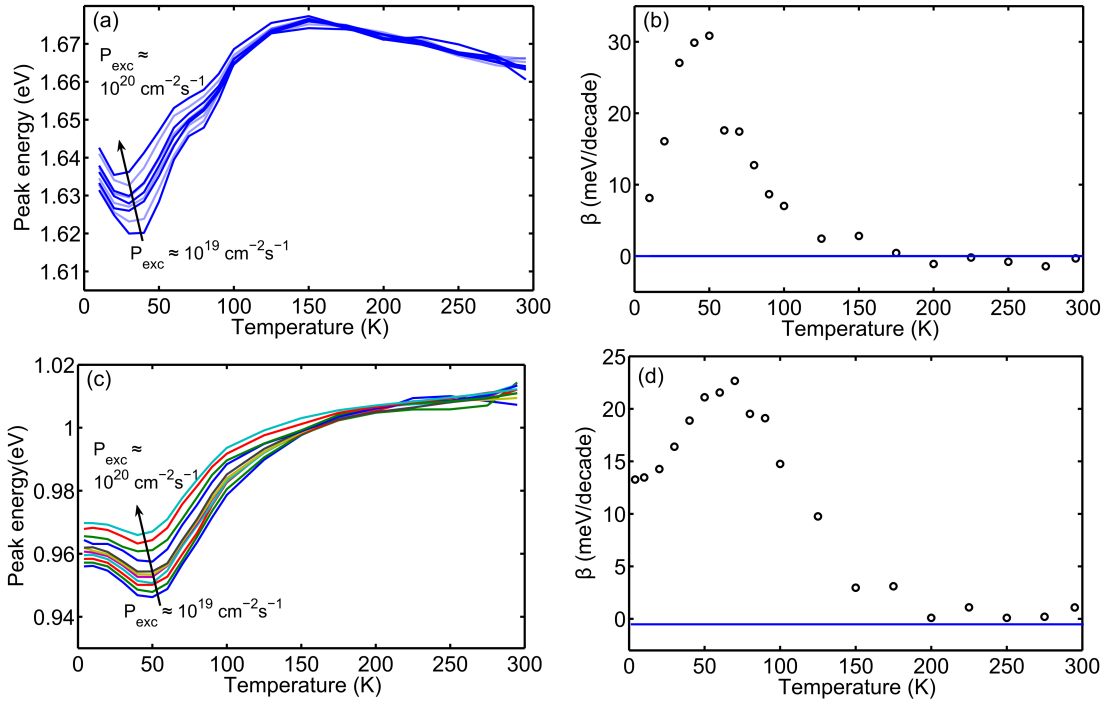

Figure 4.9: (a) Temperature dependence of the peak energy of sample $CuGaSe_2$ #1 for different excitation densities. (b) Excitation dependent peak shift β as a function of temperature. (c) same as (a) for $CuInSe_2$. (d) same as (b) for $CuInSe_2$.

The behaviour illustrated in figure 4.9 can be explained in analogy with the model described earlier (see figure 4.8). At temperatures below T_{min} the peak energy depends on excitation intensity due to the presence of potential fluctuations, since the fluctuations flatten with increasing excitation. The effective amplitude of these fluctuations seen in PL increases towards T_{min} since the photogenerated carriers are able to redistribute towards the deepest potential valleys as the temperature is increased. In the temperature region between T_{min} and 150 K the curves approach each other and the peaks shift significantly to higher energies. Both effects can be explained by flattening of the bands due to increased screening by thermally generated charge carriers. The absence of a peak shift with excitation intensity at temperatures above 150 K is a sign that the fluctuations are completely flattened in this temperature region. This is for the $CuGaSe_2$ sample further supported by the fact that the peak energy decreases with the same rate as the band gap in this region. T_{min} decreases slightly as the excitation density increases. This occurs since the higher excitation intensity flattens the bands already at lower temperatures due to screening by photo generated carriers.
From the temperature and excitation dependent PL measurement of sample #1 it is possible to extract the exponent k in the power law $I_{PL} \propto P_{exc}^k$. The value of k as a function of the temperature is shown in figure 4.10.
This give insight into the character of the dominating recombination process. At high

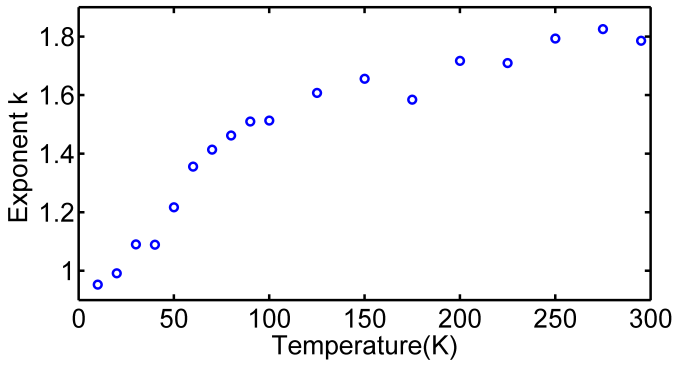

Figure 4.10: The exponent k in the power law of PL intensity as a function of temperature extracted from the measurement of $CuGaSe_2$ shown in figure 4.9(a).

temperatures a $k \approx 1.8$ is observed. This can be understood as an indication that band–to–band recombination dominates. For band–to–band recombination the PL intensity depends on the concentration of both electrons and holes $I_{PL} \propto n \cdot p$, where n and p are both proportional to P_{exc} under high injection conditions. This therefore gives rise to the exponent $k = 2$. At low temperature the exponent is observed to be $k \approx 1$. This is very typically observed for low temperature PL measurement of Cu–poor absorbers. An exponent of $k = 1$ shows that the PL intensity depends on only the concentration generated of one of the carriers. This is typically observed in defect related recombination [10]. The transition between defect correlated luminescence at low temperature and band–to–band related luminescence at high temperature happens smoothly. Since k increases strongest in the range 10–100 K and flattens out above 100 K it can be assumed that the band–to–band recombination already dominates above 100 K. A part of the blue shift observed between T_{min} and the plateau described previously must be therefore be ascribed to the change of recombination mechanism.

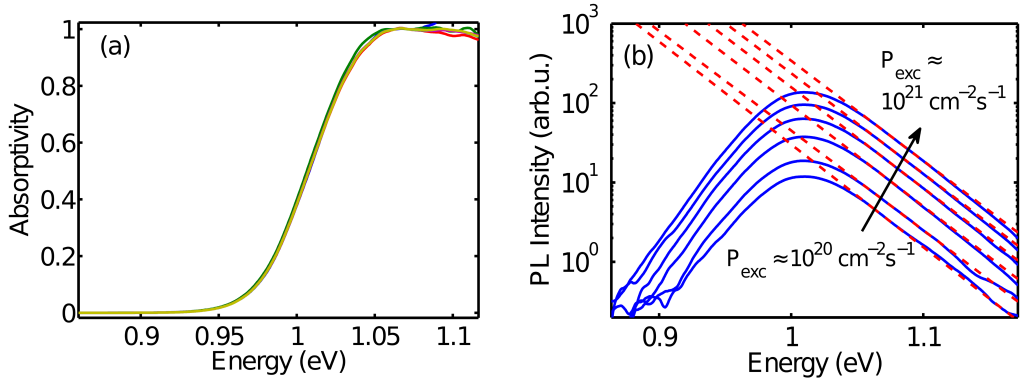

Figure 4.11: (a) Absorption edge of $CuInSe_2$ sample calculated from PL spectra measured at room temperature with excitation varying between 10^{20} – 10^{21} photons/(cm^2·s) using fit of Plancks generalized radiation law shown in (b).

It is finally possible to verify the low amplitude of the potential fluctuations at elevated temperatures by analysing the spectral shape of the PL measured at room temperature. Using the fact that band–to–band recombination dominates at room temperature, it is possible to extract the absorptivity spectrum from the measured PL spectum. The details of the evaluation are presented in section 5.1.1. The discussion here will merely deal with

the result of the calculation seen in figure 4.11.
The absorption edge is calculated for the Cu–poor $CuInSe_2$ sample also shown in figure 4.11 based on PL spectra measured with excitation densities varying between 10^{20} – 10^{21} photons/(cm^{-2}·s) . The result clearly shows that the absorption edge does not change when varying the excitation density over one order of magnitude. One would expect that the absorption edge would change in the presence of strong potential fluctuations, since the effective band gap appears smaller in the presence of the fluctuations. When the absorption edge stays constant over one order of magnitude of excitation variation this clearly indicates that the potential fluctuations present at room temperature are no more than a few meV if present at all. It should be kept in mind that this measurement is performed with an excitation flux down to the order of 600 suns. The illumination clearly contributes to flattening of the bands. Based on the excitation and temperature dependence seen in figure 4.9 it can, however, be expected that the fluctuations will also flatten at room temperature under 1 sun equivalent illumination.
This method of evaluation is applied to all samples discussed in this section with the same result: the absorption edge at room temperature is unaffected by the excitation density independently of the fluctuation amplitude measured at 10 K. According to this evaluation it can therefore be argued that the potential fluctuations flatten to below the uncertainty of this method, which is in the order of a few meV. An observation that should be compared to the result of the temperature dependent measurements that indicated that weak fluctuations could remain at room temperature for the most Cu–poor samples. According to the evaluation of the band edge it must be concluded that these fluctuations are very weak if present at all.

4.5.3 The Appearance of Two Peaks

For sample #1 and #2 it is interestingly observed that more than one peak appeared in the otherwise broad asymmetric peak observed at 10 K as the temperature is increased. Figure 4.12 shows PL spectra of sample #1 as the temperature is increased from 10 K to room temperature.

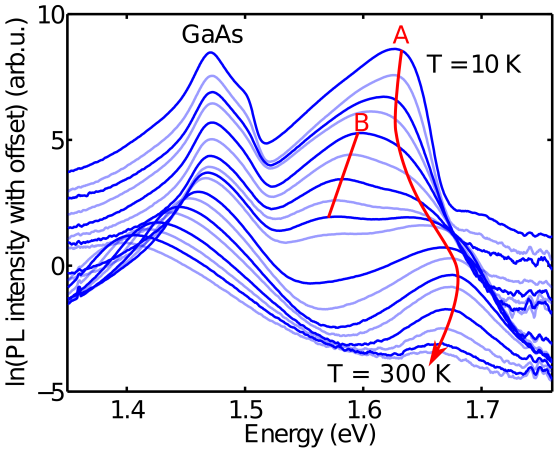

Figure 4.12: PL spectra of sample #1 with increasing temperature. The peak labelled A is related to BI recombination and the peak labelled B is related to TI recombination.

The peak labelled A is the one plotted in figure 4.9, the B peak is ignored in the previous discussion but will be discussed in the following. At low temperatures the spectrum

is dominated by one broad asymmetric peak (A in figure 4.12). As the temperature is increased a second peak (labelled B in figure 4.12) appears in the spectrum. At 60 K the second peak B with lower energy dominates the spectrum. When the temperature is increased further the intensity of peak B decreases again until the peak is no longer visible at 125 K. The reason for peak B must therefore be a transition that is quenched at low and high temperature with a maximum transition probability around 60 – 80 K. The peak here labelled A is on the other hand present at all temperatures with an intensity that decreases continuously and a non–monotonous energy shift as the temperature is increased. The presence of two peaks with different temperature dependent behaviour is in fact predicted theoretically [150] and previously observed experimentally [152]. The explanation of be observed behaviour could be related to the difference between TI and BI recombination briefly introduced in section 4.2. Depending on the temperature and excitation either TI or BI recombination dominates [150]. Since these two transition types have slightly different characteristics it is possible that the appearance of the second peak can be associated to competition between the two recombination pathways. It is possible that the B peak is related to TI recombination that does not dominate at the lowest temperature because of the energy barriers between the valleys mentioned earlier. One can similarly imagine that the B peak vanishes at higher temperatures because of flattening of the deep fluctuations and release of holes from the acceptor levels [152]. At higher temperatures the spectrum is dominated by peak A. This peak is probably due to recombination from typical shallow fluctuations of the BI type that dominates at high temperature [152]. The temperature dependence of the BI type recombination is theoretically described by Osipov et al. [150]. A numerical simulation of the BI theory is performed by Jagomägi et al. [158]. The calculated temperature dependence of the peak shape and position of BI recombination shows the same characteristics as discussed in the previous section. This supports that the main peak observed in this experiment is in fact of BI type.
The fact that two peaks are only observed in the samples with the highest [Cu]/[Ga] ratio is also interesting. Fit of the low energy slope in section 4.5.1 shows that the first two samples are best described by the tail–like model, which is analogous to BI–like recombination. The other samples with deeper fluctuations are fitted better with the defect–like model, which can be interpreted as TI–like recombination. This shows that in samples with low fluctuation amplitude recombination is dominated by BI recombination at low temperatures. When the temperature is increased it is possible to observe both BI and TI recombination in these samples. Samples that have deeper fluctuations (#3 – #6) are already dominated by TI–like recombination at low temperature and does therefore not show the appearance of a second peak as the temperature is increased.

4.6 Summary

The temperature and excitation dependence of the photoluminescence observed in $CuGaSe_2$ and $CuInSe_2$ can both be explained with the model of potential fluctuations. Several methods to evaluate the fluctuation amplitude from 10 K PL measurement have been applied. The result of all methods show that the fluctuation amplitude increases as the [Cu]/[III] ratio decreases. This is in agreement with the conclusion of previous studies. Temperature dependent PL indicates that the potential fluctuations are present in Cu–poor chalcopyrite at low temperatures but flatten for temperatures higher than about

150 K. In slightly Cu–poor material the fluctuations totally disappear at elevated temperatures. In samples with larger Cu–deficiency the fluctuations seem to remain even at room temperature, but the magnitude of the fluctuations is significantly reduced to a few meV.

Spatial Variations in Epitaxial $CuGaSe_2$ Thin Films

5

Common methods for study of defects in semiconductors include a wide range of electrical methods such as Hall measurements, deep level transient spectroscopy or admittance spectroscopy. These methods have the disadvantage that the measured properties represent an average value of properties that might vary on a short length scale [164]. In order to study these effects on a μm or sub–μm length scale various methods have been applied (see section 5.2). One approach to directly obtain information about defects in the material on this length scale is spatially resolved μ–PL. With this technique it is possible to investigate and quantify variations of material properties that can be directly related to the performance of the solar cell material [165].

The purpose of the studies presented in this section is to investigate the properties of epitaxial $CuGaSe_2$ on the μm–length scale without the influence of grain structure and alloying disorder. In order to extract quantitative information from the measurements Planck's generalized law of radiation is applied. The approach of the analysis is therefore described and discussed in the beginning of this chapter. Several previous μ–PL experiments on polycrystalline $Cu(In,Ga)Se_2$ have been reported in literature. Since lessons can be learned from earlier studies, these results are summarized and discussed in the second section.

The subsequent sections of this chapter deal with the experiments performed in this work. This is initiated by a presentation and discussion of the experimental setup used for spatially resolved measurements.

Various effects occurring in epitaxial thin films are investigated. The first issues that are addressed are related to defects in the material. This includes a study of the spatial variations of certain donor–acceptor–pair transitions and phonon replicas. This is followed by a section that deals with a study of the spatial variation of a low energy luminescence peak found to be anti–correlated to excitonic and band–to–band recombination. The defects responsible for this luminescence peak are therefore expected to be deteriorating for the material performance.

The subsequent sections focus on the spatial variation of the quasi–Fermi level splitting and the band gap. This includes a study of the strain and cracks appearing due to the thermal mismatch between $CuGaSe_2$ and GaAs. It is shown by μ–PL and CL that local relaxation near the cracks leads to an increased band gap.

A study of the effect of the secondary phase Cu_xSe on the material properties is a central topic in this chapter. This effect is therefore studied in details to reveal that Cu_xSe enhances the quality of the surrounding $CuGaSe_2$ layer. The effects observed in these studies of epitaxial layers are also expected to affect polycrystalline material. The chapter is finalized with a section discussing this issue.

5.1 Theory of Spatial Variation of Room Temperature Photoluminescence

This section contains a discussion of theory that describes experimentally observed room temperature photoluminescence. This theory gives a tool to analyse the spectral shape of a photoluminescence peak. By measurement of spatially resolved photoluminescence local changes in the PL spectra can give valuable insight into the variations of material properties. Here it will be explained how the theory can be utilized for analysis of spectral changes through an approach presented in [11, 165, 166].

5.1.1 Spatial Variation of Photoluminescene at Room Temperature

Photoluminescence emitted from a semiconductor at room temperature is due to the radiative recombination of an electron in the conduction band with a hole in the valence band under the condition that the defect density is not too high. This is referred to as band–to–band recombination (BB). As described in section 2.3 illumination of a semiconductor by light with energy higher than the band gap leads to generation of excess charge carriers in the conduction and valence bands. These charge carriers rapidly thermalize to the band edges before they recombine radiatively or non–radiatively. This is illustrated in figure 5.1. Here the quasi–Fermi levels E_{Fn} and E_{Fp} have been introduced. The quasi–Fermi distributions describe the populations of electrons (f_n) and holes (f_p) in the bands in thermal equilibrium with the lattice. The splitting of the quasi–Fermi levels $\mu = E_{Fn} - E_{Fp}$ occurs as a consequence of the non–equilibrium situation caused by excitation with light.

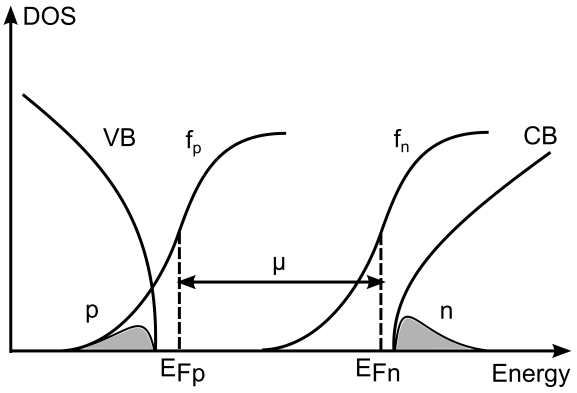

Figure 5.1: Illustration of quasi–equilibrium charge carrier distribution in the bands [146].

The emission from a semiconductor in thermal and chemical equilibrium with the irradiation from the surroundings can be described by Planck's generalized radiation law [146, 167], expressed as:

$$\mathrm{d}j = A(\hbar\omega)\frac{\Omega}{4\pi^3\hbar^3 c_l^2}\frac{(\hbar\omega)^2}{\exp\left(\frac{\hbar\omega-(E_{Fn}-E_{Fp})}{k_B T}\right)-1}\mathrm{d}\hbar\omega, \tag{5.1}$$

where j is the photon current density, $A(\hbar\omega)$ is the absorptivity, c_l is the speed of light, $\hbar$ is the reduced Planck constant, Ω is the solid angle of detection, $\hbar\omega$ is the photon energy, k_B is the Boltzmann constant, T is the temperature, and $E_{Fn}-E_{Fp}=\mu$ is the splitting of quasi-Fermi levels. It is of great interest to be able to investigate μ, since it can be directly related

to the maximum achievable open circuit voltage V_{oc} of the final solar cell [146, 168].
Planck's generalized radiation law describes the photons emitted from the semiconductor due to the thermal distribution of charge carriers ($\mu = 0$) as well as emission due to recombination of charge carriers created by illumination ($\mu \neq 0$) [146].
Equation (5.1) describes the spectrum of photons emitted per energy interval per second i.e. $\frac{\mathrm{d}j}{\mathrm{d}\hbar\omega}$ into the solid angle Ω. In an experimental PL measurement the detector, however, measures an intensity, which is a power with the unit J/s. In order to convert equation (5.1) to a form describing the measured data, it must therefore be multiplied by the energy of each photon $\hbar\omega$. By definition of a constant $C = \frac{C_{setup}(\Omega)}{4\pi^3 c_l^2}$ and introduction of the spectral PL intensity as $I_{PL}(\hbar\omega) = \frac{\mathrm{d}j}{\mathrm{d}\hbar\omega}\hbar\omega$, equation (5.1) can be simplified to:

$$I_{PL}(\hbar\omega) = C \cdot A(\hbar\omega)\frac{\omega^3}{\exp\left(\frac{\hbar\omega-\mu}{k_B T}\right) - 1}. \tag{5.2}$$

The constant C_{setup} introduced here depends on the solid angle Ω of the collected PL and the response of the measurement setup. In actual PL measurements one typically measures "counts" and not a photon flux. It is therefore necessary to absolute calibrate the system in the experiment in order to determine the value of C. A careful calibration of this kind facilitates to measure the absolute value of μ. C can, however, safely be assumed to be constant during a spatially resolved measurement and is therefore not determined for the measurements discussed in the following sections. With this assumption we limit ourselves to study only variations of quasi-Fermi levels and not absolute quantities. Applying the Boltzmann approximation valid for $\hbar\omega - (E_{Fn} - E_{Fp}) >> k_B T$ equation (5.2) can be further simplified to

$$I_{PL} = C \cdot A(\hbar\omega)\omega^3 \exp\left(-\frac{\hbar\omega - \mu}{k_B T}\right). \tag{5.3}$$

This equation will be applied to extract information about relative spatial variations of the quasi-Fermi level splitting and absorptivity from the measured PL spectra. Rearranging and taking the logarithm of equation (5.3) yields

$$\ln\left(\frac{I_{PL}}{C\omega^3}\right) = \ln(A(\hbar\omega)) - \left(\frac{\hbar\omega - \mu}{k_B T}\right). \tag{5.4}$$

For energies sufficiently higher than the band gap we can assume that all photons are absorbed i.e. $A(\hbar\omega) \approx 1$ [169]. With this assumption the absorptivity term in equation (5.4) vanishes and the high energy slope of the measured PL spectrum can be described by the remaining Bose term containing the quasi-Fermi level and the temperature. Figure 5.2 illustrates a fit of the Bose term to the high energy slope of the spectrum. The slope of the line is, according to equation (5.4), determined by the sample temperature. For locations on the sample with different μ this line will be parallel shifted and the differences of quasi-Fermi level splitting can be quantified.
In order to extract the lateral variation of μ it is useful to label one location with index i and another location on the sample j. The quasi-Fermi level splitting in location i is according to equation (5.4) given by

$$\mu_i = \ln\left(\frac{I_{PL,i}(E^*)}{C\omega^3}\right) k_B T + \hbar\omega, \tag{5.5}$$

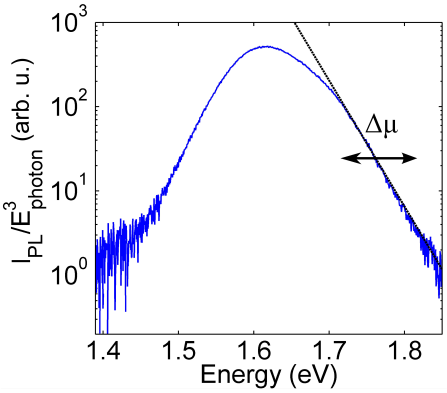

Figure 5.2: Example of a PL measurement of an epitaxial $CuGaSe_2$ sample at room temperature. The temperature is determined by fitting the slope of the high energy tail, and the variations in quasi-Fermi level splitting are determined from the shift of the line.

where E^* is an energy sufficiently high above the band gap where $A(\hbar\omega) \approx 1$ can be assumed to be valid. As mentioned earlier it is not possible to determine the absolute value of μ without calibrating the setup [170]. It is however possible to measure variation of μ since C cancels out when calculating the difference of μ between location i and location j [165]:

$$\Delta\mu = \mu_i - \mu_j = \left[\ln\left(\frac{I_{PL,i}(E^*)}{C\omega^3}\right) k_B T + \hbar\omega\right] - \left[\ln\left(\frac{I_{PL,j}(E^*)}{C\omega^3}\right) k_B T + \hbar\omega\right] \quad (5.6)$$

$$= \ln\left(\frac{I_{PL,i}(E^*)}{I_{PL,j}(E^*)}\right) k_B T \quad (5.7)$$

This idea can be directly applied to map the local variations in μ, assuming that C, T are constant and that $A(\hbar\omega) \approx 1$ throughout the scan area.

5.1.2 Spatial Variation of the Absorptivity Edge

Once the temperature and local variation of quasi–Fermi level splitting $\Delta\mu$ have been extracted by analysis of the high energy slope of the PL spectrum it is possible to evaluate the local absorptivity spectrum $A(\hbar\omega)$ [171].
Following the evaluation in the previous section the Bose term responsible for the shape of the high energy slope can be determined. The Bose term bt can be expressed as

$$bt = -\frac{\hbar\omega - \mu}{k_B T} \quad (5.8)$$

With introduction of this term equation (5.4) can be written in the form

$$\ln(A(\hbar\omega)) = \ln\left(\frac{I_{PL}}{C\omega^3}\right) - bt \quad (5.9)$$

Once the Bose term is known from analysis of energies higher than the band gap, the shape of the absorptivity edge at lower energies can be evaluated using equation (5.9).
Figure 5.3 shows the absorbance curve extracted using this approach from the PL measurement shown in figure 5.2. A curve similar to this one can be extracted from each measured spectrum in a μ–PL scan.

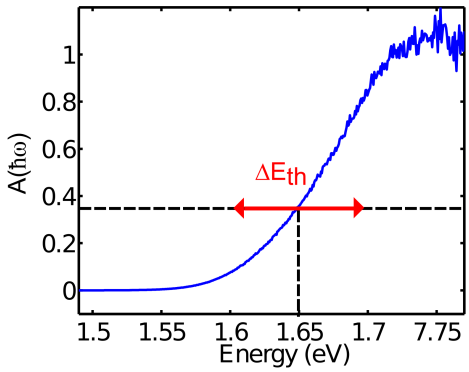

Figure 5.3: Example of an absorbance spectrum extracted from the photoluminescene spectrum shown in figure 5.2. The optical treshold E_{th} is here defined as the energy where $A(\hbar\omega) = e^{-1}$. Variation of E_{th} can be observed when this energy changes from point to point on the sample.

By analysis of the absorptivity edge it is now possible to extract information about lateral band gap variation in a μ–PL map. One approach to achieve this, is to define a threshold of the absorptivity, which corresponds to the band gap. In this work an optical threshold E_{th} is defined as the energy where the absorptivity spectrum has the value e^{-1}. This value can, in principle, be chosen arbitrarily, but one should avoid defining a too low threshold value in order to avoid a strong influence of Urbach tails on the threshold energy. The threshold energy obtained by this approach is illustrated in figure 5.3. If the absorptivity edge shifts from one spectrum to another in a μ–PL measurement this gives rise to variation of the obtained optical threshold. Such variations can be interpreted as band gap variations even though the optical threshold energy is not the same as the band gap. One can instead think of the threshold energy as a pseudo band gap that is related to the real band gap of the material via $E_{th} = E_g + E^c$. If one assumes that the term E^c is simply a constant, one can directly investigate variations in the band gap with this approach. In this case the variations of the threshold and the band gap are equal $\Delta E_{th} = \Delta E_g$ [165]. This approach will be used to evaluate band gap variations in absorbers.

5.1.3 Simulation of Spectral Changes

Both local changes in the band gap ΔE_g and variations on the local quasi–Fermi level splitting $\Delta\mu$ affect the photoluminescence spectrum. Variation of both therefore also affect the photoluminescence intensity obtained by spectrally integrating the peak. In order to understand the separate effect of each of these, a simulation will be presented in the following.
To calculate the PL peak shape from equation (5.3), it is necessary to assume an absorptivity spectrum for the sample. In this example this will be done by assuming an absorption coefficient α for a direct semiconductor [63] described by:

$$\alpha(\hbar\omega) = A^* \sqrt{\hbar\omega - E_g}, \tag{5.10}$$

where a pre–factor of $A^* = 10^5\ \mathrm{cm}^{-1}\mathrm{eV}^{-1/2}$, and a band gap of $E_g = 1.65$ eV are assumed. With this absorption coefficient the absorptivity curve is determined according to the relationship [63]:

$$A(\hbar\omega) = 1 - e^{-\alpha(\hbar\omega)d}, \tag{5.11}$$

where a layer thickness $d = 800$ nm has been assumed. By inserting this absorptivity spectrum into equation (5.2) the spectral shape of the expected PL peak $I_{PL}(\hbar\omega)$, can be simulated. In the following it will be assumed that the material has a temperature of $T = 300$ K. With these parameters changes in PL spectrum due to variation of E_g and μ can be simulated, as illustrated in figure 5.4.

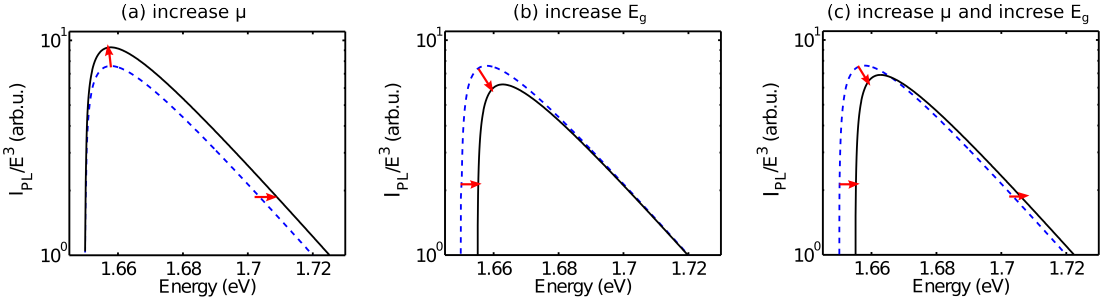

Figure 5.4: Simulation of the effect of variation of μ and E_g on the photoluminescence spectrum. (a) Increase of μ leads to a higher integrated photoluminescence intensity. (b) An increase of the band gap leads to a lower integrated photoluminescence intensity. (c) When both μ and E_g change simultaneously the PL intensity can either increase or decrease. In this case a decrease in PL intensity is seen due to an increase of μ and an increase of E_g.

Figure 5.4(a) shows the effect of increasing the quasi–Fermi level splitting while keeping the band gap constant. The increase of μ leads, as expected, directly to an increase of the integrated PL intensity. Figure 5.4(b) shows another case, where the band gap is increased while μ is kept constant. Experimentally this could e.g. happen due to release of strain in a $CuGaSe_2$ layer. In this case it is observed that the integrated PL intensity decreases. It is now interesting to investigate the effect of simultaneous variation of both μ and E_g. An example of this situation is illustrated in figure 5.4(c). Here it is assumed that the both band gap and the quasi–Fermi level splitting are increased. In this particular example this results in a decrease of the integrated PL intensity. One could of course also imagine a case where the balance of the two effects is different leading to an increase of the PL intensity.

This example clearly illustrates that the PL intensity not only depends on the quasi–Fermi level splitting as one would often assume. In cases where the band gap varies, it is necessary to evaluate the changes with the approach described in the previous sections in order to separate the two effects [165].

In case the band gap does not vary spatially one will observe that I_{PL} and μ are highly spatially correlated. In this case it is possible to extract information about the local optoelectronic properties of the material based on only the integrated PL intensity. The measured PL intensity is, under the assumption of constant E_g, proportional to the excess minority charge carrier concentration $I_{PL} \propto n$ [146]. An increase of n in some areas of the sample compared to other areas under the same excitation conditions can be related to different local recombination lifetimes. It is expected that material where a higher n or μ is obtained is of better optoelectronic quality. This is due to less pronounced non–radiative recombination via bulk or surface defects. By studying spatial variations in μ it is therefore possible to identify areas of the absorber with properties that are potentially better for solar cell applications.

5.1.4 The Cross–Correlation Coefficient

When variations of local material properties such as presence of excitons, DAP transitions or band gap variations are observed it is often interesting to be able to determine whether the effects are correlated to each other or not. Determination of degree of correlation often aids to identify and understand the observed effects. The cross correlation between maps showing different properties can be expressed as a single number C_c. The cross correlation $C_c(A,B)$ between two maps represented by matrices $A(i,j)$ and $B(i,j)$ is expressed as

$$C_c(A,B) = \frac{1}{n}\sum_{i,j}\frac{\left(A(i,j)-\overline{A(i,j)}\right)\left(B(i,j)-\overline{B(i,j)}\right)}{\sigma(A(i,j))\sigma(B(i,j))}, \tag{5.12}$$

where n is the number of pixels in each matrix, $\overline{A(i,j)}$ is the mean value of the matrix, and $\sigma(A(i,j))$ is the standard deviation of the matrix. The correlation C_c can vary between 1 for totally correlated maps and -1 for totally anti–correlated maps. If values in the range $-0.3 < C_c < 0.3$ are found, it can be argued that the maps are uncorrelated [172].

5.2 Review: Inhomogeneities in Chalcopyrite Absorbers

The approach presented in the previous sections has been utilized to analyse PL measurements in several investigations. An overview of some of the results of these studies will be given in the following.

Many types of inhomogeneities have been found in Cu(In,Ga)Se_2. Often these effects are associated with effects observed in polycrystalline materials. Examples of inhomogeneities that have been investigated with different techniques include: composition variation studied by micro–spot X–ray photoelectron spectroscopy [173], morphology and variation in the defect chemistry studied by spatially resolved PL and atomic force microscopy [174], open circuit voltage studied by an electron beam induced voltage technique [175], chemical fluctuations investigated by transmission electron microscopy and x–ray energy-dispersive spectroscopy [176], electronic surface properties studied by scanning tunnelling spectroscopy [177].

The diversity of these studies makes it impossible to cover all of them here. Instead this section will be limited to the results of spatially resolved μ–PL studies of inhomogeneities in Cu(In,Ga)Se_2 and the theoretical effect of these inhomogeneities on solar cell performance. Effects that have been experimentally investigated with this technique include band gap fluctuations due to alloying (composition) or strain inhomogeneities [11, 166, 169, 178], variations of quasi–Fermi level splitting e.g. [12, 11, 166], and defect concentrations [19, 178].

The influence of band gap fluctuations have been investigated from a theoretical point of view [16, 179]. The change in power conversion efficiency has been investigated based on an idealized system, where all light above the band gap is absorbed and all photo–generated charge carriers are collected. The only loss in this ideal system is due to spontaneous radiative recombination [179]. Since the light emission in the material depends on the light absorption, as discussed in section 5.1.1, variation of the band gap influences the loss due to light emission. Based on the assumption of a Gaussian distribution of band gaps the efficiency loss is calculated. The calculation shows that band gap fluctuations degrade the maximum achievable efficiency. A reduction of the solar cell efficiency

by 1.7 % (absolute) was found for band gap fluctuations with a standard deviation of σ_{E_g} =50 meV [179]. It should, however, be kept in mind that the magnitude of the variations assumed in the evaluation are rather large compared to experimentally determined band gap variations. Studies of polycrystalline Cu(In,Ga)Se_2 absorbers have revealed band gap distributions ΔE_g with a $\Delta_{FWHM}(E_g)$ of 5 – 13 eV [11, 166]. Assuming these are Gaussian distributions the relationship $2.35\sigma_{E_g} \approx \Delta_{FWHM}(E_g)$ applies. The actual effects of band gap fluctuations on device performance will therefore be limited [9].
Though the theoretical studies indicate a deteriorating influence of absorber inhomogeneities on solar cell parameters, the experimental evidence is missing. This further supports that band gap fluctuations in the 5 – 13 eV range do not significantly reduce the device performance. A μ–PL study of the band gap and quasi–Fermi level distributions of material used in polycrystalline Cu(In,Ga)Se_2 solar cells with high efficiencies in the range 15–18 % has been performed [166] to investigate a relationship to device performance. The result, surprisingly, showed a tendency of higher V_{oc} with increasing inhomogeneities. One possible reason for this behaviour could be that more regions with better properties than average could exist in the more inhomogeneous samples [166].
Inhomogeneities on various length scales have been reported in spatially resolved PL studies. Variations on a length scale smaller than the size of the grains have been found by scanning near field optical microscopy [11]. With this high resolution approach structures with sizes in the range 0.2–1.5 μm could be observed in the recorded PL signal. In spatially resolved PL studies with a lower resolution of $\approx$ 0.8μm, larger structures ranging from the resolution limit to the 3–5 μm [169] scale and even up to the 3–10 μm scale [164, 180] have been observed. This clearly shows that non–uniformities on various length scales exist. The variations are not related to individual grains but exist inside individual grains [11] and stretch across several grains [164, 169].
The approach described in the previous section has been applied in numerous studies to examine the spatial variations of band gaps and quasi–Fermi level splitting from μ–PL measurements e.g. [164, 166, 169, 180, 181]. Most of these studies focus on polycrystalline Cu(In,Ga)Se_2. Here investigations of the quasi–Fermi level splitting found variations in the range $\Delta_{FWHM}(\Delta\mu) \approx$ 8–18 meV [166], 10–30 meV [12], 18 meV [11]. It has to be mentioned here that it has been shown that $\Delta_{FWHM}(\Delta\mu)$ is strongly dependent on the experimental conditions. It was found that $\Delta_{FWHM}(\Delta\mu)$ is increasing with increasing temperature, but decreasing with increasing excitation density [12, 164].
The influence of the surface topography on the structures measured in PL have been commented on in several cases. Generally it is found that there is only a very weak influence of the surface topography and the grain structure on the effects observed in PL [11, 164, 182].
The results summarized here demonstrate some effects that must be kept in mind when analysing the experimental results in the following sections. Most studies discussed here, however, focus on polycrystalline Cu(In,Ga)Se_2, where the effects of both grains and alloying contribute to the results. It is therefore interesting to investigate inhomogeneities in the absence of these effects. The studies presented in the following focus on epitaxial $CuGaSe_2$, where both these effects can be excluded.

5.3 Experimental Setup for Spatially Resolved Photoluminescence

Spatially resolved PL measurements are performed with a home built setup constructed for this work. The spatial resolution is obtained by scanning a laser beam across the sample while detecting the PL with confocal optics. The setup used for spatially resolved μ–PL measurements has many similarities with the setup described in section 4.4. The same Ar^+ laser is used in both experiments, and the detection system is also identical for both setups. The main differences between the two setups will be pointed out in the following.
A microscope lens with a high numerical aperture (NA) of 0.65 with a long working distance of 13 mm is used for the spatially resolved measurements. Based on the numerical aperture, the spot size can be estimated as the first minimum of the Airy disc: $r_1 \approx 1.22\lambda\frac{f}{D} \approx 1.22\lambda\frac{1}{2NA}$. For the laser wavelength of 514.5 nm a spot size with a diameter of ≈ 0.9 μm can be estimated. This defines the maximum resolution that can be obtained by the method.

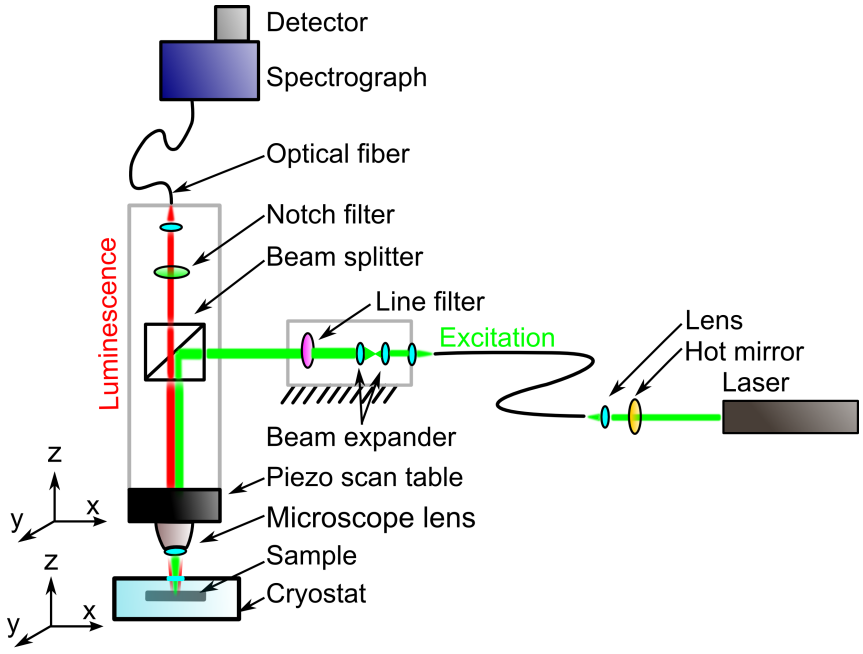

Figure 5.5: Experimental setup used to measure laterally resolved PL maps of sample surfaces with micrometer resolution.

Figure 5.5 shows the setup constructed for μ–PL experiments. The optics is separated in two parts. The first part that is stationary collects the laser light from the fiber and directs it onto a beam splitter placed in the movable second part of the optics. In the stationary optics the beam is first made parallel when emerging from the fiber by a lens. The beam is widened in order to take advantage of the full aperture of the microscope lens. This is achieved using two lenses with different focal lengths. By placing the long focal length lens in the beam after the short-focal length lens in the way that the focal points of the two co-inside the beam is widened while staying parallel. The line filter is placed in the parallel beam after passing the laser light through the fiber, since it was observed that fluorescence from the fiber gives rise to artefacts in the measurements.
The spatial resolution is achieved by placing the collection optics in a tower on a piezo-

electric table. In this way the collection optics can then be moved in three directions x, y, z with very high precision. Resolution of the piezoelectric table is according to the manufacturer less than 1 nm [183], which is much lower than the resolution of the optics. The movable tower contains a beam splitter that directs the laser beam from the stationary optics into the microscope lens. The use of the beam splitter allows the luminescence collected by the same microscope lens to pass to the detection system. A notch filter is placed in the beam path after the beam splitter, but before a lens that is responsible for focusing the luminescence onto the optical fiber that brings the luminescence to the spectrograph.
A cryostat containing the sample is placed on a x, y, z–stage under the tower containing the microscope lens. When performing measurements the coarse adjustment of the focus and the position of the sample is performed by moving the cryostat on the x, y, z–stage. Once the sample is in position the fine focus can be adjusted by varing the z–axis in small steps $< 1\mu$m of the piezoelectric table. When perfect focus is found the outgoing laser beam reflected from the sample surface will be perfectly parallel. After making sure that this is the case, the scan in the (x, y) plane can be started. The range of the piezoelectric table allows for scans up to $80 \cdot 80$ μm^2. Typically smaller scans are measured with a size of $25 \cdot 25$ μm^2 and $80 \cdot 80$ pixels. Results presented in this section have been measured with different excitation densities. Typically excitation densities are in the order $\approx 10^{22} - 10^{23}$ cm^{-2}s^{-1}.
When the spatially resolved measurements are performed a complete spectrum is recorded for each pixel of the scan. This allows for analysis of spectral changes between regions of the film with micrometer resolution. All the samples studied in this chapter have been etched in 5 % KCN for 2 minutes prior to μ–PL investigations in order to remove the secondary Cu_xSe phase [184], unless something else is stated.

5.4 Spatially Resolved Defect Spectroscopy

The remaining sections of this chapter contains the results and discussion of the μ–PL investigations performed in this work. This is divided into two main parts. The first topic discussed in this section deals with spatial variations of defects. The second part in section 5.5 is focused on the results obtained by evaluation of $\Delta\mu$ and ΔE_g.

5.4.1 Donor Acceptor Pair Recombination or Phonon Replica

This section deals with effects observed in low temperature μ–PL experiments. This includes a discussion of several observations made during the measurements. Further discussions of the effect of the excitation flux are collected in appendix B.
A model explaining the DAP transitions observed in low temperature PL measurements on $CuGaSe_2$ and $CuInSe_2$ was introduced in section 2.3.8. In this model a DAP transition referred to as DA3 is introduced. It was argued that the transition with an energy around 1.58 eV in $CuGaSe_2$ is due to a third DAP transition and not a phonon replica of the DA2 transition as previously assumed. This conclusion was reached by realization that the 1.58 eV peak was spatially independent of the DA2 peak in cathodoluminescence studies [91]. This section will partly confirm this conclusion with μ–PL studies, but it will also be demonstrated that the peak observed at 1.58 eV can not always unambiguously be ascribed to the DA3 recombination.

Two slightly different samples both showing an identifiable DA3 transition will be discussed. This will be compared to a sample where a DA3 transition cannot be unequivocally identified.

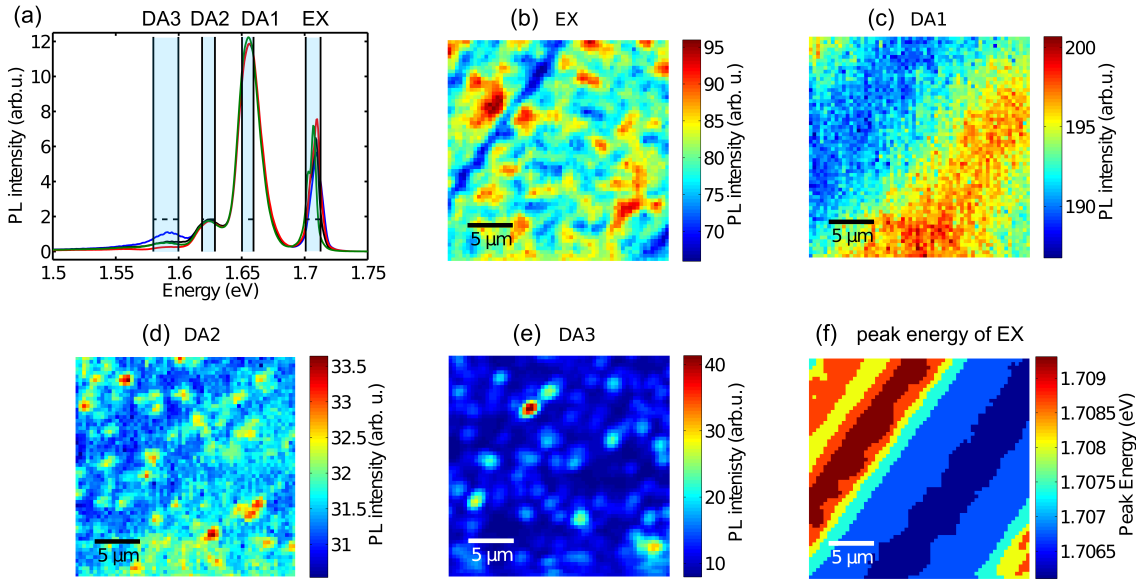

Figure 5.6: Example of a spatially independent DA3 transition. (a) Local spectra and indication of regions of evaluation. (b) Map of the integrated PL intensity of the excitonic region. Similar maps integrated over (c) the DA1 region, (d) the DA2, (e) the DA3. (f) the energy of the peak in the excitonic region.

Figure 5.6 shows the result of a μ–PL measurement of a $CuGaSe_2$ layer with a composition close to stoichiometry on the Cu–rich side measured with a photon flux of $\approx 10^{23}$ $s^{-1}cm^{-2}$. A map showing the PL intensity spectrally integrated over each peak is shown. In this sample it is observed that all peaks are essentially uncorrelated. This is also illustrated in the correlation coefficients shown in table 5.1.

Figure 5.6(a) shows examples of local 10 K PL spectra from the analysed area. Two properties of the spectrum should be noticed. First it is seen that the spectrum is dominated by a strong DA1 peak and a less dominant DA2 peak. Secondly it is recognised that strong excitonic recombination is observed. These two features are found in all measured samples where an independent DA3 transition could be observed.

The excitonic region in figure 5.6(b) show randomly appearing brighter areas appearing like a network structure. A line of low intensity can be identified in the upper left corner of the map and another very short line is seen in the lower right corner. This can be explained by the presence of cracks in the layer. This is confirmed by the map of the exciton peak energy. The peak shifts locally to higher energies along the crack as seen in figure 5.6(f). This is due to strain release as discussed in section 5.5.1.

The map of the DA1 peak is shown in figure 5.6(c). It is noticed that no well defined structure is observed for this peak. In this case the peak intensity instead seems to be correlated with the presence of the cracks. For this sample the DA1 peak has higher intensity in the area far away from the cracks and lower intensity near the cracks. It should, however, be mentioned that in a similar sample it has been observed that the DA1 peak increased in intensity along the crack (see figure 5.7). The reason for the different behaviour of the peak intensity along the crack remains unclear. One could speculate that it is related to different geometry of the cracks. If the cracks have different crystal

orientation, it could possibly influence the PL.
Figure 5.6(d) shows a PL intensity map of the DA2 peak. Here it can be seen that the DA2 appears locally stronger in dots with a size around 2 μm. The dots are only slightly brighter than the surrounding giving rise to around 1.05 times higher luminescence. Since the variation is so slight the image appears rather noisy. The appearance of such dots could be related to the locally increased [Cu]/[Ga] ratio due to Cu_xSe crystallites as discussed in details in section 5.5.2.
Figure 5.6(e) finally shows the PL intensity map of the DA3 peak. This peak is the weakest in the spectrum. It is, however, possible to observe strong local variations in its intensity. Also this peak appears as dots with high intensity. Unlike the DA2 peak the dots in the DA3 map are a lot stronger than the surroundings by a factor between 2 and 4. By careful study of the spatial distribution of the bright spots it is realized that the DA1, DA2 and DA3 peaks are spatially independent. This is in agreement with the CL study that concluded that the 1.58 eV peak is a third DAP transition [91].
The fact that the DA3 peak is uncorrelated to the other peaks is also reflected in the correlation coefficients collected in table 5.1. A very weak correlation below 0.3 is observed between the maps for all regions except between DA1 and DA2. This value is, however, misleading since the DA2 peak shows a spatial structure whereas the DA1 is more smoothly distributed showing only a gradient due to the crack.

	EX	DA1	DA2	DA3
EX	1	0.16	0.03	-0.25
DA1	0.16	1	0.57	-0.02
DA2	0.03	0.57	1	0.3
DA3	-0.25	-0.02	0.3	1

Table 5.1: Cross–correlation coefficients C_c of the maps shown in figure 5.6.

Another μ–PL measurement is included here in order to show that the slightly different correlations can be obtained from otherwise similar samples.
Figure 5.7 shows a μ–PL measurement on a sample similar to the one discussed in the beginning of the section. This sample measured at 10 K with a photon flux of $\approx 10^{21}$ $s^{-1}cm^{-2}$ shows a strong exciton and DA1 transition, just like the sample discussed previously. This spectrum interestingly also shows another peak around 1.56 eV, that has been observed in various other samples (see also appendix B).
The PL intensity maps are generally similar to the ones shown in figure 5.6 discussed in the beginning of this section. Some differences should, however, be pointed out.
The intensity map the exciton region shown in figure 5.7(b), shows a detailed pattern with structure sizes close to the resolution limit. The length scale of these structures is smaller than the variations observed in figure 5.6. Larger variations on a longer length scale of 5–10 μm are additionally observed with higher intensity in the lower part of the scan area than in the upper part. One possible explanation for the different size of the structures appearing in the two measurements is that the resolution decreases with increasing excitation as discussed in appendix B. Since different excitations were used for the measurement in figure 5.7 and figure 5.6 this could be a part of the reason for the observed difference.
Figure 5.7(c) shows that the DA1 transition is, like the DA1 in figure 5.6, structureless except for the influence of a crack that stretches from the lower left corner to the right

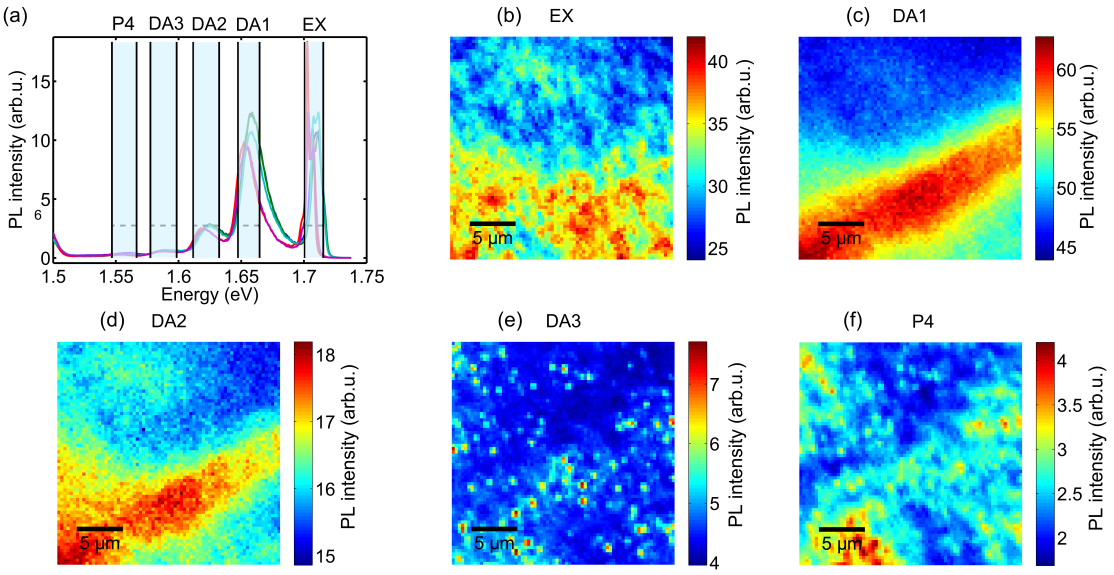

Figure 5.7: An example of a spatially independent DA3 transition. (a) Local spectra and indication of regions of evaluation. (b) Map of the integrated PL intensity of the excitonic region. Similar maps integrated over (c) the DA1 region, (d) the DA2, (e) the DA3. (f) The region labelled P4.

edge of the map. In this case the crack gives rise to increased PL intensity compared to the surrounding layer. This is accompanied by a blue–shift as visible by comparison of the high intensity peaks in the DA1 region to the peaks with lower intensity (figure 5.7(a)). The fact that the intensity of the DA1 increases along the crack in this sample, whereas it decreases for the sample shown in figure 5.6 is not easy to explain. It could possibly be related to the geometry around the crack and the width of the crack. This could influence the way light is scattered.

The intensity map of the DA2 transition shown in figure 5.7(c), does, unlike the sample in figure 5.6, not show the spotty structure. In this case the DA2 is also dominated by the appearance of the crack. It is seen that the intensity variations induced by the crack vary by a factor of 1.2 from the darkest to the brightest areas. This is higher than the very weak variations with a factor of only 1.05 between the bright spots and the darker areas seen in the DA2 map in figure 5.6. One can therefore speculate whether the spotty structure is simply hidden due to the stronger effect of the crack.

Figure 5.7(e) shows the spatial variation of the PL intensity integrated over the DA3 peak. Again it is clearly seen that the DA3 peak is spatially independent of the other peaks observed in the spectrum. It appears in randomly distributed bright dots. The main difference in the DA3 region between the result presented in figure 5.6 and figure 5.7 is that the bright dots appear smaller in the latter. The size of the bright spots observed here is around the resolution limit of 0.9 μm. This difference could be related to the focus of the optics. In this case the focus is clearly perfect, since structures with the smallest measurable size are seen. It can not be similarly be concluded that the measurement shown in figure 5.6 is not perfectly focused. It is for example possible that the size of the structures are different due to slightly different growth conditions. Another, probably more likely explanation for this difference is the influence of the excitation density as discussed in appendix B.

The final map in figure 5.7(f) shows the map of the weak peak labelled P4 in figure 5.7(a).

This peak is spatially highly correlated to the DA3 transition with $C_c(P4, DA3) = 0.7$. It can therefore be proposed that this peak is a phonon replica of the DA3. The energy of the P4 peak is $\approx$ 32 meV lower than the DA3. This is very close to 34 meV, the highest energy LO phonon reported in literature [112, 185].
Though several samples have shown spatially independent DA3 recombination as demonstrated with these two examples, not all samples show this tendency. An example will be discussed in the following.

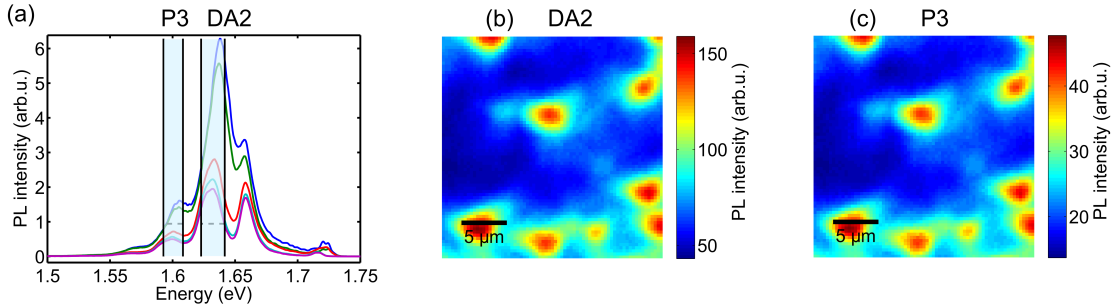

Figure 5.8: (a) Spectra measured locally in the mapped area. (b) Map of PL intensity spectrally integrated over the DA2 region. (c) Map of PL intensity spectrally integrated over the region labelled P3.

Figure 5.8 shows the result of a μ–PL study of a Cu–rich epitaxial layer measured at 10 K with a photon flux of $\approx 10^{21}$ $s^{-1}cm^{-2}$. The intensity maps extracted from each peak of this measurement turned out to be highly correlated. Not all maps are shown since the correlation coefficient was found to be $C_c = 0.7 - 0.95$ between all the maps extracted by spectrally integrating each peak. Because of high similarity of all the maps only two are shown. These show the spatial distribution of the DA2 peak and the peak previously attributed to DA3 recombination, but here labelled P3.
Even though all peaks are highly correlated it is noticed that the DA2 increases stronger than the DA1 at the locations where both are high. These locations correspond to the bright dots in figure 5.8(b). The strong local increase of at these locations can be explained as an effect of Cu_xSe crystals as discussed in section 5.5.2. By inspection of the peak positions of the spectra it is noticed that all peaks are shifted to higher energies compared to the other two samples discussed in this section (see figure 5.6 and figure 5.7). This behaviour can be explained by lower strain in the sample shown in figure 5.8. An argument that is supported by the fact that no cracks are observed in this sample.
Figure 5.8(b) shows the spatial variation of the DA2 peak. It is immediately recognized that the spatial variation of this peak is highly correlated to the peak labelled P3 in figure 5.8(c) with a correlation coefficeint $C_c(DA2, P3) = 0.94$. This peak correspond to the one that has been assigned to the DA3 transition. In this case the peak is, however, spatially correlated to the all other peaks. In this case it is therefore not possible to unambiguously identify it as being a third DAP transition.
The energy of the peak labelled P3 is $\approx$33 meV lower than the DA2 peak, and another shoulder is observed with an energy $\approx$66 meV lower than the DA2 peak. This could be an indication that these two peaks could also be due to phonon replicas involving a phonon with an energy of 33 meV, very close to 34 meV reported in literature [112, 185].
It can therefore not be excluded that the peak sometimes referred to as the DA3 peak can in fact be due to phonon replica of the DA2 peak. It is likely that the peak is in fact composed of a mixture of the DA3 and a phonon replica of the DA2 peak in many cases. Based on the experiences made in this work, it is, only possible to observe the

spatially independent DA3 transitions in samples where the DA2 peak is not dominating. This could be related to the formation of Cu_xSe when growing more Cu–rich. When the Cu_xSe form on the surface this has a strong effect on the underlying absorber properties (see section 5.5.2). Based on the measurement shown in figure 5.8 it seems that this effect shows up more strongly than a spatially varying DA3 transition.
One can also wonder if the high correlation is an effect of the analysis approach. In figure 5.8(a) it can be seen that the DA2 tail clearly affects the P3 peak. A more sophisticated analysis, where each spectrum is fitted with several Gaussians was tested to remove this effect. The result obtained with this method was, however, practically identical to the one shown in figure 5.8.

5.4.2 Spatial Variation of Deep Defects

In addition to the well known peaks discussed in the previous section a low energy broad luminescence peak was found in PL measurements. This section will deal with the spatial variation of this low energy luminescence peak that is related to defects much deeper in the band gap than the DAP transitions previously discussed. Measurements on two different samples are shown here. The first measurement is performed at 10 K on a slightly Cu–rich absorber (figure 5.9(a-c)) and the second measurement is performed at room temperature on a sample with a composition very close to the stoichiometric point (figure 5.9(d-f)). These two measurements are shown here to demonstrate that the deep defects can be observed in both high and low temperature and for samples with different composition. It should be mentioned that the deep defect luminescence peak discussed in this section is extremely weak if even observable in the vast majority of the samples measured in this work. The samples investigated here are special in the sense that they display an unusually strong deep defect luminescence.
Figure 5.9(a) shows the local spectra measured in the positions indicated in figure 5.9(b) by circles. The measurement is performed on a slightly Cu–rich $CuGaSe_2$ epitaxial layer at 10 K. Only the exciton luminescence and the deep luminescence peak (DP) are labelled. Several DAP transitions and phonon replicas of these are also observed in the spectrum. The large peak around 1.49 eV is due to the GaAs substrate.
Figure 5.9(b) shows the intensity map of the excitonic region (EX) and figure 5.9(c) shows the intensity map of the DP region. When leaving maps of the other peaks out it is needed to add one comment. One could wonder if the strong GaAs peak could influence the map extracted in the DP region, where a much weaker broad peak is seen. A very small correlation coefficient of $C_c(GaAs, DP) = -0.18$ obtained between the GaAs peak and the DP peak, however, clearly demonstrates that this is not the case.
When comparing the intensity maps of the EX and DP peaks it is clear that there is a strong anti–correlation. The exciton is strong when the DP peak is weak and vice versa. This tendency is very pronounced in the entire studied area. The strong anti–correlation is also manifested in a correlation coefficient between the maps of $C_c(EX, DP) = -0.8$.
Strong excitonic recombination is, as previously mentioned, often interpreted as a sign of good material quality. Recombination via deep defects is, on the other hand, usually a sign of lower quality. The deep peak observed here can be ascribed to defect states deep inside the band gap, states that are deleterious to the material. The fact that the intensity of these two peaks are spatially anti–correlated in this experiment is therefore in agreement with the expectation.
In the following it will be demonstrated that the deep luminescence peak is not a phe-

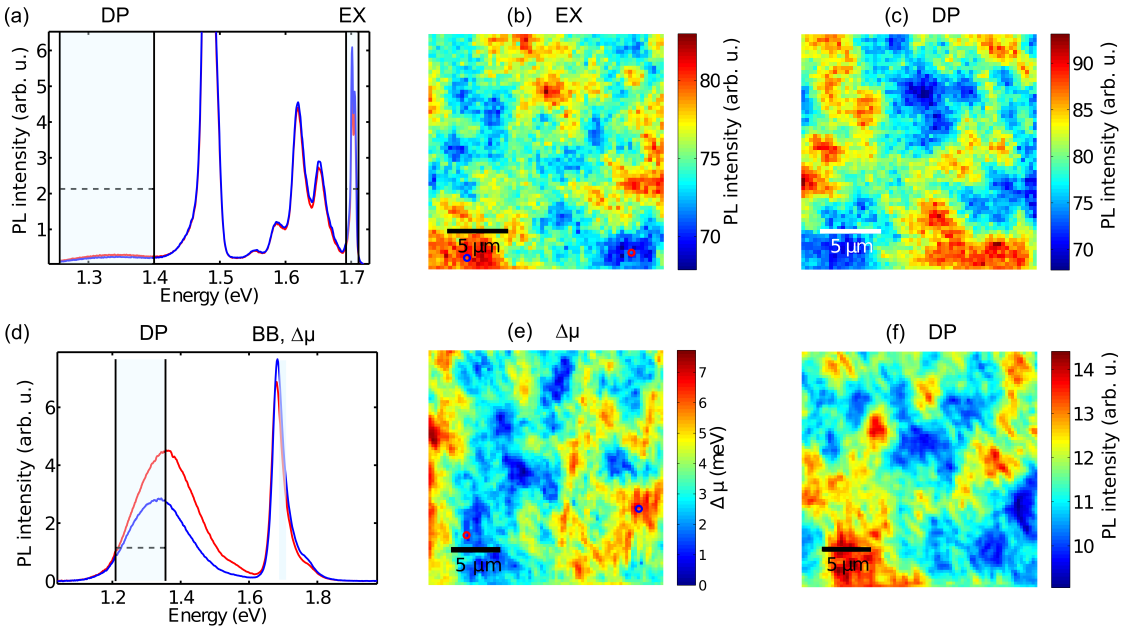

Figure 5.9: (a) 10 K PL spectra measured on a slightly Cu–rich $CuGaSe_2$ absorber at the positions indicated with circles in (b). The spectra are color coded according to the position where it is measured. (b) PL intensity map obtained by spectrally integrating the EX region. (c) PL intensity map of the DP region. (d) A $CuGaSe_2$ absorber with stoichiometric composition measured at room temperature. (e) Map of the $\Delta\mu$ variation extracted from the band–to–band luminescence. (f) Map of the PL intensity integrated over the DP region.

nomenon only observed in one sample. Another sample with a composition close to the stoichiometric point is studied for this purpose. The measurement, furthermore, has the purpose of demonstrating that the effect can be observed at room temperature.
Figure 5.9(d) shows two local PL spectra measured at room temperature in two locations indicated in figure 5.9(e). The strongest peak is in both cases due to band–to–band recombination (BB). By inspection of the spectra it is noticed that the DP peak is higher in the red curve than the blue curve. For the BB transistion the situation is reversed and the peak is stronger in the blue curve than in the red one. This clearly indicates an anti–correlation between the peaks at these two points. A similar anti–correlation of $\Delta\mu$ can be found throughout most of the mapped area. This is illustrated in figure 5.9(e) and 5.9(f).
Figure 5.9(e) shows a map of the spatial variation of the quasi–Fermi level splitting $\Delta\mu$. This map is obtained by fitting the high energy slope of the BB peak as described in section 5.1.1. The amount of quasi–Fermi level splitting can, as previously mentioned, be related to the quality of the absorber. A local high quasi–Fermi level splitting might be related to a local lower density of defect states through which the excited charge carriers can recombine (see discussion in section 5.5.2).
The map showing the spatial variation of the DP luminescence is obtained by integration over the low energy part of the DP peak indicated in figure 5.9(d). The high energy part of the peak is not included in the integral since this part contains a contribution from the GaAs substrate (seen as a weak shoulder in figure 5.9(d)). When comparing the $\Delta\mu$ map to the DP map, one will notice some degree of anti–correlation. This is also reflected in the correlation coefficient of $C_c(\Delta\mu, DP) = -0.6$ between the two maps. Even though the anti–correlation is less strong in this case, the result shows the same tendency demonstrated in the low temperature PL measurement in figure 5.9(a-c).

One possible explanation for the observed behaviour is, in analogy with the previous discussion, that the density of deep DP defects varies spatially. When the defect density is locally high this results in a decreased $\Delta\mu$. These deep defects would be deleterious to the performance of a cell made from this material, since the local decrease of $\Delta\mu$ would in turn lead to a lower achievable V_{oc}. A similar result has been obtained in a study of the spatial variation of the quasi–Fermi level splitting in $CuInS_2$ [181]. A luminescence peak due to deep defects with an energy around 1.3 eV has similarly been observed in earlier studies of $CuGaSe_2$ [106]. In [106] it was found that this peak is present in both polycrystalline material and single crystals and decreases significantly in intensity when the Ga content is increased. It is proposed that intrinsic defects in $CuGaSe_2$ are responsible for the deep defect luminescence [106]. Since this peak appears in material grown by chemical vapor transport (single crystals), physical vapor deposition (polycrystalline) and here by MOVPE (epitaxial) it seems plausible that intrinsic defects is the cause of this deep defect luminescence.

5.5 Spatial Variations of μ and E_g

This section deals with the spatial variations of the optoelectronic quality of the excited state. The discussion is based on an evaluation of $\Delta\mu$ and ΔE_g from room temperature PL measurements.

5.5.1 Spatial Variations due to Strain and Cracks in Epitaxial Layers

When growing $CuGaSe_2$ epitaxially on GaAs strain builds up in the layer during cool down due to different thermal expansion coefficients as discussed in section 2.2. If the strain in the layer exceeds a critical level cracks develop in the layer. Cracks and strain in the layer are investigated in this section. This is interesting since the inhomogeneities observed due to strain variation around cracks will also be present in polycrystalline layers where the different grains strain each other because of their different orientations. Here samples exhibiting cracks have been investigated by μ–PL, CL and XRD. A description of the CL and XRD techniques is included in appendix D. Similar results regarding strain near cracks have been obtained studying both Cu–poor and Cu–rich absorbers. In this section results are exemplarily shown for a Cu–poor sample with μ–PL and a Cu–rich sample with CL.
Figure 5.10 shows the room temperature μ–PL study of a Cu–poor $CuGaSe_2$ layer. A SEM micrograph of the sample surface under investigation is shown in figure 5.10(a). Please note that the μ–PL scan of this sample is not performed at exactly the same position as the SEM micrograph. The micrograph is merely included here to show the surface morphology. Figure 5.10(a) shows that the layer is rather smooth except for cracks in the layer appearing as dark straight lines. These cracks have been investigated by SEM cross section and TEM measurements and mostly extend from the surface down to the $CuGaSe_2$/GaAs interface. From SEM images it has been observed that the cracks in the layer in some cases continues into Cu_xSe crystals. This indicates that the cracks develop during cool down.
Figure 5.10(b) shows a map of the spectrally integrated PL measured at room temperature. The sample exhibits variations of the measured PL intensity by a factor of $I_{PL,max}/I_{PL,min} \approx 2.2$. Two different regimes of intensity can be identified: A high intensity area,

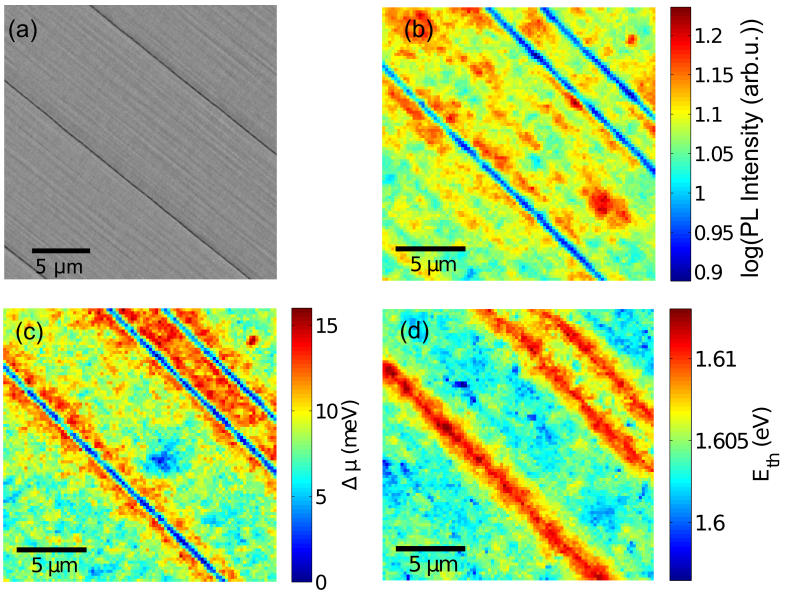

Figure 5.10: (a) SEM of sample surface (not same area as the μ–PL measurement). (b) Spectrally integrated room temperature PL intensity map. (c) Map displaying the extracted variation in splitting of quasi–Fermi levels. (d) Map of the evaluated optical threshold.

and lines of low intensity. Within the high intensity area PL intensity varies with a comparatively low ratio of $I_{PL,max}/I_{PL,min} \approx 1.4$. Within this area of the film the PL intensity forms a lateral pattern which shows variations with a length scale between the resolution limit of about 0.9 μm up to 6 μm. The main variations visible in 5.10(b) are introduced by the continuous lines with low luminescence. Comparing this PL pattern to the SEM image of the same layer in 5.10(a) it is concluded that the continuous lines of low PL correspond to the cracks observed in the $CuGaSe_2$ layer. The significant drop in PL intensity at the cracks is self-evident, as firstly there is no material within the narrow cracks to emit PL, and secondly the PL light emitted in proximity of the cracks is scattered and does not reach the microscope lens.
The spatial variation in the quasi–Fermi level splitting $\Delta\mu$ is evaluated as described in section 5.1.1. Figure 5.10(c) shows the resulting map. It is noticed that the map of $\Delta\mu$ differs from the one showing only the spectrally integrated PL intensity in figure 5.10(b). This is an indication that the band gap of the material is inhomogeneous as explained in section 5.1.1. In the case where no band gap variations are present one would expect that the map of the integrated PL intensity and the quasi–Fermi level splitting would be well correlated. In the map of $\Delta\mu$ presented in figure 5.10(b) it is noticed that $\Delta\mu$ increases locally near the cracks. This is interpreted as a result of an increase of the band gap adjacent to the cracks. An alternative interpretation could be that the excess charge carrier density in the relaxed region near of the crack increases. This could be related to charge carrier diffusion. When free charge carriers are generated by excitation they are able to diffuse in the absorber. Diffusion lengths in the range 0.5 – 2 μm have been reported in $Cu(In,Ga)Se_2$ devices [186]. Since the charge carriers are not able to diffuse across the crack one can image that the charge carrier density builds up near the crack.
Figure 5.10(d) shows a map of the optical threshold energy extracted as explained in section 5.1.1. As previously mentioned, it is possible to interpret variation of the optical threshold as variation of the band gap of the material $\Delta E_{th} = \Delta E_g$. It is seen in figure

5.10(d) that the band gap varies only slightly in between the cracks in the material. Adjacent to the cracks a local increase in the band gap is observed. An increase in the order $\Delta E_g \approx 10 - 15$ meV can be estimated from this measurement. As described in section 2.2.4 this effect can be attributed to the reduction of strain along the cracks. The result shows that the layer relaxes near the crack, but the strain remains further away from the crack.
The increase of E_g along the cracks also explains the local increase of μ in these areas. If E_g increases locally while the free charge carrier concentration remains more or less constant this will naturally lead to an increase of μ.
The distributions of the variation of $\Delta\mu$ and E_{th} of the sample studied here will be further discussed in section 5.5.4, where the results will be compared to the distributions measured for a Cu–rich epitaxial layer (section 5.5.2) and related to results obtained on polycrystalline absorbers.
In order to verify the observations made by μ–PL of strain variation near cracks the result is compared to a CL study performed at the University of Magdeburg of a cracked absorber. One advantage of this method is that it is possible to measure a CL and SEM image of the surface simultaneously. This allows to relate the luminescence directly to sample morphology. Figure 5.11 shows a 7 K CL study of a slightly Cu–rich sample with cracks. The measurement is performed at 7 K instead of room temperature, since this is the experimental conditions available. The spectrum of the CL integrated over the scanned surface in figure 5.11(a) shows excitonic recombination as well as DAP recombination that can be attributed to the DA1 and DA3 transitions. This indicates that the sample is grown under conditions very close to stoichiometry.

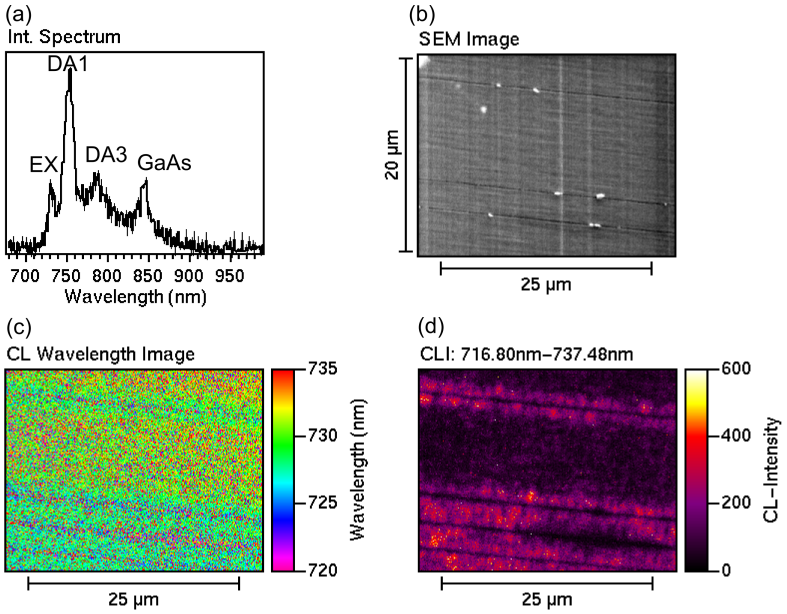

Figure 5.11: (a) CL spectrum integrated over the entire surface measured at 7 K. (b) SEM micrograph of the studied area. (c) Wavelength image showing the wavelength corresponding to the maximum intensity in the region 716 nm – 737 nm where excitonic recombination is observed. (d) CL intensity in the excitonic region.

Three cracks are visible in the SEM micrograph of the studied region (figure 5.11(b)). In the CL (figure 5.11(c),(d)) obtained from the sample, it is clearly observed that these cracks affect the properties of the surrounding material.
The wavelength image in figure 5.11(c) shows the wavelength corresponding to the max-

imum intensity in the exciton region. This can be understood as the local energy of excitonic recombination i.e. a measure for the band gap. It is seen that the exciton shifts to lower wavelengths (higher energies) in regions near the crack. This is in agreement with the observation from μ–PL, where a band gap increase is observed near the cracks. A similar band gap shift due to local strain release along cracks has been observed in various samples with different compositions. Typically a shift around $10 - 20$ meV is observed in the CL measurements. The magnitude of the shift agrees well with the observations from μ–PL.
Figure 5.11(d) shows the spatially resolved CL intensity in the excitonic energy range. Here one clearly observes that the intensity of the exciton increases near the cracks. This agrees with the observations from μ–PL, where a higher quasi–Fermi level splitting is observed near cracks. One could also speculate that the material quality is superior in the relaxed material near the cracks, due to a decrease in the dislocation density. For this to be true one has to assume that the dislocations are able to annihilate in the material as the strain is reduced. If this is the case, it could be an explanation for the higher intensity of excitonic recombination in these relaxed regions.
In order to support the argumentation that the effects observed near the cracks can be related to strain a XRD study is performed. The sample showing cracks studied with μ–PL in the present section is compared to a layer where cracks are not observed (the sample also discussed in section 5.5.2). Figure 5.12 shows the (008) reflection measured for these two samples.

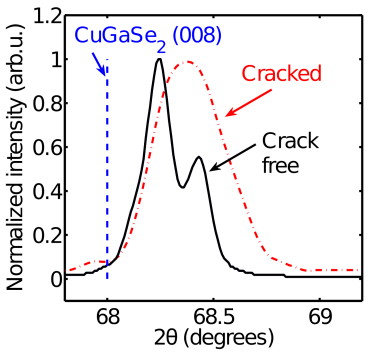

Figure 5.12: XRD diffractogram showing the (008) reflection of a crack free $CuGaSe_2$ layer compared to a $CuGaSe_2$ layer where cracks have been observed.

The result of the XRD measurement in figure 5.12 shows that the peak is shifted to a higher angle relative to relaxed $CuGaSe_2$ in both samples. This shift can be used to estimate the strain in the layer along the c–axis. The shift towards higher angles is due to compression along the c–axis caused by the tensile stress of the a–axis at the interface as discussed in section 2.2. From the peak position the average compression along the c–axis can be estimated to Δc(cracked)$\approx 0.8\%$ and Δc(crack free) $\approx 0.3\%$ for the two studied samples. This observation is in agreement with the expectation that a larger amount of strain should be observable in cracked layers of approximatively the same thickness. One should, however, be aware that a slight thickness difference could also result in different strain in layers as discussed in section 2.2.
The main difference between the samples is seen in the peak widths. The width of the peak in the crack free layer is much narrower than in the cracked layer. In the first case one can clearly distinguish a peak due the Cu Kα_1 and Kα_2 lines. The cracked sample

only shows a broad peak with a shoulder indicating the Kα_2 line. Broadening of the peak can be due to a wider strain distribution in the layer. An observation that is in agreement with the observation from μ–PL and CL, where it could be observed that the strain is locally reduced in the neighbourhood of the cracks, but remained established further away.
In summary it has been demonstrated that strain release near cracks leads to band gap variations in the epitaxial layer of the order 10 – 20 meV. It can be expected that strain has a similar effect in polycrystalline samples where each grain can in principle be differently strained. The inhomogeneities observed in epitaxial samples will be compared to their polycrystalline counterparts in section 5.5.4.

5.5.2 Influence of Secondary Phase Cu_xSe

In the study presented in this section the effect of secondary phase Cu_xSe on the absorber quality of epitaxial $CuGaSe_2$ films is studied by spatially resolved photoluminescence combined with scanning electron microscopy. Cu_xSe crystals are expected to develop on $CuGaSe_2$ layers grown under Cu-rich conditions, as the excess copper segregates in the secondary phase (see section 2.1.2 and 3.7). The size of these crystals is mostly in a range of $\approx 1-2$ μm, and their density on the $CuGaSe_2$ surface strongly depends on the Cu-excess during deposition. The fact that the Cu_xSe forms crystals on the surface makes it possible to examine the effect of Cu_xSe on the material properties, since the effect will be localised. This study would not have been possible with polycrystalline material since the grain structure of the material would hinder the interpretation.
The focus of the study is a characteristic area with the dimensions $50 \cdot 60$ μm^2. A μ–PL scan is performed on the same position before and after etching in 5% KCN for 5 min, which removes the Cu_xSe crystals from the sample surface. To find the same area in photoluminescence before and after etching as well as in the SEM, the surface has been marked by a small scratch.

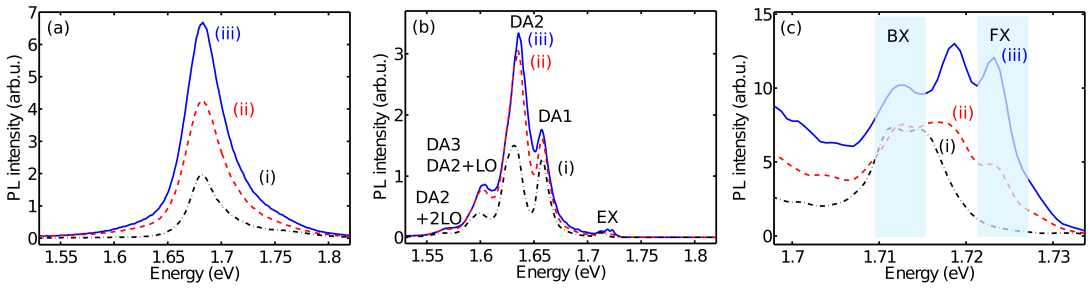

Figure 5.13: Local photoluminescence spectra recorded at the positions indicated by (i),(ii),(iii) in figure 5.14. (a) PL measured at room temperature. (b) PL measured at 10 K, and (c) magnification of exciton region of the 10 K PL spectra.

Figure 5.13(a) and 5.13(b) show typical local PL spectra measured at different positions within the examined area after etching at room temperature (a) and at 10 K (b). At room temperature the PL is dominated by band–to–band recombination and the spectrum contains only one peak with a maximum at 1.68 eV, which corresponds to the band gap of $CuGaSe_2$ at room temperature [184].
The 10 K PL spectra exhibit four distinct peaks and a shoulder at low energy. The energetic position and excitation dependency of these peaks are in good agreement with

results of previous studies discussed in section 2.3.8. The peaks can therefore be assigned as follows: The peak at 1.66 eV and 1.63 eV are the DA1 and DA2 transition, respectively. The peak at 1.60 eV corresponds to the DA3 and is most likely a mixture of the DA3 transition and a phonon replica of DA2 as discussed in section 5.4.1. The region around 1.71 eV that can be attributed to excitonic recombination contains several peaks as seen in the magnified spectra in figure 5.13(c). The peak in the exciton region with the highest energy above 1.72 eV is only seen in spectrum (ii) and (iii). This peak is most likely due to recombination of free excitons. Several peaks are seen at lower energies from around 1.72 eV to slightly below 1.71 eV. These are probably due to excitons bound to different defects in the material. The coloured regions in figure 5.13 refer to areas over which the intensity has been integrated in figure 5.14(g). The peak in between these two regions is most likely due to bound exciton recombination.
As discussed in section 2.3.8 the ratio between the PL intensity of the DA1 and the DA2 peak is a reliable measure of the [Cu]/[Ga] ratio. A dominant DA1 indicates a ratio of [Cu]/[Ga]≈1, whereas an increase of the DA2 indicates higher copper excess during growth. Note that these ratios refer to the [Cu]/[Ga]–ratio during the growth process, whereas the resulting sample contains a stoichiometric chalcopyrite and a Cu_xSe secondary phase. As the Cu–excess during growth determines the defect structure of the $CuGaSe_2$ absorber, these different PL signatures can be observed on the sample, even after etching away the Cu_xSe [48]. The corresponding composition changes are extremely slight and cannot be detected by composition measurements, which always find stoichiometric chalcopyrite after etching.

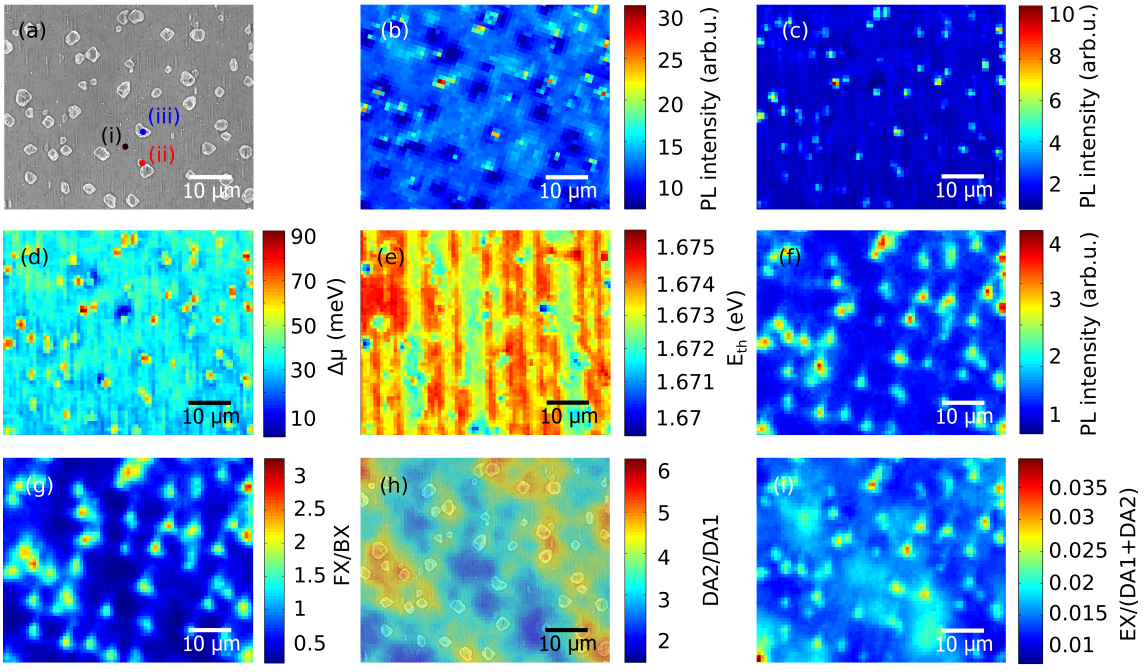

Figure 5.14: (a) SEM micrograph of the studied area. (b) PL map of the spectrally integrated PL at room temperature before etching. (c) Room temperature PL map after etching. (d) $\Delta\mu$ extracted from (c), and (e) band gap variation evaluated from (c). (f) Spectrally integrated intensity of the exciton region measured at 10 K after etching. (g) The ratio of the high energy part of the exciton region (FX) to the low energy part (BX) (see regions in figure 5.13(c)). (h) The DA2/DA1 ratio at 10 K after etching. (i) The ratio of exciton and DAP integrated intensities.

Figure 5.14(a) shows an SEM micrograph of the area of interest before the etching process

exhibiting the Cu_xSe crystallites distributed randomly across the $CuGaSe_2$ surface. These appear as differently shaped crystals in lighter contrast than the underlying $CuGaSe_2$ layer.
Figure 5.14(b) shows a map of the spectrally integrated PL intensity at room temperature (see spectra in figure 5.13(a)). The PL map, that has been measured prior to etching, exhibits spots of strong and weak luminescence. The main area of the scan shows an approximately homogeneous PL intensity of the film between the spots. By comparison of this map and the corresponding SEM micrograph in 5.14(a) it is concluded that the PL emission from the homogeneous appearing area represents the emission of $CuGaSe_2$ without the influence of Cu_xSe crystals, whereas each spot (light and dark ones) in the PL map can be related to a Cu_xSe crystal. The sample was subsequently etched to remove the Cu_xSe crystals.
The resulting PL map of the etched $CuGaSe_2$ layer is shown in 5.14(c), exhibiting only bright spots, aside from one dark spot. Comparison of the PL map in figure 5.14(c) with the SEM micrograph in figure 5.14(a) demonstrates that the luminescence intensity of $CuGaSe_2$ is increased in the vicinity of each former Cu_xSe crystal, exhibiting a PL intensity up to a factor 6 brighter than the surrounding areas. The bright spots indicate that the material in the vicinity of the former Cu_xSe has properties that differ from the rest of the film, leading to locally increased PL intensity.
The difference of the PL maps before and after etching can be explained by the removal of the Cu_xSe crystals from the surface. As long as the Cu_xSe crystals remain on the surface the PL from the underlying $CuGaSe_2$ is locally scattered and shadowed by the crystals. The effective strength of this effect is determined by the shape and size of these crystals. Thus, depending on these properties of each Cu_xSe crystal, the unetched sample exhibits Cu_xSe positions where the locally detected PL signal of the underlying $CuGaSe_2$ is strongly decreased, and other locations where it is only weakly decreased. After removal of the Cu_xSe crystals by etching, the PL from the $CuGaSe_2$ film can reach the detection optics unhinderedly. Figure 5.14(c) therefore shows the results not dominated by Cu_xSe scattering, where the spots of the former Cu_xSe crystals show a locally increased PL signal.
The result in figure 5.14(c) clearly indicates that the Cu_xSe crystals have a locally enhancing effect on the intensity of the band–to–band luminescence of the underlying $CuGaSe_2$ material. This behaviour may be interpreted as a result of locally enhanced excess charge carrier concentrations at these positions. For this interpretation to be strictly true the band gap must remain constant. This can be investigated by applying Planck's generalized radiation law. Based on the approach presented in section 5.1.1, the variations of the quasi–Fermi level splitting $\Delta\mu$ and the optical threshold E_{th} are extracted from the room temperature measurement on the etched sample. The resulting maps are shown in figure 5.14(d),(e).
Figure 5.14(d) displays the spatial variation of $\Delta\mu$ extracted from the room temperature PL measurement shown in figure 5.14(c). By comparison of the integrated PL intensity and the extracted quasi–Fermi level splitting it is noticed that the maps are practically identical. The spots of high intensity in the PL are therefore caused by a local increase of μ and not by variation of the band gap. This conclusion is in agreement with the map in figure 5.14(e) showing E_{th}. The variation of E_{th}, which can be interpreted as variation of the band gap, is of the order $\Delta_{max} \approx 3$ meV. The dominating structure in the map are horizontal lines. Only a few dark spots that relate to the Cu_xSe positions can be identified. At these locations a very slight band gap reduction is observed. This could

indicate a small local compressive strain, though the effect is close to the resolution limit of the evaluation.
The results furthermore allow for quantification of the improvement of the quality of the photo excited state and of the potential solar cell performance. The evaluation indicate an increase of up to $\Delta\mu \approx +60$ meV below the Cu_xSe crystals compared to the values found in the surrounding area between the Cu_xSe crystals. As the maximum open circuit voltage is determined by the splitting of the quasi–Fermi levels, this increase consequently enhances the maximum achievable open circuit voltage in a device.
The reason for the high luminescence in the vicinity of Cu_xSe is attributed to a local enhancement of the Cu–excess during growth in the areas adjacent to the Cu_xSe crystals, where the crystals act as an additional source of Cu. Higher Cu–excess has been reported to result in a lower defect concentration [187]. This leads to a lower defect recombination rate, which consequently will lead to a higher local excess charge carrier concentration under illumination, hence a higher PL intensity. Another effect that could influence the quality of the material is re–evaporation of Se during cool down. It is possible that the presence of Cu_xSe on the surface locally reduce the Se evaporation thereby increasing the material quality under the Cu_xSe crystallites. Also surface recombination could influence the PL intensity. Since the measurement is performed several days after KCN etching it is, however, assumed that the surface recombination is homogeneous in the studied area. It should also be mentioned that XPS studies indicated the presence of a very thin continuous Cu_xSe layer in addition to the Cu_xSe crystallites as discussed in section 3.7.1. It is, however not expected that this layer will affect the effect discussed here since the layer is less than ≈ 2 nm thick.
To further verify the idea that the defect concentration is locally reduced, the area is re–measured with μ–PL at 10 K. Figure 5.14(f) shows the resulting PL map of the spectrally integrated excitonic emission region (labeled EX in figure 5.13(b)). The image demonstrates that the excitonic PL exhibits approximately the same lateral pattern as the band–to–band transition at room temperature (figure 5.14(c)). Since presence of strong excitonic recombination indicates high crystal quality [63], i.e. lower concentration of recombination centres, the presence of stronger excitonic recombination in the vicinity of the removed Cu_xSe crystals is another indication that the crystal quality is locally improved by the presence of Cu_xSe during growth.
A detailed investigation of the excitonic region reveals that the peak shape and position in vicinity of Cu_xSe crystals is different from the surrounding area (see figure 5.13(c)). Excitonic luminescence with higher energy is observed only on the former Cu_xSe locations. This high energy excitonic luminescence is most likely due to free exciton recombination compared to the lower energy recombination, which is probably due to bound exciton recombination. The latter is found everywhere on the sample. Figure 5.14(g) shows a map of the ratio of the integrated intensity of the high energy region and the low energy region indicated in figure 5.13(c). The map clearly demonstrates that the high energy excitonic recombination increases very significantly compared to the lower energy part at the positions of the former Cu_xSe crystals. If the interpretation if the high energy part as FX and the low energy part as BX is true, this is a further indication of locally improved crystal quality by the presence of Cu_xSe crystals.
Figure 5.14(h) shows the local DA2/DA1 intensity ratio for the investigated area overlaying the SEM micrograph, indicating the local degree of Cu–excess during layer growth. The ratio varies roughly by a factor of 2 between the maxima on the former Cu_xSe locations and the minima located at the Cu_xSe free areas, which can e.g. be seen by compari-

son of spectrum (i) and (iii) in figure 5.13(b).
This clearly demonstrates that the presence of the Cu_xSe during layer growth increases the local DA2/DA1 ratio meaning an increase of the effective local copper excess during growth at these positions. It is expected that the areas with high DA2/DA1 ratio below the Cu_xSe have higher crystal quality, as higher Cu–saturation leads to lower defect density [187], which is in accordance with the results discussed above.
For further evidence of this interpretation the ratio of the integrated excitonic emission and the defect related transitions (all DAP peaks) is plotted in figure 5.14(i). The map shows an increase of this ratio at the positions of the Cu_xSe crystals, indicating a local decrease of the defect related recombination, supporting the interpretation above.
All results presented here demonstrate that the presence of the secondary phase Cu_xSe during growth of $CuGaSe_2$ epitaxial layers under Cu–excess enhances the local quality of the underlying $CuGaSe_2$ absorber. By consideration of the ratio between DA2/DA1 transitions it could be shown that this enhancement is due to a higher local copper excess at these locations during growth.
The effects presented here furthermore seem to play a key role in the understanding of the origin of inhomogeneities in chalcopyrites discussed in section 5.2. This issue will be discussed further in section 5.5.4.
Since the effect remains after removal of Cu_xSe, this can also be expected to play a role in Cu–poor chalcopyrite films, which undergo a copper rich stage during the growth process.

5.5.3 Effect of Going Through a Cu–rich Stage

This section will briefly discuss if the effects of the Cu_xSe crystals on the material quality remains, if the material passes through a Cu–rich stage during the growth, after which it is turned Cu–poor. This is interesting since a copper rich stage during the growth process, is used in the three stage process by which the record efficiency $Cu(In,Ga)Se_2$ devices are achieved [4, 188]. In order to investigate this effect a series of samples are grown. A standard Cu–rich recipe is used in all cases, but each sample is treated differently in a final step before cool down.

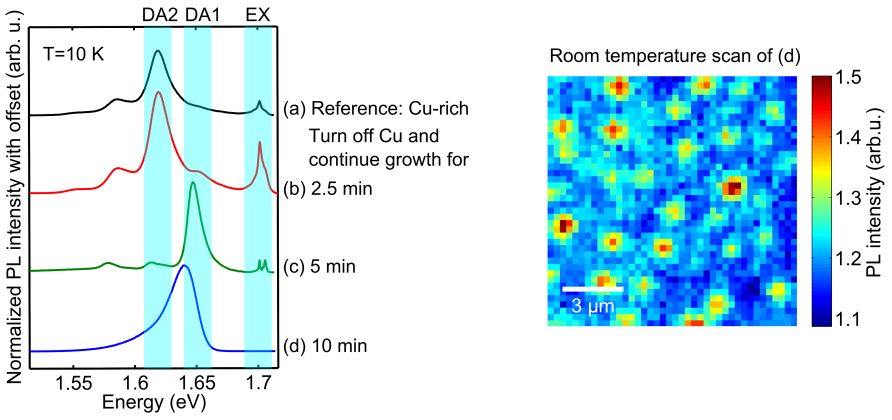

Figure 5.15: *Left:* Global photoluminescence spectra measured at 10 K of four samples grown with the same Cu–rich process, but with different growth conditions during a final step. (a) is stopped after the standard recipe. The Cu–supply is switched off during the final growth step while Ga and Se sources are kept open for (b) 2.5 min (c) 5 min and (d) 10 min. *Right:* Map of the spectrally integrated PL intensity obtained from a room temperature measurement of sample (d).

The first sample ((a) in figure 5.15) is simply grown with the standard Cu–rich process without a final step. For the three other samples (b),(c), and (d) a final step is added to the growth process. In this step the temperature and flows of Ga and Se are kept constant, but the Cu–supply is stopped. The duration of this final step is different for each sample: (b) 2.5 min (c) 5 min (d) 10 min. All the samples are etched in KCN prior to the PL studies presented here.
Figure 5.15 shows the resulting 10 K PL spectra obtained from the four samples. It is noticed that sample (a) expectedly shows a dominating DA2 transition always found in Cu–rich material. Sample (b) shows a weak shoulder due to DA1 recombination in addition to the DA2 peak. This is an indication that the material composition is less Cu–rich. Sample (c) shows a dominating DA1 peak and a weak peak in the region where the DA2 is normally observed, an indication that the material composition is close to the stoichiometric point. The last sample in the series finally shows a broad asymmetric peak that is red shifted relative to the DA1 peak typical for a compensated material, a signature that is always found in Cu–poor material as discussed in chapter 4. These observations all agree with and support the defect model discussed in section 2.3.8. The result shows clearly that the material becomes less Cu–rich with increasing time of the final step as expected.
It can be expected that the Cu–poor sample (d) has been through a Cu–rich stage before becoming Cu–poor during the last 10 minutes of the growth where no Cu was supplied. It is therefore interesting to examine whether a spatial structure similar to the one discussed in the previous section can be found on this sample. A room temperature μ–PL investigation of this sample is shown in figure 5.15. Here one can observe spots of high intensity, a result very similar to the one shown in figure 5.14. One main difference compared to the measurement shown in figure 5.14 is that the magnitude of the intensity increase observed in the spots is weaker. The measurement discussed in section 5.5.2 showed a variation of $I_{PL,max}/I_{PL,min}$ up to 6, whereas the measurement in figure 5.15 shows a much smaller variation of $I_{PL,max}/I_{PL,min} \approx 1.4$. If the origin of the spotty structure is the same, the effect is therefore significantly reduced when passing the Cu–poor growth stage.
The result presented here is an indication that the effects of the Cu_xSe in fact persist after passing through a Cu–poor growth step. It is hereby not postulated that the bright locations remain with a different composition. This is probably not the case, since Cu has a high diffusion coefficient as discussed in section 3.7. It is rather proposed that the observed effect can be due to a locally enhanced crystal quality.
It should, however, be pointed out that the result presented here is not strongly supported by μ–PL studies of the other samples ((a), (b) and (c)) shown in figure 5.15. The expected bright spots did not show up in any measurement on these samples. A fact that certainly questions this conclusion. One can wonder why these samples did not show the expected tendency. One possible explanation is the observed structures depend on the excitation density as discussed in appendix B. The result presented here can therefore only be regarded as an indication that the effect of the Cu_xSe might be present after passing into Cu–poor conditions. Further careful studies would be needed to confirm this.

5.5.4 Comparison to Polycrystalline Absorbers

Polycrystalline $CuGaSe_2$ thin films grown by PVD on glass substrates are investigated here in order to compare the results with those obtained on epitaxial layers. For the study a Cu–rich and a Cu–poor $CuGaSe_2$ absorber are investigated. The Cu–poor sample is grown by a 3–stage co–evaporation process; and a 2–stage process is used when growing the Cu–rich sample. In the first stage, Ga is deposited with high Se flux at 350 °C. The substrate is then heated to 540 °C after the first stage. In the second stage, Cu is deposited under high Se flux until the $CuGaSe_2$ film becomes Cu–rich. Ga is deposited with high Se flux again in a third stage to obtain the Cu–poor film. The thickness of the final film is ≈ 2 μm. This 3–stage process is optimized for Cu(In,Ga)Se_2 with Ga-contents of around Ga/(In+Ga)=0.3. The solar cells from this process yield efficiencies of more than 15%. As the process was not re–optimized for $CuGaSe_2$ growth, the samples analysed here could be of non–ideal quality.
The samples are etched in KCN and investigated with μ–PL. The spatial variations on an area of $25 \cdot 25$ μm^2 are quantified in terms of distributions of band gap variations and variation of $\Delta\mu$. The results will be compared to the variations extracted from the Cu–poor epitaxial $CuGaSe_2$ sample studied in section 5.5.1 and the Cu–rich epitaxial $CuGaSe_2$ sample studied in section 5.5.2.
Figure 5.16 shows the distributions of $\Delta\mu$ obtained from evaluation of the spatial inhomogeneities measured by μ–PL with an excitation flux of $\approx 5 \cdot 10^{22}$ $cm^{-2}s^{-1}$. In all samples shown in figure 5.16 there seems at least two different distributions that contribute to the overall distribution found in the samples.

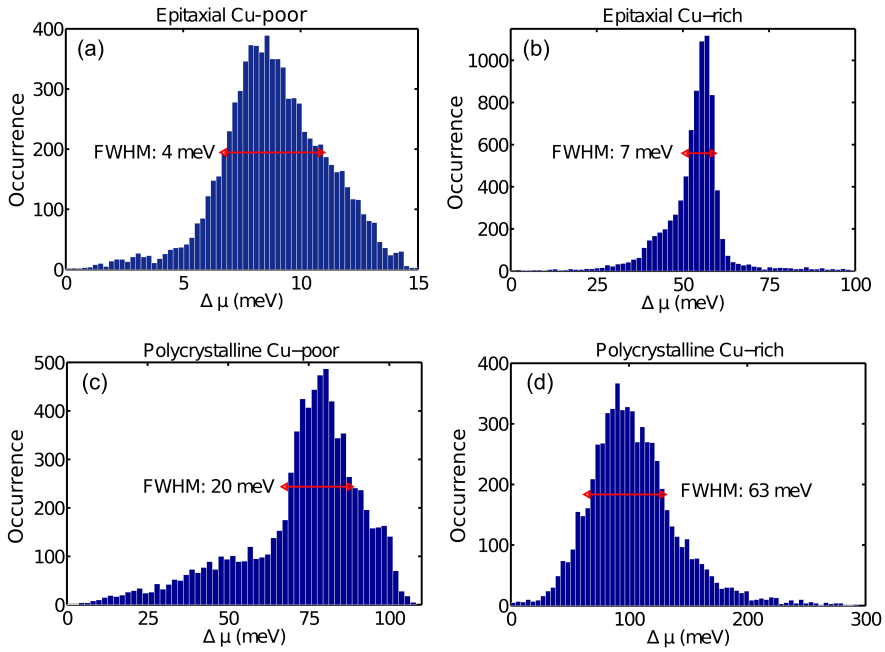

Figure 5.16: Distributions of $\Delta\mu$ extracted from spatially resolved room temperature PL measurements. $\Delta_{max}(\Delta\mu)$ correspond to the length of the x–axis of each distribution.

Two properties of the distributions are interesting. The full width at half maximum of the distribution $\Delta_{FWHM}(\Delta\mu)$ and the total width of the distribution quantified as the maximum variation in the scan area $\Delta_{max}(\Delta\mu)$. The value $\Delta_{max}(\Delta\mu)$ is of interest because of the effect of Cu_xSe discussed in section 5.5.2. Around the spots influenced by Cu_xSe

a strong local enhancement of the splitting of the quasi-Fermi levels compared to the surrounding area was found. As the areas of these extreme maxima in $\Delta\mu$ are only a very small fraction of the total area, these are not represented in the FWHM values.
For the epitaxial layers it is found that $\Delta_{FWHM}(\Delta\mu)$ is very similar for both samples. The main difference between them is found in $\Delta_{max}(\Delta\mu)$ that is 6 times larger in the Cu–rich sample than the Cu–poor counterpart. This is interpreted as a result of the previously discussed Cu_xSe effect.
The quasi–Fermi level variations for the polycrystalline films in figure 5.16(c),(d) are significantly larger than those of the epitaxial layers in terms of both $\Delta_{FWHM}(\Delta\mu)$ and $\Delta_{max}(\Delta\mu)$. Similarly to the observation for epitaxial films, the polycrystalline sample grown under Cu–rich conditions shows much higher quasi–Fermi level splitting variations than the Cu–poor specimen. $\Delta_{FWHM}(\Delta\mu)$ for the Cu–poor sample is in the same range as the values found in Cu–poor Cu(In,Ga)Se_2 in literature: $\Delta_{FWHM}(\Delta\mu) \approx$ 8–18 meV [166], 10–30 meV [12], 18 meV [11]. The maximum variation $\Delta_{max}(\Delta\mu)$ in the scan area for the Cu–poor sample a bit larger than the range as previously reported: $\Delta_{max}(\Delta\mu) \approx 74$ meV [12], ≈ 45 meV [12], > 70 meV [11]. When comparing these numbers it is important to bear in mind that the distribution of $\Delta\mu$ depends on the excitation flux and temperature. Experimental conditions can therefore lead differences in the observations in this order.
The Cu–rich sample in figure 5.16(d) shows a distribution that is significantly wider than the one previously observed in Cu–poor Cu(In,Ga)Se_2. Following the discussion in section 5.5.2, this effect can be related to a spatially non-uniform degree of Cu–excess during the growth process. This may result in an inhomogeneous distribution of Cu_xSe at the $CuGaSe_2$ surface at the end of the process, before etching. The resulting effects are large spatial variations of the defect concentrations and accordingly of the splitting of quasi–Fermi levels.
The FWHM of the band gap distributions extracted from room temperature PL measurements on these samples are collected in table 5.2.

	Epi Cu–poor	Epi Cu–rich	Poly Cu–poor	Poly Cu–poor
$\Delta_{FWHM}(E_g)$	6 meV	3 meV	5 meV	5 meV

Table 5.2: FWHM of band gap distributions extracted from spatially resolved μ–PL measurements. Epi: epitaxial films, Poly: polycrystalline films

The widths of the band gap distributions are similar for both polycrystalline samples and the Cu–poor epitaxial sample (5–6 meV), whereas the Cu–rich epitaxial sample has a narrower distribution of only 3 meV. When interpreting this result it should be noticed that cracks are observed in the Cu–poor epitaxial layer, whereas the Cu–rich layer is crack free. The cracked sample contains a broad strain distribution, caused by the lattice relaxation around the cracks, and exhibits a clearly measurable amount of band gap fluctuations, whereas the crack free shows a very narrow strain distribution and accordingly almost no band gap fluctuations. Following the discussion in section 5.5.1, it is proposed that the band gap variations in the polycrystalline films are caused by strain variations as well. Generally, in polycrystalline $CuGaSe_2$ each grain can be strained differently, which intrinsically results in a broad strain distribution. The band gap distribution found here in $CuGaSe_2$ is significantly narrower than the value reported for Cu(In,Ga)Se_2 of up to 13 meV [11]. This difference is expected since alloying disorder present in Cu(In,Ga)Se_2 is

not possible in $CuGaSe_2$. This result, furthermore, points out that a part of the variation of $\Delta_{FWHM}(E_g)$ in Cu(In,Ga)Se_2 observed previously should be ascribed to strain effects. According to these results this contribution is in the order of 5 meV.
To summarize: Both, the polycrystalline and epitaxial samples, reveal spatial inhomogeneities of the splitting of quasi-Fermi levels and band gap. The epitaxially grown specimens exhibit a significantly smaller amount of variations of the quasi–Fermi level splitting than the polycrystalline ones. The variations of $\Delta\mu$ turns out to be significantly higher in samples grown under Cu–rich conditions, for both deposition methods. This trend for Cu–rich samples is attributed to locally fluctuating amounts of Cu–excess during the deposition process, caused by secondary phase Cu_xSe crystals on the $CuGaSe_2$ surface.
The band gap variations are considerably smaller than those observed previously in polycrystalline Cu(In,Ga)Se_2 samples. The band gap variations, observed in the ternary compounds studied here, are attributed to strain effects in the absorber layer. It can be expected that strain has a similar effect in Cu(In,Ga)Se_2. Larger band gap inhomogeneities observed in Cu(In,Ga)Se_2 can therefore be attributed to combined alloying and strain effects, with alloying disorder having the stronger effect.

5.6 Summary

Several effects have been investigated with μ–PL performed at different temperatures and various excitation densities.
A number of 10 K μ–PL measurements reveals that a third DAP transition (DA3) is found to be spatially independent from the DA1 and DA2 peaks typically seen in epitaxial $CuGaSe_2$ samples. In some cases, it is, however, not possible to unambiguously ascribe this peak to the DA3 transition. In these cases it seems that the peak is a mixture of the DA3 peak and a phonon–replica of the DA2 peak. In relation to this study it is important to notice that the appearance and size of structures depend on the excitation density used in the experiment (see appendix B).
Luminescence due to radiative recombination via deep defects has been found at both room temperature and 10 K measurements. It is revealed that this low energy luminescence is spatially anti–correlated to BB and EX recombination, indicating that these defects are deleterious for the performance of the material.
By μ–PL and CL experiments it is found that the strain near cracks formed in epitaxial layers is locally reduced. This leads to an increase of the band gap in these regions of the layer. It is expected that strain variation in a similar way affect polycrystalline materials. A band gap distribution in polycrystalline $CuGaSe_2$ similar to the one found in the cracked epitaxial layer confirms this.
Several μ–PL measurements of the effect of Cu_xSe on the absorber material reveals that the presence of the secondary phase enhances the material quality of the underlying $CuGaSe_2$ absorber by reducing the local defect concentration. It could be demonstrated that this is related a local increase of the Cu–excess.

6 Summary

The aim of this thesis is to study various types of inhomogeneities in chalcopyrite $CuInSe_2$ and $CuGaSe_2$. In order to achieve this epitaxial layers of these materials have been grown by MOVPE on GaAs. This is done in order to study the material without the influence of grain boundaries. A large part of this work has therefore been focused on the development of a growth process for fabrication of high quality samples. This has been achieved through a series of growth experiments varying various parameters.
The main tool for basic characterization as well as advanced investigations applied in this work is photoluminescence. Photoluminescence is used as a tool to monitor the influence of growth conditions during development of the growth process. But the technique is also used in more detailed studies of the properties of Cu–poor as well as Cu–rich chalcopyrites. For Cu-poor materials this has given a deeper understanding of potential fluctuations as a function of temperature.
When the spot size of the exciting light source is reduced to less than a μm and the photoluminescence measurement is performed with spatial resolution detailed studies can be performed. Spatially resolved photoluminescence has been proven in this work to be a powerful tool to investigate inhomogeneities in chalcopyrites. Especially the effect of Cu_xSe on the surrounding material properties should be emphasized as an interesting result.
Experiments of different character have been performed in this work. The main conclusions that can be drawn from these studies are summarised in the following.

Growth Experiments

A MOVPE process for growth of epitaxial $CuInSe_2$ and $CuGaSe_2$ on GaAs(001) is successfully developed. Low temperature photoluminescence is used as a tool to control the process ex situ and understand the effect of various growth parameters. By taking advantage of the ability of PL to provide information about the sample composition, it is possible to adjust the process parameters and fabricate samples with the desired composition. The process recipe is improved through a series of optimization growth experiments where the influence of various parameters is tested. This made it possible to grow epitaxial $CuInSe_2$ and $CuGaSe_2$ with a wide range of compositions from Cu–poor to Cu–rich.
A study of the growth dynamics at 570°C demonstrates the importance of the growth temperature. By study of four samples grown with the same recipe but for different growth times, a model for the dynamics of the growth is developed. A recipe developed to obtain Cu–rich samples after four hours of growth is used in this study. It is shown that the sample composition develops from Cu–poor to Cu–rich with increasing process duration under these conditions. This is explained by supply of Ga from the GaAs substrate due to decomposition of GaAs. The additional supply of Ga especially affects the composition of the thinnest layers. Interestingly, this evolution of layer composition does not lead to an in–depth gradient in the final samples. The depth profile shows a very uniform [Cu]/[Ga] ratio. This is explained by the very high diffusion coefficient of Cu,

which rapidly homogenizes the layer composition at the growth temperature.
When chalcopyrite grow under Cu–rich conditions a secondary Cu_xSe phase appears on the surface. The epitaxy of $CuGaSe_2$ is not obstructed by the presence of the secondary Cu_xSe phase on the surface. EBSD measurements indicate that Cu_xSe is converted continuously to $CuGaSe_2$ during the epitaxial growth. There is no reason to assume a different behaviour for $CuInSe_2$ regarding the effect of Cu_xSe.

Potential Fluctuations In Chalcopyrites

One type on inhomogeneities studied with photoluminescence are potential fluctuations in Cu–poor chalcopyrites. Three approaches have been applied to estimate the average amplitude of the potential fluctuations at 10 K. These are investigation of the peak position, analysis of the low energy peak shape and monitoring the shift of the peak position with increasing excitation density. Samples with different Cu–deficiencies are investigated and it was found with all evaluation methods that the fluctuation amplitude increases with decreasing [Cu]/[III] ratio. An average fluctuation amplitude at 10 K of $\approx$ 20 meV is estimated for almost stoichiometric material increasing to $\approx$ 60 meV for the most Cu–poor sample studied in the series with [Cu]/[Ga] $\approx$ 0.84.
The temperature dependence of the potential fluctuations is interesting since it is often assumed that these fluctuations remain at room temperature. Temperature dependent PL performed from 10 K to 300 K reveal a non–monotonous shift of the PL peak with increasing temperature. When the temperature is initially increased from 10 K to around 75 K the peak red shifts. This is explained by an increase of the effective potential fluctuations due to collection of charge carriers in deeper valleys. As the temperature is increased even further the peak shifts to higher energies indicating that the fluctuations are flattened by thermally excited charge carriers. At room temperature the PL peak position becomes independent of the excitation density. Evaluation of the absorption edge from room temperature PL measurements show no change with the excitation density either. This indicates that potential fluctuations are screened by free charge carriers at room temperature. In slightly Cu–poor material the fluctuations totally disappear at elevated temperatures. In samples with larger Cu–deficiency the fluctuations seem to remain even at room temperature, but the magnitude of the fluctuations is significantly reduced to a few meV if present at all. Previously it was often assumed that potential fluctuations in Cu–poor chalcopyrites affect the solar cell performance (see e.g. [16, 17]). The result presented here clearly shows that potential fluctuations are not expected to affect the performance of solar cells operated at room temperature.

Spatially Resolved Photoluminescence

In this work spatially resolved photoluminescence has for the first time been applied to study epitaxial chalcopyrites. With this approach inhomogeneities not related to the polycrystalline structure can be investigated. By study of $CuGaSe_2$ without indium it is furthermore possible to study a material without effects related to alloying disorder. The investigated inhomogeneities are therefore of very fundamental character.
It is demonstrated that spatially resolved photoluminescence with micrometer resolution is a powerful tool to study inhomogeneities in chalcopyrites. Several effects have been investigated with μ–PL performed at different temperatures and various excitation densities. At low temperature spatial variations of defect related transitions can be studied.

When performing the spatially resolved PL experiment at room temperature it is possible to analyse the results applying Planck's generalized law of radiation. This opens the possibility to investigate variations of quasi–Fermi level splitting and band gap.
μ–PL measurements performed at 10 K provide information about the spatial distribution of DAP transitions. A third DAP transition (DA3) is found to be spatially independent from the DA1 and DA2 peaks typically seen in epitaxial $CuGaSe_2$ samples. This confirms the conclusion from previous CL studies that the DA3 transition is not a phonon replica of the DA2 peak. In some cases, it is, however, not possible to unambiguously ascribe this peak to the DA3 transition because it occurs highly correlated with the DA2 peak. This probably occurs due to the overlap of a phonon–replica of the DA2 peak and the DA3 transition.
A broad peak around 1.35 eV was found on some $CuGaSe_2$ samples at both room temperature and 10 K. This peak is ascribed to radiative recombination via deep defects in the band gap. A 10 K photoluminescence measurement reveals that the spatial appearance of this peak is highly anti correlated to the excitonic luminescence. A similar room temperature measurement show that the 1.35 eV peak is spatially anti correlated to the quasi–Fermi level splitting. These results both indicate that the defects related to this peak are deleterious for the performance of the material.
It is realized that cracks often observed in $CuGaSe_2$ layers grown on GaAs are easily identified in spatially resolved μ–PL measurements. In both μ–PL and CL experiments it is found that the strain near the cracks is locally reduced. This leads to an increase of the band gap of the layer near the cracks of around 10–20 meV. It is expected that strain variation also affects polycrystalline materials. A band gap distribution measured for polycrystalline $CuGaSe_2$ of $\Delta_{FWHM}(E_g) = 5$ meV similar to the one found in the cracked epitaxial $CuGaSe_2$ layer ($\Delta_{FWHM}(E_g) = 6$ meV) is in agreement with this expectation. It can be expected that the strain effect investigated here has a similar effect on $Cu(In,Ga)Se_2$. The band gap variations measured in epitaxial and polycrystalline $CuGaSe_2$ are considerably smaller than those observed previously in polycrystalline $Cu(In,Ga)Se_2$ samples. Larger band gap inhomogeneities ($\Delta_{FWHM}(E_g) = 5 - 13$ meV [11, 166]) observed previously in $Cu(In,Ga)Se_2$ can therefore be attributed to combined alloying and strain effects, with alloying disorder having the stronger effect. The band gap variations measured in chalcopyrites in this and previous studies are, however, so low that the effect on device performance is limited [9].
Several μ–PL measurements of the effect of the presence of Cu_xSe on the absorber material have been presented. It is demonstrated that $CuGaSe_2$ in areas around the Cu_xSe crystallites display higher excitonic recombination at low temperature and larger quasi–Fermi level splitting than the surrounding material at room temperature. This indicates that the presence of the Cu_xSe secondary phase enhances the material quality of the underlying $CuGaSe_2$ absorber by reducing the local defect concentration. By consideration of the spatial variation of the DA2/DA1 ratio it could be verified that this enhancement is due to a higher local Cu–excess at the Cu_xSe locations during growth. The result shows that material grown under Cu–excess has superior material quality compared to Cu–poor material. There are furthermore indications that this effect remains in material with a Cu–poor composition after passing through a Cu–rich growth stage. The effect of the Cu–excess could therefore be a part of the explanation for the importance of a Cu–rich growth step in the widely used three stage process.

Acknowledgements

A lot of people have contributed to this work in different ways and deserve my sincere acknowledgements.
First I would like to thank my advisor Susanne Siebentritt for giving me the opportunity to do my Ph.D. in Luxembourg. I highly appreciated your guidance, support, and deep insight. Our many discussions of results, ideas, literature, and interpretations have been a great help.
I also thank Levent Gütay for guidance and great collaboration during development of the μ–PL setup and MOVPE growth process and for many discussions of the interpretation of the results, but also for bringing high spirits in the office and laboratory at all times.
I would also like to thank Thomas Schuler for being an excellent problem solver making sure that everything in the laboratories is working, should it be an error in the measurement software or a MOVPE breakdown.
I am also grateful to Danielle Schoder and later Patricia Ramoa for taking care of various practical and administrative matters. This surely made my work much easier.
I have received measurements and results from several people in the group. This I highly appreciate. Particularity I acknowledge:

- Dominik Berg and Alex Redinger for performing SEM and EDS measurements and subsequent discussions
- Katja Hönes for collaboration with XRD measurements and an introduction to the PL setup
- Yasuhiro Aida for growing great polycrystalline samples
- Karin Burger for performance of some PL measurements

Only a few group members are mentioned here, but the rest of the group is certainly not forgotten. I would like to express my gratitude to the entire LPV group at the university of Luxembourg. I really enjoyed the many informative talks and discussions of our results and ideas at our weekly group meetings. I also thank you for the great ambience in the group and three wonderful summer retreats together.
Several people from other universities and institutes have contributed to this work with various measurements. I would like to thank you for your efforts. This includes:

- Jürgen Blässing at Otto-Von-Guericke Universität, Magdeburg for discussion of XRD artefacts
- Jürgen Albert at Helmholtz Zentrum Berlin introduction of MOVPE and a basic recipe
- Jörg Schmauch at Universität des Saarlandes for EBSD measurements

- Nathalie Valle at CRP Lippmann for SIMS measurements and discussion of the results
- Jérôme Guillot at CRP Lippmann for XPS and AES measurements and discussion of the results
- Stefanie Bierwirth at Georg-August-Universität Göttingen for TEM measurements
- Jürgen Christen, Frank Bertram, and Mathias Müller at Otto-Von-Guericke Universität, Magdeburg for a warm welcome in Magdeburg and CL measurements

At last, but by no means least, I thank Alice for her endless support and great patience during the last three years and my family and friends for their encouragement.

Influence of Excitation Density in μ–PL

B

During this work it was realized that the excitation density plays an important role when performing μ–PL measurements. It will be demonstrated in the following that the structures revealed in μ–PL maps strongly depend on the excitation density. A sample with a composition close to stoichiometry etched in KCN to remove Cu_xSe is used in the study. In order to investigate the effect of the excitation density, the sample is measured under various excitation conditions starting with a photon flux of $I_0 \approx 10^{20}$ $s^{-1}cm^{-2}$ in measurement (a). In the subsequent measurements the photon flux is increased to (b) $\approx 75I_0$, (c) $\approx 920I_0$, (d) $\approx 4170I_0$. Two additional measurements are performed in the series, one with a lower excitation density ($\approx 0.1I_0$) and one in between ($\approx 320I_0$). Since these show the same tendencies found in the experiment these measurements are, however, excluded here to keep the complexity at a minimum.

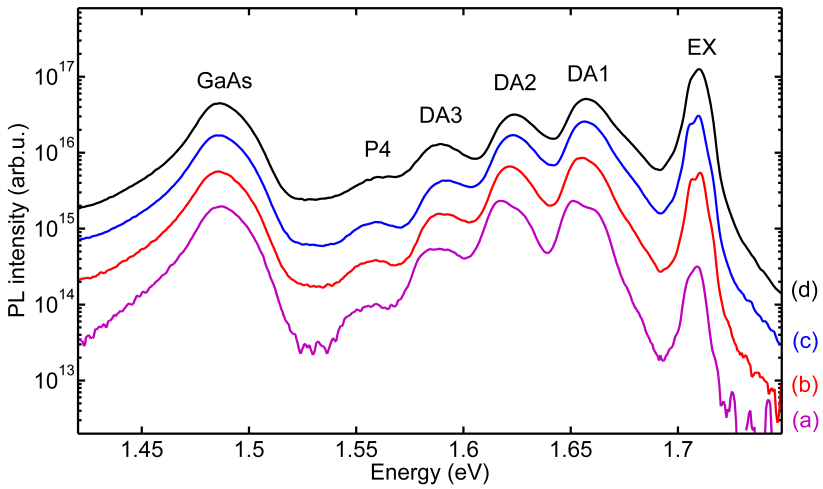

Figure B.1: Local PL spectra from as a function of excitation density. Photon fluxes of the excitation are (a) $I_0 \approx 10^{20}$ $s^{-1}cm^{-2}$, (b) $\approx 75I_0$, (c) $\approx 920I_0$, (d) $\approx 4170I_0$.

Figure B.1 shows a local PL spectrum from each map recorded at different excitation conditions. The PL intensity is shown in a logarithmic scale because of the large variation in intensity between the measurements. It is not surprisingly noticed that the exciton intensity increases with a higher rate than the other transitions.
Three DAP transitions can be identified as well as a peak here labelled P4. The low energy peak around 1.49 eV is due to luminescence from the GaAs substrate. It is noticed that the DA1 and partly also the DA2 peak at low excitation densities seem to be composted of two peaks. It is possible that this splitting is due to the presence of FB transitions in addition to the DA transition. When the excitation density is increased these merge into one peak, possibly due to the Coulomb term that is responsible for a shift of DAP transitions. When the Coulomb contribution increases at higher excitation densities the DAP transition shift closer to the FB transition and they merge.
A μ–PL map stretching $25 \cdot 25$ μm^2 is measured with each excitation density. The mea-

surements are analysed by spectrally integrating each peak giving a PL intensity map for each transition under the four different excitation conditions.

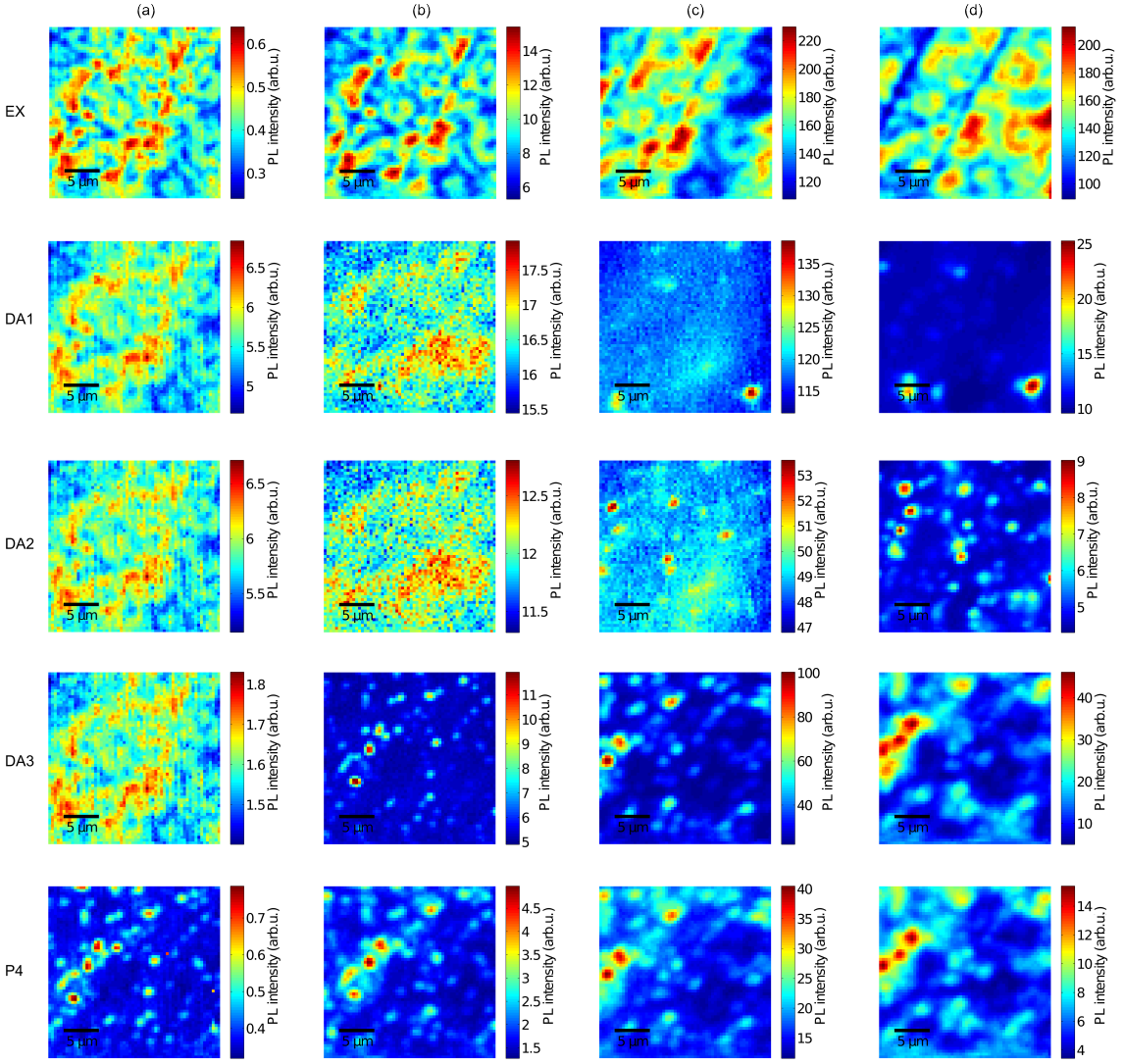

Figure B.2: Maps showing the spatial variations of the EX, DA1, DA2, DA3, and P4 transitions (see figure B.1) with increasing excitation density. The figure can be read as a table where each column corresponds to an excitation density with (a) $I_0 \approx 10^{20}$ s^{-1}cm^{-2}, (b) $\approx 75I_0$, (c) $\approx 920I_0$, (d) $\approx 4170I_0$, while each row contains a peak.

Figure B.2 collects all the maps with columns corresponding to the increasing excitation densities and rows containing the different peaks. One should be aware that small lateral shifts can be observed between measurements with different excitation densities. The easiest way to judge the shift is to locate the position of the three brightest dots in transition P4 in the last row. Such shifts are often observed when comparing measurements performed one after the other without moving the sample. It is believed that these small shifts, here in the order of a few μm, is caused by small thermal fluctuations. Such shifts can also contribute to deformation of the maps. When the sample is drifting during a scan this leads to elongation of the structures.
The number of maps in the figure might at first seem overwhelming, but several similarities between the maps are easily found. In order to understand the figure start by

the exciton map and compare the different excitation densities (a),(b),(c), and (d). For the lowest excitation density (a) and (b) the lateral structure recorded for the excitonic region appears more detailed with finer structures visible. As the excitation is increased the structures seem to smear out and the resolution appears decreased in (c) and (d). This could at first sight seem to be due to less ideal focus for the highest excitation measurement (d). This explanation can, however, be excluded, since fine structures with sizes close to the resolution limit are visible in the DA1 and DA2 transition from the same measurement (DA1(d), DA2(d)). A similar tendency has been observed earlier in a room temperature μ–PL study of Cu(In,Ga)Se_2, where it is found that the spatial extension of the measured structures seemed to increase with increasing excitation density [180]. One can speculate what the origin of this is. One possible explanation is that the high excitation conditions create a steep charge carrier concentration gradient in the excited area compared to the surroundings. This leads to stronger out–diffusion of charge carriers from the excited area. The area in which the charge carriers recombine therefore increases, giving rise to reduced resolution.
The second row in figure B.2 contains the maps of the DA1 transition. For low excitation densities the DA1 intensity is strongly correlated to the EX intensity with $C_c(DA1(a), EX(a)) = 0.93$. This relationship gradually disappears as the excitation is increased in (b) and (c). At the highest excitation density (d) it is found that the DA1 transition is spatially independent from the exciton with a correlation coefficient of $C_c(DA1(d), EX(d)) = -0.05$. The DA1 shows up in small bright spots, two of which having much higher intensity than the rest. When comparing the spatial variation of the DA1 peak to the other maps of measurement (d) it is furthermore found that it is spatially independent from the DA2 ($C_c(DA1(d), DA2(d)) = 0.2$) and the DA3 ($C_c(DA1(d), DA3(d)) = -0.07$). It is interesting that this behaviour could not be revealed at low excitation density. The explanation for this behaviour is, however, unclear.
The third row in figure B.2 contains the maps of the DA2 transition. For this transition the tendency is very similar to the one observed for the DA1 peak. At low intensity the peak appears to be spatially dependent on the exciton ((a) and (b)), as the excitation is increased in (c) and (d) it is revealed that the DA2 appears in spots of high PL intensity. In measurement (d) the DA2 peak is spatially uncorrelated to the exciton ($C_c(DA2(d), EX(d)) = -0.2$), the DA1 transition ($C_c(DA2(d), DA1(d)) = 0.2$) and largely uncorrelated to the DA3 transition ($C_c(DA2(d), DA3(d)) = 0.3$).
The fourth row of figure B.2 shows the maps of the spatial variation of the DA3 transition. A similar behaviour like the DA1 and DA2 transitions is observed. The main difference is that the DA3 transition appears with a spatially independent spotty structure already in (b) at lower excitation density than the DA1 and DA2. As mentioned previously the DA3 is spatially uncorrelated to the DA1 and DA2 transitions. This is also the case for the exciton transition where a correlation coefficient of $C_c(DA3(d), EX(d)) = 0.28$ is found for measurement (d). For the DA3 transition it is furthermore observed that the spatial resolution seems to decrease with increasing excitation as discussed for the exciton map. The transition labelled P4, is the same peak discussed in section 5.4.1. This peak is spatially highly correlated to the DA3 peak with a correlation coefficient of $C_c(P4(d), DA3(d)) = 0.95$ in map (d). It is therefore proposed that it is a phonon replica of the DA3. As observed for other transitions, it is found that the map smears out when increasing the excitation density. One interesting observation is that this transition appears as bright dots already in (a) at lower excitation density than the DA3 transition.
In summary it was observed that the maps tend to smear out when increasing the exci-

tation density. This loss of resolution might be related to the stronger diffusion due to a steeper gradient of the charge carrier concentration. This behaviour is most prominent for the excitonic recombination and the DA3/P4 peaks. For the DA1, DA2 and DA3 transitions it was found that their independent spatial variations only appears as the excitation is increased. At low excitation densities these peaks appear to be spatially correlated to the excitonic recombination. As the excitation is increased this dependency gradually disappears and it is found that they vary spatially independently form the other peaks.
The results presented here demonstrates that care must be taking when performing μ–PL experiments. The structure that appears in the subsequent evaluation depends strongly on the excitation density during the measurement. One therefore must take care when concluding on shapes of such structures obtained from μ–PL measurements.
The results presented here does, however, not alter the conclusions of the experiment presented in section 5.4.1 of the study of the spatial variation of the DA3 transition. Since a uncorrelated DA3 transition and the correlated phonon replica in different samples are measured with the same excitation density. The spatially uncorrelated DA3 transition could furthermore be seen with higher excitation density as also found here.

Physical Properties of Chalcopyrites

C

It is often desirable to be able compare experimental results to theoretical models. In order to apply the theory various physical properties of the material are needed. Table C.1 therefore contains a collection of various material properties that are applied in calculations and estimations throughout this work.

Material property	**$CuGaSe_2$**
m_e^*	$0.101m_0$[189] ,$0.14m_0$[79],$0.13m_0$ [66]
m_h^*	$0.64m_0$[68],$\|0.15m_0/\perp 0.47m_0$[66]
$\epsilon_r(0)$	11[80]
E_a	1.65 eV [144]
E_b	1.72 eV [144]
E_c	1.92 eV [144]
dE_g/dT (100–300K)	$-2 \pm 1 \cdot 10^{-4}$eVK^{-1} [48]
$\alpha(2.4eV)$	$1.05 \cdot 10^5$ cm^{-1} [144] $\approx 10^5$ cm^{-1}[190]
$\alpha^{-1}(2.4eV)$	95 nm [144]
$n_r(2.4eV)$	3.16 [144], $\approx$ 3.2 [190]
a	5.614 Å[25]
c	11.022 Å[25]
Material property	**$CuInSe_2$**
m_e^*	$0.09m_0$[65, 191] , $0.077m_0$[192], $\|0.08m_0/\perp 0.09m_0$[66]
m_h^*	$0.71m_0$[65, 193], $0.73m_0$[194],$\|0.66m_0/\perp 0.14m_0$[66]
$\epsilon_r(0)$	13.6 [81, 195, 196]
E_a	1.04 eV [144]
E_b	1.039 eV [144]
E_c	1.27 eV [144]
dE_g/dT (100–300K)	$-2 \pm 1 \cdot 10^{-4}$eVK^{-1} [65]
$\alpha(2.4eV)$	$1.81 \cdot 10^5$ cm^{-1} [144] $\approx 2 \cdot 10^5$ cm^{-1} [190, 197]
$\alpha^{-1}(2.4eV)$	55 nm [144]
$n_r(2.4eV)$	2.97 [144], $\approx$ 3.0 [190]
a	5.760 Å[24]
c	11.591 Å[24]

Table C.1: Various material properties of $CuInSe_2$ and $CuGaSe_2$. m_e^* and m_h^* are the effective electron and hole masses respectively, $\|$, and $\perp$ refer to the anisotropy of the effective masses. ϵ_r is the static relative dielectric constant. E_a, E_b, and E_c are the a, b, c fundamental band gaps (see figure 2.3). dE_g/dT is the variation of the band gap with increasing temperature. $\alpha(2.4eV)$ is the absorption coefficient at the laser wavelength. $\alpha^{-1}(2.4eV)$ is the inverse of the absorption coefficient which is an estimate of the penetration depth. $n_r(2.4eV)$ is the refractive index at the laser wavelength, a, and c are the lattice parameters.

Other Measurement Techniques

D

This appendix contains a brief description of the background necessary to understand the techniques applied in this work.

D.1 Energy dispersive X–ray Spectroscopy

Energy dispersive X–ray Spectroscopy in short EDS or EDX is a technique to measure the elemental composition of a material. EDS measurements are performed in an SEM equipped with a X–ray detector. The sample is irradiated with a high energy electron beam. The primary electrons, typically with energies in the range 5 keV – 30 keV, slow down when entering the material due to interaction with the atoms in the material. Core electrons in the deepest states are excited during this process. Typically one observes that electrons in the innermost shells (e.g. the K shell) are ejected leaving a hole in the shell. This is an energetically unfavourable configuration. A transition of an electron from a higher energetic outer state to the empty state in the K shell will therefore follow. The transition of an electron from an outer shell to the K shell leads to emission of characteristic X–rays with an energy equal to the energetic difference between the involved states. The X–rays observed due to the transition from the L shell to the K shell is called $K\alpha$. If an electron electron from the M state is involved one observes the $K\beta$ line etc. In a similar fashion it is possible to kick out an electron from the L shell after which an electron from the M shell recombines with the hole giving rise to the $L\alpha$ line [115].
Since the energy difference between the shells differ from element to element the characteristic X–ray lines can be utilized to identify the presence of an element in a material. The intensity of the characteristic lines depends on the amount of a given element present in the sample. Evaluation of the relative intensities of the lines therefore gives composition information about the composition of the sample. The accuracy of EDS for quantification of element concentrations is not excellent. One can expect an accuracy of about ± 5 % (relative) and a detection limit around 0.1 % (weight) under ideal conditions [115].
The information depth depends on the density of the material and the energy of the electron beam. When the energy of the beam is increased the probed volume gets larger. For thin Cu(In,Ga)Se_2 films of e.g. 400 nm it is necessary to use low energy electrons around of 7 keV in order to avoid a contribution to the results from to the GaAs substrate. The energy of the beam can, however, not be reduced further since one would otherwise lose accuracy since the necessary characteristic lines are not observable at low energies. In Cu(In,Ga)Se_2, the lower limit is around 7 keV, since the indium L line would otherwise not be observable [115].
Accuracy of EDS measurements are effected by several factors. Some of the problems that lead to reduced accuracy is the overlap of lines from different elements, influence of surface roughness, inhomogeneity of the probed volume etc. If the layer is e.g. inhomogeneous in depth the quantification of the results might be inaccurate. This is also an issue in Cu–rich material that contains a secondary Cu_xSe phase on the surface. In EDS measurements one typically performs a so-called ZAF correction in order to enhance the

accuracy. This correction takes into account the influence of three effects. These include the atomic number Z, which affects the efficiency of emission of characteristic X–rays due to scattering. A is a correction for re–absorption of X–rays emitted. The F correction takes into account that the count rate of one element can increase due absorption of X–rays and re–emission with another elements characteristic energy (X–ray fluorescence) [115]. Even when performing these corrections one has to be careful when interpreting results of EDS measurements. Effects induced by surface roughness, cracks or an inhomogeneous distribution of an element in depth is not corrected.

D.2 Electron Backscatter Diffraction

Electron Backscatter Diffraction (EBSD) is a technique used for e.g. determination of crystal orientation and quality on a microscopic scale. For polycrystalline Cu(In,Ga)Se_2 EBSD has for example been applied to identify individual grain orientations and study grain boundaries [198]. The technique is, however, not limited to study of grains, it has also many other applications such as examination of imperfections or strain.
The measurements are performed in an SEM equipped with an EBSD detector, which typically consist of a phosphor screen and a CCD camera. One measures electrons that are backscattered from the sample (deflected more than 90°). The back scattered electrons form an electron back scatter pattern also known as a Kikuchi pattern on the screen due to interaction of the electrons with the crystal lattice of the sample. The formation of the pattern can either be understood as diffraction or channelling of electrons.
When the electrons hit the atoms in the sample they are scattered in all directions. Under certain angles the scattered electrons will travel parallel to crystal planes. These electrons will channel thorough the material with low probability of further scattering events. Electrons scattered into angles with high packing density will on the other hand encounter further scattering events with high probability. These electrons are less likely to escape the material as back scattered electrons. The back scattered electrons will therefore form a pattern that depends on the lattice on which they are scattered. If one considers the electron as a wave rather than a particle the channelling effect can be understood as diffraction of the electrons on the lattice. Both explanations are complementary. In terms of the wave model back scattering occurs when the Bragg condition is fulfilled (see section D.3). EBSD can therefore be applied to obtain information about local crystal structure and orientation [116, 115].
EBSD is an extremely surface sensitive technique. The information depth depends on the energy of the electron beam and the material under investigation [116]. Once typically only obtain information from a depth of a few tens of nm [117, 115]. The lateral resolution of EBSD is influenced by the spot size of the electron beam and the tilt of the sample. Under a tilt angle of 70° the resolution perpendicular to the tilt axis is roughly three times the resolution parallel to the tilt axis. In various experiments a lateral resolution in the range 10–100 nm has been found [115].
It has been shown that quality of the EBSD pattern measured in terms of the number and sharpness of lines is an useful measure of crystal quality [116, 117]. It was for example found that the image quality decreases with increasing dislocation concentration in the sample [116]. The quality of the pattern furthermore depends on the surface of the sample. A rough surface will give rise to loss of pattern quality [117]. The pattern quality finally also depends on the instrument parameters. Shaper lines can e.g. be obtained

by increasing electron energy (increasing acceleration voltage) and lowering of chamber pressure [115].

D.3 X–ray Diffraction

X–ray diffraction (XRD) is a technique used to investigate the crystal structure of materials. X–rays with photon energies in the range 3 – 8 keV have a wavelength that is comparable to the inter atomic distances in crystals (0.15 – 0.4 nm). Diffraction effects are therefore observable when X–rays in this energy range are incident on a crystal. The X–rays elastically scattered by crystal planes interfere either constructively or destructively. The Bragg condition describes the conditions under which the diffracted X–rays with wavelength λ interfere constructively [199]:

$$2d_{hkl}sin\theta_B = n_i\lambda, \tag{D.1}$$

where n_i is an integer, λ is the wavelength of the X–rays, d_{hkl} is the inter-planar spacing for planes with the Miller indices hkl, and θ_B is the Bragg angle measured between the incoming beam and the sample surface. In a tetragonal lattice the inter–planar distances d_{hkl} between planes with Miller indices hkl is given by [199]:

$$\frac{1}{d_{hkl}^2} = \frac{h^2 + k^2}{a^2} + \frac{l^2}{c^2}, \tag{D.2}$$

where a and c are the lattice parameters.
The setup used in this work is commonly used for measurement of the Bragg reflections of a thin film uses a θ–2θ configuration. In this setup the sample is positioned in the center of the instrument and an X–ray beam is directed onto the sample with an angle θ relative to the surface of the layer. During the scan the angle of the incoming beam θ_{in} and the angle of detector relative to the sample surface θ_{out} are kept the same $\theta_{in} = \theta_{out}$. Since the angle between the incoming beam and the detected X–rays is 2θ, measurements done with this approach are known as θ–2θ scans. A scan is performed by moving the X–ray source and the detector with the same rate. To keep the θ–2θ geometry the source moves clockwise while the detector moves anti—clockwise. The quantity that is measured during the scan is the intensity of the X–rays that are scattered into the detector and the result is presented as I(2θ). Due to the geometry of the setup only the planes hkl that are parallel to the sample surface contribute to the measured signal [199].
For measurements performed in this work a parallel beam is used. A Cu X–ray tube with λ(Cu Kα_1) = 1.5406 Å and λ(Cu Kα_2) = 1.5444 Å is used as source [119].

D.4 Auger Electron Spectroscopy

Auger electron spectroscopy (AES) is a standard analysis technique used in surface physics for determining the elemental composition of the few outermost atomic layers of materials. AES is based on the analysis of kinetic energy of so–called Auger electrons ejected from core–levels in the material. Since the well defined energy of the ejected electrons can be related to specific core levels in atoms it is possible to identify the presence of different elements. AES is very surface sensitive, because of the very limited escape depth of electrons. Typically the probing depth is in the order 1-3 nm, depending on the kinetic energy of the electrons [138].

AES measurements are often performed with an electron gun, which supply a primary electron beam with energies in the range 2–5 keV. Alternatively an X–ray source can be applied to excite electrons in the material. The ejected Auger electrons created in the sample are commonly studied with hemispherical analysers that can resolve the kinetic energy of the electrons to generate an Auger spectrum. In cases where an ion sputtering system is integrated in the machine, it is furthermore possible to perform depth profiling experiments [138].
An Auger process is relatively complex involving several steps and electrons from different states. Step–by–step the process proceeds as follows: a deep core–level (K or L shell) in the atom is ionized by a primary electron. Both the primary electron and the core electron leave the atom with an ill-defined energy due to the complexity of the scattering process. The ionization is followed by a relaxation process in which an electron from an energetically higher–lying shell "falls" into the empty state. This process could give rise to emission of X–rays. The energy released in the relaxation process can alternatively be transferred to another electron, which is therefore ejected. When the latter happens the emitted electron is called an Auger electron. The energy of the Auger electron is very close to the X–ray that would alternatively have been emitted, but not exactly identical due to many body interactions in the ionized atom. Since the emitted electron has a well–defined energy related directly to the differences between the core–level energies the atom can be identified [138].
Auger processes are classified with a specific notation that reflects the core–levels involved in the process. An example of a typical Auger process is the KL_1L_2 process. In this case the primary electron ionizes the K shell, while an electron from the L_1 level relaxes into the empty state. The energy is transferred to an electron in the L_2 shell that is emitted. In this case the kinetic energy of the emitted electron will be $E_{kin} = E_K - E_{L_1} - E_{L_2} - \Delta E$, where E_K,E_{L_1} and E_{L_2} are the energies of the involved core–levels. ΔE is a correction term taking the many–electron effect, due to rearrangement in the ionized atom, into account [138].
In AES measurements the sensitivity limit is usually not better than 1 atomic %. AES is therefore not a technique used to study small amounts of surface impurities. Other disadvantages of AES is that the surface can have a composition that is quite different from the bulk material, due to contamination, oxidation, or processing. If the bulk of the material is of interest one have to be aware of this. Another problem of AES is that the high energy and high current density electron beam can create defects in semiconductors. High defect densities created this way have especially been observed in compound semiconductors [138].

D.5 X–ray Photoelectron Spectroscopy

X–ray Photoelectron Spectroscopy (XPS) is, much like AES, a technique for study of elemental composition of the topmost surface of a sample. In XPS measurements one takes advantage of the photoelectric effect. The sample is irradiated with mono energetic X–rays that possess enough energy to ionize the atoms by ejecting core–level electrons. By analysis of the kinetic energy of the emitted photo electrons one can determine their binding energy. The kinetic energy of the detected electrons E_K can be described with the simple relation: $E_K = \hbar\omega - E_B - \phi$, where $\hbar\omega$ is the (known) energy of the X–rays, E_B is the binding energy of the core–level electron and ϕ is the work function of the instrument.

Since the binding energy is specific to a particular core–level in a particular element, it is possible to determine the surface composition from a XPS measurement [138, 200].
XPS measurements are usually performed in ultra high vacuum chambers equipped with an X–ray source, an electron analyser and a detector system. X–rays with energies in the range 1.2 – 1.5 kV are commonly used (a Mg X–ray source with $\hbar\omega = 1253.6$ eV is used in this work). In systems where a monochromator is installed to decrease the linewidth of the X–ray beam, it is possible to observe small chemical shifts of peaks in the XPS spectra due to the chemical surrounding of the studied elements.
The information depth is, like for AES, related to the mean free path of the electrons in the material. This depends on the material under study (density, number of valence electrons and atomic mass) and the kinetic energy of the analysed electrons [139]. Typically the information depth ranges form 5 Å to a few 100 Å [138] depending on these parameters. Electrons liberated deeper inside the material will be either recaptured or inelastically scattered on their way to the surface and loose information about their origin. The scattered electrons form a background of low kinetic energy electron in the measurement [138, 200].
Problems with XPS are similar to AES in terms of surface contamination. One should also be aware that elemental quantification based on elements from different depth can be wrong if the elemental depth composition is heterogeneous. To be as accurate as possible, it is there better to consider contributions with similar kinetic energies when performing a quantification. Also one has to be aware that a higher amount of contamination with e.g. carbon or oxygen affect the low kinetic energy more than the high kinetic energy electrons. This can lead to problems when quantifying the results. Generally, quantification with XPS is 10 % relative accurate (i.e. a measurement of Cu content of 25 % has an uncertainty of $\pm 2.5\%$) [200, 138].

D.6 Secondary Ion Mass Spectroscopy

Secondary ion mass spectroscopy (SIMS) is a technique for the study of the elemental composition of a surface. In SIMS ions e.g. Cs^+ are incident on the sample surface, typically with energies between 1 and 10 keV. When the primary ion hits the surface its energy is transferred to the atoms and molecules in the layer. A cascade of collisions in the material then leads to emission of small molecules or ions called secondary ions. These secondary ions are accelerated from the surface by an applied voltage before entering in an analyser and detector system. As analyser a time–of–flight or quadrupole mass spectrometer are commonly used to separate the ions with different mass/charge ratio. Elements present in the surface can therefore be identified by its mass. One distinguishes between dynamic SIMS and static SIMS. In static SIMS a low primary beam current (10^{-9} – 10^{-9} A/cm^2) is used and the sputter rate is kept low (the order of 10^{-5} – 10^{-4} monolayers per second). Only the topmost surface layers are therefore studied in this mode of operation. In dynamic SIMS beam current is increased to (10^{-5} – 10^{-4} A/cm^2) leading to an increased sputter rate (several monolayers per second). The surface is therefore removed layer by layer in this mode of operation. In this mode of operation it is possible to obtain a depth profile of the chemical composition of the sample [138].
The SIMS technique is generally sensitive to very low element concentrations in the layer. The detection limit is, however, strongly dependent on the analysis conditions. For an idea of the approximate order of magnitude, the setup for this work has a detection limit

for As in Si of $7 \cdot 10^{15}$ cm^{-3} when As is detected as As^- ions. The detection limit can, however, be expected to be different in the measurement presented in this work since no Si is present in the sample. In the measurement the elements are additionally detected as MCs^+ molecular ions, where M here is an element in the matrix. One can expect the detection limit of this ion to be different from the single M^+ ions. In order to determine the exact detection limit under the conditions used in SIMS measurements further detailed studied should be performed [201].
One of the major problems of SIMS is the so–called matrix effect. This complicates quantitative analysis. The problem relates to the fact that the yield of secondary ions depends on the matrix composition. If the composition e.g. changes in depth, so does the yield of the different ions making it very difficult to quantify the results. The matrix effect essentially leads to a non–linear relationship between the concentration of an element in the matrix and its yield. One approach, which is found to reduce this effect is to bombard the sample with Cs^+ ions and detect the molecular MCs^+ ions rather than M^+ ions. It was realized that this approach leads to a more or less linear relationship between the concentration of an element in the matrix and the measured secondary ion yield [202]. Since this approach reduces the matrix effect it is applied in this work.

D.7 Cathodoluminescence

The term cathodoluminescence (CL) describes the process of light emission as the result of electron bombardment. In general when a sample is irradiated with a beam of primary electrons several other processes occur. Some of the primary electrons are absorbed in the material and loose their kinetic energy through various electronic excitations. When the excited electrons in the material relax, this leads to emission of characteristic X–rays (used in EDS), Auger electrons and photons in the spectral range from ultraviolet to infra–red depending on the material (cathodoluminescence). The incident electrons can be also elastically backscattered or inelastically scattered giving rise to generation of secondary electrons in the material. When scanning the primary election beam across the sample surface and collecting these electrons an image of the surface morphology can be obtained (SEM imaging). All these processes can be utilized to obtain information about the structural, chemical and optoelectronic properties of the sample with high spatial resolution [203, 204].
Performance of CL experiments requires a high vacuum chamber. Typically CL measurements are performed with an apparatus similar to the one used for SEM measurements equipped with optical windows, a monochromator and detector. In order to avoid using high electron beam powers an efficient system for collection of the emitted photons must be used. One approach is to utilize a semiellopsiodal mirror, where the sample is placed in one focal point. The luminescence is then collected in the second focal point and coupled into an optical fiber bringing it to the detection system [204].
The CL phenomenon is very similar to photoluminescence with the main difference being that electron–hole pairs are created due to electron irradiation instead of light irradiation. Most of the general theory of PL described in section 2.3 therefore also applies to CL. The characteristic EX and DAP transitions observed in $CuGaSe_2$ and $CuInSe_2$ are similarly found in CL measurements [91, 205]. Possible differences between PL and CL lies in the details of the electron–hole pair creation such as different generation rate and excitation volume [203, 204]. Excitation of a semiconductor by an electron beam generally leads to

emission via all the luminescence mechanisms available in the material. In PL, on the other hand one can observe a dependence of the luminescence on the excitation wavelength. This effect, that is investigated with photoluminescence excitation spectroscopy, can not be utilized in CL experiments. An advantage of CL compared to PL is that in–depth variation can by studied by variation of the primary electron beam energy [203].
The spatial resolution of CL intensity maps depends on the energy of the primary electron beam. In order to achieve a small generation volume it is necessary to reduce the energy of the primary energy electrons as much as possible. A high lateral resolution of around 40 nm e.g. can be obtained with a primary electron beam energy of 2 keV [206]. This resolution will of course decrease if the conditions are not ideal (e.g. if the electron beam is not ideally focused). When performing CL experiments it is advantageous to be able to record a full CL spectrum for each scan pixel ($I_{CL}(x, y, \lambda)$). This approach also called cathodoluminescence wavelength imaging opens the possibility to investigate various effects. It is for example possible to study quantum confinement effects in quantum wells and lateral band gap variations [207].
One of the main advantages of the CL technique is that it is possible to utilize the complementary modes of operation of the SEM equipment. When measuring a CL map, collection of the secondary electrons is used to form an SEM image of the surface. In this way one directly obtains information about the morphology of the studied sample. In equipment with a X–ray detector for EDS measurements one can additionally study the chemical composition of the area investigated with CL. This is a great option since it can be valuable to compare to the optoelectronic properties obtained by CL with the morphology or chemical composition [203].

Sample Names

E

Figure	Sample name
2.6	CISe-epi092,093,094,095,096,098,099
2.10	CGSe-epi034,035,036,045,048
3.4	CGSe-epi009,017,028
3.7	CISe-epi017,020,021,022
3.8	CGSe-epi079,080,081,082,083,084,085
3.9	CGSe-epi046
3.10	CGSe-epi069,CISe-epi151
3.12	CGSe-epi071
3.13	CGSe-epi005,054
3.14 , 3.16, 3.17, 3.23, 3.24 3.15, 3.18	CGSe-epi062
3.19	CGSe-epi052
3.21	CGSe-epi062,063,064,065,069
3.22	CGSe-epi069
3.25	CGSe-epi062,082
3.26	CISe-epi033,CGSe-epi062
4.3,4.4,4.5,4.7	CGSe-epi046,049,058,059,061,094
4.6	CGSe-epi061
4.9	CGSe-epi094, CISe-epi082
4.10, 4.12	CGSe-epi094
4.11	CISe-epi082
5.2 5.3	CGSe-epi061
5.6	CGSe-epi0112
5.7	CGSe-epi0162
5.8	CGSe-epi054
5.9	CGSe-epi109,134
5.10	CGSe-epi061
5.11	CGSe-epi067
5.12	CGSe-epi054,061
5.13,5.14	CGSe-epi054
5.15	CGSe-epi129,130,131,134
5.16	CGSe-epi054,061, YA104, YA105

Table E.1: Names of samples studied in each figure for future reference.

List of Publications and Conferences

F

Publications

- J. K. Larsen, L. Gütay, S. Siebentritt: Influence of secondary phase Cu_xSe on the optoelectronic quality of chalcopyrite thin films, *Applied Physics Letters*, **98**, 201910–201910–3 (2011)
- J. K. Larsen, L. Gütay, Y. Aida, S. Siebentritt: Spatial variations of optoelectronic properties in single crystalline $CuGaSe_2$ thin films studied by photoluminescence, *Thin Solid Films*, **519(21)**, 7332–7336 (2011)
- J. K. Larsen, L. Gütay, S. Siebentritt: Temperature dependence of potential fluctuations in chalcopyrites, *Proceedings of the 37th IEEE Photovoltaic Specialists Conference*, Seattle, USA (2011)
- L. Gütay, J. K. Larsen, J. Guillot, M. Müller, F. Bertram, J. Christen, S. Siebentritt: MOVPE of $CuGaSe_2$ on GaAs in the presence of a Cu_xSe secondary phase, *Journal of Crystal Growth*, **315(1)**, 82–86 (2010)
- M. Steichen, J. K. Larsen, L. Gütay, S. Siebentritt, P.J. Dale: Preparation of $CuGaSe_2$ absorber layers for thin film solar cells by annealing of efficiently electrodeposited Cu–Ga precursor layers from ionic liquids, *Thin Solid Films*, **519(21)**, 7254 – 7258 (2011)
- J. Fischer, J. K. Larsen, J–C. Lambrechts, S. Siebentritt, P. J. Dale: Pressure dependent synthesis of $CuInSe_2$ thin film solar cells from electrodeposited binary selenide stacks, *Proceedings of the 37th IEEE Photovoltaic Specialists Conference*, Seattle, USA (2011)
- L. Gütay, D. Regesch, J. K. Larsen, Y. Aida, A. Redinger, S. Caneva, S. Schorr, C. Stephan, S. Siebentritt: Experimental test of the theoretical feedback loop to stabilize the band gap in chalcopyrites, *Submitted*, (2011)
- E. Korhonen, K. Kuitunen, F. Tuomisto, A. Urbaniak, M. Igalson, J. K. Larsen, L. Gütay, S. Siebentritt: Vacancy defects in epitaxial thin–film $CuGaSe_2$ and $CuInSe_2$, *Submitted*, (2011)
- L. Gütay, D. Regesch, J. K. Larsen, Y. Aida, S. Siebentritt: Influence of copper excess on the absorber quality of $CuInSe_2$, *Submitted to Applied Physics Letters*, (2011)
- A. Krysztopa, M. Igalson, L. Gütay, J. K. Larsen, Y. Aida: Defect Signatures in Copper Gallium Diselenide, *Proceedings of the 37th IEEE Photovoltaic Specialists Conference*, Seattle, USA (2011)
- A. Krysztopa, M. Igalson, P. Zabierowski, J. K. Larsen, Y. Aida, S. Siebentritt, L. Gütay: Defect levels in $CuGaSe_2$ by modulated photocurrent spectroscopy , *Thin Solid Films*, **519(21)**, 7308–7311 (2011)

- V. Depredurand, Y. Aida, J. K. Larsen, T. Eisenbarth, A. Majerus, S. Siebentritt: Surface Treatment of CIS Solar Cells Grown Under Cu-Excess, *Proceedings of the 37th IEEE Photovoltaic Specialists Conference*, Seattle, USA (2011)
- Y. Aida, V. Depredurand, J. K. Larsen, H. Arai, T. Eisenbarth, A. Majerus, S. Siebentritt: Improved CIS solar cells with absorbers grown under Cu–excess, *Proceedings of the 26th EU PVSEC conference*, Hamburg, Germany (2011)

Conference Contributions

- Euromat 2011 – European Congress and Exhibition on Advanced Materials and Processes, September 12–15, 2011, Montpellier, France.
- 37th IEEE Photovoltaic Specialist Conference, June 19–24, 2011, Seattle, USA.
- 15th International Conference on Metal Organic Vapor Phase Epitaxy (ICMOVPE), May 23–28, 2010, Lake Tahoe, USA.
- European Materials Research Society (EMRS), June 8–10, 2010, Strasbourg, France.

Acronyms and Symbols

G

Acronyms

AES	Auger Electron Spectroscopy
BB	Band–to–Band Recombination
BI	Band–Impurity Recombination
BX	Bound Exciton
CB	Conduction Band
CCD	Charge Coupled Device
$CuGaSe_2$	Copper Galium Selenide
$CuInSe_2$	Copper Indium Selenide
$Cu(In,Ga)Se_2$	Copper Indium Galium Selenide
$Cu(In,Ga)(S,Se)_2$	Copper Indium Galium Sulphur Selenide
CL	Cathodoluminescence
CpCuTEP	Cyclopentadienyl-Copper-Triethylphosphine
Cu_xSe	Copper Selenide
DA	Donor–Acceptor Pair recombination
DAP	Donor–Acceptor Pair
DOS	Density of States
DP	Deep luminescence peak (Dirt Peak)
DTBSe	Ditertiarybutylselenium
EBSD	Electron backscatter diffraction
EDS	Energy Dispersive X-ray Spectroscopy
FB	Free–to–Bound recombination
FX	Free Exciton
ICDD	International Centre for Diffraction Data
MFC	Mass Flow Controller

MOVPE	Metal Organic Vapour Phase Epitaxy
ODC	Ordered Defect Compound
PC	Pressure Controller
PF	Potential Fluctuations
PL	Photoluminescence
PVD	Physical Vapour Deposition
SEM	Scanning Electron Microscopy
SIMS	Secondary Ion Mass Spectroscopy
TEM	Transmission Electron Microscopy
TI	Tail–Impurity Recombination
TEGa	Triethylgallium
TMI	Trimethylindium
VB	Valence Band
XPS	X–ray Photoelectron Spectroscopy
XRD	X–ray Diffraction
μ**–PL**	Micrometer Resolved Photoluminescence

Symbols

a	Lattice constant of the unit cell short axis
a_B	Effective Bohr radius
$A(\hbar\omega)$	Absorptivity
A^*	Absorption coefficient prefactor in equation (5.10)
b	Proportionality constant in equation (2.12)
bt	Bose term defined in equation (5.8)
c	Lattice constant of the unit cell long axis
c_l	Speed of light, $c_l = 299792458\ \mathrm{m{\cdot}s^{-1}}$
C	Constant introduced in equation (5.2)
C_c	Cross–correlation coefficient
C_{xy}	Element xy in elastic stiffness tensor
d	Layer thickness

d_c	Critical thickness
d_{hkl}	Distance between lattice planes with Miller indices *hkl*
e	Elementary charge, $e = 1.6022 \cdot 10^{-19}$ C
E_a	The fundamental *a* band gap
E_{act}	Activation energy
E_A	Acceptor ionization energy
E_b	The fundamental *b* band gap
E_B	Binding energy
E_{BX}	Binding energy of bound exciton
E_c	The fundamental *c* band gap
E_C	Coulomb energy
E_D	Donor ionization energy
E_{Fn}	Quasi–Fermi level for electrons
E_{Fp}	Quasi–Fermi level for holes
E_{FX}	Binding energy of free exciton
E_g	Band gap
E_K	Kinetic energy of electron
E_{th}	Optical threshold energy
f_n	Fermi distribution of electrons
f_p	Fermi distribution of holes
G	Generation rate
$\hbar$	Reduced Planck constant, $\hbar = 1.0546 \cdot 10^{-34}$ m$^2\cdot$ s$^{-1}\cdot$ kg
$\hbar\omega$	Photon energy
$I_{PL}(\hbar\omega)$	Energy dependent photoluminescence intensity (PL spectrum)
j	Photon current density
k	Exponent in equation (2.11)
K	Degree of compensation
k_B	Boltzmann constant, $k_B = 1.3806 \cdot 10^{-23}$ m$^2\cdot$ kg$\cdot$ s$^{-2}\cdot$ K^{-1}
m	Lattice mismatch
m_{GT}	Lattice mismatch at growth temperature

m_0	Electron rest mass, $m_0 = 9.109 \cdot 10^{-31}$ kg
m_e^*	Electron effective mass
m_h^*	Hole effective mass
m_r	Reduced effective mass
n	Free electron concentration
n_i	Integer in equation (D.1)
n_r	Index of refraction
NA	Numerical aperture
N_A	Acceptor concentration
N_C	Total charged defect concentration
N_D	Donor concentration
N_M	Mott concentration
n_q	Quantum number
p	Free hole concentration
p_{bub}	Metalorganic bubbler pressure
p_{Cu}	Partial pressure of Cu in reactor
p_{Ga}	Partial pressure of Ga in reactor
p_{In}	Partial pressure of In in reactor
p_{MO}	Partial pressure of metalorganic
p_{Se}	Partial pressure of Se in reactor
p_R	Reactor pressure
$p_v(T)$	Metalorganic vapour pressure at temperature T
P_{exc}	Excitation density
Q_s	Flow through metalorganic source
Q_{tot}	Total gas flow through reactor
r	Distance
r_g	Growth rate
R	Degree of relaxation
R_f	Length of potential fluctuations
R_{I-VI}	Bond length of group I element to group VI element

R_{III-VI}	Bond length of group III element to group VI element
R_s	Screening length
S	Huang-Rhys parameter
t	Time
T	Temperature
T_{bub}	Temperature of bubbler
u	Anion position in unit cell
V_{oc}	Open circuit voltage
α	Absorption coefficient
α_a	Thermal expansion coefficient along a–axis
α_c	Thermal expansion coefficient along c–axis
β	Peak shift with excitation density in equation (2.16)
γ	Average amplitude of potential fluctuations
Δ_{CF}	Crystal field splitting
Δ_{FWHM}	Full width at half maximum of distribution
Δ_{max}	Total width of distribution
Δ_{SO}	Spin–orbit splitting
η	Tetragonal distortion
θ_B	Bragg angle
ϵ_r	Static relative dielectric constant
ϵ_0	Permittivity of free space, $\epsilon_0 = 8.854 \cdot 10^{-12}\ \mathrm{C^2{\cdot}N^{-1}{\cdot}m^{-2}}$
$\epsilon_{\perp,c}$	Strain of the c–axis with the c-axis being perpendicular to substrate surface
$\epsilon_{\parallel,c}$	Strain of the c–axis with the c-axis being parallel to substrate surface
$\epsilon_{\parallel,a}$	Strain of the a–axis with the a-axis being parallel to substrate surface
θ	Angle relative to sample surface in XRD measurement
λ	Wavelength of light
μ	Quasi–Fermi level splitting
τ	Minority charge carrier life time
ϕ	Work function
Ω	Solid angle
ω	Angular frequency of light

Bibliography

[1] H. Hahn, G. Frank, W. Klingler, A.D. Meyer, and G. Störger. Untersuchungen über ternäre chalkogenide. V. Über einige ternäre chalkogenide mit chalkopyritstruktur. *Zeitschrift für anorganische und allgemeine Chemie*, 271(3-4):153–170, 1953.

[2] J.L. Shay, S. Wagner, and H.M. Kasper. Efficient $CuInSe_2$/CdS solar cells. *Applied Physicis Letters*, 27(2):89–90, 1975.

[3] W.N. Shafarman, S. Siebentritt, and L. Stolt. *Handbook of photovoltaic science and engineering*. John Wiley & Sons Inc, 2011.

[4] P. Jackson, D. Hariskos, E. Lotter, S. Paetel, R. Wuerz, R. Menner, W. Wischmann, and M. Powalla. New world record efficiency for Cu(In,Ga)Se_2 thin–film solar cells beyond 20%. *Progress in Photovoltaics: Research and Applications*, In press:–, 2011.

[5] G. Hering. Expanding frontier. *Photon International*, April:158–168, 2011.

[6] M.A. Green, K. Emery, Y. Hishikawa, and W. Warta. Solar cell efficiency tables (version 37). *Progress in Photovoltaics: Research and Applications*, 19(1):84–92, 2011.

[7] Q-Cells. Q-Cells achieves with 13.4% new efficiency world record for CIGS thin film solar module out of mass production, Press Release from March 29, 2011.

[8] R. Scheer and H.W. Schock. *Chalcogenide Photovoltaics: Physics, Technologies, and Thin Film Devices*. Wiley-VCH, 2011.

[9] S. Siebentritt. What limits the efficiency of chalcopyrite solar cells? *Solar Energy Materials and Solar Cells*, 95(6):1471–1476, 2011.

[10] S. Siebentritt and U. Rau. *Wide–Gap Chalcopyrites*. Springer Berlin, Heidelberg, New York, 2006.

[11] L. Gütay, C. Lienau, and G.H. Bauer. Subgrain size inhomogeneities in the luminescence spectra of thin film chalcopyrites. *Applied Physics Letters*, 97:052110, 2010.

[12] L. Gütay and G.H. Bauer. Local fluctuations of absorber properties of Cu(In,Ga)Se_2 by sub–micron resolved PL towards real life conditions. *Thin Solid Films*, 517(7):2222–2225, 2009.

[13] A. Bauknecht, S. Siebentritt, J. Albert, and M.C. Lux-Steiner. Radiative recombination via intrinsic defects in $CuGaSe_2$. *Journal of Applied Physics*, 89:4391, 2001.

[14] S. Siebentritt, N. Rega, A. Zajogin, and M.C. Lux-Steiner. Do we really need another PL study of $CuInSe_2$? *physica status solidi (c)*, 1(9):2304–2310, 2004.

[15] I. Dirnstorfer, Mt. Wagner, D.M. Hofmann, M.D. Lampert, F. Karg, and B.K. Meyer. Characterization of CuIn(Ga)Se_2 Thin Films III. In-rich layers. *phys. stat. sol. a*, 168:163–, 1998.

[16] J.H. Werner, J. Mattheis, and U. Rau. Efficiency limitations of polycrystalline thin film solar cells: case of Cu(In,Ga)Se_2. *Thin Solid Films*, 480:399–409, 2005.

[17] S. Siebentritt, N. Papathanasiou, and M.C. Lux-Steiner. Potential fluctuations in compensated chalcopyrites. *Physica B: Condensed Matter*, 376:831–833, 2006.

[18] S. Siebentritt and S. Schuler. Defects and transport in the wide gap chalcopyrite $CuGaSe_2$. *Journal of Physics and Chemistry of Solids*, 64(9-10):1621–1626, 2003.

[19] J.K. Larsen, L. Gütay, and S. Siebentritt. Influence of secondary phase Cu_xSe on the optoelectronic quality of chalcopyrite thin films. *Applied Physics Letters*, 98 (20)(20):201910–201910–3, 2011.

[20] K. Sakurai, R. Hunger, R. Scheer, C.A. Kaufmann, A. Yamada, T. Baba, Y. Kimura, K. Matsubara, P. Fons, and H. Nakanishi. In situ diagnostic methods for thin–film fabrication: utilization of heat radiation and light scattering. *Progress in Photovoltaics: Research and Applications*, 12(2-3):219–234, 2004.

[21] M. Powalla, M. Cemernjak, J. Eberhardt, F. Kessler, R. Kniese, H.D. Mohring, and B. Dimmler. Large–area CIGS modules: Pilot line production and new developments. *Solar energy materials and solar cells*, 90(18-19):3158–3164, 2006.

[22] R. Noufi, Y. Yan, J. Abu-Shama, K. Jones, M. Al-Jassim, B. Keyes, J. Alleman, and K. Ramanathan. Investigation of the microstructure of Cu(In,Ga)Se_2 thin films used in high–efficiency devices. In *Proceedings of the 29th IEEE Photovoltaic Specialists Conference*, pages 508–510, 2002.

[23] J.L. Shay and J.H. Wernick. *Ternary Chalcopyrite Semiconductors: Growth, electronic properties, and Applications*. Pergamon Press, Oxford, 1975.

[24] M. Rabadanov and I.A. Verin. X–ray diffraction study of $CuInSe_2$ single crystals. *Inorganic materials*, 34(1):14–16, 1998.

[25] L. Mandel, R.D. Tomlinson, and M.J. Hampshire. Crystal data for $CuGaSe_2$. *Journal of Applied Crystallography*, 10(2):130–131, 1977.

[26] A. Zunger and J.E. Jaffe. Structural origin of optical bowing in semiconductor alloys. *Physical Review Letters*, 51(8):662–665, 1983.

[27] C.H. Chang, S.H. Wei, W. Johnson, R. Bhattacharya, B. Stanbery, T. Anderson, and R. Duran. Long and Short Range Ordering of $CuInSe_2$. *Japanese Journal of Applied Physics Supplement*, 39:411–412, 2000.

[28] J.E. Jaffe and A. Zunger. Anion displacements and the band–gap anomaly in ternary ABC_2 chalcopyrite semiconductors. *Physical Review B*, 27(8):5176, 1983.

[29] J.C. Mikkelsen. Ternary phase relations of the chalcopyrite compound $CuGaSe_2$. *Journal of Electronic Materials*, 10(3):541–558, 1981.

[30] T. Godecke, T. Haalboom, and F. Ernst. Phase equilibria of Cu–In–Se. I. Stable states and nonequilibrium states of the In_2Se_3–Cu_2Se subsystem. *Zeitschrift für Metallkunde*, 91(8):622–634, 2000.

[31] B.J. Stanbery. Copper indium selenides and related materials for photovoltaic devices. *Critical reviews in solid state and materials sciences*, 27(2):73–117, 2002.

[32] I.V. Bodnar. Growth, transmission spectra, and thermal expansion of $CuGa_3$ Se_5 single crystals. *Inorganic Materials*, 44(2):104–109, 2008.

[33] G. Marin, S.M. Wasim, C. Rincon, G.S. Perez, P. Bocaranda, I. Molina, R. Guevara, and J.M. Delgado. Crystal growth, structural, and optical characterization of the ordered defect compound $CuGaSe_2$. *Journal of applied physics*, 95:8280, 2004.

[34] M.I. Alonso, M. Garriga, CA Durante Rincón, E. Hernández, and M. León. Optical functions of chalcopyrite $CuGa_xIn_{1-x}Se_2$ alloys. *Applied Physics A: Materials Science & Processing*, 74(5):659–664, 2002.

[35] H. Gao and W.D. Nix. Surface roughening of heteroepitaxial thin films. *Annual Review of Materials Science*, 29(1):173–209, 1999.

[36] M. Grundmann. *The Physics of Semiconductors: An Introduction Including Devices and Nanophysics*. Springer Berlin Heidelberg New York, 2006.

[37] S. Siebentritt, M. Igalson, C. Persson, and S. Lany. The electronic structure of chalcopyrites: bands, point defects and grain boundaries. *Progress in Photovoltaics: Research and Applications*, 18(6):390–410, 2010.

[38] W. Bollmann. *Crystal defects and crystalline interfaces*. Springer Berlin, 1970.

[39] S.B. Zhang, S.H. Wei, A. Zunger, and H. Katayama-Yoshida. Defect physics of the $CuInSe_2$ chalcopyrite semiconductor. *Physical Review B*, 57(16):9642, 1998.

[40] C. Persson, Y.J. Zhao, S. Lany, and A. Zunger. n-type doping of $CuInSe_2$ and $CuGaSe_2$. *Physical Review B*, 72(3):035211, 2005.

[41] R. Suzuki, T. Ohdaira, S. Ishibashi, A. Uedono, S. Niki, PJ Fons, A. Yamada, T. Mikado, T. Yamazaki, and S. Tanigawa. Characterization of intrinsic defects in $CuInSe_2$ films by monoenergetic positron beams. In R. D. Tomlinson, A. E. Hill, and R. D. Pilkington, editors, *Institute of Physics Conference Series 152*, volume 152, pages 757–760. Bristol [England]; Boston: Adam Hilger, Ltd., c1985-, 1998.

[42] E. Korhonen, K. Kuitunen, F. Tuomisto, A. Urbaniak, M. Igalson, J.K. Larsen, L. Gütay, and S. Siebentritt. Vacancy defects in epitaxial thin–film $CuGaSe_2$ and $CuInSe_2$. *Submitted*, -:–, 2011.

[43] A.E. Romanov, W. Pompe, G.E. Beltz, and J.S. Speck. An approach to threading dislocation reaction kinetics. *Applied physics letters*, 69:3342, 1996.

[44] L.B. Freund. A criterion for arrest of a threading dislocation in a strained epitaxial layer due to an interface misfit dislocation in its path. *Journal of Applied Physics*, 68(5):2073–2080, 1990.

[45] L. Liu and J.H. Edgar. Substrates for gallium nitride epitaxy. *Materials Science and Engineering: R: Reports*, 37(3):61–127, 2002.

[46] R. Hull and J.C. Bean. Misfit dislocations in lattice-mismatched epitaxial films. *Critical reviews in solid state and materials sciences*, 17(6):507–546, 1992.

[47] C.H. Lei, A.A. Rockett, I.M. Robertson, N. Papathanasiou, and S. Siebentritt. Interface reactions and Kirkendall voids in metal organic vapor-phase epitaxy grown Cu(In,Ga)Se_2 thin films on GaAs. *Journal of applied physics*, 100:114915, 2006.

[48] A. Bauknecht. *$CuGaSe_2$ für die Anwendung in der Photovoltaik – Metallorganische Gasphasenepitaxie und Optische Charakterisierung*. PhD thesis, Freie Universität Berlin, 1999.

[49] D.J. Dunstan, S. Young, and R.H. Dixon. Geometrical theory of critical thickness and relaxation in strained–layer growth. *Journal of applied physics*, 70(6):3038–3045, 1991.

[50] D. Dunstan. *Semiconductor Heteroepitaxy: Growth Characterization and Device Applications*. World Scientific Publishing, 1996.

[51] E.D. Pierron, D.L. Parker, and J.B. McNeely. Coefficient of Expansion of GaAs, GaP, and Ga (As, P) Compounds from-62 degrees to 200 degrees C. *Journal of Applied Physics*, 38(12):4669–4671, 1967.

[52] P. Kistaiah, Y.C. Venudhar, K.S. Murthy, L. Iyengar, and K.V. Rao. Temperature dependence of tetragonal distortion and thermal expansion of copper indium selenide. *Journal of Physics D: Applied Physics*, 14:1311, 1981.

[53] H.G. Brühl, H. Neumann, T. Pfeiffer, and G. Kühn. Anisotropic thermal expansion of Cu–III–VI2 compounds. *physica status solidi (a)*, 66(2):597–600, 1981.

[54] H.G. Bruhl and H. Neumann. Thermal expansion of $CuGaSe_2$. *Solid State Communications*, 34(4):225–227, 1980.

[55] T. Soma, J. Satoh, and H. Matsuo. Thermal expansion coefficient of GaAs and InP. *Solid State Communications*, 42(12):889–892, 1982.

[56] S. Adachi. *Properties of Gallium Arsenide, 3rd Edition, p. 23*. Inspec/IEE, 1996.

[57] S. Shirakata and S. Chichibu. Photoreflectance of Cu-based I–III–VI2 heteroepitaxial layers grown by metalorganic chemical vapor deposition. *Journal of applied physics*, 79(4):2043–2054, 1996.

[58] J. Lazewski, H. Neumann, P.T. Jochym, and K. Parlinski. Ab initio elasticity of chalcopyrites. *Journal of applied physics*, 93:3789, 2003.

[59] N. Rega. *Photolumineszenz von epitaktischen Cu(In,Ga)Se_2-Schichten*. PhD thesis, Freie Universität Berlin, 2004.

[60] N. Shibata, A. Ohki, S. Zembutsu, and A. Katsui. Thermoelastic strain in ZnSe films grown on GaAs by metalorganic vapor phase epitaxy. *Japanese journal of applied physics*, 27(4):L487–L489, 1988.

[61] Y. Harada, H. Nakanishi, and S.F. Chichibu. Structural studies of Cu–III–VI chalcopyrite semiconductor heteroepitaxial films grown by low-pressure metalorganic vapor phase epitaxy. *Journal of Applied Physics*, 89:5406, 2001.

[62] S. Shirakata, S. Isomura, and S. Chichibu. Photoreflectance Characterization of Lattice Strain in Wide-Gap Cu-III-VI2 Epitaxial Layers. *Transactions of the Materials Research Society of Japan*, 20:782–785, 1996.

[63] J.I. Pankove. *Optical processes in semiconductors*. Dover publications, 1975.

[64] P.Y. Yu and M. Cardona. *Fundamentals of semiconductors: physics and materials properties*. Springer Verlag, 4th edition, 2010.

[65] H. Neumann. Optical properties and electronic band structure of $CuInSe_2$. *Solar cells*, 16:317–333, 1986.

[66] C. Persson. Anisotropic hole–mass tensor of $CuIn_{1-x}Ga_x(S,Se)_2$: Presence of free carriers narrows the energy gap. *Applied Physics Letters*, 93(7):072106–072106, 2008.

[67] M.V. Yakushev, R.W. Martin, A. Babinski, and A.V. Mudryi. Effects of magnetic fields on free excitons in $CuInSe_2$. *physica status solidi (c)*, 6(5):1086–1088, 2009.

[68] F. Luckert, M.V. Yakushev, C. Faugeras, A.V. Karotki, A.V. Mudryi, and R.W. Martin. Diamagnetic shift of the A free exciton in $CuGaSe_2$ single crystals. *Applied Physics Letters*, 97(16):162101–162101, 2010.

[69] S. Niki, H. Shibata, P.J. Fons, A. Yamada, A. Obara, Y. Makita, T. Kurafuji, S. Chichibu, and H. Nakanishi. Excitonic emissions from $CuInSe_2$ on GaAs(001) grown by molecular beam epitaxy. *Applied physics letters*, 67:1289, 1995.

[70] S. Chichibu, T. Mizutani, K. Murakami, T. Shioda, T. Kurafuji, H. Nakanishi, S. Niki, P.J. Fons, and A. Yamada. Band gap energies of bulk, thin-film, and epitaxial layers of $CuInSe_2$ and $CuGaSe_2$. *Journal of Applied Physics*, 83:3678, 1998.

[71] R.J. Elliott. Intensity of optical absorption by excitons. *Physical Review*, 108(6):1384, 1957.

[72] J.R. Haynes. Experimental proof of the existence of a new electronic complex in silicon. *Physical Review Letters*, 4(7):361–363, 1960.

[73] H. Atzmüller, F. Fröschl, and U. Schröder. Theory of excitons bound to neutral impurities in polar semiconductors. *Physical Review B*, 19(6):3118, 1979.

[74] R.R. Sharma and S. Rodriguez. Theory of excitons bound to ionized impurities in semiconductors. *Physical Review*, 153(3):823, 1967.

[75] T. Schmidt, K. Lischka, and W. Zulehner. Excitation-power dependence of the near-band-edge photoluminescence of semiconductors. *Physical Review B*, 45(16):8989, 1992.

[76] H. Neumann, W. Hörig, E. Reccius, W. Möller, and G. Kühn. Temperature dependence of the fundamental absorption edge in $CuGaSe_2$. *Solid State Communications*, 27(4):449–451, 1978.

[77] M. Wagner, I. Dirnstorfer, D.M. Hofmann, M.D. Lampert, F. Karg, and B.K. Meyer. Characterization of Cu(In,Ga)Se_2 Thin Films - Part I Cu rich layers. *physica status solidi (a)*, 167(1):131–142, 1998.

[78] K. Yoshino, T. Shimizu, A. Fukuyama, K. Maeda, P.J. Fons, A. Yamada, S. Niki, and T. Ikari. Temperature dependence of photoacoustic spectra in $CuInSe_2$ thin films grown by molecular beam epitaxy. *Solar Energy Materials and Solar Cells*, 50(1-4):127–132, 1998.

[79] M. Quintero, C. Rincón, and P. Grima. Temperature variation of energy gaps and deformation potentials in $CuGa(S_zSe_{1-z})_2$ semiconductor alloys. *Journal of applied physics*, 65(7):2739–2743, 1989.

[80] N.N. Syrbu, M. Bogdanash, V.E. Tezlevan, and I. Mushcutariu. Lattice vibrations in $CuIn_{1-x}Ga_xSe_2$ crystals. *Physica B: Condensed Matter*, 229(2):199–212, 1997.

[81] P.W. Li and R. Anderson. Dielectric Constant of $CuInSe_2$ by Capacitance Measurements. *Journal of Physics and Chemistry of Solids*, 40(4):333–334, 1979.

[82] N.F. Mott. *Metal-insulator transitions*. Taylor & Francis, 1990.

[83] S.A. Schumacher, J.R. Botha, and V. Alberts. Photoluminescence study of potential fluctuations in thin layers of Cu(In,Ga)$(S,Se)_2$. *Journal of Applied Physics*, 99:063508, 2006.

[84] E. Zacks and A. Halperin. Dependence of the Peak Energy of the Pair-Photoluminescence Band on Excitation Intensity. *Physical Review B*, 6(8):3072, 1972.

[85] D.G. Thomas, J.J. Hopfield, and W.M. Augustyniak. Kinetics of radiative recombination at randomly distributed donors and acceptors. *Phys. Rev*, 140:202, 1965.

[86] N. Rega, S. Siebentritt, J. Albert, S. Nishiwaki, A. Zajogin, M.C. Lux-Steiner, R. Kniese, and M.J. Romero. Excitonic luminescence of Cu(In, Ga)Se_2. *Thin solid films*, 480:286–290, 2005.

[87] D. Kovalev, B. Averboukh, D. Volm, B.K. Meyer, H. Amano, and I. Akasaki. Free exciton emission in GaN. *Physical Review B*, 54(4):2518, 1996.

[88] C. F. Klingshirn. *Semiconductor Optics*. Springer Berlin Heidelberg New York, 2006.

[89] L. Gütay, J.K. Larsen, J. Guillot, M. Müller, F. Bertram, J. Christen, and S. Siebentritt. MOVPE of $CuGaSe_2$ on GaAs in presence of a Cu_xSe secondary phase. *Journal of Crystal Growth*, 315:82–86, 2010.

[90] B.I. Shklovskii and A.L. Efros. *Electronic properties of doped semiconductors*, volume 1. Springer-Verlag, 1979.

[91] S. Siebentritt, I. Beckers, T. Riemann, J. Christen, A. Hoffmann, and M. Dworzak. Reconciliation of luminescence and Hall measurements on the ternary semiconductor $CuGaSe_2$. *Applied Physics Letters*, 86(9):091909–091909, 2005.

[92] U. Rau, K. Taretto, and S. Siebentritt. Grain boundaries in Cu(In,Ga)$(Se,S)_2$ thin–film solar cells. *Applied Physics A: Materials Science & Processing*, 96(1):221–234, 2009.

[93] G.B. Stringfellow. *Organometallic Vapor–Phase Epitaxy: Theory and Practice*. Academic Press, 2 edition, 1999.

[94] R.K. Jones, P. Hebert, P. Pien, R.R. King, D. Bhusari, R. Brandt, O. Al Taher, C. Fetzer, J. Ermer, A. Boca, et al. Status of 40% production efficiency concentrator cells at Spectrolab. In *Proceedings of the 35th IEEE Photovoltaic Specialists Conference*, pages 189–195, 2010.

[95] *Laytec Epiras 200 manual*.

[96] S. Chichibu, S. Shirakata, S. Isomura, and H. Nakanishi. Visible and Ultraviolet Photoluminescence from Cu-III-VI_2 Chalcopyrite Semiconductors Grown by Metalorganic Vapor Phase Epitaxy. *Japanese Journal of Applied Physics*, 36:1703–1714, 1997.

[97] P.W. Lee, T.R. Omstead, D.R. McKenna, and K.F. Jensen. In situ mass spectroscopy and thermogravimetric studies of GaAs MOCVD gas phase and surface reactions. *Journal of Crystal Growth*, 85(1-2):165–174, 1987.

[98] N.I. Buchan, C.A. Larsen, and G.B. Stringfellow. Mass spectrometric studies of trimethylindium pyrolysis. *Journal of Crystal Growth*, 92(3-4):591–604, 1988.

[99] G.H. Fan, N. Maung, T.L. Ng, P.F. Heelis, J.O. Williams, A.C. Wright, D.F. Foster, and D.J. Cole-Hamilton. Thermal decomposition of di-tertiarybutyl selenide and dimethylzinc in a metalorganic vapour phase epitaxy reactor. *Journal of crystal growth*, 170(1-4):485–490, 1997.

[100] Shinriki. United states patent, no. 5,973,402, 1999.

[101] M.C. Artaud-Gillet, S. Duchemin, R. Odedra, G. Orsal, N. Rega, S. Rushworth, and S. Siebentritt. Evaluation of copper organometallic sources for $CuGaSe_2$ photovoltaic applications. *Journal of crystal growth*, 248:163–168, 2003.

[102] K. Oishi, S. Kobayashi, S. Ohta, N. Tsuboi, and F. Kaneko. Orientation of $CuGaS_2$ thin films on (100) GaAs and GaP substrates. *Journal of crystal growth*, 177(1-2):88–94, 1997.

[103] T. Kampschulte. *MOCVD von ZnSe für Sperrkontakte in Heterosolarzellen auf der Basis von Chalkopyriten*. PhD thesis, Freie Universität Berlin, 1998.

[104] E. Wallin, T. Jarmar, U. Malm, M. Edoff, and L. Stolt. Influence of the average Se–to–metal overpressure during co–evaporation of $Cu(In_xGa_{1-x})Se_2$. *Thin Solid Films*, In press:–, 2011.

[105] G. Hanna, J. Mattheis, V. Laptev, Y. Yamamoto, U. Rau, and H.W. Schock. Influence of the selenium flux on the growth of $Cu(In,Ga)Se_2$ thin films. *Thin Solid Films*, 431:31–36, 2003.

[106] A. Meeder, D. Fuertes Marrón, V. Tezlevan, E. Arushanov, A. Rumberg, T. Schedel-Niedrig, and M.C. Lux-Steiner. Radiative recombination in CVT-grown $CuGaSe_2$ single crystals and thin films. *Thin solid films*, 431:214–218, 2003.

[107] A. Meeder, D. Fuertes Marrón, V. Chu, J.P. Conde, A. Jäger-Waldau, A. Rumberg, and M.C. Lux-Steiner. Photoluminescence and sub band gap absorption of $CuGaSe_2$ thin films. *Thin solid films*, 403:495–499, 2002.

[108] M.V. Yakushev, Y. Feofanov, R.W. Martin, R.D. Tomlinson, and A.V. Mudryi. Magneto–photoluminescence study of radiative recombination in $CuInSe_2$ single crystals. *Journal of Physics and Chemistry of Solids*, 64(9-10):2011–2016, 2003.

[109] J.H. Schön and E. Bucher. Excitonic luminescence in $CuInSe_2$. *Applied Physics Letters*, 73(2):211–213, 1998.

[110] G. Marin, S.M. Wasim, C. Rincón, G. Sanchez Perez, Ch. Power, and A.E. Mora. Temperature dependence of the fundamental absorption edge in $CuIn_3Se_5$. *Journal of Applied Physics*, 83(6):3364, 1998.

[111] A.J. Nelson, G.S. Horner, K. Sinha, and M.H. Bode. Ordered vacancy compound $CuIn_3Se_5$ on GaAs (100): Epitaxial growth and characterization. *Applied physics letters*, 64(26):3600–3601, 1994.

[112] J. F. Ramírez and C. Rincón. Polarized micro-Raman spectra in $CuGaSe_2$. *Solid state communications*, 84(5):551–556, 1992.

[113] V. Depredurand, Y. Aida, J.K. Larsen, T Eisenbarth, Majerus A, and S. Siebentritt. Surface treatment of solar cells grown under Cu–excess. In *Proceedings of the 37th IEEE Photovoltaic Specialists Conference*, pages 874–877, 2011.

[114] C.H. Lei, M. Duch, I.M. Robertson, and A.A. Rockett. Effects of solution-grown CdS on Cu(In,Ga)Se_2 grain boundaries. *Journal of applied physics*, 108:114908, 2010.

[115] J. Goldstein, D. Newbury, D. Joy, C. Lyman, P. Echlin, E. Lifshin, L. Sawyer, and J. Michael. *Scanning electron microscopy and X-ray microanalysis*, volume 1. Springer, third edition edition, 2003.

[116] D.C. Joy, D.E. Newbury, and D.L. Davidson. Electron channeling patterns in the scanning electron microscope. *Journal of Applied Physics*, 53(8):R81–R122, 1982.

[117] T.L. Matteson, S.W. Schwarz, E.C. Houge, B.W. Kempshall, and L.A. Giannuzzi. Electron backscattering diffraction investigation of focused ion beam surfaces. *Journal of electronic materials*, 31(1):33–39, 2002.

[118] B.H. Tseng, S.B. Lin, G.L. Gu, and W. Chen. Elimination of orientation domains and antiphase domains in the epitaxial films with chalcopyrite structure. *Journal of applied physics*, 79(3):1391–1396, 1996.

[119] National Institute of Standards and Technology (NIST). X–ray transition energy, June.

[120] Private communication with Jürgen Bläsing. University of Magdeburg, June 2010.

[121] D.D. Thornton. The gallium melting-point standard: a determination of the liquid-solid equilibrium temperature of pure gallium on the international practical temperature scale of 1968. *The Gallium melting-point standard*, -:719, 1977.

[122] C.D. Thurmond. Phase equilibria in the GaAs and the GaP systems. *Journal of Physics and Chemistry of Solids*, 26(5):785–802, 1965.

[123] G. Gagnon, A. Houdayer, J.F. Currie, and A. Azelmad. Rapid thermal annealing effect on near-surface stoichiometry of GaAs by heavy-ion Rutherford backscattering. *Journal of applied physics*, 70(2):1036–1038, 1991.

[124] D. Schroeder, A.A. Rockett, and G.D. Berry. Gallium Diffusion and Difussivity in $CuInSe_2$ epitaxial layers. *Applied Physics Letters*, 69(26):4068–4070, 1996.

[125] C. Xue, D. Papadimitriou, Y.S. Raptis, W. Richter, N. Esser, S. Siebentritt, and M.C. Lux-Steiner. Micro–Raman Study of Orientation Effects of CuSe–Crystallites on Cu–rich $CuGaSe_2$ Thin Films. *Journal of applied physics*, 96:1963, 2004.

[126] U. Fiedeler. *Rekombination und Diffusion in $CuGaSe_2$ Solarzellen: Photolumineszenz and Quanteneffizienzuntersuchungen an MOCVD gewachsenen Absorbern*. PhD thesis, Freie Universität Berlin, 2001.

[127] D.E. Aspnes and A.A. Studna. Dielectric functions and optical parameters of Si, Ge, GaP, GaAs, GaSb, InP, InAs, and InSb from 1.5 to 6.0 eV. *Physical Review B*, 27(2):985, 1983.

[128] K. Gartsman, L. Chernyak, V. Lyahovitskaya, D. Cahen, V. Didik, V. Kozlovsky, R. Malkovich, E. Skoryatina, and V. Usacheva. Direct evidence for diffusion and electromigration of Cu in $CuInSe_2$. *Journal of applied physics*, 82:4282, 1997.

[129] T.E. Haynes, W.K. Chu, T.L. Aselage, and S.T. Picraux. Initial evaporation rates from GaAs during rapid thermal processing. *Journal of applied physics*, 63(4):1168–1176, 1988.

[130] A. Piotrowska, E. Kaminska, S. Kwiatkowski, and A. Turos. Quantitative analysis of arsenic losses during the formation of Au (Zn)/p-GaAs ohmic contacts. *Journal of applied physics*, 73(9):4404–4408, 1993.

[131] M. Marudachalam, I. Hichri, R.W. Birkmire, J.M. Schultz, A.B. Swartzlander, and M.M. Al-Jassim. Diffusion of In and Ga in selenized Cu–In and Cu–Ga precursors. In *Proceedings of the 25th IEEE Photovoltaic Specialists Conference*, pages 805–807, 1996.

[132] M. Marudachalam, R.W. Birkmire, H. Hichri, J.M. Schultz, A. Swartzlander, and M.M. Al-Jassim. Phases, morphology, and diffusion in $CuInGaSe_2$ thin films. *Journal of Applied Physics*, 82:2896, 1997.

[133] H.J. Von Bardeleben. Selenium self–diffusion study in the $1–3–6_2$ semiconductor: $CuInSe_2$. *Journal of applied physics*, 56(2):321–326, 1984.

[134] S. Niki, P.J. Fons, A. Yamada, Y. Lacroix, H. Shibata, H. Oyanagi, M. Nishitani, T. Negami, and T. Wada. Effects of the surface $Cu_{2-x}Se$ phase on the growth and properties of $CuInSe_2$ films. *Applied physics letters*, 74:1630, 1999.

[135] R. Klenk, T. Walter, H.W. Schock, and D. Cahen. Physical Vapor Deposition of $CuInX_2$ (X= S, Se) Thin Films: A Model for the Growth Mechanism. *Solid State Phenomena*, 37:509–514, 1994.

[136] S. Yoon, S. Kim, V. Craciun, W.K. Kim, R. Kaczynski, R. Acher, T.J. Anderson, O.D. Crisalle, and S.S. Li. Effect of a Cu–Se secondary phase on the epitaxial growth of $CuInSe_2$ on (1 0 0) GaAs. *Journal of crystal growth*, 281(2-4):209–219, 2005.

[137] P. Fons, S. Niki, A. Yamada, and H. Oyanagi. Direct observation of the $Cu_{2-x}Se$ phase of Cu-rich epitaxial $CuInSe_2$ grown on GaAs (001). *Journal of applied physics*, 84(12):6926–6928, 1998.

[138] H. Lüth. *Solid surfaces, interfaces and thin films*. Springer, 2010.

[139] S. Tanuma, C.J. Powell, and D.R. Penn. Calculations of Electron Inelastic Mean Free Paths (IMFPs). *Surface and Interface Analysis*, 20:77–89, 1993.

[140] D. Schmid, M. Ruckh, F. Grunwald, and H.W. Schock. Chalcopyrite/defect chalcopyrite heterojunctions on the basis of $CuInSe_2$. *Journal of applied physics*, 73(6):2902–2909, 1993.

[141] S. Siebentritt, N. Papathanasiou, and M. Lux-Steiner. Photoluminescence excitation spectroscopy of highly compensated $CuGaSe_2$. *physica status solidi (b)*, 242(13):2627–2632, 2005.

[142] H.P. Gislason, B.H. Yang, and M.K. Linnarsson. Shifting photoluminescence band in high-resistivity Li-compensated GaAs. *Phys. Rev. B*, 47(15):9418–24, 1993.

[143] C. Kothandaraman, G.F. Neumark, and R.M. Park. Modified donor–acceptor pair luminescence in heavily nitrogen-doped zinc selenide. *Applied Physics Letters*, 67:3307, 1995.

[144] M. I. Alonso, K. Wakita, J. Pascual, M. Garriga, and N. Yamamoto. Optical functions and electronic structure of $CuInSe_2$, $CuGaSe_2$, $CuInS_2$ and $CuGaS_2$. *Phys. Rev. B*, 63(7):075203, Jan 2001.

[145] H. Nagel, C. Berge, and A.G. Aberle. Generalized analysis of quasi-steady-state and quasi-transient measurements of carrier lifetimes in semiconductors. *Journal of applied physics*, 86:6218, 1999.

[146] P. Würfel. *Physics of solar cells*. Wiley Online Library, 2005.

[147] W.K. Metzger, I.L. Repins, and M.A. Contreras. Long lifetimes in high-efficiency $Cu(In,Ga)Se_2$ solar cells. *Applied Physics Letters*, 93:022110, 2008.

[148] S. Shirakata and T. Nakada. Time-resolved photoluminescence in $Cu(In,Ga)Se_2$ thin films and solar cells. *Thin Solid Films*, 515(15):6151–6154, 2007.

[149] A.P. Levanyuk and V.V. Osipov. Edge luminescence of direct-gap semiconductors. *Soviet Physics Uspekhi*, 24:187, 1981.

[150] V.V. Osipov, T.I. Soboleva, and M.G. Foigel. Interimpurity radiative recombination in heavily doped semiconductors. *Sov. Phys. Semicond*, 11:752, 1977.

[151] P.W. Yu. Excitation dependent emission in Mg-, Be-, Cd-, and Zn- implanted GaAs. *J. Appl. Phys.*, 48(12):5043–51, 1977.

[152] S.H. Park and B.D. Choe. Interimpurity transitions in heavily doped semiconductors. *Journal of applied physics*, 68(11):5916–5918, 2009.

[153] J. Krustok, J. Raudoja, M. Yakushev, R.D. Pilkington, and H. Collan. On the shape of the close-to-band-edge photoluminescent emission spectrum in compensated $CuGaSe_2$. *physica status solidi (a)*, 173(2):483–490, 1999.

[154] M.J. Romero, K.M. Jones, J. AbuShama, Y. Yan, M.M. Al-Jassim, and R. Noufi. Surface-layer band gap widening in Cu(In, Ga)Se_2 thin films. *Applied Physics Letters*, 83:4731, 2003.

[155] M. Kauk, M. Altosaar, J. Raudoja, K. Timmo, T. Varema, M. Danilson, M. Grossberg, and E. Mellikov. The influence of doping with donor type impurities on the properties of $CuInSe_2$. *physica status solidi (c)*, 5(2):609–611, 2008.

[156] A.Y. Shik. *Electronic properties of inhomogeneous semiconductors*. CRC, 1995.

[157] E.O. Kane. Thomas-Fermi Approach to Impure Semiconductor Band Structure. *Phys. Rev.*, 131(1):79–88, 1963.

[158] A. Jagomägi, J. Krustok, J. Raudoja, M. Grossberg, M. Danilson, and M. Yakushev. Photoluminescence studies of heavily doped $CuInTe_2$ crystals. *Physica B: Condensed Matter*, 337(1-4):369–374, 2003.

[159] C.A. Gueymard, D. Myers, and K. Emery. Proposed reference irradiance spectra for solar energy systems testing. *Solar Energy*, 73(6):443–467, 2002.

[160] National Renewable Energy Laboratory (NREL). Reference solar irradiance spectrum AM 1.5 available at http://rredc.nrel.gov/solar/spectra/am1.5/. Downloaded July 2008.

[161] S. Siebentritt. Hole transport mechanisms in $CuGaSe_2$. *Thin solid films*, 480:312–317, 2005.

[162] D. Redfield, J.P. Wittke, and J.I. Pankove. Luminescent Properties of Energy-Band-Tail States in GaAs: Si. *Physical Review B*, 2(6):1830–1839, 1970.

[163] L. Gütay, D. Regesch, J.K. Larsen, Y. Aida, A. Redinger, S. Caneva, S. Schorr, C. Stephan, and S. Siebentritt. Experimental test of the theoretical feedback loop to stabilize the band gap in chalcopyrites. *Submitted*, -:–, 2011.

[164] G.H. Bauer, L. Gütay, and R. Kniese. Structural properties and quality of the photoexcited state in Cu $(In_{1-x}Ga_x)$ Se_2 solar cell absorbers with lateral submicron resolution. *Thin solid films*, 480:259–263, 2005.

[165] L. Gütay. *Konfokale Photolumineszenz von Cu(In,Ga)Se_2 - Charakterisierung optoelektronischer Eigenschaften mit lateraler Sub-Mikrometer-Auflösung*. PhD thesis, Universität Oldenburg, 2008.

[166] L. Gütay and G.H. Bauer. Non–uniformities of opto-electronic properties in Cu(In,Ga)Se_2 thin films and their influence on cell performance studied with confocal photoluminescence. In *Proceedings of the 34th IEEE Photovoltaic Specialists Conference*, pages 874–877, 2009.

[167] P. Würfel. The chemical potential of radiation. *Journal of Physics C: Solid State Physics*, 15:3967, 1982.

[168] G.H. Bauer, R. Brüggemann, S. Tardon, S. Vignoli, and R. Kniese. Quasi–Fermi level splitting and identification of recombination losses from room temperature luminescence in $Cu(In_{1-x}Ga_x)$ Se_2 thin films versus optical band gaps. *Thin solid films*, 480:410–414, 2005.

[169] L. Gütay and G.H. Bauer. Spectrally resolved photoluminescence studies on $Cu(In,Ga)Se_2$ solar cells with lateral submicron resolution. *Thin solid films*, 515(15):6212–6216, 2007.

[170] K. Bothe, G.H. Bauer, and T. Unold. Spatially resolved photoluminescence measurements on $Cu(In,Ga)Se_2$ thin films. *Thin solid films*, 403:453–456, 2002.

[171] E. Daub and P. Würfel. Ultralow values of the absorption coefficient of Si obtained from luminescence. *Physical review letters*, 74(6):1020–1023, 1995.

[172] R.E. Walpole, R.H. Myers, S.L. Myers, and K. Ye. *Probability and statistics for engineers and scientists*. Prentice Hall Upper Saddle River, 2002.

[173] D. Eich, U. Herber, U. Groh, U. Stahl, C. Heske, M. Marsi, M. Kiskinova, W. Riedl, R. Fink, and E. Umbach. Lateral inhomogeneities of $Cu(In,Ga)Se_2$ absorber films. *Thin solid films*, 361:258–262, 2000.

[174] N.G. Dhere, S.R. Ghongadi, MB Pandlt, A.A. Kadam, A.H. Jahagirdar, and V.S. Gade. AFM, micro-PL, and PV analyses of $CuIn_{1-x}Ga_xS_2$ thin films solar cells on stainless steel foil. In *Proceedings of the 29rd IEEE Photovoltaic Specialists Conference*, pages 876–879, 2002.

[175] P.O. Grabitz, U. Rau, B. Wille, G. Bilger, and J.H. Werner. Spatial inhomogeneities in $Cu(In,Ga)Se_2$ solar cells analyzed by an electron beam induced voltage technique. *Journal of applied physics*, 100:124501, 2006.

[176] Y. Yan, R. Noufi, K.M. Jones, K. Ramanathan, M.M. Al-Jassim, and B.J. Stanbery. Chemical fluctuation–induced nanodomains in $Cu(In,Ga)Se_2$ films. *Applied Physics Letters*, 87(12):121904–121904, 2005.

[177] H. Mönig, R. Caballero, C.A. Kaufmann, T.L. Schmidt, M.C. Lux-Steiner, and S. Sadewasser. Nanoscale investigations of the electronic surface properties of $Cu(In,Ga)Se_2$ thin films by scanning tunneling spectroscopy. *Solar Energy Materials and Solar Cells*, 95(1):1537–1543, 2010.

[178] J.K. Larsen, L. Gütay, Y. Aida, and S. Siebentritt. Spatial variations of optoelectronic properties in single crystalline $CuGaSe_2$ thin films studied by photoluminescence. *Thin Solid Films*, 519 (21):7332–7336, 2011.

[179] U. Rau and J.H. Werner. Radiative efficiency limits of solar cells with lateral band-gap fluctuations. *Applied physics letters*, 84:3735, 2004.

[180] L. Gütay and G.H. Bauer. Lateral variations of optoelectronic quality of $Cu(In_{1-x}Ga_x)$ Se_2 in the submicron–scale. *Thin solid films*, 487(1-2):8–13, 2005.

[181] F. Heidemann, R. Brüggemann, and G.H. Bauer. The correlation between local defect absorbance and quasi–Fermi level splitting in $CuInS_2$ from photoluminescence. *Journal of Physics D: Applied Physics*, 43:145103, 2010.

[182] F. Heidemann, L. Gütay, A. Meeder, and G.H. Bauer. Ensemble analyses by Minkowski–operations for spatially resolved structural and optoelectronic features of Cu(In,Ga)(Se_2,S_2) absorbers. *Thin Solid Films*, 517(7):2427–2430, 2009.

[183] *Piezosystem Jena: Manual for Tritor 102 piezo translation stage*.

[184] R. Caballero, C. Guillén, M.T. Gutiérrez, and C.A. Kaufmann. $CuIn_{1-x}Ga_xSe_2$–based thin–film solar cells by the selenization of sequentially evaporated metallic layers. *Progress in Photovoltaics: Research and Applications*, 14(2):145–153, 2006.

[185] I.V. Bodnar, A.G. Karoza, and G.F. Smirnova. Lattice reflectivity spectra of $CuGaS_2$-$CuGaSe_2$ solid solutions. *physica status solidi (b)*, 84(1):k65–k69, 1977.

[186] G. Brown, V. Faifer, A. Pudov, S. Anikeev, E. Bykov, M. Contreras, and J. Wu. Determination of the minority carrier diffusion length in compositionally graded Cu(In,Ga)Se_2 solar cells using electron beam induced current. *Applied Physics Letters*, 96(2):022104–022104, 2010.

[187] S. Siebentritt, A. Gerhard, S. Brehme, and M.C. Lux-Steiner. Composition Dependent Doping and Transport Properties of $CuGaSe_2$. In *Materials research society symposium proceedings*, volume 668, page 4, 2001.

[188] I. Repins, M. Contreras, M. Romero, Y. Yan, W. Metzger, J. Li, S. Johnston, B. Egaas, C. DeHart, J. Scharf, B.E. McCandless, and R. Noufi. Characterization of 19.9%-efficient CIGS absorbers. In *Proceedings of the 33rd IEEE Photovoltaic Specialists Conference*, pages 1–6, 2008.

[189] M. Quintero, C. Rincon, R. Tovar, and J.C. Woolley. Optical energy gap values and deformation potentials in four Cu-III-VI_2 chalcopyrite compounds. *Journal of Physics: Condensed Matter*, 4:1281, 1992.

[190] T. Kawashima, S. Adachi, H. Miyake, and K. Sugiyama. Optical constants of $CuGaSe_2$ and $CuInSe_2$. *Journal of applied physics*, 84:5202, 1998.

[191] H. Weinert, H. Neumann, H.J. Höbler, G. Kühn, and N. Van Nam. Infrared Faraday Effect in n-Type $CuInSe_2$. *physica status solidi (b)*, 81(1):K59–K61, 1977.

[192] E. Arushanov, L. Essaleh, J. Galibert, J. Leotin, M.A. Arsene, J.P. Peyrade, and S. Askenazy. Shubnikov–de Haas oscillations in n-$CuInSe_2$. *Applied physics letters*, 61(8):958–960, 1992.

[193] H. Neumann, W. Kissinger, H. Sobotta, V. Riede, and G. Kühn. Hole effective masses in $CuInSe_2$. *physica status solidi (b)*, 108(2):483–487, 1981.

[194] T. Irie, S. Endo, and S. Kimura. Electrical properties of p-and n-type $CuInSe_2$ single crystals. *Japanese Journal of Applied Physics*, 18(7):1303–1310, 1979.

[195] S.M. Wasim. Transport properties of $CuInSe_2$. *Solar cells*, 16:289–316, 1986.

[196] H. Neumann. Influence of intrinsic defects on the electrical properties of AIBIIIC$_2$VI compounds. *Crystal Research and Technology*, 18(4):483–490, 1983.

[197] W. Hörig, H. Neumann, H. Sobotta, B. Schumann, and G. Kühn. The optical properties of $CuInSe_2$ thin films. *Thin Solid Films*, 48(1):67–72, 1978.

[198] D. Abou-Ras, S. Schorr, and HW Schock. Grain-size distributions and grain boundaries of chalcopyrite-type thin films. *Journal of Applied Crystallography*, 40(5):841–848, 2007.

[199] M. Birkholz. *Thin film analysis by X-ray scattering*. Wiley–VCH, 2nd edition, 2009.

[200] C.S. Fadley. *Basic Concepts of X–ray Photoelectron spectroscopy in Electron spectroscopy*, volume 2. Mittal Publications, 1978.

[201] Private communication with Nathalie Valle. CRP Lippmann, Luxembourg, June 2011.

[202] Y. Gao. A new secondary ion mass spectrometry technique for III-V semiconductor compounds using the molecular ions CsM^+. *Journal of applied physics*, 64(7):3760–3762, 1988.

[203] B.G. Yacobi and D.B. Holt. *Cathodoluminescence microscopy of inorganic solids*. Springer, 1990.

[204] B.G. Yacobi and D.B. Holt. Cathodoluminescence scanning electron microscopy of semiconductors. *Journal of applied physics*, 59(4):R1–R24, 1986.

[205] M.J. Romero, K. Ramanathan, M.A. Contreras, M.M. Al-Jassim, R. Noufi, and P. Sheldon. Cathodoluminescence of $Cu(In,Ga)Se_2$ thin films used in high–efficiency solar cells. *Applied physics letters*, 83:4770, 2003.

[206] M. Schirra, A. Reiser, GM Prinz, A. Ladenburger, K. Thonke, and R. Sauer. Cathodoluminescence study of single zinc oxide nanopillars with high spatial and spectral resolution. *Journal of applied physics*, 101:113509, 2007.

[207] J. Christen, M. Grundmann, and D. Bimberg. Scanning cathodoluminescence microscopy: A unique approach to atomic-scale characterization of heterointerfaces and imaging of semiconductor inhomogeneities. *Journal of Vacuum Science & Technology B: Microelectronics and Nanometer Structures*, 9(4):2358–2368, 1991.